

Flow and Plate Motion in Compressor Valves

Flow and Plate Motion in Compressor Valves
R.A. Habing

Cover Image: 4-stage reciprocating compressor system, Courtesy of Ariel Corporation

Thesis University of Twente, Enschede - With ref. - With summary in Dutch.
ISBN 90-365-2179-3

Copyright ©2005 by R.A. Habing, Enschede, The Netherlands

FLOW AND PLATE MOTION IN COMPRESSOR VALVES

PROEFSCHRIFT

ter verkrijging van
de graad van doctor aan de Universiteit Twente,
op gezag van de rector magnificus,
prof. dr. W.H.M. Zijm,
volgens besluit van het College voor Promoties
in het openbaar te verdedigen
op vrijdag 29 april 2005 om 16.45 uur

door

Reinder André Habing

geboren op 30 juli 1975
te Hengelo (O)

Dit proefschrift is goedgekeurd door de promotoren:

prof. dr. ir. H.W.M. Hoeijmakers

en

prof. dr. ir. A. Hirschberg

en de assistent-promotor:

dr. ir. R. Hagmeijer

TABLE OF CONTENTS

<i>Nomenclature</i>	v
1 Introduction	1
1.1 Motivation of Research	1
1.2 Dimensionless Numbers	4
1.3 Objective and Approach	7
1.4 Outline of Thesis	8
2 Valves in Nature and Engineering	11
2.1 Introduction	11
2.2 Survey of Literature	12
2.2.1 Non-Compressor Valves	12
2.2.2 Compressor Valves	15
2.2.3 Summary of Valve Theories	17
2.3 Valves and Fluid Dynamics	19
3 Valve Theory	25
3.1 Introduction	25
3.2 Basic Valve Theory	25
3.3 Analysis of Basic Valve Theory	28
3.3.1 Semi-Empirical Coefficients	28
3.3.2 Linear Stability Analysis	31
3.3.3 Non-Linear Time Domain Analysis	39
3.4 Extended Valve Theory	44
3.4.1 Hovering Insect Flight	44
3.4.2 Unsteady Valve Flow	45
3.5 Diagnostics of Leaking Valves in Reciprocating Compressors	49
4 Computational Fluid Dynamics	55
4.1 Introduction	55
4.2 Flow Solver	56
4.3 Local Preconditioning	64
4.3.1 Literature Survey	64
4.3.2 Time-Derivative Preconditioning	66

4.3.3	Boundary Conditions	71
4.3.4	Flux Scheme	73
4.3.5	Time Accuracy	74
4.4	Test Cases	76
5	Laboratory Experiments	87
5.1	Introduction	87
5.2	Design of Model Valve	88
5.3	Experimental Setup	90
5.4	Valve Plate Displacement	91
5.5	Static Measurements	92
5.5.1	Valve Pressure Difference	92
5.5.2	Valve Volume-Flow Rate	93
5.6	Dynamic Measurements: Two-Microphone Method	93
5.6.1	Introduction	93
5.6.2	Wave Reconstruction	94
5.6.3	Time and Frequency Filtering	96
5.7	Mechanical Parameters of Valve	98
6	Valve Dynamics	101
6.1	Semi-Empirical Coefficients	101
6.1.1	Laboratory Experiments	101
6.1.2	Computational Fluid Dynamics	102
6.1.3	Reverse Flow	109
6.2	Unsteady Flow	112
6.2.1	Restitution Coefficient	112
6.2.2	Validation of Basic Valve Theory	112
6.3	Model Valve versus Compressor Valve	116
7	Conclusions and Discussion	119
7.1	Conclusions	119
7.2	Discussion	122
A	Nearly Incompressible Flow	125
A.1	Local Mach Number	125
A.2	Global Mach Number	126
B	Two-Stage Air Compressor	129
B.1	Nomenclature	129
B.2	Governing Equations	131
B.3	Input Parameters	134
C	Vena Contracta	135
C.1	Theory	135
C.2	Computational Fluid Dynamics	137
	References	141

<i>Summary</i>	149
<i>Samenvatting (Summary in Dutch)</i>	151
<i>Dankwoord (Acknowledgements in Dutch)</i>	155
<i>Curriculum Vitae (in Dutch)</i>	157

NOMENCLATURE

(Most symbols used once and explained in the text are not listed.)

Symbol	Description	Unit
A_p	valve port area	m^2
C_p	specific heat at constant pressure	J/kgK
C_v	specific heat at constant volume	J/kgK
CFL	Courant-Friedrich-Lewy number	-
c	speed of sound	m/s
c_g	gas force coefficient of valve	-
d_{sr}	sealing rim length of valve	m
E	total energy density	J/kg
e_{res}	restitution coefficient	-
F_g	gas force acting on valve plate	N
H	total enthalpy density	J/kg
h	valve opening	m
h_e	enthalpy density	J/kg
h_{max}	maximum valve opening	m
h_{pl}	preload distance	m
i	$\sqrt{-1}$	-
k	spring stiffness	N/m
\bar{k}	wavenumber	m^{-1}
k_c	characteristic condition number	-
$k^{(2)}, k^{(4)}$	artificial dissipation coefficients	-
L_g	total edge length of valve plate	m
L_p	valve port length	m
M	local Mach number	-
m	effective plate mass	kg
\mathbf{n}	unit normal vector	-
p	static pressure	Pa
p_{atm}	atmospheric pressure	Pa
p_{up}	pressure of flow at valve inlet	Pa

R	ideal gas constant	J/kgK
R_1	inner radius of model valve plate	m
R_2	outer radius of model valve plate	m
Re	Reynolds number	-
r	radial position	m
Sh	Shear number	-
St	Strouhal number	-
T	temperature	K
t	time	s
t^-	time instant just before collision	s
t^+	time instant just after collision	s
U_r	preconditioning reference velocity	m/s
u, v, w	Cartesian components of the velocity vector	m/s
V	volume	m ³
x, y, z	Cartesian coordinates	m
Y	admittance of pipe	m ⁴ s/kg

Greek Symbols

α	vena contracta factor of valve	-
β	complex-valued circular frequency	s ⁻¹
$\beta^{(4)}$	artificial dissipation coefficient	-
γ	ratio of specific heats ($= C_p/C_v$)	-
Δp	pressure difference across valve	Pa
Δt	time-step	s
ϵ	preconditioning cut-off parameter	-
$\epsilon^{(2)}, \epsilon^{(4)}$	artificial dissipation coefficients	-
ϵ_c	valve flow compressibility factor	-
ζ	damping constant of spring	Ns/m
θ	inclination of plate	rad
μ	dynamic viscosity	Pas
ν	kinematic viscosity ($= \mu/\rho$)	m ² /s

ρ	mass density	kg/m^3
ρ_{up}	mass density of flow at valve inlet	kg/m^3
Φ_v	volume-flow rate in valve	m^3/s
ω	real-valued circular frequency	s^{-1}

Notations

\dot{s}	time derivative of s , i.e. $\frac{ds}{dt}$
[...]	functional argument
$\text{sign}[s]$	sign of s ($\text{sign}[s] = 1$ for $s > 0$ and $\text{sign}[s] = -1$ for $s < 0$)
δs	variation or accuracy of s
s	vector (bold normal)
S	matrix (bold capital)

Abbreviations

1D	one-dimensional
2D	two-dimensional (planar)
3D	three-dimensional
CFD	computational fluid dynamics
Eq.	equation
Fig.	figure
JST	Jameson-Schmidt-Turkel (flux scheme)

1.1 Motivation of Research

Reciprocating compressors are widely used in gas transportation, gas storage and petrochemical industries. Reciprocating compressors are able to compress gas in a wide range of pressure ratios within a large range of flow rates (e.g. Cierniak 2001). The compressor can be considered as the heart of an installation and must operate reliably for several years. A schematic diagram of a reciprocating compressor is shown in Fig. 1.1. Characteristic of the way of op-

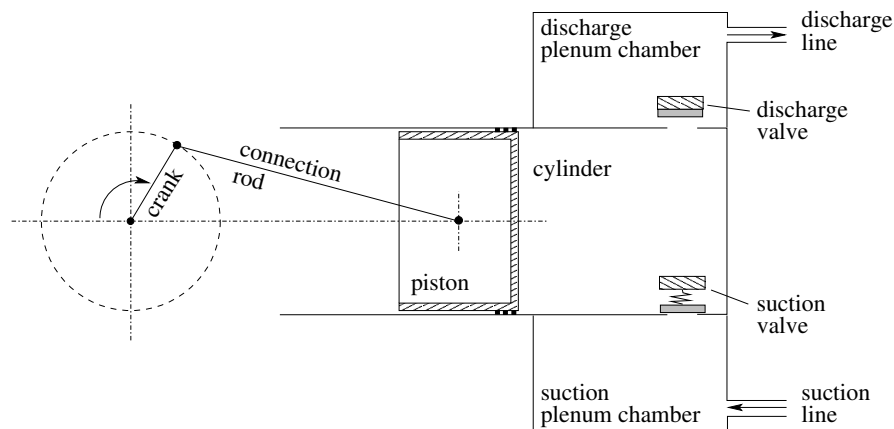


FIGURE 1.1: Sketch of a single-acting reciprocating compressor.

eration of such a compressor is: i) a periodically increasing and decreasing chamber volume (cylinder) controlled by the action of a reciprocating piston, and ii) suction and discharge of gas governed by ports which are alternatively opened and closed at certain intervals. These opening and closing elements are called valves. Fig. 1.2 shows the indicator diagram and opening of valves during a cycle for the case of an ideal working compressor, i.e. isentropic compression and expansion of a calorically perfect gas with fully closed valves. During discharge at pressure p_d the suction valve is assumed to be fully closed and the discharge valve is assumed to be fully open. During suction at pressure p_s the discharge valve is assumed to be fully closed and the suction valve is assumed to be fully open. However, actual compressor

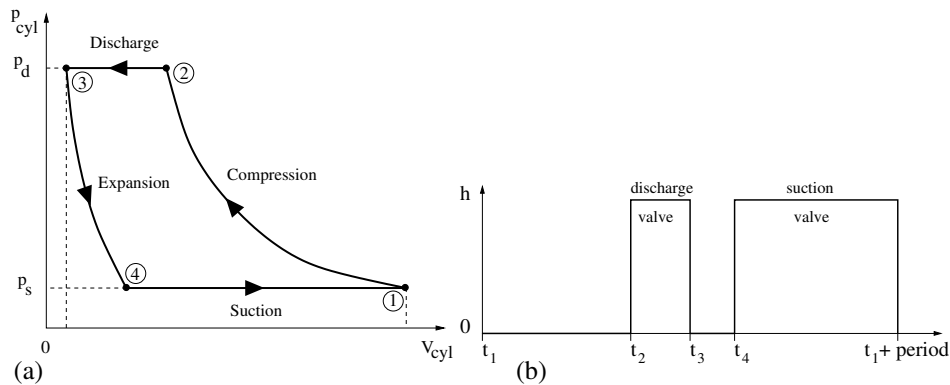


FIGURE 1.2: *Ideal reciprocating compressor cycle: (a) indicator diagram (p_{cyl} is the cylinder pressure, V_{cyl} is the cylinder volume), (b) opening of valves.*

cycles show a different behaviour, i.e. during discharge and suction, respectively, the cylinder pressure reaches values above p_d and below p_s , respectively, as a result of pressure losses in the valves. These valve pressure drops can introduce expensive pressure losses (e.g. Frenkel 1969). Furthermore, the valves can show flutter, i.e. the valve opening h does not always behave like a step function in time t as shown in Fig. 1.2b, but often shows oscillations*.

At the end of the 19th century a newspaper presented the Hall air compressor[†]. The last sentence of that article showed a rather optimistic view about the lifetime of these compressors: "(...) and they are not liable to get out of order, even when run at high speeds". However, a compressor is a complex machine and many things can go wrong. A worldwide distributed and returned questionnaire (Leonard 1996) identifies the compressor valves as primary cause (36%) of unscheduled reciprocating compressor shutdowns (Fig. 1.3a). This figure only

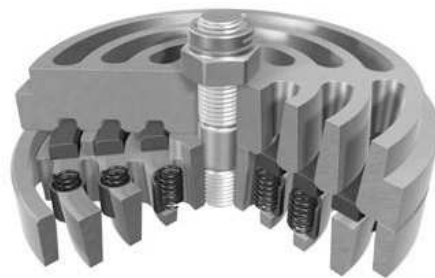
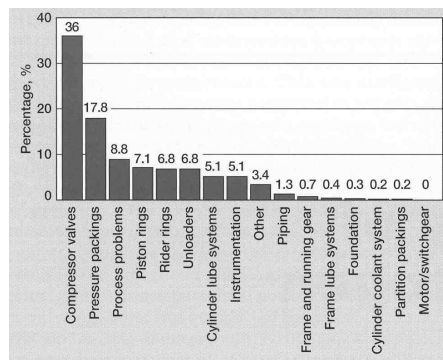


FIGURE 1.3: (a) *Unscheduled reciprocating compressor shutdowns. From Leonard (1996).* (b) *Example of a compressor valve. From <http://www.hoerbiger-compression.com>.*

*In Section 3.5 a reciprocating compressor system is considered quantitatively. The simulations show some non-ideal behaviour as discussed above.

[†]The Hall air-compressor, *Science* (1889) **14**, 431-432.

shows the reliability of an operating compressor. However, human error in maintenance can account for up to 15% of machine failures (Middleton 2001). Fig. 1.3b shows the geometry of a typical valve as it is used today, indicating its geometric complexity. It is designed to avoid, minimize, or delay, typical damage during operational conditions, e.g. i) fracture of sealing elements due to liquid slugs or high impact speeds resulting from stiction, ii) spring failure, and iii) high pressure losses due to clogging of flow channels. Examples of failure are given in Fig. 1.4. Practice shows that there is a direct connection between impact speed and

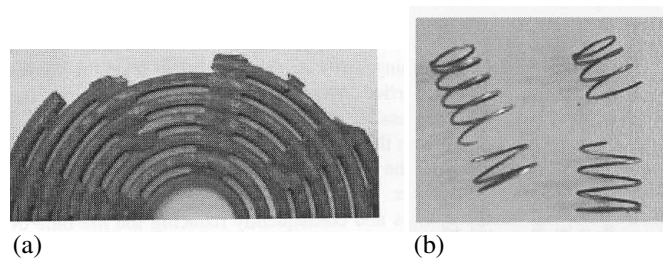


FIGURE 1.4: (a) Impact failure of valve plate caused by stiction. (b) Spring failure due to abrasive wear. From Stehr et al. (2003).

fracture behaviour. Non-parallel collisions can lead to locally high loads, crack generation and eventually fracture. Crack growth models have been reported in literature (e.g. Pandey and Chand 2003). Böswirth (2000) formulated a hypothesis to explain valve fracture:

- The cause of fracture is the *non-parallel* impact of the plate with high impact speed. The occurrence of valve plate tilting -especially at the closing event- is in practice a highly frequent phenomenon.
- At non-parallel impact large local peak values of the tangential tensions are generated because of the so-called *Dynamic Stress Concentration Effect*. This effect occurs when the propagation speed of the contact front equals the speed of the elasticity waves, which induces a strong increasing tension peak leading to radial cracks. The general tension level resulting from elasticity waves causes cracks to grow until fracture occurs.

This Dynamic Stress Concentration Effect has been observed in numerical simulations by Spiegl et al. (1999). At present the usual method to aim at sufficiently long valve lifetime is twofold. Firstly, the impact velocity is reduced by making use of computer simulations of plate motion and changing design parameters. Either traditional valve models are employed (Section 3.5) or mechanical stresses in a colliding plate are computed without taking into account gas flow behaviour. Secondly, non-parallel collisions are reduced by increasing the distance between springs and by using non-linear springs.

1.2 Dimensionless Numbers

For more than a hundred years reciprocating compressors have been the 'working horses' boosting the pressure of gases in various consumer and industrial applications. Much of the design knowledge has been acquired by experience, rather than by academic research (Steinrück 2003). The process for the market release of a new compressor valve usually consists of i) the prototype phase, in which different design principles are investigated, and ii) the field test phase, in which the life time requirements have to be met (Ottitsch and Scarpinato 2000). The prototype phase consists of finding a compromise between e.g. the available effective valve area, the required spring force for closing of the sealing element, the allowable valve pressure losses and the required operating conditions.

Prediction of the behaviour of the flow and the structural dynamics of a compressor valve by academic research encounters several difficulties. Most of these difficulties are related to fluid dynamical phenomena, i.e. the flow is expected to be a three-dimensional turbulent compressible flow, with i) fast transient (i.e. unsteady) processes, ii) large variations in local Mach number, iii) moving solid boundaries with complex geometries (and possibly plate elasticity waves) and iv) possibly multi-phase flow due to lubrication oil contamination and condensation. Additionally, the inlet and outlet boundary conditions of the valve flow are difficult to formulate because of the interaction of the valve with its environment (i.e. cylinder and plenum chamber / piping system). In some compressors the piston even overlaps the valve ports at minimum cylinder volume. In order to formulate the objective of our research we reduce the problem of compressor valves to the problem of a calorically perfect gas flowing through a valve with a single rigid plate.

Although structural details may differ considerably, the principle of operation of all types of automatic valves is similar (Touber 1976). Therefore, it is possible to distinguish the same basic functional elements in valves of different design, see Fig. 1.5. Consider the suction-

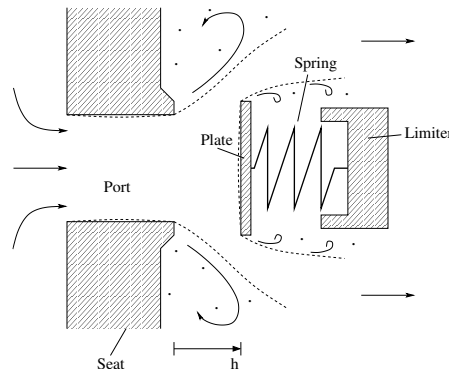


FIGURE 1.5: Sketch of a compressor valve with details of various elements (h denotes the valve opening).

and discharge of gas, respectively. When gas is flowing from the high pressure side in the plenum chamber or cylinder, respectively, through the port, it separates at the edges of seat and plate. Because of the action of the gas force the plate is pushed against the limiter (also

referred to as guard), which is assumed to be fixed in space (in absence of damper plates). Fig. 1.6 shows a typical time history of the valve opening h as function of time t . Initially the

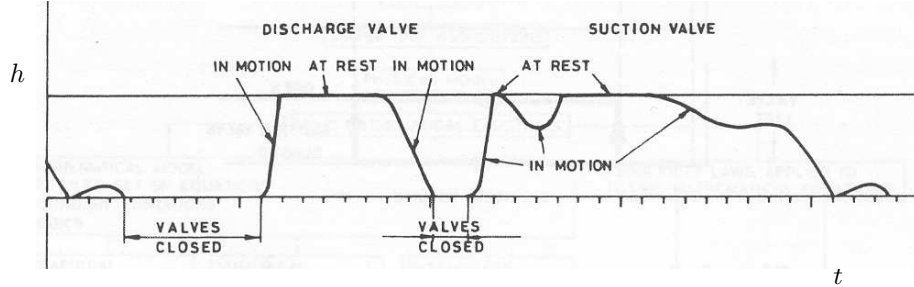


FIGURE 1.6: Typical valve opening in a real compressor cycle. After Touber (1976).

valve plate is pressed against the seat. The leakage flow through the valve is determined by the equilibrium between the pressure gradient force along the flow channel and the viscous force. A lubrication theory assuming a fully developed viscous channel flow will be adequate because $\frac{Uh^2}{\nu L} \ll 1$, where U is the characteristic flow speed, ν is the kinematic viscosity and L is the channel length. As the valve opens ($\dot{h} > 0$) stiction effects due to the unsteady viscous flow force and possibly the presence of oil will be important. When stiction has been reduced the valve opens quite rapidly to reach its maximum opening h_{max} , as the plate is pressed against the limiter. For a typical design, the valve plate is light in order to reduce the time delay due to inertia. During this opening phase the flow through the valve will need a time interval of the order L/U to approach a quasi-steady condition, where $U \equiv \sqrt{\frac{2}{\rho} \Delta p}$ for a given pressure difference Δp across the valve and a fluid density ρ . The typical ratio of opening time τ and convection time L/U is

$$\frac{\tau U}{L} = \mathcal{O}(10^2), \quad (1.1)$$

so that the flow is quasi-steady during the opening event. A second effect of the opening event is that the valve plate pushes away the air cushion between the downstream-facing side of the plate and the limiter. This results in an essentially unsteady flow which we will assume to be inviscid. The flow separation at the edges of the valve will result in turbulent free jets in which energy is dissipated. This dissipation and the resulting pressure built up in the air cushion will slow down the valve as it approaches the limiter. Potential rebound of the plate will be countered by the resulting low pressure in this air cushion when the valve tries to move away from the limiter. Valve closure will only occur when the pressure difference across the valve has dropped sufficiently to allow the spring force to close the valve. This complex behaviour induced by the presence of the air cushion at the limiter results in an effectively zero recovery of the plate kinetic energy during the interaction with the limiter. The collision is non-elastic. The interaction between the valve and its environment ($\frac{d}{dt} \Delta p$) is responsible for a relatively slow valve closing compared to the valve opening. The closing event of the valve is rather complex. It is postulated that the plate hits the seat at one point because the plate is not parallel to the seat. This results in a rocking motion with several rebounds because there is some kinetic energy recovery during a collision.

One could characterize the flow through the valve during most of its cycle as a quasi-steady subsonic flow with a high Reynolds number. In terms of the Strouhal number St based on the piston frequency f and the flow channel length L we have

$$St \equiv \frac{fL}{U} = \mathcal{O}(10^{-4}) \ll 1, \quad (1.2)$$

so that a quasi-steady flow approximation could be reasonable. The typical Reynolds number is

$$Re \equiv \frac{Uh_{max}}{\nu} = \mathcal{O}(10^4) \gg 1, \quad (1.3)$$

so that the free jets formed by flow separation at the valve outlet will be turbulent. The channel geometry ratio is

$$\frac{h_{max}}{L} = \mathcal{O}(1), \quad (1.4)$$

which implies that we do not expect the establishment of a fully developed channel flow, i.e. we expect $Re \frac{h_{max}}{L} \gg 1$. Because the flow will remain subsonic, i.e.

$$M \equiv \frac{U}{c} < 1, \quad (1.5)$$

where c is the speed of sound, compressibility effects are considered to be corrections of essentially incompressible flow behaviour.

In the present study we focus on all the flow conditions as described above. The viscous dominated flow for very small valve openings or the unsteady flow in the air cushion between the plate and the limiter will only be discussed briefly. Characterization of compressor valves requires determination of a large number of parameters. Some important parameters are presented in Table 1.1. These parameters are applicable to a broad range of different types of

TABLE 1.1: *Range of important parameters for compressor valves.*

Description	Value
maximum plate height	1 - 3 mm
port area	15 - 35 cm ²
resonance frequency	20 - 80 Hz
discharge pressure	(25 - 250) × 10 ⁵ Pa
piston frequency	10 - 30 Hz
process gas	H ₂ , CO ₂ , CO, NH ₃ , air

compressor valves and their range is estimated from data available in the literature.

1.3 Objective and Approach

In order to obtain results which are applicable to valves of different design, we consider the valve as a *black box*, see Fig. 1.7. The overall behaviour of a compressor valve is described in

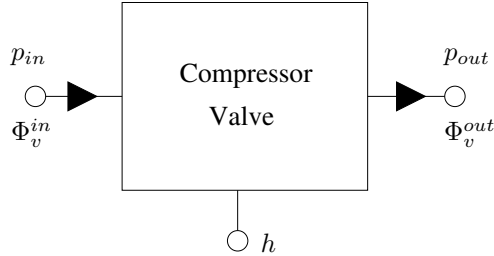


FIGURE 1.7: Sketch of a compressor valve as a black box (p is the pressure, Φ_v is the volume-flow rate and h is the valve opening).

terms of valve parameters (such as semi-empirical flow coefficients and ratios of geometrical length scales). The variables that characterize this overall behaviour should be related to each other, viz. i) upstream pressure p_{in} and downstream pressure p_{out} and upstream volume-flow rate Φ_v^{in} and downstream volume-flow rate Φ_v^{out} , and ii) valve opening h . Naturally the question rises of how to relate these variables. In general gas flowing through the valve results in plate motion. The gas force acting on the plate is a function of the valve pressure difference or flow rate and valve opening. The plate forms a bluff body in the flow and mutually changes the valve flow rate. Therefore, the flow rate must be related to the pressure difference and the valve opening. These phenomena form the base of the fluid-structure interaction mechanisms that must be considered.

For more than a century people have been modeling these mechanisms in valves of various types, i.e. not only compressor valves but also e.g. mechanical heart valves, clarinets and water pumps. The majority of these theories makes use of semi-empirical coefficients. These coefficients must be determined experimentally for steady flows. Numerous studies even assume these coefficients to be unity. We will refer to these theories as traditional valve theories. The objective of the present research is twofold, i.e.

- the analysis of the semi-empirical coefficients as they appear in traditional valve theory,
- the validation of the quasi-steady flow assumption in traditional valve theory.

The first objective is related to prediction of coefficients that are defined with experimentally obtained data. Are we able to estimate theoretically the parameter dependence of these coefficients? If not, are we able to predict these coefficients by making use of Computational Fluid Dynamics? We will use the flow model based on the Euler equations for conservation of mass, momentum and energy in a three-dimensional inviscid compressible flow. It is expected that the local Mach number varies substantially within the flow. Therefore local preconditioning of these equations is necessary in order to increase the convergence speed of the numerical method. Furthermore, the flux scheme is modified to yield accurate solutions of the flow field in regions characterized by very low Mach number. What is the difference

between semi-empirical relations for valves of different geometry? To that aim we will compare experimentally obtained coefficients for a *commercially available compressor valve* and a *model valve* of own design. This model valve has a less complex geometry than a compressor valve and is more suited for Computational Fluid Dynamics analysis and for theoretical modeling.

The second objective is related to the question whether the quasi-steady flow assumption used in the traditional valve theories can predict the actual behaviour in compressor valves. In most articles dealing with valves, the response of the environment of the valve is emphasized to explain instabilities. However, we will not consider the subject of self-excited valve vibrations (by means of laboratory experiments). Are we able to design a method to measure simultaneously the instantaneous valve pressure difference, the instantaneous valve flow rate and the instantaneous valve opening? This would allow to isolate the valve behaviour from its environment in the measurement method, in order to validate the traditional valve theory for unsteady flow conditions.

1.4 Outline of Thesis

In order to put the objective of the present research in a relevant perspective, a literary survey is performed. Chapter 2 discusses the historical developments of valve design, application, research and modeling. The valve theories are characterized by distinguishing four items, i.e. i) fluid dynamics, ii) structural dynamics, iii) flow force on plate and iv) valve environment. These valve theories often emphasize issues related to the immediate surroundings of the valve and comprise rather simple steady flow models. Therefore Section 2.3 discusses the valve physics with concepts available in the literature on fluid dynamics.

In Chapter 3 these traditional valve theories are assigned to one theory which we will refer to as the Basic Valve Theory. This chapter investigates the linear and non-linear properties of this theory by means of stability analysis and numerical simulations. Subsequently a theoretical prediction of the parameter dependence of the semi-empirical coefficients is given. Section 3.4 suggests some model improvements concerning unsteady flow effects. Finally, a full compressor system is analysed in order to show the diagnostic properties of the simple Basic Valve Theory.

Chapter 4 presents the numerical algorithms that are employed to compute the flow through a valve. Special attention is given to the concept of local preconditioning of the Euler equations because this technique is necessary to obtain accurate solutions within acceptable computation time for flows in which parts of the flow can be considered incompressible. Several test cases show the ability of the method to simulate steady and unsteady low Mach number flows.

Chapter 5 presents the experimental methods that are employed to validate the Basic Valve Theory for unsteady flows. First the design of the model valve is discussed. Special attention is given to the valve plate displacement measurements. The values of the unsteady valve pressure difference and the volume-flow rate are obtained by making use of the linear theory of sound propagation and superposition of dynamic and static quantities. The well-known Two-Microphone Method is discussed and extended for application in the time domain.

Chapter 6 shows the semi-empirical coefficients of the model valve and some reverse flow effects. The ability of the preconditioned Euler method to predict these coefficients is dis-

cussed. The Basic Valve Theory considers quasi-steady flow. Therefore this model is validated for unsteady flow conditions. The collisions of plate with seat and limiter are discussed. Finally, the results for the model valve are compared with a commercially available compressor valve.

In Chapter 7 conclusions are drawn with respect to the objective of this study. Additionally, a discussion is presented on the limitations of the present computational and experimental method. Finally, a future line of research is suggested.

2.1 Introduction

Valves are older than human life and could already be found in the hearts of mammals and dinosaurs to enable the pumping of blood through the body. When the giraffe lowers its head to drink, valves in the arteries in the neck close to stop the blood flowing to the brain. In the Ancient Roman Time valves were used in piston pumps (Fig. 2.1). Their function was to

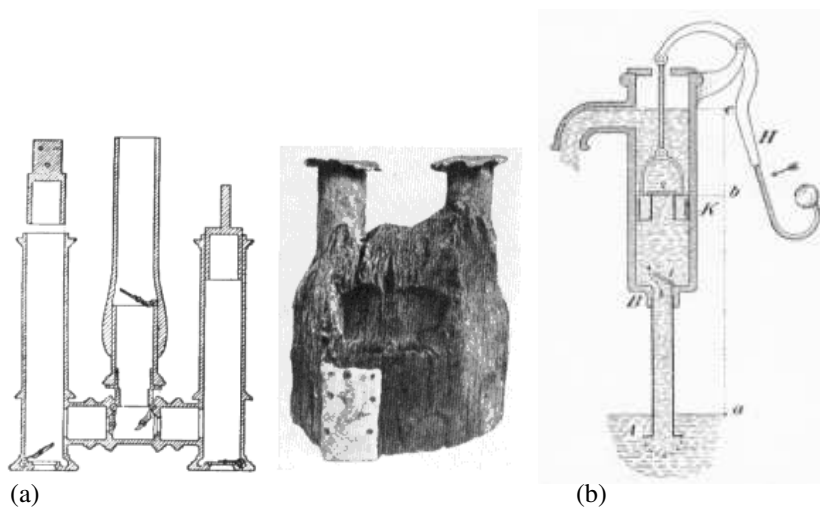


FIGURE 2.1: (a) Roman piston pump (double acting), (b) classic water pump (single acting).
From <http://www.hp-gramatke.net>.

suck water out of a reservoir. They can be dated from 250 BC. Section 2.2 presents a brief historical overview of valve application and research. The summary of valve theories will be used to justify the objective of this thesis. Finally, Section 2.3 presents the fluid dynamics framework in which compressor valve theories should be placed in.

2.2 Survey of Literature

Literature dealing with the subject of valves ranges over a wide field of application. Therefore the first distinction in this survey will be non-compressor valves versus compressor valves.

2.2.1 Non-Compressor Valves

Heart Valves In traditional Galenic physiology (second century) there were two types of blood with distinct pathways and functions, relating to the liver, the heart and the brain. Blood was assumed to originate in both the liver and the heart without returning to it. Around 1510, Leonardo da Vinci was the first to carry out a detailed hemodynamic study of the aortic valve and identified the small valves as one-way mechanical regulating valves (Gharib et al. 2002). At present we know that the vortex in the sinus cavity initiates valve closure in early deceleration, even though the inflow velocity is still directed forward (Van Steenhoven and Van Dongen 1979). In 1628, William Harvey published his famous *Exercitatio Anatomica* in which he stated the circulation of blood and the heart as a driving pump.

Today the number of publications on (mechanical or artificial) heart valves is overwhelming. Some of the major problems with these valves are haemolysis (disruption of red blood cells), thrombus formation and tissue overgrowth. These problems are closely related to the flow pattern in the vicinity of the heart valves. Often *in vivo* and *in vitro* experimental data are difficult to obtain (e.g. Horsten 1990, Firstenberg et al. 2000, Bluestein et al. 2000, Marassi et al. 2004). In a number of studies the unsteady Navier-Stokes equations are solved in a 2D computational model, restricted to laminar flow and a fixed valve (e.g. Horsten 1990, Huang et al. 1994, Rosenfeld et al. 2002). These numerical simulations predict vortex shedding frequencies and magnitude and spatial distribution of fluid stresses. More realistic simulations are performed when fluid-structure interaction is taken into account in a 3D computational model (e.g. De Hart et al. 2003). These numerical simulations show that e.g. the aortic root compliance has a significant contribution to the functionality of the valve.

Industrial Revolution Many of the important inventions of the Industrial Revolution required much more power than horses or water wheels could provide. Industry needed a new, cheap and efficient source of power and found it in the steam engine.

In 1698, Thomas Savery patented the first practical steam engine, which acted as pump to drain water from mines. The valves were the only moving parts and had to be operated by hand. In 1712, Thomas Newcomen invented another steam engine, which contained a large rocking beam. One of his improvements was that of replacing the manual operation of valves by an automatic device whereby the valves were triggered by a rod connected to the main beam, with each valve counterbalanced to give a quick cut-off and opening action which could not be performed by the slow-moving beam. The valves controlled the intake of steam, the injection of a spray of water to condense the steam, and the snifting valve to exhaust the condensate and the air introduced into the cylinder with the steam. Contrary to persistent legend, James Watt did not invent the steam engine. He reduced the cost of operating condensing engines and made it possible to use these engines for other kinds of work than pumping. Watt took out his first patent for the separate condenser in a steam engine in 1769.

Valves were necessary to admit the steam in order to act upon the piston, and to release it after the work has been performed. So valves were an important detail in the design of an

engine. The evolution of steam valves is clearly discussed in the textbooks of Buchanan and Watkins (1976) and Rolt (1963). The application of Watt's steam engine is overwhelming. It varies from usage in e.g. the coal industry (drainage pumps for mine shafts), the iron industry (to power reciprocating compressors!), the textile industry (spinning and weaving) to usage in the transportation industry (steam locomotives and steam ships).

Fuel-Injection Valves Today's internal combustion engine designs demand low emissions, fuel economy and reliability with high power output. The design requirements for more efficient and environmentally clean engines result in the need for detailed fluid flow data in the valves. Separation of the inlet flow around the valve gap is frequently analysed experimentally under conditions with *fixed* valve lifts (e.g. Weclas et al. 1998, Maier et al. 2000a, Maier et al. 2000b, Belmabrouk and Michard 2001, Milton et al. 2001). The experiments comprise the measurement of mass-flow rate, pressure drop, spatial and temporal distributions of velocity components for valves of different geometry. The results show that the four-mode model* widely used in literature is not sufficient to describe the complex flow separation process. The onset of instability of a fuel-injection valve can be characterized from simple fluid-structure interaction models. Resonances could be addressed to leakage-flow pulsations when the valve model couples a body oscillator (mass-spring system) to a fluid (Helmholtz) oscillator (e.g. Naudascher and Rockwell 1994).

Musical Reed Instruments In most applications valve instabilities are not desired and research aims to avoid these instabilities. Literature exists of e.g. gate vibrations (Kolkman 1980), fuel-injection valve oscillations and artificial heart valve instabilities. However, in musical reed instruments oscillations are essential.

Since the early work of Backus (1963) and Nederveen (1969), which was based on a linear stability analysis, many papers have been published dealing with non-linear solutions of the reed excitation problem. Consider a simplified model of a clarinet, where acoustical oscillations are coupled to mechanical vibrations (e.g. Rienstra and Hirschberg 2001). A linear stability analysis then determines the threshold of the pressure above which oscillations occur and the frequency of the most unstable mode. However, the coupling between a body oscillator and a fluid oscillator can feature complex phenomena. In 1920, Vogel found that the dominant frequency of flow oscillations in a reed pipe as function of the pipe length is characterized by subsequent jumps near resonance points, as well as by hysteretic shifts of these jumps depending on whether the pipe length is increased or decreased (e.g. Naudascher and Rockwell 1994). Hirschberg et al. (1990) postulated the occurrence of hysteretic behaviour of the volume-flow rate to pressure relationship in reed instruments. This has not been confirmed by experiments.

Musicians are familiar with the influence of the vocal tract on both timbre and pitch. Fritz et al. (2003) presented a mechanism in which the playing frequency will shift by changes in the vocal tract geometry, as musicians claim to do. Dalmont et al. (2003) presented a method for measuring the static non-linear pressure - flow rate relation of a clarinet mouthpiece. It was shown that the ratio of the effective surface of the jet and the reed opening are constant

*The four-mode model characterizes the flow separation in a valve gap by distinguishing four regimes as function of the valve opening.

within a large range of openings. This corresponds to the Basic Valve Theory which will be described in Section 3.2.

In the field of biomechanics, research focuses on voiced sound production produced by a modulation of the flow while the vocal folds are self-oscillating. Typically, the glottis (i.e. the narrow opening between the vocal folds) forms a converging channel when the vocal folds are separating and a diverging channel when the vocal folds are approaching. In the literature many articles can be found on quasi-steady theories for the flow, experimental work and to a lesser extent numerical simulations (e.g. Hofmans 1998, De Vries et al. 2002, Vilain et al. 2004). Research aims at the development of prosthetic vocal folds and the development of artificial speech models.

Safety Relief Valves Safety relief valves are commonly used in e.g. steam generation processes, nuclear power plants and hydraulic circuits for protecting pressure loaded vessels and pipelines against overpressure. In the literature, criteria are described for the different assumed reasons for valve oscillation. The most commonly applied rules in practice to avoid oscillations are discussed in e.g. Cremers et al. (2001). They found that none of these rules is adequate for a broad range of conditions. Hayashi et al. (1997) studied the instability of a pilot-type poppet valve circuit (consisting of a valve, an upstream plenum chamber, a supply pipeline and an orifice between the plenum and pipeline). Although the valve rests on the seat stably for a supply pressure lower than the cracking pressure[†], the circuit becomes unstable for an initial disturbance beyond a critical value. This self-excited vibration is found to follow the Feigenbaum route to chaos.

Some Other Valves In engineering there exist many non-compressor valve types other than the ones mentioned above. *Butterfly valves* are one of the oldest types of industrial valves known, because they have been used extensively for steam engines. They are mainly used for both on-off and throttling services involving large flows of gases and liquids at low pressure (e.g. Huang and Kim 1996, Caillé and Laumonier 1998, Danbon and Sollic 2000). A *V-ball valve* is a control valve used in many industrial applications. Testing of Strouhal frequency for shed vortices in a wide range of operating conditions is often considered (e.g. Merati et al. 2001). Sub-Kelvin refrigerators use special working fluids and special *low-temperature valves*. Research aims at minimizing the leakage rates (e.g. Miller and Brisson 1999). *Air release valves* are designed to remove undissolved gas bubbles from pipelines carrying multi-phase fluids. Research aims to characterize pressure surges (e.g. Lee 1999). *Check valves* are commonly used when sustained reverse flow in a pipeline is not allowed. The check valve closes under reverse flow and valve slam is common. Kruisbrink (1996) presented a semi-empirical method to describe the hydrodynamic behaviour of check valves in pipeline systems. McElhaney (2000) reported a review and analysis of check valve failures. Applications of *microvalves* can be found in medicine, where drug-delivery systems are planned for implantation, as well as in chemical analysis systems. Ulrich and Zengerle (1996) found the direction of the net fluid transport through the valve to depend on the driving frequency of the pressure, i.e. a micropump was born.

[†]The cracking pressure is the pressure difference at which the valve starts to open.

2.2.2 Compressor Valves

Main objective in this subsection is to extract from literature a historical line in the development of compressor valve theories. Quantitative aspects will be presented in Chapter 3 and experimental techniques will be discussed in Chapter 5. The literature can be found in various sources, i.e.

- proceedings of the bi-annual International Compressor Engineering Conference at Purdue,
- proceedings of the bi-annual European Forum for Reciprocating Compressors,
- proceedings of the bi-annual International Conference on Compressors and their Systems of IMechE and City University in London,
- monographs, which are not easily accessible for some readers because of the frequent use of the German language (e.g. Frenkel 1969, Thiel 1990, Böswirth 2000),
- publications in international journals (to a lesser extent).

Pioneering Work The work of Westphal in 1893 became a milestone for the computation of valve openings, see e.g. Thiel (1990). The model contained an equation of motion for the valve plate, using a spring force, gravity force and flow force. The flow force was modelled as the valve pressure difference times the port area. The continuity equation, assuming incompressible flow, contained the change of flow rate caused by the plate motion. Costagliola (1950) was the first to model the behaviour of compressor valves in the full environment of a reciprocating compressor. The flow through the valves is modelled based on steady isentropic flow through an orifice, thus taking into account subsonic compressibility effects. It is assumed that the valve plate does not rebound, when reaching the limiter. Two empirical coefficients had to be found from steady flow experiments. Costagliola compared his theory with experiments and assumed the discrepancies to be caused by leakage and heat transfer. The valve opening was recorded as function of time by making use of a mechanical device. In the following decades Costagliola's work forms a starting point for numerical simulations (first on analog-, later on digital computers) of reciprocating compressors. In the middle of the 20th century, compressor valve theories were at the dawn of evolution in many directions.

Semi-Empirical Theories Linke et al. (1974) were the first to incorporate a restitution coefficient for plate collisions. Comparison of the valve opening predicted by simulations and the one measured in experiments yielded good agreement, although several coefficients were used as 'fit-parameters'. Hamilton and Schwerzler (1978) realized the importance of predicting valve impact speeds for the estimation of valve lifetime. They correlated the impact speed to the compressor speed, although some discrepancies between theory and experiments occur in the closing times of the valves.

Gas pressure oscillations are inherent to the suction and discharge processes of reciprocating compressors. These processes yield a time dependent pressure distribution in the plenum chambers and piping system. In practice significant pressure oscillations can be present and these may affect both the valve operation and the thermodynamic performance of the compressor. In addition, the high sound pressure level radiated from the compressor can be

undesired. Early investigations of the interaction of compressor valves with the acoustics in the plenums and discharge lines have been performed by e.g. Elson and Soedel (1974). The acoustical plane wave theory applied to the plenum chambers and piping system yielded good agreement with experiments. MacLaren et al. (1975) considered the equations for conservation of mass and energy for the plenums and the 1D Euler equations for the piping system.

The first time a semi-empirical theory included the 2D motion of the valve plate was given by Machu (1994). This theory closely matches real valve plate motion, i.e. i) a plate tumbling on the seat does not seal the valve port tightly, hence pressure gradients remain small; and ii) impact speeds are higher, resulting from the high angular acceleration of the plate after the first impact of the plate in oblique position. This theory was elaborated by Machu (2001). Two semi-empirical coefficients as function of the valve opening were used, that need to be determined from steady flow experiments. Unfortunately, not all the necessary parameters (e.g. eccentricities of forces or peripheral plate stiffness) are always known in detail.

Oil films between valve plate and seat have been shown to cause the plate to adhere to the seat and open much later than they would have in the absence of oil. This phenomenon is referred to as valve stiction and has been studied both analytically (e.g. Khalifa and Liu 1998, Böswirth 2000) and experimentally (e.g. Toubert 1976, Joo et al. 2000). However, in practice different operating conditions may appear, i.e. i) the oil management arrangement in the compressor determines the amount of oil, and ii) viscosity will not remain constant because of heat transfer and unsteady concentration of refrigerant in the oil. Recently, Böswirth (2001) presented some engineering tools to reduce the high impact speeds of the valve plate resulting from oil stiction.

For high efficiency of the compressor the maximum valve opening should be rather large. However, to obtain reliability and long lifetime of the valve this opening should be small. Selecting materials with higher resistance to impact stresses, such as non-metallic sealing elements, could enable simultaneous improvement of valve efficiency and valve life (e.g. Artner 1999, Spiegl et al. 1999, Artner and Spiegl 2001). In the last two references the impact of a valve plate in oblique position against a seat is simulated with a Finite Element Method. However, coupling of the elastic deformations with the flow is absent.

Computational Fluid Dynamics Cyklis (1994) was amongst the first ones to investigate the suitability of Computational Fluid Dynamics (CFD) for analysis of compressor valves. The computed steady planar mass-flow rate as function of the pressure difference was slightly lower than measured data. The simplified geometry of a compressor valve consisting of a radial diffuser with axial feeding is frequently used for CFD applications. Deschamps et al. (1996) considered turbulent flow using the Renormalization Group k - ϵ model and fixed walls. The pressure distribution along the front disc showed good agreement with experimental data, for different valve openings and Reynolds numbers. However, Pérez-Segarra et al. (1999) considered three different k - ϵ turbulence models and showed significant difference in computed flow force and effective flow area. This outcome agrees with the comparisons of Ottitsch and Scarpinato (2000) applied for different types of valves. A next step in using CFD for compressor valves was the computation of fluid-structure interaction. Until 1999 almost all investigations available in literature related to compressor valves either model the structural dynamics in detail but pay little attention to the description of the flow field, or focus on the fluid dynamics without considering the coupling between plate motion and pressure distribution on the plate. Matos et al. (1999) considered axisymmetric laminar flow around

a circular plate with prescribed pressure difference. The structure was modelled as a mass-spring system with a single degree of freedom. The gas force is found to be in phase with the harmonically varying pressure difference, except near valve closure when this force experiences a temporary drop. When both pressure difference and flow force become negative, the mass-flow rate at the exit becomes negative too.

A next step in using CFD for compressor valves was the computation of flow around inclined disks. Possamai et al. (2001) computed laminar flow between concentric inclined disks and conclude that this flow is significantly affected by the inclination for inclinations as small as 0.1° . For some combinations of Reynolds number, valve opening and inclination, the pressure distribution showed regions of negative pressure difference which produce a restoring moment tending to force the disks to become parallel. The state-of-the-art of parallel plate movement is the work of Matos et al. (2002) who computed axisymmetric turbulent flow around a circular plate which is modelled as a mass-spring system. Plate impacts against the limiter and compressibility effects have not been considered yet.

2.2.3 Summary of Valve Theories

The number of publications on valve theories is overwhelming. In order to extract the historical line of theory developments, literature is ordered by distinguishing four items, i.e. i) fluid dynamics, ii) structural dynamics, iii) fluid-structure interaction and iv) valve environment. Table 2.1 summarizes some literature chronologically. It reveals that for most of the cases a valve is considered as a mechanical device, and fluid dynamical aspects are secondary for valve design. Even today, papers appear in which practical conclusions are drawn from semi-empirical valve theories. Additionally, it reveals the emphasis that authors have put on the valve environment. Self-excited valve vibration mechanisms are often related to acoustical feedback from the valve environment, whereas e.g. flow separation and flow inertia in the valve is ignored. Only during the last decade the use of Computational Fluid Dynamics is increasing rapidly to replace the semi-empirical valve theories. Advances are made from 1D to 3D flows and from laminar to turbulent flows[‡]. Increase of computer capacity and speed, additional to developments in CFD algorithms, can be seen as the reason for these improvements.

[‡]Actually the problem of theoretical prediction of turbulence is still unsolved (e.g. Gharib 1996).

TABLE 2.1: Evolution of valve theories (CF/IF = compressible/incompressible flow, SF/UF = steady/unsteady flow, FEM/FDM/FVM = finite element/difference/volume method, MS = mass-spring system, D = damping coefficient).

Authors	Valve Type & Environment	Fluid Dynamics	Structural Dynamics	Coupling Force Coeff.
Westphal (1893)	liquid pump	1D, IF, SF	MS, D:0	1
Costagliola (1950)	recip. compressor	1D, CF, SF	MS, D:0	empirical
Linke et al. (1974)	recip. compressor	1D, CF, SF	MS, D:1	empirical
MacLaren et al. (1975)	two-stage rec.compr.	1D, CF, SF	MS, D:1	constant
Thomann (1976)	plug valve + pipe	1D, IF, SF	MS, D:0	constant
Touber (1976)	recip. compressor	1D, CF, SF	MS, D:1	empirical
Nieter and Singh (1984)	recip. compressor	1D, CF, SF	MS, D:1	?
Den Hartog (1985)	fuel-injection valve	1D, IF, SF	MS, D:1	1
Ingard (1988)	plug valve + pipe	1D, IF, SF	MS, D:1	1
Thiel (1990)	liquid pump	1D, IF, SF	MS, D:1	empirical
Horsten (1990)	mechanical heart valve	2D, IF, UF FEM, laminar	linked rigid segments	exact
Huang et al. (1994)	mechanical heart valve	2D, IF, UF FDM, laminar	fixed	exact
Cyklis (1994)	recip. compressor	2D, CF, SF FVM	fixed	exact
Deschamps et al. (1996)	circular plate valve	2D, IF, SF FVM, turbulent	fixed	exact
Hayashi et al. (1997)	poppet, pl.ch.+pipe	1D, IF, SF	MS, D:1	empirical
Kerh et al. (1997)	control valve in pipe	2D, IF, UF FEM	MS, D:1	exact
Khalifa and Liu (1998)	circular plate valve	2D, IF, SF	MS, D:0	visc. theory
Pérez-Segarra et al. (1999)	circular plate valve	2D, IF, UF FVM, turbulent	fixed	exact
Matos et al. (1999)	circular plate valve	2D, IF, UF FVM, laminar	MS, D:1	exact
Tarnopolsky et al. (2000)	reed valve, cylinder	1D, IF, UF	MS, D:1	1.5
Böswirth (2000)	comp., cyl.+pl.ch.	1D, CF, UF	MS, D:1	empirical
Machu (2001)	circular plate valve	1D, IF, SF	MS, D:0 2D tumbling	empirical
Possamai et al. (2001)	inclined disks	3D, IF, SF FVM, laminar	fixed inclined	exact
Matos et al. (2002)	circular plate valve	2D, IF, UF FVM, turbulent	MS, D:1	exact
Misra et al. (2002)	control valve	1D, IF, SF	MS, D:1	constant

2.3 Valves and Fluid Dynamics

The preceding section shows that in literature involving semi-empirical valve theories, the valve environment is often emphasized and simple flow models are employed. This section aims to discuss the valve physics with the concepts available in the literature of fluid dynamics.

The central problem of external fluid dynamics is the prediction and/or measurement of the force and moment exerted upon a body immersed in an arbitrary flowfield by the surrounding fluid (Quartapelle and Napolitano 1983). In case of incompressible flow, only two general expressions are available: i) the force acting on a sphere immersed in a steady viscous creeping flow, and ii) the force acting on an arbitrary 3D body immersed in an irrotational unsteady flow[§]. For compressor valves both results are not applicable. Characterizing compressor valves can be considered as a problem involving almost every subject of fluid dynamics. These subjects are e.g. multi-phase internal flow, unsteady 3D high-Reynolds number flow, moving boundaries, boundary layer separation and compressibility effects (perhaps even transonic flow). The moving part of a compressor valve can be considered as a *sharp-edged bluff body*. The flow around sharp-edged bluff bodies has been investigated extensively. Therefore, in the following paragraphs phenomena related to such flows reported in literature are discussed.

Flow around Fixed Objects with Steady Inlet Flow Fage and Johansen (1927) were amongst the first to determine the flow behaviour behind a very long flat plate experimentally. Fig. 2.2 shows the flow situation schematically. Smoke photographs reveal the essential

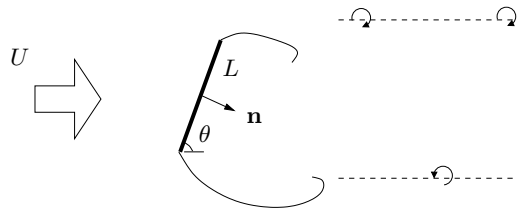


FIGURE 2.2: *Flow of air around an inclined flat plate of infinite span.*

features of the flow. At the edges, thin sheets of vorticity are generated, which separate the freely-moving fluid from the 'dead-water' region in the wake of the plate. At some distance behind the plate, these vortex sheets -on account of their lack of stability- roll up and form a vortex street. One of the earliest theories for calculating the resistance of the plate[¶] has been developed by Kirchhoff and Rayleigh. They obtained the expression

$$\mathbf{f} = \frac{\pi \sin \theta}{4 + \pi \sin \theta} \rho U^2 L \mathbf{n}, \quad (2.1)$$

[§]Moreover, for the case of steady 2D inviscid irrotational flows, Blasius has derived general relationships for both the force and moment exerted by the flow, see e.g. Batchelor (2000).

[¶]Note that for steady *irrotational* flow D'Alembert's paradox holds, i.e. the inviscid fluid offers no resistance to a non-accelerating object. Kirchhoff developed the 2D 'free-streamline theory', see e.g. Batchelor (2000).

for the flow force per unit length in spanwise direction, where θ is the plate angle, ρ is the fluid density, U is the velocity of the undisturbed fluid, L is the length of the plate and \mathbf{n} is the outward pointing unit normal vector of the plate area at its downstream side. According to wind-tunnel experiments, it appears that this theory considerably underestimates the force acting on the plate. The vortices generated at each edge pass downstream with a frequency which increases as the inclination θ of the plate decreases. The frequency at constant inclination is proportional to the wind speed. The longitudinal spacing of the vortices decreases as the inclination of the plate decreases. The vortices pass downstream at a speed which increases as the inclination decreases. Vorticity is shed from the two edges at the same rate. This rate decreases slowly as the inclination θ decreases.

Popiel and Turner (1991) presented experimentally obtained visualization results of the high blockage flow behind a flat plate in a rectangular channel, see Fig. 2.3. Flow past a

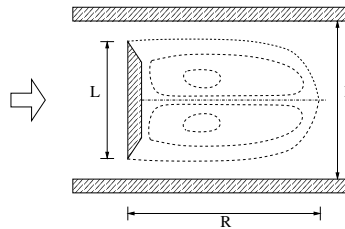


FIGURE 2.3: Length of recirculating wake in a planar high blockage flow.

normal flat plate in an infinite domain (external flow) is characterized by a recirculating wake, surrounded by two separated shear layers springing from the edges of the plate and at some conditions by regular vortex shedding. However, when the frontal area of the blunt object relative to the channel cross section, i.e. the blockage ratio L/h , becomes sufficiently large (internal flow), significant changes in the mean flow distribution occur and vortex shedding may be suppressed. No large-scale (of order L) regular vortex shedding could be found by Popiel and Turner. Three regions of distinct flow behaviour could be distinguished depending on the ratio of recirculating wake length and channel height R/h as function of the Reynolds number Re (based on mean gap velocity and channel height h).

- *Laminar Region.* At low Reynolds number ($Re < 300$), the flow in the wake was characterized by the presence of two large elongated and essentially-steady 'twin vortices' (for $L/h = 0.5$, $R/h = 1.2$ and for $L/h = 0.7$, $R/h = 1.3$).
- *Transient Region.* For $300 < Re < 8000$ the flow in the near-wake is characterized by a growing instability of the initially-laminar free shear layers.
- *Turbulent Region.* When $Re > 8000$ the flow in the wake is characterized by a mixture of small and large eddy scales and a very strong reverse flow along the axis. The turbulence appears to be initiated in the free shear layers at the separation points and then develops further due to strong interactions between the side wall jet-like flow and the reversed flow in the wake.

Chow et al. (1995) investigated the interaction between a planar inviscid jet flow and a finite-length flat plate, see Fig. 2.4. When the impinging jet approaches a flat plate of infinite

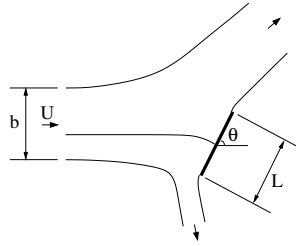
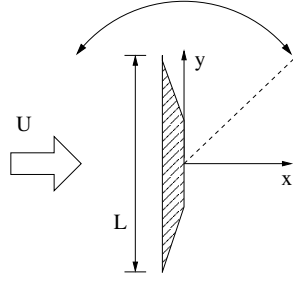


FIGURE 2.4: Schematic sketch of a planar jet past a plate.

length in the normal direction, i.e. $L \rightarrow \infty$ and $\theta = 90^\circ$, the interior portion of the jet slows down due to the obstruction of the plate, while the free surfaces gradually turn in the direction of the plate. A stagnation point appears on the front surface of the plate, and the jet is divided in two separated jets. The method of hodograph transformation has been employed to solve the problem in the incompressible potential flow approximation. In this method the local speed of magnitude U , streamline angle of the flow, jet width b and plate angle θ are treated as independent variables. Other quantities including the coordinates are treated as dependent variables. When the plate has an angle of attack $\theta = 90^\circ$, numerical computations show that a jet deflection of $\sim 90^\circ$ is obtained when $L/b \sim 4$.

Flow around Fixed Objects with Pulsating Inlet Flow Sung et al. (1994) presented a numerical study of the planar inviscid separated flow around a flat plate. The plate is placed normal to the direction of the inlet flow, consisting of a mean velocity and a harmonically pulsating part. The temporal behaviour of vortex shedding patterns is investigated over a range of two externally specified parameters, i.e. the pulsation amplitude and the pulsation frequency f_p . When f_p is low, the shedding frequency f_s is nearly constant, i.e. independent of f_p . The vortex shedding is modulated at a lower frequency $\sim |f_p - f_s|$. However, when f_p exceeds a certain threshold value *lock-on* of the shedding frequency is observed as $f_s \sim 0.5f_p$. The range of f_p in which lock-on takes place is broadened as the pulsation amplitude is increased.

Flow around Forced-Moving Objects It is well recognized that vortex streets are formed in the wake of bluff bodies over a wide range of Reynolds numbers. The periodic shedding of vortices may result in a considerable fluctuating load on the body. When the shedding frequency is close to one of the characteristic frequencies of the body, resonance of the body can cause damage. On the other hand, when the body is periodically oscillated by external forcing, the shedding frequency may be shifted from its natural shedding frequency to the forcing frequency. This *lock-on* of vortex shedding induced by rotational oscillations of a flat plate normal to a uniform flow in its neutral position has been studied experimentally by Chen and Fang (1998), see Fig. 2.5. The Reynolds number (based on free-stream velocity U and plate length L) is set in the range 3000 – 8000. The forcing frequency is set to a fixed value, between 0.8 and 1.2 times the natural shedding frequency of the stationary flat plate normal to the flow, while the angular forcing amplitude is varied to search for the lock-on regime. This regime is found to become narrower with increasing U . For forcing frequencies below and above the natural frequency, significant differences are observed in the distributions of

FIGURE 2.5: *Rotationally oscillating flat plate.*

the time-averaged and fluctuating pressure on the plate surface.

Investigations of flows with moving boundaries are mostly experimental studies. Only a few papers report analytical solutions. Goldsworthy (1953) considered an idealized valve consisting of two cones, initially joined at their apices. By prescribing the cross-section as a special function of space and time, the quasi-1D Euler equations can be transformed to obtain simple unsteady motion in the transformed space-time plane. The solution yields e.g. the distribution of Mach number as function of space over time. Recently, Pullin and Wang (2004) considered planar inviscid starting flow around a flat plate. By prescribing the plate motion as a power-law form in time, the force on the moving plate can be split into the added mass force (attached flow) and the vortex force (separated flow).

Fluid-Structure Interaction The interaction of a flexible structure with the flow around it gives rise to a rich variety of physical phenomena with applications in many fields of engineering, e.g. the stability and response of aircraft wings, the flow of blood through arteries, the response of bridges and tall buildings to wind, the vibration of turbine and centrifugal compressor blades and the oscillation of heat exchangers. The modeling of fluid-structure interaction has been reviewed recently by Dowell and Hall (2001), who put emphasis on the flow rather than on the structure. They report applications largely drawn from aerospace applications. Our primary interest comprises the moving *non-deforming* valve plates in a reciprocating compressor. Therefore the fluid-structure interactions are illustrated with some elementary examples, proposed by Naudascher and Rockwell (1994).

Consider a *stationary* body placed in a flow. The flow force acting on the body can be subdivided into a mean and a fluctuating part, $\bar{F} + F[t]$. The former is of interest for the mean hydrodynamic loading of a structure. The latter is caused by flow fluctuations that are produced either by an extraneous source such as turbulence or by a flow instability such as vortex shedding. In cases of an extraneous source, $F[t]$ remains independent of the motion of the body $h[t]$ except for added-mass and fluid-damping effects. In cases of flow instability, $F[t]$ is altered when the body starts moving. If a body is *free to vibrate* (Fig. 2.6), therefore, one must distinguish between the corresponding extraneously- and instability- induced excitation. Consider a body with mass m , structural damping coefficient ζ and spring stiffness k , then the equation of motion equals

$$m\ddot{h} + \zeta\dot{h} + kh = F. \quad (2.2)$$

In case the flow force would be a function of time only, e.g. $F = \hat{F}e^{i\omega t}$ and $h = \hat{h}e^{i\omega t}$ for $\omega \in \mathbb{R}$ and $i \equiv \sqrt{-1}$, the familiar resonance curves of mass-spring systems will appear (Fig.

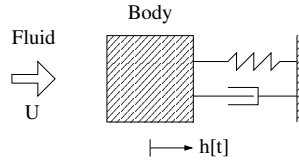


FIGURE 2.6: *Freely moving body surrounded by fluid flow.*

2.7). However, in practice the need for fluid-structure interaction modeling is inevitable,

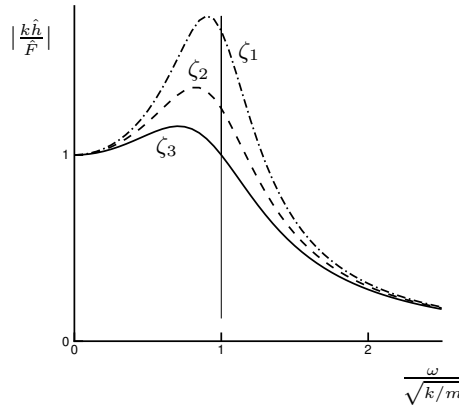


FIGURE 2.7: *Resonance curves of a mass-spring system ($\zeta_1 < \zeta_2 < \zeta_3$).*

i.e. $F = F[h, t]$. Simplified by the use of linear expressions, the fluctuating force can generally be described in terms of components in phase with the acceleration \ddot{h} , speed \dot{h} and displacement h of the body, i.e.

$$F[t] = -m'\ddot{h} - \zeta'\dot{h} - k'h. \tag{2.3}$$

The equation of motion then indicates that the system behaves like a body oscillator with added mass m' , added damping ζ' and added stiffness k' , undergoing free vibration. In the absence of damping ($\zeta + \zeta' = 0$), the natural frequency of the system is

$$f_0 = \frac{1}{2\pi} \sqrt{\frac{k + k'}{m + m'}}. \tag{2.4}$$

Consider the following example in which the added coefficients are expressed in terms of flow physics. An infinitesimally thin circular disk with radius R is moving with velocity U parallel to its axis in an infinite mass of stagnant fluid, see Fig. 2.8. Lamb (1932) derived two limiting solutions analytically:

- Consider a steady translation of the disk in a Stokes flow with dynamic viscosity μ . Then the resistance force experienced by the disk is $16\mu RU$. The added damping is therefore $\zeta' = 16\mu R$.

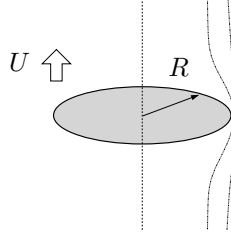


FIGURE 2.8: *Disk moving in an infinite mass of fluid.*

- Consider the irrotational unsteady inviscid flow of a fluid with density ρ . Then the kinetic energy of the fluid is $\frac{4}{3}\rho R^3 U^2$, yielding an added mass of $m' = \frac{8}{3}\rho R^3$.

Note that in both cases the system is unconditionally stable ($\zeta' \geq 0$). Considering the complex case of a compressor valve (Section 1.2), it seems that prediction of the behaviour of the flow and the structural dynamics by academic research introduces severe difficulties.

If a body vibrates in a flow, the added coefficients can become negative as a result of mechanisms by which energy is transferred from the flow to the body. The body vibrations become self-excited. To see whether this can occur, it is convenient to analyse purely harmonic motion, e.g. $h = \hat{h} \sin \omega t$. Consider small vibration velocities, so that $F[t]$ is linearly related to h , \dot{h} and \ddot{h} , defined by $F[t] = F_1 \sin \omega t + F_2 \cos \omega t$. Then the work done by the fluid force acting on the body is

$$W = \int_{\text{cycle}} F[t] dh = \int_0^{2\pi/\omega} F[t] \dot{h} dt = \pi F_2 \hat{h}. \quad (2.5)$$

Only a force in phase with the velocity \dot{h} and working in the same direction will transfer energy. In general one can distinguish three mechanisms which are responsible for valve instabilities, i.e.

- acoustical feedback (e.g. Thomann 1976),
- flow inertia (e.g. Kolkman 1980),
- flow separation (e.g. Van Zon 1989).

When Eq. (2.5) is written as function of the added coefficients, i.e.

$$W = -\zeta' \pi \omega \hat{h}^2, \quad (2.6)$$

it is clear that only a negative ζ' can cause self-excitation. The drawback of the analysis using added coefficients, or stability diagrams based on them, is their failure to predict non-linear behaviour. They are appropriate if one wishes to predict processes involving small amplitudes such as the onset of vibration from rest ('soft' excitation). In cases involving large amplitude fluid forces ('hard' excitation), for which a finite disturbance is required to trigger the body vibration, the expression for $F[t]$ would have to contain higher-order terms (e.g. $\zeta'' \dot{h}^2$ and $\zeta''' \dot{h}^3$).

3.1 Introduction

The literature survey in Chapter 2 reveals that most valve theories make use of semi-empirical coefficients. Although since the 1990s Computational Fluid Dynamics and laboratory experiments are used more intensively, today's publications still involve the traditional valve theories in which the valve environment forms the major difference. In the following section the most reduced form of the traditional valve theories appearing in the literature is described, which we will refer to as the Basic Valve Theory. It is followed by an analysis of the semi-empirical coefficients for a circular disk valve. Furthermore, the Basic Valve Theory with unspecified coefficients is analyzed by means of linear stability analysis (rocking valve plate, valve positioned at downstream end of pipe, valve positioned at downstream end of pipe with flow originating from reservoir) and non-linear analysis (valve with flow originating from hydrodynamic or gasdynamic pipe flow, valve closure events). The discussion on valve theory is elaborated by making use of unsteady flow effects that are known in literature on insect flight and lubrication theory. Finally, an application of the Basic Valve Theory is presented by investigation of a leaking valve in a two-stage reciprocating compressor.

3.2 Basic Valve Theory

Although structural details may differ considerably, the principle of operation of all types of automatic valves is similar (Touber 1976). It is possible to distinguish the same basic functional elements in valves of different design, see Fig. 3.1. During discharge gas is flowing from the high pressure side in the cylinder through the port and separates at the edges of seat and plate. The maximum opening of the valve is attained when the plate is pushed against the fixed limiter. The elements of the Basic Valve Theory are described below.

Fluid Dynamics Consider quasi-steady flow. Then the volume-flow rate Φ_v is expressed as

$$\Phi_v = \alpha \epsilon_c L_g h \sqrt{\frac{2}{\rho_{\text{up}}} \Delta p}, \quad (3.1)$$

where L_g is the total edge length of the plate, h is the valve opening (commonly referred to as valve lift or plate height, see Fig. 3.1), ρ_{up} is the upstream density, Δp is the valve flow

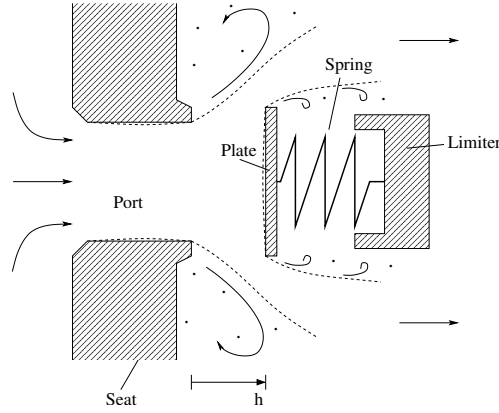


FIGURE 3.1: Sketch of various elements of a compressor valve during discharge.

pressure difference, α is a semi-empirical coefficient and ϵ_c is the compressibility factor.

In case of incompressible flow $\epsilon_c = 1$. Compressibility effects are accounted for by choosing ϵ_c equal to $1 - \frac{1}{\gamma} \frac{\Delta p}{p_{up}}$. This factor is obtained by assuming steady isentropic flow of a calorically ideal gas with a ratio γ of specific heats (e.g. Fox and McDonald 1994, Brower et al. 1993). When the pressure ratio $\Delta p/p_{up}$ exceeds $1 - (\frac{2}{\gamma+1})^{\frac{\gamma}{\gamma-1}}$, the gas velocity becomes critical and the valve is referred to as choked. For air $\gamma = 1.4$ and we obtain choking if $\Delta p/p_{up} > 0.47$.

The effects of viscosity and vena contracta after flow separation are taken into account by the semi-empirical coefficient $\alpha \sim \mathcal{O}\{1\}$. When a 2D planar jet flow emerges from a slit in a thin plate of infinite extent, the vena contracta factor (ratio of jet cross-section and slit area) was found by Helmholtz as $\frac{\pi}{\pi+2} = 0.61$ via Kirchhoff's free-streamline theory (e.g. Batchelor 2000). However, valve flows are not inviscid planar flows through a slit in an infinitely extended thin plate. The coefficient α is found to depend on Reynolds number and geometry (e.g. Touber 1976). It is expressed as function of h . Minute modifications of the shape of the edges of the orifice have drastic effects on α . Determination of $\alpha[h]$ is performed by obtaining a (quasi-)steady flow, i.e. a *hovering* valve plate, and measuring the values of h , Φ_v and Δp .

Structural Dynamics The majority of valve theories consider the moving parts of a valve as a mass-spring system with a single degree of freedom, i.e.

$$\begin{cases} m \frac{d^2 h}{dt^2} + \zeta \frac{dh}{dt} + k(h + h_{pl}) = F_g & , \quad 0 < h < h_{max} \\ \frac{dh}{dt}[t^+] = -e_{res} \frac{dh}{dt}[t^-] & , \quad h[t^\pm] \in \{0, h_{max}\} \end{cases} \quad (3.2)$$

where m is the plate mass, ζ is the damping constant, k is the spring stiffness, h_{pl} is the preload distance, t is the time and F_g is the gas force acting on the valve plate. The valve plate is limited in its travel by the valve seat ($h = 0$) and by the limiter ($h = h_{max}$). When a moving body impacts a fixed wall it will bounce with a velocity that is generally lower than the velocity before impact. The restitution coefficient e_{res} is related to the ratio of plate kinetic energy just after (t^+) and just before (t^-) the collision. This coefficient cannot

be predicted from the elastic properties of the materials alone, there are many other (fluid-structure interaction) effects involved.

In order to correct for the inertial effect of the spring, the mass m in equation (3.2) must include the equivalent mass of the spring. The equivalent mass can be estimated theoretically if one assumes a quasi-static deformation of the spring (Method of Rayleigh). In the case of a coil spring, the coil is assumed to be helically wound with equal distances between the windings, see Fig. 3.2. The mass of the spring is denoted by m^* . It is assumed that

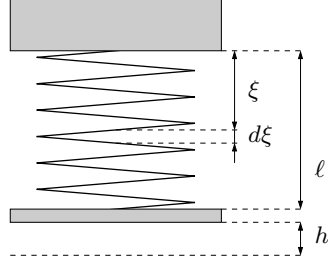


FIGURE 3.2: Equivalent spring mass.

the free end of the spring has displacement h and velocity \dot{h} . It is assumed further that an intermediate point of the spring at a distance ξ from the fixed end, has a velocity $\frac{\xi}{l}\dot{h}$, where l is the instantaneous length of the spring. Consider the system to vibrate with one degree of freedom. The kinetic energy dE_{kin}^* of an element of the spring with length $d\xi$ is equal to $\frac{1}{2} \frac{d\xi}{l} m^* (\frac{\xi}{l} \dot{h})^2$. The kinetic energy of the valve-spring system is then equal to

$$E_{kin} = \frac{1}{2} m \dot{h}^2 + \int_{\xi=0}^{\xi=l} dE_{kin}^* = \frac{1}{2} (m + \frac{1}{3} m^*) \dot{h}^2. \quad (3.3)$$

Thus the inertial effect of the spring can be accounted for by adding a mass of one third of the spring mass, to the mass of the valve plate.

Fluid-Structure Interaction The gas force acting on the plate is modelled as the force exerted on the plate in quasi-steady flow, i.e.

$$F_g = c_g A_p \Delta p, \quad (3.4)$$

where A_p is the port area. The semi-empirical coefficient $c_g \sim \mathcal{O}\{1\}$ is determined by obtaining a (quasi-)steady flow, i.e. a *hovering* valve plate, and measuring the values of h and Δp . Coefficient c_g is expressed as function of h , i.e. $c_g[h]$.

In fluids such as water one should add to this quasi-static force a force proportional to the valve plate acceleration. This force takes into account the acceleration of the fluid around the valve plate and corresponds to an added mass (Section 2.3). When wave propagation is neglected this added mass is determined by means of potential flow theory for an incompressible fluid (e.g. Kolkman 1980). When compressibility is significant this effect is included in the acoustical impedance representing the environment of the valve.

Valve Environment Based on Eqs. (3.1) - (3.4) several types of valves can be modelled. This is related to the simplicity of the theory and the unspecified relations for $\alpha[h]$ and $c_g[h]$. This leaves the valve environment to determine the type of valve and its field of application. Common elements of the valve environment are a pipe segment, plenum chamber or an infinitely large reservoir. Self-excited vibration mechanisms are often related to water hammer and/or acoustical feedback (in the downstream piping) from the valve environment (e.g. Misra et al. 2002). In Section 3.5 an application of the Basic Valve Theory is presented in which the valves interact with the complex environment of a reciprocating compressor.

3.3 Analysis of Basic Valve Theory

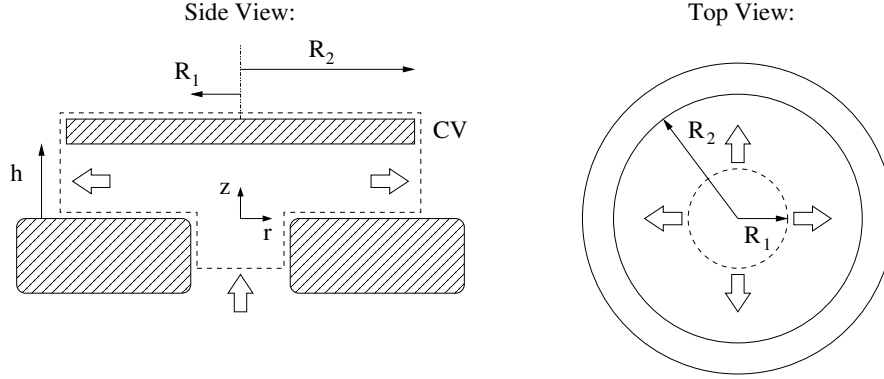
We have defined the valve model as it is used traditionally in engineering (Section 3.2). In this Basic Valve Theory the semi-empirical coefficients α and c_g are set to be functions of the valve opening h . It is however not certain whether this is sufficient. For e.g. a clarinet reed (Hirschberg et al. 1990) the hysteresis effects cannot be explained by the Basic Valve Theory. Therefore the coefficients should also be functions of the valve speed \dot{h} , i.e. $\alpha[h, \dot{h}]$ and $c_g[h, \dot{h}]$. The question of the validity of the Basic Valve Theory will be addressed in Chapter 6, in which we discuss the dynamics of a model valve.

This section presents mainly an analysis of the Basic Valve Theory with unspecified semi-empirical coefficients $\alpha[h]$ and $c_g[h]$. Firstly, the parametric dependence of these coefficients for a circular disk valve is investigated. Secondly, linear stability analysis is applied on several systems (rocking valve plate, valve positioned at downstream end of pipe, valve positioned at downstream end of pipe with flow originating from reservoir). Thirdly, non-linear analysis is applied on several systems (valve with flow originating from hydrodynamic or gasdynamic pipe flow, valve closure events).

3.3.1 Semi-Empirical Coefficients

The Basic Valve Theory needs to be closed with the semi-empirical coefficients $\alpha[h]$ and $c_g[h]$. Formally these coefficients should be determined experimentally for a hovering valve plate. However, in this subsection two examples will yield a first insight of the parametric dependence of these coefficients.

Consider steady incompressible axi-symmetric flow around a circular disk valve (Fig. 3.3), where R_1 is the port radius, R_2 is the disk radius and h the valve opening. The cross-section of the boundary of the axi-symmetric control volume CV used for analysis is shown as a dashed line.

FIGURE 3.3: *Circular disk valve.*

Viscous Flow As a first limiting case we consider a Stokes flow. Conservation of mass and momentum for fully developed purely radial steady flow ($u_z = 0$) in the region $R_1 \leq r \leq R_2$ yield,

$$\frac{1}{r} \frac{\partial}{\partial r}(r u_r) = 0, \quad (3.5)$$

$$0 = -\frac{\partial p}{\partial r} + \frac{\mu}{r} \frac{\partial}{\partial r}\left(r \frac{\partial u_r}{\partial r}\right) - \frac{\mu}{r^2} u_r + \mu \frac{\partial^2 u_r}{\partial z^2}, \quad (3.6)$$

$$0 = -\frac{\partial p}{\partial z}, \quad (3.7)$$

where u_r is the radial component of the velocity vector \mathbf{u} , p is the pressure, μ is the dynamic viscosity and (r, z) are the cylindrical coordinates. Eq. (3.5) gives $u_r = C[z]/r$ and Eq. (3.7) gives $p = p[r]$. Substituting these relations into Eq. (3.6), splitting the r -dependent and z -dependent parts, applying the no-slip boundary conditions $u_r[z = 0] = u_r[z = h] = 0$, pressure condition $p[r = R_2] = p_2$ and the flow rate condition $\int_0^h u_r[r, z] 2\pi r dz = \Phi_v$, yield the solution for the velocity- and pressure distribution, i.e.

$$u_r[r, z] = \frac{3\Phi_v}{\pi r h} \left(\frac{z}{h}\right) \left(1 - \frac{z}{h}\right), \quad (3.8)$$

$$p[r] = p_2 + \frac{6\mu\Phi_v}{\pi h^3} \ln\left[\frac{R_2}{r}\right]. \quad (3.9)$$

The gas force F_g on the plate can be determined by integrating the pressure over the plate surface, yielding

$$F_g = (p_1 - p_2)S_1 + \int_{R_1}^{R_2} (p[r] - p_2) 2\pi r dr = \frac{1}{\ln\left[\frac{S_2}{S_1}\right]} (p_1 - p_2)(S_2 - S_1), \quad (3.10)$$

where $S_1 \equiv \pi R_1^2$, $S_2 \equiv \pi R_2^2$ and p_1 is the pressure for $r < R_1$, assumed to be constant. The two semi-empirical coefficients can be determined as $\alpha \propto \sqrt{(\Phi_v h)} \propto \sqrt{\Delta p} h^2$ and $c_g = \frac{S_2/S_1 - 1}{\ln[S_2/S_1]}$.

Inviscid Flow As a second limiting case we consider an inviscid flow within the valve. Assume uniform flow at the inlet surface and in the region ($R_1 \leq r \leq R_2, 0 \leq z \leq h$). The integral conservation form of the mass and momentum equations yields,

$$\int_{cs} \mathbf{u} \cdot \mathbf{n} dS = 0, \quad (3.11)$$

$$\rho \int_{cs} \mathbf{u} (\mathbf{u} \cdot \mathbf{n}) dS = - \int_{cs} p \mathbf{n} dS - F_s \mathbf{e}_z, \quad (3.12)$$

where the spring force F_s is balanced by the resulting gas force. The pressure distribution along the surfaces ($R_1 \leq r \leq R_2, z \in \{0, h\}$) can be determined by substitution of the velocity distribution ($u_r \propto 1/r$) in Bernoulli's relation. This configuration is a diffuser, i.e. the fluid particles are transported towards a state of increasing pressure. The gas force acting on the disk can be found to be

$$F_g = \left\{ 1 - \ln \left[\frac{S_2}{S_1} \right] + \frac{4\pi}{S_1} h^2 \right\} \frac{1}{2} \rho u_2^2 S_2, \quad (3.13)$$

where u_2 is the outlet velocity. However, the h^2 -term is not significant since the uniform flow assumption is not realistic in case of flow separation (h is large). Fig. 3.4a reveals that for $S_2/S_1 \gg 1$ and a moderate value of h/R_1 , the gas force is negative, i.e. the flow tends to close the valve and a steady flow can only be maintained when an external force pulls the disk from the seat. Assume for convenience that $h \ll R_1$ and $R_1 \approx R_2$. The two semi-empirical

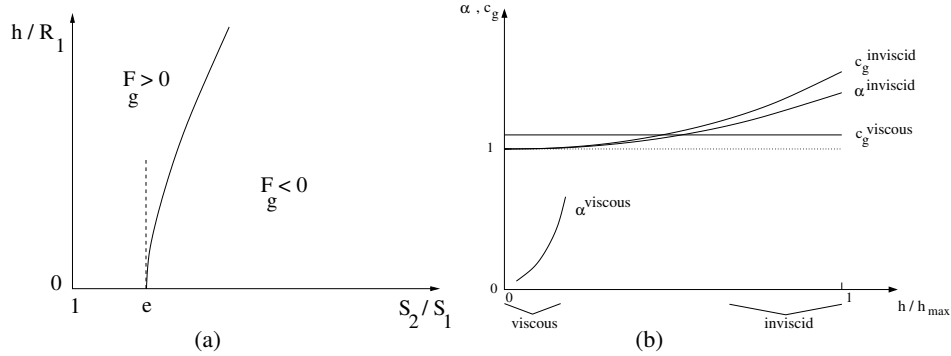


FIGURE 3.4: Circular disk valve: (a) inviscid flow force, (b) coefficients. Curved lines are sketched.

coefficients can then be determined as $\alpha \approx 1 + 2(h/R_1)^2$ and $c_g \approx 1 + 8(h/R_1)^2$.

Coefficients In order to obtain an estimate for the valve opening dependence of the semi-empirical coefficients, i.e. $\alpha[h]$ and $c_g[h]$, the two limiting cases are presented in Fig. 3.4b. It is stated that this result is only an approximation of the actual flow. The viscous flow solution can only apply to very small valve openings, while the inviscid flow solution can only apply to large valve openings.

3.3.2 Linear Stability Analysis

Stability analysis is based on the study of small perturbations around a steady state by analyzing the properties of the linearized equations. Stability analysis yields valuable information to avoid or explain undesired valve oscillations. In the following, examples are presented of: i) a rocking valve plate, ii) a valve positioned at the downstream end of a pipe in which the flow emerges into free space (the flow in the pipe is assumed to be incompressible), iii) an extension of case ii) in which the flow is originating from a reservoir connected to the upstream side of the pipe, and finally iv) an extension of case ii) in which acoustical waves are considered in the pipe flow.

Rocking Valve Plate Consider a stationary valve in a steady flow, where the valve plate is in *oblique* position. This example is based on the monograph of Böswirth (2000), see Fig. 3.5. The valve consists of two circular disks connected by a rigid rod. Each disk closes a

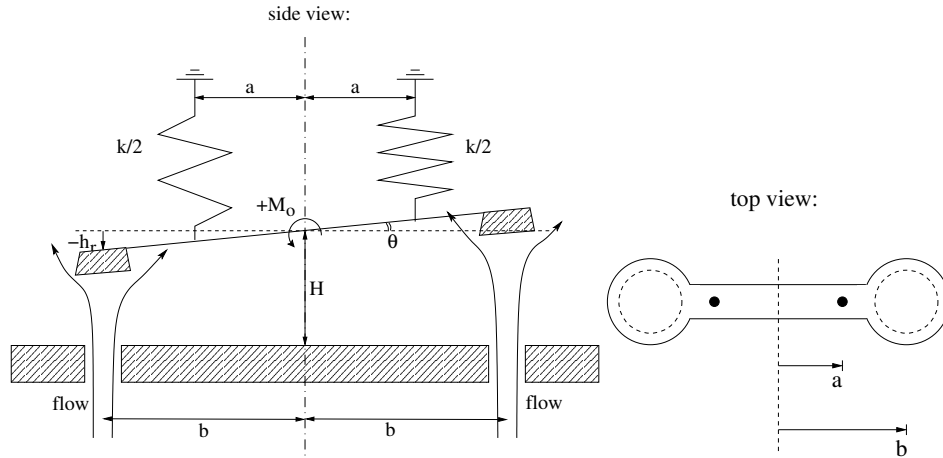


FIGURE 3.5: Valve plate in oblique position (k is the total spring stiffness, M_o is the resultant moment).

hole as shown in the top view of Fig. 3.5. The two holes have a distance $2b$ from each other and are positioned in an infinite plate. The valve is supported by means of two linear springs at a distance $2a$ from each other. Assume small tilting angles of the plate, i.e. $|\theta| \ll 1$. We decompose the position of the stationary valve into a parallel-plate part H and a tilting-plate part h_r . The latter is defined at the center of the right-hand side inflow port area. The gas forces F_r and F_l acting on the right- and left part of the valve plate, respectively, are approximated by application of Eq. (3.4), i.e.

$$F_r = (c_g[H] + \frac{dc_g}{dH}h_r)\frac{1}{2}A_p\Delta p, \quad (3.14)$$

$$F_l = (c_g[H] - \frac{dc_g}{dH}h_r)\frac{1}{2}A_p\Delta p. \quad (3.15)$$

The resultant moment M_o on the valve plate around the axis of symmetry equals

$$\sum M_o = +a\frac{1}{2}k(h_{pl} + H - \frac{a}{b}h_r) - a\frac{1}{2}k(h_{pl} + H + \frac{a}{b}h_r) - bF_l + bF_r, \quad (3.16)$$

where h_{pl} is the preload distance of the springs. The oblique plate becomes *divergent* if $\sum M_o > 0$, i.e.

$$\left(\frac{h_{pl} + H}{c_g[H]}\right) \frac{dc_g}{dH} > \frac{a^2}{b^2}, \quad (3.17)$$

where we found from the equilibrium state that $\Delta p = \frac{k(h_{pl}+H)}{A_p c_g[H]}$. For given c_g , H and b divergence can thus be avoided by two mechanical precautions:

- decreasing preload distance h_{pl} ,
- increasing inter spring distance $2a$.

The valve *dynamics* can be revealed by setting the resultant moment equal to $\sum M_o = J\ddot{\theta}$, where the moment of inertia of the plate is given by $J = \int r^2 dm$. The normal distance between the axis of rocking and the infinitesimally small mass element dm of the plate is denoted by r . We neglect the mass of the springs, i.e. $m^* = 0$. For small tilting angles, i.e. $|\theta| \ll 1$, this yields the linear equation $\ddot{\theta} + \omega^2\theta = 0$, where

$$\omega^2 = \frac{ka^2}{J} \left[1 - \frac{b^2}{a^2} \frac{dc_g}{dH} \frac{A_p \Delta p}{k}\right]. \quad (3.18)$$

If the mass is concentrated in the plate only for $|r| < a$, and $\frac{dc_g}{dH} \equiv 0$, then the circular rocking frequency reduces to $\omega = \sqrt{3\frac{k}{m}}$. Thus the rocking plate frequency is a factor $\sqrt{3} \approx 1.73$ larger than the resonance frequency of a valve with a single translational degree of freedom.

Low Frequency Added Mass Effect of Pipe Flow Consider the steady flow through a valve mounted at the end of a pipe (Fig. 3.6a). The gas force acting on the valve plate depends

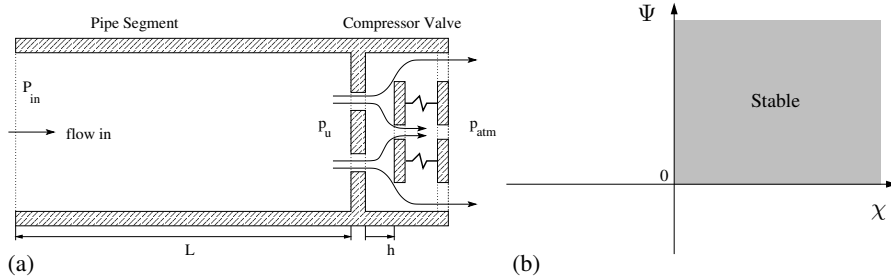


FIGURE 3.6: (a) Pipe-valve system. (b) Stability map hydrodynamic pipe flow.

on the valve opening h and the pressure difference Δp . However, the pressure difference is a function of the valve volume-flow rate Φ_v and the valve opening. This forms the base of the fluid-structure interaction mechanism. Consider the valve to be opened ($0 < h < h_{max}$) and

the flow to possess a negative pressure gradient along the valve ($p_u - p_{atm} > 0$). The pipe inlet pressure p_{in} and the valve outlet pressure p_{atm} are assumed to be constant. We assume incompressible flow ($\epsilon_c = 1$) in the valve and inviscid incompressible 1D flow in the pipe.

- The *governing equations* are

$$m\ddot{h} + \zeta\dot{h} + k(h + h_{pl}) = c_g[h]A_p(p_u - p_{atm}), \quad (3.19)$$

$$\Phi_v = \alpha[h]L_g h \sqrt{\frac{2}{\rho}(p_u - p_{atm})}, \quad (3.20)$$

$$p_{in} - p_u = \frac{\rho L}{A_c} \dot{\Phi}_v, \quad (3.21)$$

where ρ is the density, assumed to be constant, and A_c is the cross-sectional area of the pipe with length L . Eq. (3.19) resembles the valve structural dynamics (Eqs. (3.2,3.4)). Eq. (3.20) relates the valve flow rate to the valve opening and pressure difference (Eq. (3.1)). Eq. (3.21) ensures the conservation of momentum of the pipe flow.

- For the stability analysis decompose the variables into a steady-state and a perturbation: $h[t] \equiv H + \hat{h}[t]$, $\Phi_v[t] \equiv \Phi_v^0 + \hat{\Phi}_v[t]$ and $p_u[t] \equiv P_u + \hat{p}_u[t]$ and assume the perturbations to be much smaller than the steady-state quantities. The *steady-state* then satisfies the following set of equations:

$$k(H + h_{pl}) = c_g[H]A_p\Delta P, \quad (3.22)$$

$$\Phi_v^0 = \alpha[H]L_g H \sqrt{\frac{2}{\rho}\Delta P}, \quad (3.23)$$

$$p_{in} - P_u = 0, \quad (3.24)$$

where we define $\Delta P \equiv P_u - p_{atm}$.

- *Linearizing* the system of equations for small perturbations yields

$$m \frac{d^2}{dt^2} \hat{h} + \zeta \frac{d}{dt} \hat{h} + k \hat{h} = c_g[H]A_p \hat{p}_u + \frac{dc_g}{dH} \hat{h} A_p \Delta P, \quad (3.25)$$

$$\begin{aligned} \hat{\Phi}_v &= \alpha[H]L_g H \frac{1}{\sqrt{2\rho}} \Delta P^{-1/2} \hat{p}_u + \alpha[H]L_g \hat{h} \sqrt{\frac{2}{\rho}\Delta P} \\ &\quad + \frac{d\alpha}{dH} \hat{h} L_g H \sqrt{\frac{2}{\rho}\Delta P}, \end{aligned} \quad (3.26)$$

$$-\hat{p}_u = \frac{\rho L}{A_c} \frac{d}{dt} \hat{\Phi}_v. \quad (3.27)$$

- Rather than solving the perturbations ($\hat{h}[t]$, $\hat{\Phi}_v[t]$, $\hat{p}_u[t]$) explicitly, we seek a solution in the form of a harmonic function*, i.e. $\hat{h}[t] \equiv \hat{h}e^{\beta t}$, $\hat{\Phi}_v[t] \equiv \hat{\Phi}_v e^{\beta t}$ and $\hat{p}_u[t] \equiv \hat{p}_u e^{\beta t}$

*The complex exponent βt does not include the imaginary unit in order to solve the characteristic equation with real coefficients.

for complex frequencies $\beta \equiv \beta_R + i\beta_I$, where $i = \sqrt{-1}$. The quasi-steady solution is stable when $\text{Re}[\beta] < 0$. Substitution of this form of the perturbations yields the system:

$$\begin{pmatrix} m\beta^2 + \beta\zeta + k - \frac{dc_g}{dH} A_p \Delta P & 0 & -c_g[H] A_p \\ -\frac{d\alpha}{dH} L_g H \sqrt{\frac{2}{\rho} \Delta P} - \alpha[H] L_g \sqrt{\frac{2}{\rho} \Delta P} & 1 & -\alpha[H] L_g H (2\rho \Delta P)^{-1/2} \\ 0 & \frac{\rho L}{A_c} \beta & 1 \end{pmatrix} \begin{pmatrix} \hat{h} \\ \hat{\Phi}_v \\ \hat{p}_u \end{pmatrix} = \begin{pmatrix} 0 \\ 0 \\ 0 \end{pmatrix}. \quad (3.28)$$

- A non-trivial solution is obtained when the matrix is singular (determinant is zero). This yields the *characteristic equation*:

$$A\beta^3 + B\beta^2 + C\beta + D = 0, \quad (3.29)$$

where

$$A = m\rho L A_c^{-1} \alpha[H] L_g H (2\rho \Delta P)^{-1/2}, \quad (3.30)$$

$$B = m + \zeta \rho L A_c^{-1} \alpha[H] L_g H (2\rho \Delta P)^{-1/2}, \quad (3.31)$$

$$C = \begin{cases} \zeta + \rho L A_c^{-1} \alpha[H] L_g H (2\rho \Delta P)^{-1/2} (k - \frac{dc_g}{dH} A_p \Delta P) \\ + \rho L A_c^{-1} c_g[H] A_p L_g \sqrt{\frac{2}{\rho} \Delta P} (\frac{d\alpha}{dH} H + \alpha[H]) \end{cases}, \quad (3.32)$$

$$D = k - \frac{dc_g}{dH} A_p \Delta P. \quad (3.33)$$

The analytical solution β of the characteristic equation can be found by using Cardano's method. The polynomial discriminant determines the type (number of unequal real roots) of the solution. However, we avoid this cumbersome method by using the Routh-Hurwitz theorem. In order to yield solutions in the left half-plane, i.e. $\text{Re}[\beta] < 0$, the three Hurwitz determinants must be positive, i.e.

$$AB > 0, \quad (3.34)$$

$$BC - AD > 0, \quad (3.35)$$

$$AD > 0. \quad (3.36)$$

For convenience we assume that the damping constant of the spring $\zeta = 0$ and obtain

$$\left. \begin{aligned} \chi &\equiv 1 + \frac{d\alpha}{dH} \frac{H}{\alpha[H]} > 0 \\ \Psi &\equiv 1 - \frac{dc_g}{dH} \frac{h_{pl} + H}{c_g[H]} > 0 \end{aligned} \right\} \rightarrow \text{stability}, \quad (3.37)$$

indicating that not only the function value of the coefficients α and c_g , but also their derivatives with respect to H are important quantities for local stability. The variables χ and Ψ will be used in the following paragraph. Fig. 3.6b shows the stability map. It follows that if α and c_g are constants, i.e. $\chi = 1$ and $\Psi = 1$, the valve is stable. It is known in literature on flow-induced vibrations that unstable behaviour requires multiple-degrees of freedom (Naudascher and Rockwell 1994).

Influence of Plenum Chamber Consider the situation of gas flowing into a large plenum chamber, subsequently entering a pipeline and then encountering a valve before exiting into the atmosphere (Fig. 3.7a). The example of the preceding paragraph is extended by inclusion

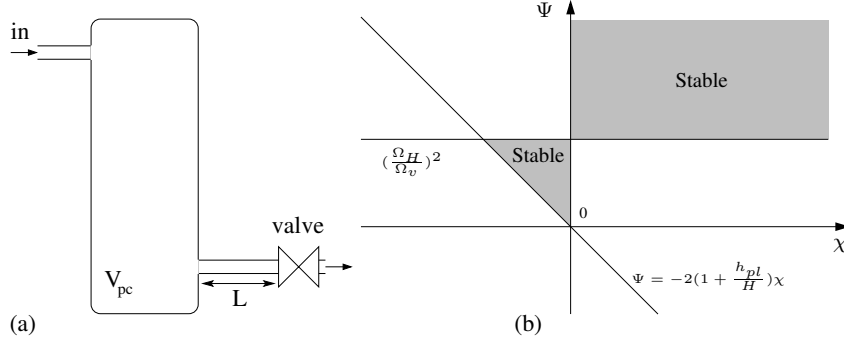


FIGURE 3.7: (a) Plenum chamber - valve system. (b) Stability map.

of a plenum chamber. We assume a calorically perfect gas to flow through this chamber without heat transfer. Furthermore in the energy balance of the gas in the chamber we neglect the kinetic energy at the inlet, outlet and chamber. The governing equations for the system are:

$$m \frac{d^2 h}{dt^2} + \zeta \frac{dh}{dt} + k(h + h_{pl}) = c_g[h] A_p (p_u - p_{atm}), \quad (3.38)$$

$$\Phi_v = \alpha[h] L_g h \sqrt{\frac{2}{\rho_{pc}} (p_u - p_{atm})}, \quad (3.39)$$

$$p_{pc} - p_u = \frac{\rho_{pc} L}{A_c} \frac{d}{dt} \Phi_v, \quad (3.40)$$

$$\frac{d}{dt} p_{pc} = \frac{\gamma}{V_{pc}} (p_{in} \Phi_{v,in} - p_{pc} \Phi_v), \quad (3.41)$$

$$\frac{d}{dt} \left(\frac{p_{pc}}{\rho_{pc}} \right) = 0, \quad (3.42)$$

where subscript pc denotes the plenum chamber, subscript in denotes the plenum inlet and γ is the ratio of specific heats. We assume the thermodynamic state of the gas in the plenum inlet to be equal to that in the plenum chamber ($p_{in} = p_{pc}$ and $T_{in} = T_{pc}$). Furthermore we assume the plenum inlet volume-flow rate $\Phi_{v,in}$ to be a given constant. The flow through the pipe is assumed to be inviscid and incompressible.

The five variables in the governing equations are decomposed into a steady state and a perturbation, i.e. $h[t] \equiv H + \hat{h}[t]$, $p_u[t] \equiv P_u + \hat{p}_u[t]$, $\rho_{pc}[t] \equiv \rho_0 + \hat{\rho}[t]$, $\Phi_v[t] \equiv \Phi_v^0 + \hat{\Phi}_v[t]$, $p_{pc}[t] \equiv P_u + \hat{p}_{pc}[t]$. When the governing equations are linearized in their perturbations around the steady state, a homogeneous system of equations for the perturbation variables is obtained. Assume the perturbations to be proportional to $e^{\beta t}$ where $\beta \in \mathbb{C}$. Then the following characteristic polynomial is derived,

$$A\beta^4 + B\beta^3 + C\beta^2 + D\beta + E = 0, \quad (3.43)$$

where $\{A, B, C, D, E\}$ are functions that depend on the steady-state. Stable solutions are obtained when $\text{Re}[\beta] < 0$. Again this form is suited for application of the Routh-Hurwitz theorem, which states that all solutions of the polynomial lie in the left-half plane when all Hurwitz determinants are positive, i.e. when $AB > 0$, $BC - AD > 0$, $AB(CD - BE) - A^2D^2 > 0$ and $AE(AB(CD - BE) - A^2D^2) > 0$ the solution is stable. For convenience we assume that the damping constant of the spring $\zeta = 0$. Then Fig. 3.7b shows the stability diagram, where the following symbols are used,

$$\Omega_H^2 \equiv \frac{\gamma A_c P_u}{\rho_0 L V_{pc}}, \quad (3.44)$$

$$\Omega_v^2 \equiv \frac{k}{m}, \quad (3.45)$$

where $\frac{1}{2\pi}\Omega_H$ is the Helmholtz frequency[†], $\frac{1}{2\pi}\Omega_v$ is the valve resonance frequency and parameters χ and Ψ are defined in Eq. (3.37). Note that when $\frac{\Omega_H}{\Omega_v} \rightarrow 0$ (e.g. very large plenum chamber or very small plate mass) the situation of hydrodynamic pipe flow is obtained (Fig. 3.6b). On the other hand, when $\frac{\Omega_H}{\Omega_v} \rightarrow \infty$, only for values of χ and Ψ inside the triangular area a stable solution is obtained.

Influence of Acoustical Response of Pipe The preceding paragraphs considered hydrodynamic pipe flow. In this paragraph acoustical perturbations of the pipe flow are considered, i.e. the flow through the pipe obeys the 1D Euler equations for conservation of mass, momentum and energy. It is assumed that the gas is a calorically perfect gas. We will investigate the coupling of valve dynamics with the pipe *acoustics*. Therefore assume a non-colliding valve plate, subsonic mean flow with small perturbations and an open pipe inlet[‡].

The linearized problem involves four unknowns, i.e. the flow pressure perturbation $\hat{p}[x, t]$, the flow velocity perturbation $\hat{u}[x, t]$, the flow temperature perturbation $\hat{T}[x, t]$ and the valve opening perturbation $\hat{h}[t]$, where $x \in [0, L]$ is the space coordinate along the pipe and t denotes the time. The *governing equations* are the linearized Euler equations:

$$\frac{\partial}{\partial t} \begin{pmatrix} \hat{p} \\ \hat{u} \\ \hat{T} \end{pmatrix} + \mathbf{S}_0 \frac{\partial}{\partial x} \begin{pmatrix} \hat{p} \\ \hat{u} \\ \hat{T} \end{pmatrix} = 0, \quad (3.46)$$

subject to the boundary conditions at $x = 0$, i.e.

$$\hat{p}[x = 0, t] = 0, \quad (3.47)$$

$$\hat{T}[x = 0, t] = 0, \quad (3.48)$$

coupled to the linearized equations of valve motion and valve flow rate at $x = L$, i.e.

$$c_1 \hat{h} + c_2 \frac{d}{dt} \hat{h} + c_3 \frac{d^2}{dt^2} \hat{h} = \hat{p}[x = L, t], \quad (3.49)$$

$$\hat{h} = c_4 \hat{p}[x = L, t] + c_5 \hat{u}[x = L, t] + c_6 \hat{T}[x = L, t]. \quad (3.50)$$

[†]Helmholtz resonators are discussed in many textbooks (e.g. Crighton et al. 1992).

[‡]A certain amount of gas in the immediate vicinity of the pipe inlet is in motion together with the gas in the pipe. This effect can be accounted for by assuming that the amount of gas involved in the flow process is larger than the amount contained in the pipe volume. In the literature it is common to express the extra amount of gas in terms of equivalent pipe length L^* . This *end correction* should be subtracted from L in order to obtain the actual pipe length.

The constants $\{\mathbf{S}_0, c_1, \dots, c_6\} \in \mathbb{R}$ are given by the steady-state situation. Matrix \mathbf{S}_0 is determined from the linearized Euler equations in primitive variables form, i.e.

$$\mathbf{S}_0 = \begin{pmatrix} u_0 & \gamma p_0 & 0 \\ \rho_0^{-1} & u_0 & 0 \\ 0 & (\gamma - 1)T_0 & u_0 \end{pmatrix}, \quad (3.51)$$

where $\{p_0, u_0, T_0, \rho_0\}$ are the mean flow pressure, velocity, temperature and density, respectively, all assumed to be constant. The valve coefficients are

$$c_1 = \frac{k\Psi}{c_g[H]A_p}, \quad (3.52)$$

$$c_2 = \frac{\zeta}{c_g[H]A_p}, \quad (3.53)$$

$$c_3 = \frac{m}{c_g[H]A_p}, \quad (3.54)$$

$$c_4 = -\frac{H(1 - \Delta P/p_0)}{2\chi\Delta P}, \quad (3.55)$$

$$c_5 = \frac{A_c}{\chi\alpha[H]L_g\sqrt{2\Delta P/\rho_0}}, \quad (3.56)$$

$$c_6 = -\frac{H}{2T_0\chi}, \quad (3.57)$$

where $\Delta P \equiv p_0 - p_{atm}$. Rather than solving the linear system of coupled partial differential equations (where boundary conditions are functions of the solution), a stability diagram will be obtained. We will follow the approach of Thomann (1976) who considered a plug valve. However, we apply the Basic Valve Theory as defined by Eqs. (3.1) - (3.4). A major simplification is that the Basic Valve Theory assumes quasi-steady flow. It does not take into account the effect of valve motion on the fluid flow through the valve. By adjusting the semi-empirical coefficients this theory describes reasonably well the behaviour of many different valves. For reasons of convenience we assume that the structural damping of the valve is zero (for compressor valves this damping is indeed very small), i.e. $c_2 = 0$.

Consider a *particular solution* of the hyperbolic system of Eq. (3.46), i.e.

$$\hat{p}[x, t] = \left[-Ae^{\beta(t + \frac{x}{c_0 - u_0})} + Be^{\beta(t - \frac{x}{c_0 + u_0})} \right] \rho_0 c_0, \quad (3.58)$$

$$\hat{u}[x, t] = \left[+Ae^{\beta(t + \frac{x}{c_0 - u_0})} + Be^{\beta(t - \frac{x}{c_0 + u_0})} \right], \quad (3.59)$$

$$\hat{T}[x, t] = \left[-Ae^{\beta(t + \frac{x}{c_0 - u_0})} + Be^{\beta(t - \frac{x}{c_0 + u_0})} \right] \frac{c_0}{C_p}, \quad (3.60)$$

where $\{A, B, \beta\} \in \mathbb{C}$ are unknown constants, C_p is the specific heat at constant pressure and $c_0 \equiv \sqrt{\gamma p_0/\rho_0}$ is the speed of sound. In the beginning of this paragraph we assume subsonic mean flow. Consider the mean flow directed from left ($x = 0$) to right ($x = L$), i.e. $0 < u_0 < c_0$. The first term on the right-hand side of each equation (Eqs. 3.58 - 3.60) represents a left (upstream) traveling wave, while the second term represents a right (downstream) traveling wave. When Eqs. (3.58) - (3.60) are substituted in Eqs. (3.49) -

(3.50) for $x = L$, an equation with two unknowns, i.e. β and A/B , is obtained. Substitution of Eq. (3.58) in Eq. (3.47) (or Eq. (3.60) in Eq. (3.48) for $x = 0$) yields $A = B$. After some algebra, an implicit algebraic equation is obtained, i.e.

$$e^{\bar{\beta}}(N_1 + \bar{\beta}^2)N_2 + \bar{\beta}^2 + N_3 = 0, \quad (3.61)$$

where the unknown dimensionless frequency is $\bar{\beta} \equiv \frac{2L}{c_0(1-M^2)}\beta$ and the Mach number $M \equiv u_0/c_0$. The three (real-valued) dimensionless parameters are

$$N_1 = \left(\frac{2L}{c_0(1-M^2)} \right)^2 \frac{k}{m} \left(\Psi + \frac{2\chi(1 + \frac{h_{pl}}{H})}{\frac{\Delta P}{\gamma p_0}(\frac{2}{M} - 1) + 1} \right), \quad (3.62)$$

$$N_2 = \frac{\frac{\Delta P}{\gamma p_0}(\frac{2}{M} - 1) + 1}{\frac{\Delta P}{\gamma p_0}(\frac{2}{M} + 1) - 1}, \quad (3.63)$$

$$N_3 = \left(\frac{2L}{c_0(1-M^2)} \right)^2 \frac{k}{m} \left(\Psi - \frac{2\chi(1 + \frac{h_{pl}}{H})}{\frac{\Delta P}{\gamma p_0}(\frac{2}{M} + 1) - 1} \right). \quad (3.64)$$

Parameters N_1 and N_3 are related to the product of pipe echo time $\frac{2L}{c_0(1-M^2)}$ and valve resonance frequency $\frac{1}{2\pi} \sqrt{\frac{k}{m}}$.

Neutral stability requires the real part of $\bar{\beta}$ to vanish, say $\bar{\beta} = i\beta_I$. Then Eq. (3.61) is split into a real part and an imaginary part, yielding $N_1 = \pm N_3$ or $N_2 = 0$ or $(-1)^n(N_1 - n^2\pi^2)N_2 + N_3 - n^2\pi^2 = 0$, where $n \in \mathbb{Z}$. In order to identify regions of stable solutions for the latter conditions we consider an arbitrary point on a neutral stability line (Fig. 3.8a). The line with slope 1 represents odd values of n , while the line with slope -1 represents even

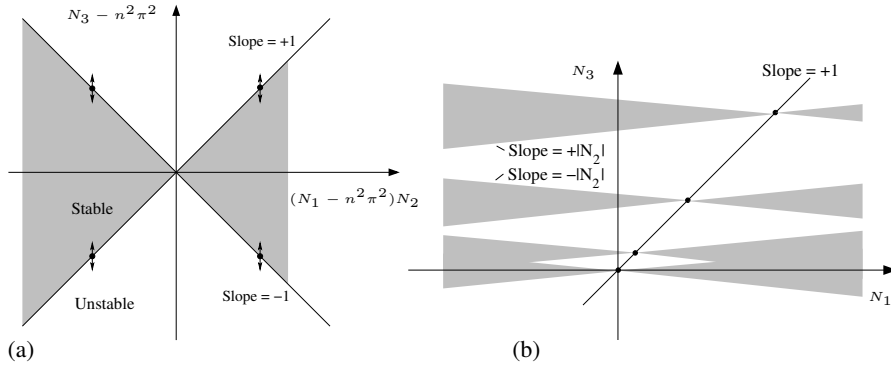


FIGURE 3.8: Stability maps gasdynamic pipe flow: (a) discrete variables, (b) continuous variables.

values of n . Eq. (3.61) is reformulated as $F_{\{N_1, N_2, N_3\}}[\bar{\beta}] = 0$. We vary parameter N_3 infinitesimally, while monitoring the variation of $\bar{\beta}$, i.e.

$$\delta F = 0 \rightarrow \frac{\partial F}{\partial \bar{\beta}} \Big|_{n,s} \delta \bar{\beta} + \frac{\partial F}{\partial N_3} \Big|_{n,s} \delta N_3 = 0, \quad (3.65)$$

where subscript ns denotes neutral stability. The real part of $\bar{\beta}$ is found to change as

$$\frac{\delta\beta_R}{\delta N_3} = \frac{(-1)^{1+n}}{(N_1 - n^2\pi^2)N_2}. \quad (3.66)$$

This yields the stability diagram spanned by continuous variables, see Fig. 3.8b. Each 'butterfly' center is located at $(N_1 = n^2\pi^2, N_3 = n^2\pi^2)$. When $N_2 > 0$ the grey areas represent stable solutions, when $N_2 < 0$ the grey areas represent unstable solutions.

In the field of compressor manufacturing the valve plate mass m is reduced as much as possible. This reduces the valve plate momentum during impacts and this increases the valve resonance frequency far above the piston frequency. Furthermore the pressure drop $\frac{\Delta P}{\gamma p_0}$ across the compressor valve is reduced as much as possible. This increases the compressor efficiency. For $M = 5 \times 10^{-2}$ and $\frac{\Delta P}{\gamma p_0} = 10^{-2}$ it follows that $N_2 = -2.36$, indicating that the grey areas in Fig. 3.8b represent unstable solutions. Furthermore the slope of the boundary lines in the stability map is not extremely steep ($\pm 67^\circ$). Apparently the stability of the system is very sensitive to the values of N_1 and N_3 (representing the pipe echo time and valve resonance frequency). When it is postulated that the pipe-valve system considered is representative for experimental setups in laboratories or for acoustical effects in reciprocating compressor systems, special care should be taken to control instabilities.

3.3.3 Non-Linear Time Domain Analysis

The governing equations of the examples in the preceding subsection cannot be solved analytically because of their non-linear nature. Therefore, this subsection aims to investigate non-linear behaviour by means of numerical simulations in the time domain.

Hydrodynamic Pipe Flow Consider again the flow in the system consisting of a valve positioned at the downstream end of a pipe (Fig. 3.6a). We recall Eqs. (3.19) - (3.21) and take into account plate collisions and a pulsation source, i.e.

$$\begin{cases} m\ddot{h} + \zeta\dot{h} + k(h + h_{pl}) = c_g[h]A_p(p_u - p_{atm}) & , \quad 0 < h < h_{max} \\ \dot{h}[t^+] = -e_{res}\dot{h}[t^-] & , \quad h[t^\pm] \in \{0, h_{max}\} \end{cases} \quad (3.67)$$

$$\Phi_v = \alpha[h]L_g h \sqrt{\frac{2}{\rho}(p_u - p_{atm})}, \quad (3.68)$$

$$p_0 + \hat{p}\sin[\omega t] - p_u = \frac{\rho L}{A_c}\dot{\Phi}_v, \quad (3.69)$$

where \hat{p} is the pulsation amplitude of the pressure and $\omega \in \mathbb{R}$ is the circular frequency of the pulsation. In order to solve this system numerically, consider a set of first-order ordinary differential equations (ODEs) for the unknowns \mathbf{s}_1 complemented by algebraic equations (AEs) for the unknowns \mathbf{s}_2 , i.e.

$$\begin{cases} \frac{d}{dt}\mathbf{s}_1 + \mathbf{f}[\mathbf{s}_1, \mathbf{s}_2] = 0, \\ \mathbf{s}_2 + \mathbf{g}[\mathbf{s}_1, \mathbf{s}_2] = 0. \end{cases} \quad (3.70)$$

Then updates of variables \mathbf{s}_1 and \mathbf{s}_2 in time can be performed by splitting the ODEs and AEs, i.e.

$$\begin{cases} \mathbf{s}_1^{n+1} = \mathbf{s}_1^n - \Delta t \mathbf{f}[\mathbf{s}_1^n, \mathbf{s}_2^n], \\ \mathbf{s}_2^{n+1} = -\mathbf{g}[\mathbf{s}_1^{n+1}, \mathbf{s}_2^n], \end{cases} \quad (3.71)$$

where $s[t = n\Delta t]$ is denoted by s^n for $n \in \mathbb{N}$. In this formulation the plate speed and plate height are independent variables, i.e. $s_1 = (\dot{h}, h, \Phi_v)^T$ and $s_2 = p_u$. The collision time t_c of plate with seat or limiter is approximated by a linear interpolation of the time before the collision $t^- = t^n$ and the time after the collision $t^+ = t^{n+1}$, i.e.

$$\begin{cases} \text{limiter} & \rightarrow t_c = \frac{(h_{max} - h^-)t^+ - (h_{max} - h^+)t^-}{h^+ - h^-} \\ \text{seat} & \rightarrow t_c = \frac{h^+t^- - h^-t^+}{h^+ - h^-} \end{cases} \quad (3.72)$$

similar to e.g. Hayashi et al. (1997). In order to illustrate typical results of the model, consider a valve with semi-empirical coefficients $c_g[h] = 1.2 + 0.1(\frac{h}{h_{max}}) + 0.1(\frac{h}{h_{max}})^2$ and $\alpha[h] = 0.7 - 0.1(\frac{h}{h_{max}})^2$. The pressure difference across a fully closed valve for which the valve tends to open is referred to as the cracking pressure. This pressure is assumed to be $\frac{k h_{pl}}{c_g[h=0]A_p} = 2256$ Pa. Figs. 3.9 and 3.10 show some results of the simulations, where $f_{puls} \equiv \frac{1}{2\pi}\omega$ is the pulsation frequency. The inlet pressure is forced to start oscillating after

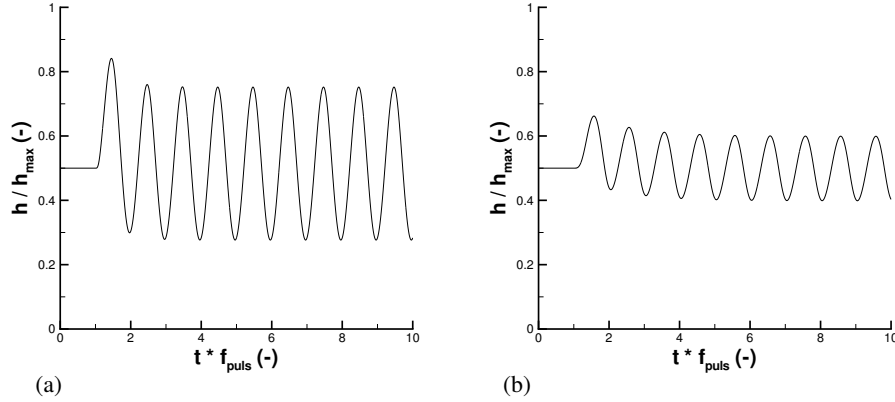


FIGURE 3.9: Simulation results of valve opening versus time for (a) $\frac{\omega}{\sqrt{k/m}} = 0.50$ and (b) $\frac{\omega}{\sqrt{k/m}} = 1.50$. Parameters: $\frac{\zeta}{m\omega} = 0.0$, $\frac{h_{pl}}{h_{max}} = 1.50$, $\frac{A_p}{L_g^2} = 1.56 \times 10^{-3}$ and time-step $\Delta t \frac{\omega}{2\pi} = 10^{-4}$.

one pulsation period. The valve immediately starts to react on the pulsation source because the pipe flow is incompressible. After approximately two pulsation periods a periodic solution is reached. In case of a high pulsation frequency level, the dynamic response of the valve is a smaller amplitude oscillation (compare to Fig. 2.7). Fig. 3.10a shows that for the case of $\omega/\sqrt{k/m} = 0.50$ the valve dynamics can be considered as quasi-steady. For the higher pulsation frequency $\omega/\sqrt{k/m} = 1.50$ significant deviation from a quasi-steady response is observed (Fig. 3.10b). However, the present results should be compared to experimental data of unsteady flow in order to draw conclusions about the validity of the results of the Basic Valve Theory.

The simulation method can also be used to verify the stability diagram (Fig. 3.6b). To that aim we added to the constant pipe inlet pressure a single sine pulse of half a period. The

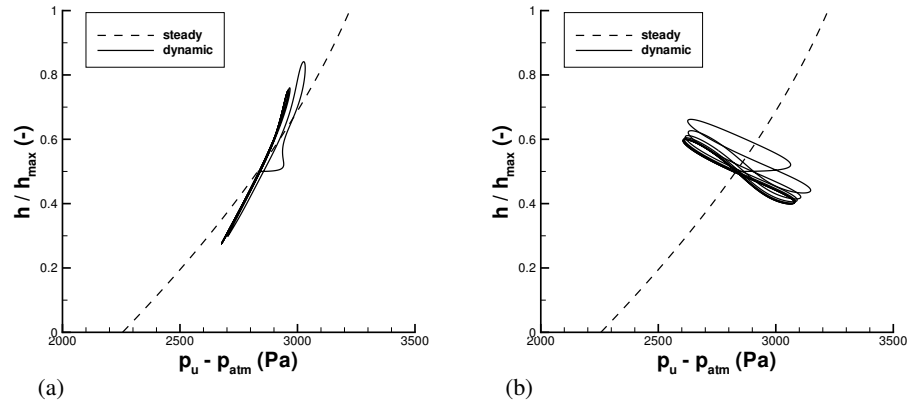


FIGURE 3.10: Simulation results of valve opening versus valve pressure difference for (a) $\frac{\omega}{\sqrt{k/m}} = 0.50$ and (b) $\frac{\omega}{\sqrt{k/m}} = 1.50$. Parameters: $\frac{\zeta}{m\omega} = 0.0$, $\frac{h_{pl}}{h_{max}} = 1.50$, $\frac{A_p}{L_g^2} = 1.56 \times 10^{-3}$ and time-step $\Delta t \frac{\omega}{2\pi} = 10^{-4}$.

amplitude was set to a very small value. The criterion of stability was checked by monitoring the valve opening, i.e. a stable solution should not increase the valve opening after some transient oscillations. Indeed, the diagram of Fig. 3.6b was found to be correct (four data points in every quadrant).

Additional simulations have been performed to study plate collisions (Eq. 3.67). Just before the plate hits the seat, strong reverse flow is observed because the valve pressure difference becomes unrealistically high. Numerically stable results have not been obtained. This can be related to the assumption of an incompressible pipe flow. Indeed we will see in the following paragraph and in Section 3.5 that when the valve environment includes effects of compressibility, the Basic Valve Theory is able to capture valve closures. Now we will proceed with the same configuration, however, including compressible pipe flow.

Gasdynamic Pipe Flow In this paragraph we consider the 1D Euler equations of a calorically perfect gas for the flow in the pipe. The coupling of valve dynamics with a compressible pipe flow has not been reported in literature. We only found the paper of Frommann and Friedel (1998) who considered the opening event of a safety relief valve. However, they did not report in which way the valve upstream pressure is updated. In agreement with experimental data severe oscillations were predicted.

When we assume subsonic flow, two characteristics are directed downstream and one characteristic is directed upstream[§]. At the pipe inlet we prescribe a constant temperature and a given velocity as harmonic function of time. At the pipe outlet we supply the pressure implicitly by application of the Basic Valve Theory, i.e.

$$x = 0 \quad : \quad \frac{\partial u}{\partial t} + (u - c) \frac{\partial u}{\partial x} = \frac{1}{\rho c} \left\{ \frac{\partial p}{\partial t} + (u - c) \frac{\partial p}{\partial x} \right\}, \quad (3.73)$$

[§]The subject of boundary conditions for compressible flows will be discussed in detail in Section 4.3.3.

$$x = L : \frac{\partial T}{\partial t} + u \frac{\partial T}{\partial x} = \frac{1}{\rho c_p} \left\{ \frac{\partial p}{\partial t} + u \frac{\partial p}{\partial x} \right\}, \quad (3.74)$$

$$x = L : \frac{\partial u}{\partial t} + (u + c) \frac{\partial u}{\partial x} = -\frac{1}{\rho c} \left\{ \frac{\partial p}{\partial t} + (u + c) \frac{\partial p}{\partial x} \right\}, \quad (3.75)$$

where Eq. (3.73) is used for updating p at the pipe inlet, Eq. (3.74) is used for updating T at the pipe outlet and Eq. (3.75) is used for updating u at the pipe outlet. The problem is how to update the pipe outlet pressure. The 1D Euler equations are discretized by making use of the Finite Volume Method. Time discretization is performed with Heun's predictor-corrector method and for the flux Roe's scheme is employed (Roe 1981, Roe 1986).

We developed the following algorithm for updating the *pipe outlet pressure* $p_u^n \rightarrow p_u^{n+1}$ in the ghost cell located at the downstream side of the pipe outlet:

1. estimate $p_u^* = p_u^n$,
2. reconstruct the ghostcell with the left state (Eq. (3.74) and Eq. (3.75)),
3. reconstruct the ghost cell with the right state ($\sqrt{\rho}\Phi_v = \alpha[h^{n+1}]L_g h^{n+1} \sqrt{2(p_u^* - p_{atm})}$),
4. compare $\sqrt{\rho}\Phi_v|_{\text{left}}$ with $\sqrt{\rho}\Phi_v|_{\text{right}}$,
5. is difference small enough? \rightarrow yes: exit, no: $p_u^* = p_{atm} + \frac{1}{2}(\alpha[h^{n+1}]L_g h^{n+1})^{-2} < \sqrt{\rho}\Phi_v >^2$ where $< \sqrt{\rho}\Phi_v > \equiv \frac{1}{2}(\sqrt{\rho}\Phi_v|_{\text{left}} + \sqrt{\rho}\Phi_v|_{\text{right}})$ and go to item 2.

Fig. 3.11a shows a comparison of valve dynamics obtained by employing gasdynamic pipe flow and the one using hydrodynamic pipe flow, for the same valve and pipe. In order to

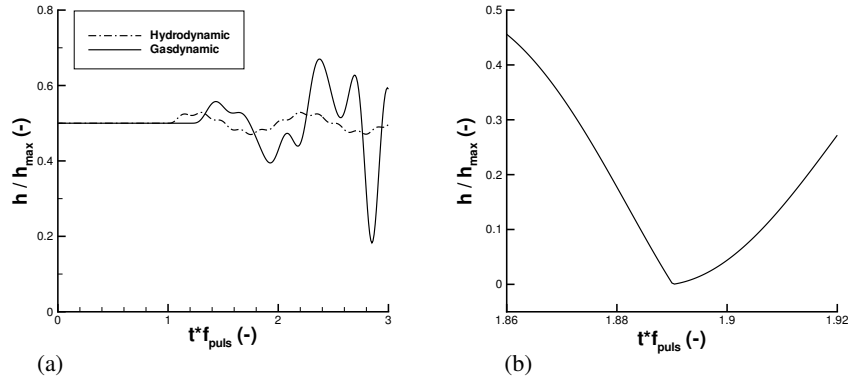


FIGURE 3.11: *Unsteady flow in pipe-valve system: (a) non-colliding plate, (b) valve closure event for gasdynamic pipe flow.*

check for consistency (ability of simulating a steady flow) we force the pipe inlet to start to pulsate after one pulsation period. In case of hydrodynamical pipe flow the valve starts to react immediately ($t^* f_{\text{puls}} = 1$), while in case of gasdynamical pipe flow the valve starts to react when the fastest wave arrives at the pipe outlet, i.e. $t^* f_{\text{puls}} = 1.223$.

Problems were found during valve closure events (parallel plate collisions with the seat), i.e. the number of iterations necessary for convergence increases to infinity. Therefore an alternative algorithm was developed. An algebraic equation on discrete level was extracted from the previous algorithm, from where p_u^{n+1} must be solved. It can be shown that this equation is a third-order polynomial. The numerical solution is found by using Newton-Raphson's method (e.g. Kreyszig 1993). In order to handle valve closure events, the algorithm presented above was complemented by setting the *pipe outlet ghost cell velocity* equal to the plate velocity after collision. The pressure and density in this ghost cell are computed from the downstream traveling Riemann invariants. This new algorithm is found to be able to simulate valve closure events (Fig. 3.11b)!

Valve Opening Speed versus Closing Speed In Section 1.2 it is noticed that the opening event of a valve in a reciprocating compressor occurs in a shorter time interval than the closing event (Fig. 1.6). In order to investigate whether this effect can be explained by the Basic Valve Theory, we consider a valve with prescribed pressure difference, i.e.

$$\begin{cases} m\ddot{h} + kh = c_g A_p \Delta p & , \quad 0 < h < h_{max} \\ \dot{h}[t^+] = -e_{res} \dot{h}[t^-] & , \quad h[t^\pm] \in \{0, h_{max}\} \end{cases} \quad (3.76)$$

$$\Delta p = \hat{p} \sin[\omega t], \quad (3.77)$$

where we assume the gasforce coefficient c_g to be constant, the absence of damping ($\zeta = 0$) and the absence of preloading ($h_{pl} = 0$). Furthermore we assume a slowly varying pressure difference ($\omega = 0.03\sqrt{k/m}$), semi-elastic collisions ($e_{res} = 0.1$) and a pulsation amplitude that is slightly larger than would be necessary to move the plate quasi-steadily to the limiter ($\hat{p} = 1.05 \frac{kh_{max}}{c_g A_p}$). Solving the system numerically yields a non-monotonous valve opening $h[t]$ initiated by a positive value of Δp , see Fig. 3.12a. After several collisions of the plate

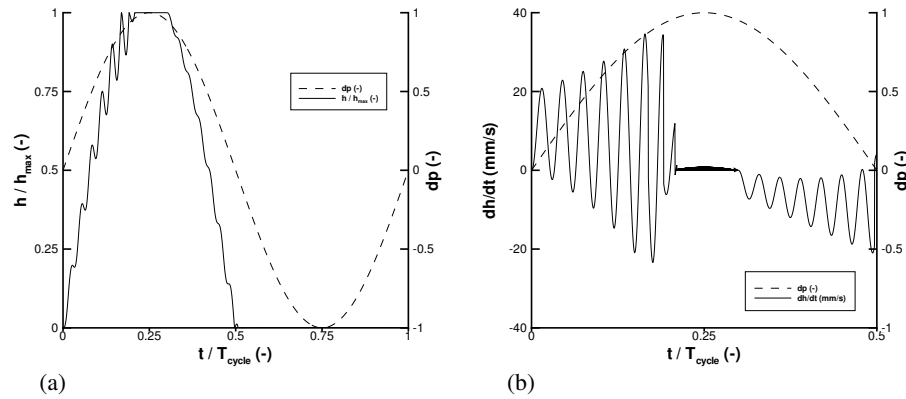


FIGURE 3.12: Valve behaviour for prescribed pressure difference: (a) plate height, (b) plate speed, (notation: $dp \equiv \Delta p/\hat{p}$, $T_{cycle} \equiv 2\pi/\omega$). Parameters: $\omega = 0.03\sqrt{k/m}$, $e_{res} = 0.1$ and $\hat{p} = 1.05 \frac{kh_{max}}{c_g A_p}$.

with the limiter, the plate is pushed steadily against this limiter. When the pressure difference equals approximately 95 % of its amplitude, the plate is released from the limiter with zero speed. The non-monotonous decreasing valve opening continues until after a single collision of the plate with the seat the valve is fully closed. Fig. 3.12b shows the plate speed as function of time. It is observed that the averaged speed during the opening event is larger than the averaged speed during the closing event. The first peak after opening shows a speed of +21 mm/s while the first peak after plate release from the limiter shows a speed of -7 mm/s. These different values can thus only be related to the different pressure rate of change. More specifically, it appears that

$$\frac{\left|\frac{d}{dt}(\Delta p)\right|_{\text{closing}}}{\left|\frac{d}{dt}(\Delta p)\right|_{\text{opening}}} = 0.30 \quad \text{and} \quad \frac{|\dot{h}|_{\text{closing}}}{|\dot{h}|_{\text{opening}}} = 0.35. \quad (3.78)$$

In a reciprocating compressor the rate of change of pressure difference across a valve is caused by the interaction of this valve with its environment. As we will see in Section 3.5, indeed not only Δp but also $\left|\frac{d}{dt}(\Delta p)\right|$ will be different for the opening and closing event. The early opening event in a real compressor valve involves effects of unsteady viscous flow. These effects together with some other extensions of the Basic Valve Theory is discussed in the following section.

3.4 Extended Valve Theory

The Basic Valve Theory as defined in Section 3.2 is able to account for fluid-structure interaction. However, the fluid dynamics model assumes quasi-steady flow, while many unsteady flow effects could be present in compressor valves. Therefore this section aims to extend the Basic Valve Theory with theories available in the literature for representing unsteady flow effects.

3.4.1 Hovering Insect Flight

Insects were the first animals to evolve active flight (Dickinson et al. 1999). Among insects, we find animals capable of taking off backwards, flying sideways and landing upside down. While such activities involve many physiological specializations that are poorly understood, perhaps the greatest puzzle is how flapping wings can generate enough force to keep an insect in the air (Dickinson et al. 1999). Conventional aerodynamic theory is based on rigid wings moving at constant velocity. When insect wings are placed in a wind tunnel and tested over the range of air velocities that they encounter when flying in nature, the measured forces are substantially smaller than those required for active flight (Ellington 1984a). Thus, some mechanism increases the lift produced by a wing, above that which it could generate according to conventional aerodynamics.

Direct measurements of the forces produced by flapping wings suggest that the aerodynamics of insect flight (Fig. 3.13) may be explained by the interaction of three mechanisms (e.g. Ellington 1984b, Ellington 1984c, Dickinson et al. 1999): i) *Delayed stall*. During the translational parts of the stroke, when the wings sweep through the air at a large angle of attack, large transient circulations can be developed before the separation associated with stall begins. ii) *Rotational circulation*. The force peak at the end of each half-stroke could be caused by the wing's own rotation serving as a source of circulation to generate an upward

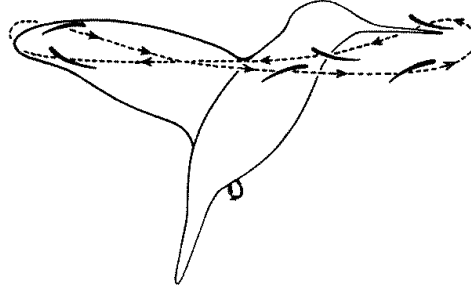


FIGURE 3.13: *The wing tip path of a hummingbird. From Ellington (1984a).*

force. iii) *Wake capture*. During stroke reversal the wing can extract energy from the shed vorticity of the previous stroke. Present research of Dickinson aims to find a general theory, incorporating both translational and rotational mechanisms, to explain the diverse patterns of wing motion of *different species* of insects (e.g. Dickinson et al. 1999, Birch and Dickinson 2001, Fry et al. 2003).

During operation of a compressor valve, the plate motion has a translational and a rotational (rocking) part. Because unsteady drag forces is a more difficult topic of 'speculation' than unsteady lift forces, the rocking of a valve plate could be surveyed with wake vorticity models (like Ellington 1984b, Ellington 1984c) and flow visualization techniques.

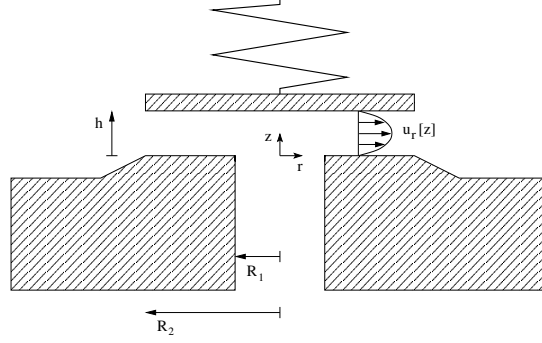
3.4.2 Unsteady Valve Flow

The Basic Valve Theory assumes quasi-steady flow. This subsection presents quantitative extensions of the Basic Valve Theory, which we will refer to as the *Extended Valve Theory*, by taking into account some unsteady flow effects.

Lubrication Theory We will use the theory of capillary flow between valve plate and seat to reformulate the Basic Valve Theory for very small valve openings. As illustrated in Fig. 3.15, we consider a circular disk valve where the port has radius R_1 and the disk has radius R_2 . The pressure in the port is assumed to be constant and equals the upstream pressure p_u . The downstream pressure is denoted by p_d . The flow is assumed to be axisymmetrical incompressible and cylindrical coordinates r and z are used to denote positions. At low Reynolds numbers in thin films, the Navier-Stokes equations reduce to the Reynolds equations of hydrodynamic lubrication, i.e.

$$\frac{\partial p}{\partial z} = 0, \quad \text{and} \quad \frac{\partial p}{\partial r} = \mu \frac{\partial^2 u_r}{\partial z^2}, \quad (3.79)$$

where p is the pressure in the film, μ is the dynamic viscosity and u_r is the radial velocity component. Before the present analysis continues we note that Ishizawa et al. (1987) presented a more elaborated theory about unsteady laminar flow between parallel disks in motion. Their analysis takes into account inertial terms, non-linear convective terms and two velocity components. However, the methods of asymptotic/multifold series expansion involve many coefficient-functions in order to describe the general solution. We only seek a simple extension of the Basic Valve Theory that takes into account some unsteady flow

FIGURE 3.14: *Capillary flow in circular disk valve.*

effects during valve opening and closing events. The integration of Eq. (3.79) for thin films yields a parabolic radial velocity distribution, i.e.

$$u_r = \frac{1}{2\mu} \frac{dp}{dr} z(z-h), \quad (3.80)$$

where the no-slip condition has been applied at $z = 0$ and $z = h$. The volume-flow rate at radial position r equals

$$\Phi_v[r] = \int_0^h u_r[z] 2\pi r dz = -\frac{\pi r}{6} \frac{dp}{dr} h^3. \quad (3.81)$$

Conservation of mass yields

$$\Phi_v[r] = \Phi_v[R_1] - \pi(r^2 - R_1^2) \frac{dh}{dt}. \quad (3.82)$$

Equating Eq. (3.81) and Eq. (3.82) yields

$$r \frac{dp}{dr} = \frac{6\mu}{h^3} \frac{dh}{dt} (r^2 - R_1^2) + R_1 \left(\frac{dp}{dr} \right)_{R_1}. \quad (3.83)$$

Let the normalized radius $r/R_1 \equiv \xi$ and $R_2/R_1 \equiv X$, then integration of Eq. (3.83) with respect to variable ξ yields

$$p = \frac{3\mu}{h^3} \frac{dh}{dt} R_1^2 (\xi^2 - 2 \ln \xi) + \ln \xi \left(\frac{dp}{d\xi} \right)_1 + C, \quad (3.84)$$

for $1 \leq \xi \leq X$. The boundary conditions $p = p_u$ at $\xi = 1$ and $p = p_d$ at $\xi = X$ determine the values of C and $(dp/d\xi)_1$ as follows,

$$C = p_u - \frac{3\mu}{h^3} \frac{dh}{dt} R_1^2, \quad (3.85)$$

$$\left(\frac{dp}{d\xi} \right)_1 = \frac{1}{\ln X} \left\{ p_d - p_u + \frac{3\mu}{h^3} \frac{dh}{dt} R_1^2 (1 - X^2 + 2 \ln X) \right\}, \quad (3.86)$$

which lead to the following equation for the pressure distribution in the film,

$$p - p_d = (p_u - p_d) \left(1 - \frac{\ln \xi}{\ln X} \right) + \frac{3\mu}{h^3} \frac{dh}{dt} R_1^2 \left(\xi^2 - 1 + \frac{\ln \xi}{\ln X} (1 - X^2) \right). \quad (3.87)$$

The force acting on the plate, introduced by the capillary flow, equals

$$\begin{aligned} F_{cap} &= \int_{R_1}^{R_2} p 2\pi r dr = \int_1^X p 2\pi R_1^2 \xi d\xi \\ &= \pi R_1^2 \left\{ X^2 p_d - p_u - \frac{(X^2 - 1)(p_d - p_u)}{2 \ln X} \right\} + \\ &\quad \frac{\mu}{h^3} \frac{dh}{dt} \frac{3\pi}{2} R_1^4 \left(1 - X^4 + \frac{1 - 2X^2 + X^4}{\ln X} \right). \end{aligned} \quad (3.88)$$

The first term on the right hand side, in addition to $(p_u - p_d)\pi R_1^2$, gives rise to a steady-flow force F_{sf} on the disk due to the pressure difference $p_u - p_d$. This force vanishes if that pressure difference is zero (identical to Eq. (3.10)). The second term gives rise to an unsteady-flow force F_{uf} which vanishes in case the viscosity is zero, in case the valve is fixed ($\dot{h} = 0$) or in case the contact area is zero ($X = 1$). These forces are derived by integrating the pressure distribution over the entire disk area, i.e. from $\xi = 0$ to $\xi = X$. Therefore the *total force* acting on the plate can be expressed as the sum of the following two components, i.e.

$$F_{sf} = \left(\frac{X^2 - 1}{2 \ln X} \right) \pi R_1^2 (p_u - p_d), \quad (3.89)$$

$$F_{uf} = \frac{\mu}{h^3} \frac{dh}{dt} \frac{3\pi}{2} R_1^4 \left(1 - X^4 + \frac{1 - 2X^2 + X^4}{\ln X} \right). \quad (3.90)$$

Note that the terms between large brackets only depend on the geometry. The presence of h^3 in the denominator of the unsteady-flow force causes this force to decrease rapidly as the film is diluted ($\dot{h} > 0$) under the action of the steady-flow force.

In the following example we will reconsider the case of hydrodynamic pipe flow, see Eqs. (3.67) - (3.69). However, the gas force acting on the plate will be split in two regimes, i.e.

$$F_g = \begin{cases} c_1 A_p (p_u - p_{atm}) + c_2 \frac{\mu R_1^4}{h^3} \dot{h} & , \quad 0 < h \leq 0.1 d_{sr} \\ c_g[h] A_p (p_u - p_{atm}) & , \quad 0.1 d_{sr} < h < h_{max} \end{cases} \quad (3.91)$$

where the coefficients are computed from the port area in the case of hydrodynamic pipe flow and a sealing rim length of 1.0 mm, i.e. $c_1 = 1.03$ and $c_2 = -1.71 \times 10^{-4}$. It appeared that the time-step has to be set on a very small value ($\Delta t f_{puls} = 10^{-5}$, where $f_{puls} \equiv \frac{\omega}{2\pi}$) in order to obtain numerically stable solutions. Fig. 3.15 shows some results. When the plate collides against the limiter, the plate kinetic energy is recovered partly and results in discontinuous derivatives of the pressure difference across the valve as function of time. However, rather than employing a restitution coefficient for the seat the gas force switches to the case of unsteady Stokes flow for very small valve opening ($h/h_{max} = 0.05$).

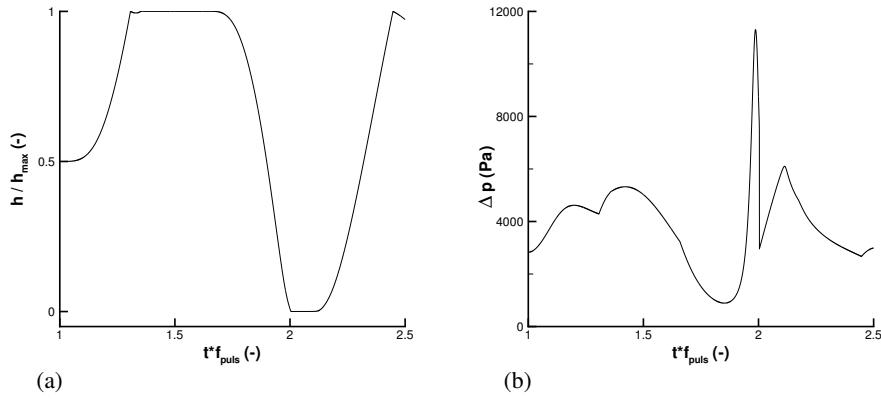


FIGURE 3.15: *Lubrication flow for small valve opening: (a) plate height, (b) pressure difference across valve. Parameters: $\omega\sqrt{m/k} = 1.50$, $e_{res} = 0.1$, $\frac{\zeta}{m\omega} = 0.0$, $\frac{h_{pl}}{h_{max}} = 1.50$ and $\frac{A_p}{L_g^2} = 1.56 \times 10^{-3}$.*

This results in a leakage flow of $3 \times 10^{-5} \text{ m}^3/\text{s}$ at a constant opening of $h/h_{max} = 2 \times 10^{-4}$. The pressure difference across the valve increases significantly but remains finite (although the flow is incompressible). Deverge et al. (2003) observed that the unsteady lubrication flow theory of Reynolds predicts the collision event of a vocal fold with a straight uniform channel better than the unsteady inviscid flow theory. The extension of the Basic Valve Theory for very small valve opening seems reasonable provided that the valve closes with parallel plate motion.

Plate Speed and Fluid Inertia Westphal (1893) already takes into account the 'breathing' of a valve when the plate speed is significant. St Hilaire et al. (1971) show that the pressure forces developed in the unsteady potential flow past a harmonium reed excite the reed vibration. Flow visualization studies are performed which indicate that the jet instability is not important in exciting the reed vibration.

The volume-flow rate of the Basic Valve Theory (Eq. (3.1)) is based on the exit flow conditions. However, even for incompressible flow the valve outlet flow rate Φ_v^{out} (at the outer edge of the plate) is not identical to the valve inlet flow rate Φ_v^{in} (at the port area) when the plate is in motion, i.e.

$$\Phi_v^{out} = \Phi_v^{in} - A_v \frac{dh}{dt}, \quad (3.92)$$

where A_v is the valve plate area. When the valve is opening with speed $dh/dt > 0$, the outlet flow rate will be slightly smaller than the inlet flow rate, due to the 'fluid suction' under the plate created additional volume.

When the port length of a valve is large, one may expect valve flow inertia effects to play a role in the valve dynamics. The Basic Valve Theory is based on a modified form of the Bernoulli equation for steady flow. However, for unsteady valve flows the pressure difference

can have a phase-shift in time compared to the flow rate, i.e.

$$\Delta p = \frac{1}{2}\rho \left(\frac{\Phi_v}{\alpha L_g h} \right)^2 + \rho \frac{L_p}{A_p} \frac{d}{dt} \Phi_v, \quad (3.93)$$

where L_p is the port length.

3.5 Diagnostics of Leaking Valves in Reciprocating Compressors

This section presents an example of the application of the Basic Valve Theory[¶]. Consider a two-stage air compressor, where two single-acting compressors are connected with an intercooler. This machine sucks air from a reservoir with a low pressure p_s . The compressed air discharging from the stage-one compressor is flowing through a pipe and cooled in the intercooler. The intercooler consists of a tube bundle with counter-current flowing cold water. After heat exchange the air is compressed in the stage-two compressor. The air flow that is discharged from the stage-two compressor has high pressure p_d .

We wish to locate a defective valve by making use of experimental data. The data consists of the temperature at the suction- and discharge chambers as well as the pressure just downstream of the intercooler. Fig. 3.16 shows a sketch of the configuration. The *full* list of

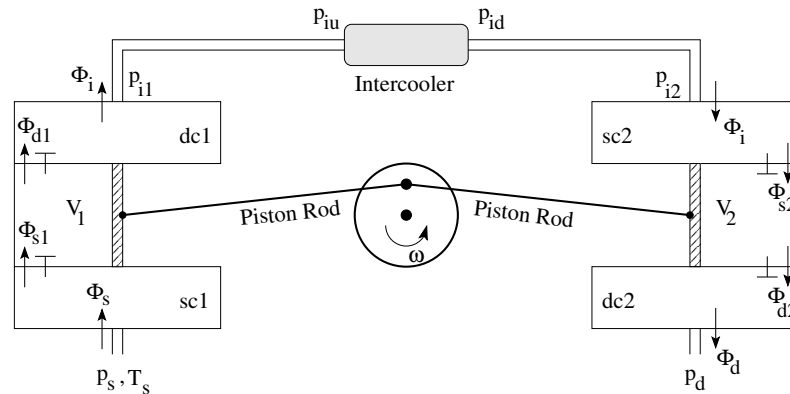


FIGURE 3.16: Sketch of a two-stage air compressor. Valves are indicated with a '┌'-symbol. The arrows indicate positive flow.

symbols that is used in this section is presented in the nomenclature of Appendix B.1. The governing equations are presented in Appendix B.2.

The strategy of locating the defective valve is the following. Firstly, the periodic solution of the non-failing system is characterized. Secondly, four simulations are performed where in each case one valve is leaking. Comparison of the changes of temperature and pressure at the

[¶]This problem of leaking valves was formulated as a task in the 2nd Students Workshop (Poland, 2004) of the European Forum for Reciprocating Compressors.

monitoring positions with the measured data, should yield a unique location of the defective valve.

The input parameters of the program can be found in Appendix B.3. Some key parameters are in the common practice range, i.e. the stroke $2x_1 = 2x_2 = 89$ mm, cylinder clearance $2V_{min1}/V_{cyl1} = 2V_{min2}/V_{cyl2} = 18\%$, piston frequency $\omega/2\pi = 12.5$ Hz and valve resonance frequency $\frac{1}{2\pi} \sqrt{k/m_v} = 50$ Hz.

The mathematical model (Appendix B.2) consists of a set of non-linear ordinary differential equations (ODEs) supplemented with algebraic equations (AEs). The numerical solution is obtained by applying the explicit Euler discretization scheme for the ODEs. A very small time-step is used to avoid numerical instability. Fortunately, for this set of equations and available computer capacity, computation time is not an issue. Every equation of motion for a valve plate, Eqs. (B.11) - (B.14), is split into two equations for independent variables h and $\frac{dh}{dt}$. In this way the resulting ODEs system is reduced to first order. The second part of the iteration step is performed by updating the remaining quantities governed by the AEs (Eq. (3.70) and Eq. (3.71)). The initial condition must be chosen with care, to avoid numerical instability! This is done by splitting the stage-one and stage-two parts. In stage one every pressure is set equal to p_s while in stage two p_d is used. In order to gain insight in the dependence of the solution on parameters, we simplify the model by setting: $\zeta = 0$, $\alpha[h] = \alpha$ is constant and $c_g[h] = c_g$ is constant for the valve dynamics, $\alpha_s = \alpha_d = \alpha_i$ and $A_s = A_d = A_i$ for the orifices, $L_{iu} = L_{id}$ and $\lambda = 0$ for the pipe flow.

After approximately 50 cycles the transient effects have disappeared and a periodic solution is established. Figures 3.17-3.19 characterize this periodic solution for the case of normal operating valves. The indicator diagrams (Fig. 3.17a) reveal that the work transferred by

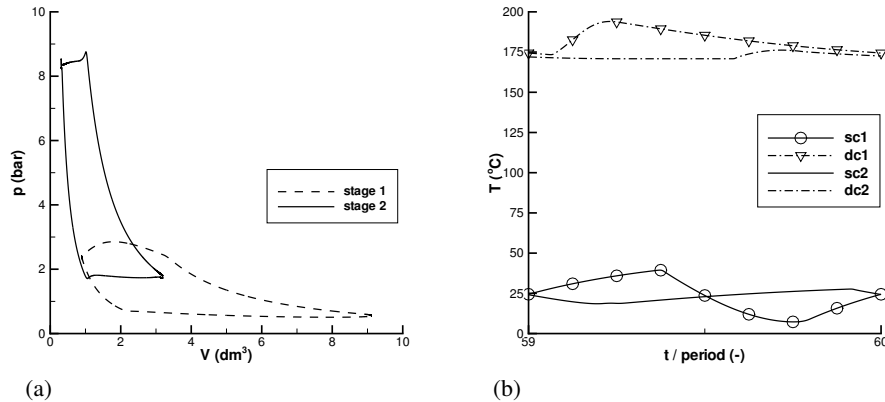


FIGURE 3.17: Simulation results for the non-failing system: (a) indicator diagrams, (b) temperature monitoring.

the piston to the gas ($-\oint p dV$) is approximately equal for both stages, although the total cylinder volume of stage 1 is larger than of that of stage 2. Non-constant discharge pressure at the top of each diagram indicates pressure loss across the discharge valve. At each stage, the temperature in the discharge chamber is significantly higher than in the suction chamber

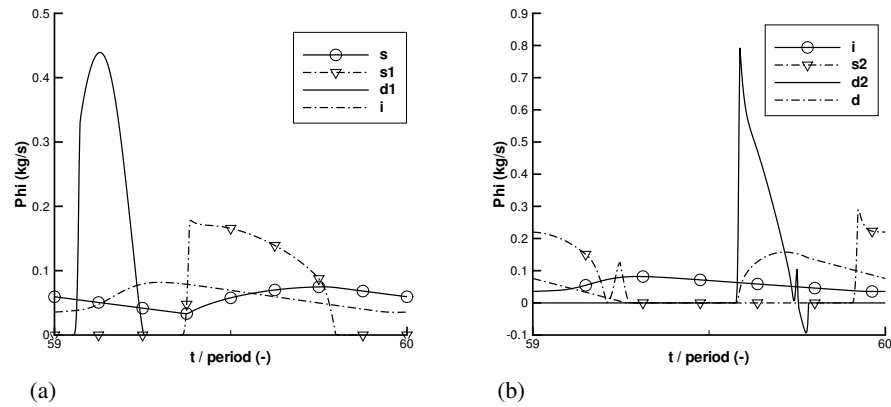


FIGURE 3.18: Simulation results for the non-failing system: (a) flow rates in stage 1, (b) flow rates in stage 2.

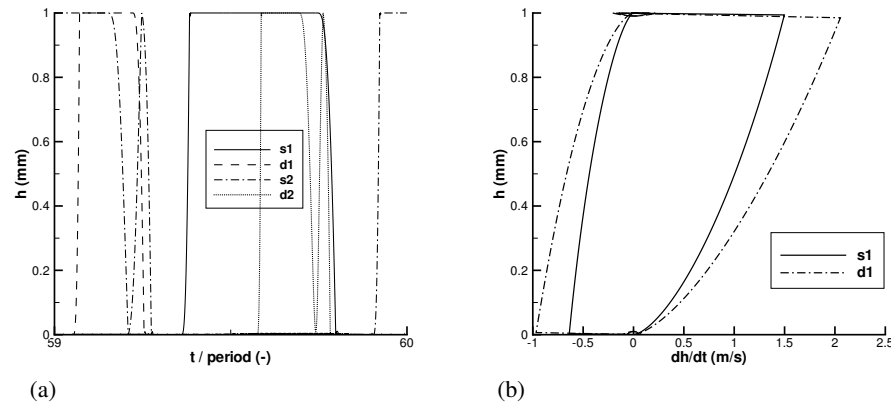


FIGURE 3.19: Simulation results for the non-failing system: (a) valve opening, (b) Poincaré map.

due to adiabatic compression (Fig. 3.17b). The peak flow rates in the discharge valves have rather large values compared to the flows through the orifices and the suction valves (Fig. 3.18). The flow through the discharge valve of stage two will even be reversed for some time (Fig. 3.18b). In stage one the suction and discharge is occurring rather smoothly, while in stage two the suction and discharge flow rate reveal plate impacts on the seat (Figs. 3.18 and 3.19a). A Poincaré map, also referred to as a phase-plane plot, reveals periodic behaviour of the valve dynamics (Fig. 3.19b). The collisions of plate with seat ($h = 0$) or limiter ($h = h_{max} = 1$ mm) induce non-linear behaviour and could result in chaotic limit cycles.

The modeling of a compression system requires modification when a defective valve is taken into account. It is expected that a defective valve has different properties than a non-failing valve. Oblique collisions of valve plate with seat (and limiter) eventually yield a fatigue problem. After crack propagation in the plate, fracture occurs and a part of the valve plate will break. The parameters $\{m_v, k, c_g, L_g\}$ are expected to decrease while ζ might increase.

It is proposed to model a defective valve with a single parameter, i.e. the reducing gap length ΔL_g . See Fig. 3.20. The new effective plate mass is reduced proportionally to ΔL_g .

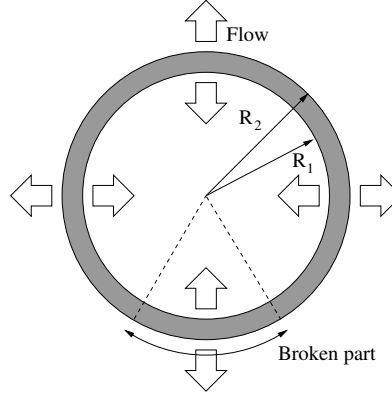


FIGURE 3.20: Top view of valve with partially broken ring plate, $L_g = 2\pi(R_1 + R_2) - \Delta L_g$.

The broken plate part is modelled as an orifice with a flow area proportionally to the maximum valve opening, i.e.

$$m_v \rightarrow m_v \left(1 - \frac{\Delta L_g}{L_g}\right), \quad (3.94)$$

$$\frac{\Phi_{s1} \text{sign}[p_{sc1} - p_1]}{\sqrt{2\rho_{sc1}|p_{sc1} - p_1|}} \rightarrow \underbrace{\alpha[h_{s1}](L_g - \Delta L_g)h_{s1}}_{\text{reduced area}} + \underbrace{\alpha[h_{max}]\Delta L_g h_{max}}_{\text{leakage area}}. \quad (3.95)$$

The equation for the flow rate is given only for the suction valve of stage one. Similar expressions hold for the three remaining valves, Eqs. (B.20) - (B.22).

The following table presents the simulation results for the case of compression with a single defective valve. The sign inside parentheses indicates an increased (+) or decreased

TABLE 3.1: *Maximum Values in Periodic Solution.*

Defect	p_{id} (bar)	T_{dc1} ($^{\circ}C$)	T_{sc2} ($^{\circ}C$)	T_{dc2} ($^{\circ}C$)
none	2.06	194	28	176
s1	1.82(-)	207(+)	28	186(+)
d1	1.88(-)	233(+)	28	184(+)
s2	3.36(+)	238(+)	32(+)	209(+)
d2	3.49(+)	243(+)	27(-)	262(+)

(-) value relative to the normal (defect=none) case, with the same accuracy as tabulated. Before we draw conclusions, let us briefly summarize the situation.

A two-stage compression system with intercooler is considered (Fig. 3.16). Various simplifications with respect to the actual situation are introduced. These simplifications include e.g. single-acting (rather than double-acting) compressors, calorically perfect gas, perfect heat exchange in intercooler, adiabatic processes in cylinder room, harmonic motion of piston, no leakage at piston rings, constant semi-empirical coefficients for valve dynamics, incompressible frictionless flow in pipelines and a single defective valve only. These model assumptions have led to a well-conditioned problem, while keeping the phenomena of interest such as fluid-structure interaction behaviour of valve dynamics and reversed flow in orifices. The conclusive results of the simulations are summarized in Table 3.1. It shows that only one situation (out of four) yields the same trend as monitored in the experiments, i.e. an increment for all measured quantities (T_{dc1} , T_{sc2} , T_{dc2} and p_{id}). From this we conclude that *the suction valve of stage-2 is the leaking valve.*

Finally, we shall discuss the mechanism of the pressure and temperatures increments. Consider the suction valve of the stage-2 compressor to be defective. When the cylinder volume of stage-2 is decreasing, adiabatic compression will rise the pressure and temperature in the cylinder. However, air is discharging not only at the valve $d2$! Although valve $s2$ will close ($h = 0$), the hot air will discharge through this valve because a leakage flow area of $\alpha[h_{max}]\Delta L_g h_{max}$ persists! Therefore, in the next stroke, hot air with relatively high pressure will be sucked into the same cylinder. Indeed, Fig. 3.21 demonstrates these effects. In the case of defective valve $s2$, an increased suction pressure can be observed (Fig. 3.21a). Additionally reversed flow is observed through this leaking suction valve (Fig. 3.21b).

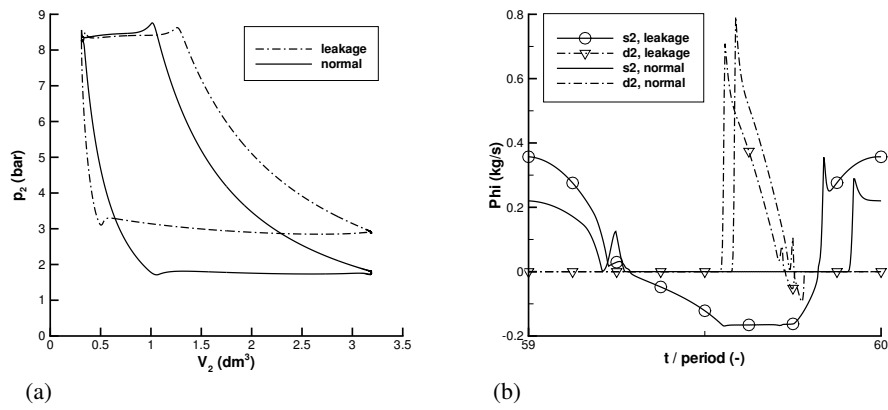


FIGURE 3.21: *Effects of leaking valve s_2 , for $\Delta L_g/L_g = 0.1$: (a) indicator diagrams, (b) flow rates.*

4.1 Introduction

This chapter presents the *numerical algorithms* that will be employed to compute the flow through a valve. The computational results of the fluid-structure interaction processes of valves are presented in Chapter 6.

The valve flow is expected to have fixed separation points at the edges of seat and plate (Fig. 1.5). In Chapter 2 the problem of turbulence modeling of flows around sharp edges was briefly touched. For the high Reynolds number flows we expect the boundary layers on the port walls and plate to be very thin. Therefore the Euler equations, describing *inviscid*, non-heat conducting compressible flows, will be used to model the flow processes. At sharp edges the effect of viscosity is accounted for by the Kutta condition which requires the velocity to be finite at the sharp edge, accomplished automatically by the artificial viscosity of the flux scheme. Additionally, compressor valves have rather complex geometries. Therefore we wish to solve the Euler equations in three spatial dimensions with an unstructured mesh.

It is well known, that it is difficult to solve the equations of compressible flow with Computational Fluid Dynamics for low Mach numbers. Preconditioning methods have been developed with the aim of solving nearly incompressible flow problems with numerical algorithms designed for compressible flows. These developments are motivated by several observations. First, there exist flow problems in which part of the flow region is essentially incompressible with locally small Mach numbers, whereas significant compressibility effects occur in other regions of the flow. Second, engineers prefer to use existing compressible flow codes over the broadest range of flow conditions possible in order to avoid dealing with multiple flow codes. In our case, the flow through a compressor valve is expected to belong to the class of mixed compressible/incompressible flows. Additionally, an available compressible flow method* is chosen to be the base of the algorithms used for simulating valve flows.

The difficulty in solving the compressible flow equations for low Mach numbers is associated with the following. Time-marching schemes provide good numerical stability and convergence characteristics when solving compressible flows at transonic and supersonic Mach numbers. At low speeds, however, system stiffness resulting from disparate particle and acoustic velocities causes convergence rates to deteriorate. The ideas of low Mach number preconditioning and artificial compressibility are combined into a unified approach, designed

*Dr. F. Put and Mr. P.H. Kelleners provided the source codes of EFD-Flow and MeshMan, which is gratefully acknowledged.

to enhance convergence rates of time-marching schemes for solving flows of variable density at all speeds.

In Section 4.2 the basic features of the computational method are presented. In Section 4.3 the subject of local preconditioning is presented in detail. Finally, Section 4.4 presents several test cases that show the ability of the present preconditioned Euler method to simulate steady and unsteady low Mach number flow.

4.2 Flow Solver

The flow solver EFD-Flow (3D steady inviscid compressible flows of a mixture of real gases with condensation, developed by Dr. F. Put) has been modified for simulation of flows of a single calorically perfect gas. This section presents the main part of that computational method. Preconditioning methods and time accuracy will be treated in the subsequent section.

Governing Equations The governing equations of motion for an inviscid flow without heat conduction are the Euler equations. Consider the spatially fixed finite volume V , also referred to as control volume, formed within the closed bounding surface $S = \partial V$. The unit normal vector of S is denoted by \mathbf{n} , pointing into the region exterior to V . The Euler equations, expressing conservation of mass, linear momentum and total energy are given by:

$$\frac{\partial}{\partial t} \iiint_V \mathbf{w} dV + \oint_S \mathbf{F} \cdot \mathbf{n} dS = 0, \quad (4.1)$$

where t is the time and \mathbf{w} is the vector of the conserved variables

$$\mathbf{w} = (\rho, \rho u, \rho v, \rho w, \rho E)^T. \quad (4.2)$$

In Cartesian coordinates the inviscid flux tensor \mathbf{F} is given by

$$\mathbf{F} = \begin{pmatrix} \rho \mathbf{u} \\ \rho \mathbf{u} \mathbf{u} + p \mathbf{e}_x \\ \rho \mathbf{u} \mathbf{v} + p \mathbf{e}_y \\ \rho \mathbf{u} \mathbf{w} + p \mathbf{e}_z \\ \rho \mathbf{u} H \end{pmatrix}, \quad (4.3)$$

where ρ is the density, $\mathbf{u} = u\mathbf{e}_x + v\mathbf{e}_y + w\mathbf{e}_z$ is the Cartesian velocity vector and p is the static pressure. The total energy per unit mass E is related to the total enthalpy per unit mass H by $H = E + p/\rho$, where $H = h_e + \frac{1}{2}|\mathbf{u}|^2$ and for the present calorically perfect gas $h_e = C_p T$. The static temperature is denoted with T and the specific heat at constant pressure is denoted with C_p which is constant. The equation of state for a perfect gas is $p = \rho R T$, where R is the ideal gas constant.

Finite Volume Method The Euler equations are discretized spatially using a Finite Volume Method wherein the physical domain is subdivided into small nondeforming tetrahedral volumes, also referred to as cells. The flow field is represented by associating with each

control volume V , consisting of cells or parts of consecutive cells, a distinct value of the discretized solution vector,

$$\bar{\mathbf{w}} \equiv \frac{1}{V} \iiint_V \mathbf{w} dV. \quad (4.4)$$

The vector $\bar{\mathbf{w}}$ is the cell-averaged value of the solution vector, and substitution of its definition in the integral equation (4.1) yields

$$\frac{\partial \bar{\mathbf{w}}}{\partial t} + \frac{1}{V} \iint_S \mathbf{F} \cdot \mathbf{n} dS = 0. \quad (4.5)$$

The surface integrals are evaluated by i) dividing the cell surface into discrete faces and ii) introducing the discrete flux tensor $\bar{\mathbf{F}}$. These fluxes are assumed to be constant over each face area S , yielding

$$\frac{d\bar{\mathbf{w}}}{dt} + \frac{1}{V} \sum_{\text{faces}} (\bar{\mathbf{F}} \cdot \mathbf{n} S)_{\text{face}} = 0. \quad (4.6)$$

Mesh Configuration The Finite Volume Method is applicable to arbitrary control volumes, which is a favorable aspect because compressor valves have complex geometries. The building block for the mesh used to discretize the three-dimensional space is the tetrahedron, see Fig. 4.1a. The black dots indicate the position of the nodes or vertices. The lines between the nodes are called edges. To simplify the following discussion we will consider the two-dimensional case. The simplex in two dimensions is the triangle. In a triangular mesh in which the triangles form the control volumes, the fluxes are restricted to the edges of the triangles. The waves carrying the information on the flow state are then restricted to only three directions. In order to circumvent this limitation a dual mesh is used. In the dual mesh, where the vertices become the new cell centers, new surface elements are defined, see Fig. 4.1b. The volume of a dual mesh (indicated in Fig. 4.1b by shaded regions) contains only one

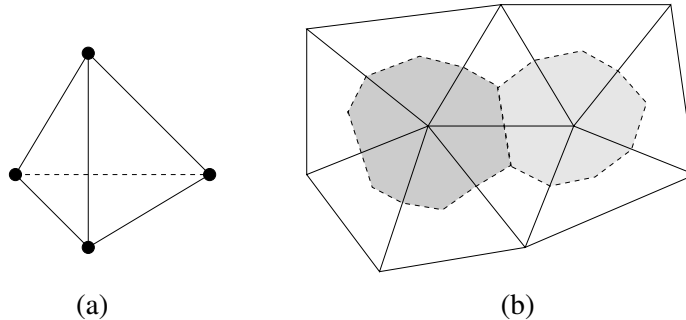


FIGURE 4.1: (a) *Tetrahedron in 3D.* (b) *Triangular grid with dual mesh in 2D.*

node of the triangular grid. The flow solver uses a *median dual mesh* because of its algebraical straightforwardness and its robustness. The construction of this dual mesh is the following. From the centroid of every triangle, lines are drawn to the midpoints of the three edges of the triangle. The triangle is now divided into three quadrilaterals. Each quadrilateral is uniquely

connected to a dual volume. By performing this operation on all triangles in the original tetrahedral mesh, the associated median dual mesh is constructed. In this study geometries and tetrahedral meshes are generated by making use of the commercial package ICEM-CFD. The generation of the dual mesh is performed with the inhouse developed package MeshMan (developed by Mr. P.H. Kelleners).

Flux Distribution The fluxes through the faces of the control volumes will be computed across the faces separating the volumes. On the median dual mesh the fluxes will be directed along the edges, see Fig. 4.2. The flux at the face related to an edge is computed by an

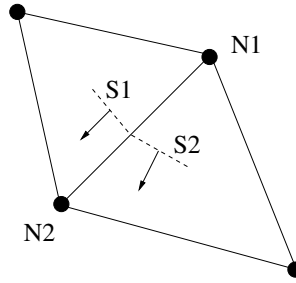


FIGURE 4.2: Two surface elements $S1$ and $S2$ related to edge $N1-N2$ in a two-dimensional mesh. The projection of tetrahedrons on a plane gives triangular elements. Flow variables are evaluated at the nodes (\bullet), which form the cell centers of the dual mesh.

operator reconstructing the flux at the surface, only using the flow states at both endpoints of the edge, say nodes $N1$ and $N2$. So the reconstructed flux will be identical for both surfaces $S1$ and $S2$. For this edge, we only need to store the sum of the contribution of surfaces $S1$ and $S2$.

Suppose we solve the discretized Euler equations for every control volume, one after another. For every control volume we then need to compute the fluxes over the faces bounding the volumes. The result is, that at all faces in the flow domain, in between two control volumes, the flux is computed twice. The expense can be prevented by unique orientation of the surfaces with respect to the edges, and performing the flux distribution in a different manner. On unstructured meshes (e.g. Mavriplis 1997), there are no major directions, along which to define positivity with respect to surface normals, as is employed for structured meshes. However, faces are related to edges and edges can be oriented in a uniform way. An edge connects two vertices or nodes and so two neighboring control volumes. The indices of these two nodes are used to orient the edge and so the associated surface.

Consider the discretized flux term $\sum_{\text{faces}} (\bar{\mathbf{F}} \cdot \mathbf{n} S)_{\text{face}}$ in Eq. (4.6). The flux vectors \mathbf{f} are calculated by a loop over all stored surfaces and distributed in the following way:

$$\mathbf{f}_{N1}^{\text{new}} = \mathbf{f}_{N1}^{\text{old}} + \bar{\mathbf{F}} \cdot \mathbf{n} S, \quad (4.7)$$

$$\mathbf{f}_{N2}^{\text{new}} = \mathbf{f}_{N2}^{\text{old}} - \bar{\mathbf{F}} \cdot \mathbf{n} S. \quad (4.8)$$

Riemann Problem Consider the following initial-value problem, resembling the one-dimensional Euler equations:

$$\begin{aligned}\frac{\partial \mathbf{w}}{\partial t} + \frac{\partial \mathbf{f}}{\partial x} &= 0, \quad t > 0, -\infty \leq x \leq \infty, \\ \mathbf{w}[x, 0] &= \mathbf{w}_0[x],\end{aligned}\tag{4.9}$$

where $\mathbf{w} = (\rho, \rho u, \rho E)^T$ and flux $\mathbf{f} = (\rho u, \rho u^2 + p, \rho u H)^T$. As usual, the following relations hold: $E = e + u^2/2 = H - p/\rho$ and for a calorically perfect gas $p = (\gamma - 1)\rho e$, where e is the internal energy per unit mass and $\gamma = C_p/C_v$.

In the 3D Finite Volume Method, the fluxes at each surface element are calculated based on this initial-value problem, which makes sense because a flow is locally one-dimensional in first approximation. When $\mathbf{w}_0[x]$ is divided into a constant left and a different but also constant right state, the Riemann problem is obtained (e.g. Laney 1998). Because the analytical solution is given in an implicit way, the evaluation of this analytical solution is too expensive for practical use. Therefore we will use an approximate Riemann solver. We introduce the discrete representation $x_j = j\Delta x$, $t_n = n\Delta t$ and suppose that \mathbf{w}_j^n is some approximation to $\mathbf{w}[x_j, t_n]$. For the numerical solution of Eq. (4.9), consider approximations \mathbf{w}_j^{n+1} defined by the explicit scheme:

$$\mathbf{w}_j^{n+1} = \mathbf{w}_j^n - \frac{\Delta t}{\Delta x} (\mathbf{f}_{j+1/2}^n - \mathbf{f}_{j-1/2}^n), \quad n \in N, j \in Z,\tag{4.10}$$

where Δt and Δx are respectively the time and space step. Here, the numerical flux defined by $\mathbf{f}_{j+1/2}^n = \mathbf{f}_{j+1/2}^n[\mathbf{w}_j^n, \mathbf{w}_{j+1}^n]$, is assumed to satisfy the consistency condition $\mathbf{f}_{j+1/2}^n[\mathbf{w}, \mathbf{w}] = \mathbf{f}[\mathbf{w}]$.

Flux Computation Roe (1986) gives a comparative description of the upwind schemes developed in the early 1980s, generally classified into the so-called flux-vector and flux-difference splittings, and points out their successes and failures. In the final stage of the present research it was found that upwind schemes are not suited for the computation of inviscid flows in valve-like geometries, even upon preconditioning of these schemes. Therefore a central difference scheme was implemented, which we will discuss in the following.

The spatially discretized flux terms in Eq. (4.6) are effectively computed with central differencing. As a consequence, the numerical dissipation which is inherently present in the discretized form of the governing equations is in general not sufficient to stabilize the time evolution of the system of equations. To prevent odd-even decoupling and to stabilize the time evolution of the system it is necessary to add artificial dissipation to the system of discretized equations. In the literature one can find a large variety of artificial dissipation terms. The only restriction is that the artificial dissipation should be of the same order of magnitude or less than the truncation error in order to have no effect on the formal accuracy of the discretization of the system of partial differential equations.

The artificial dissipation scheme used in the present research is essentially the one introduced by Jameson et al. (1981). This scheme, commonly referred to as the JST scheme, has been used and tested in a large number of studies (e.g. Pulliam 1986, Chima et al. 1987, Caughey and Turkel 1988, Jorgenson and Chima 1989, Sirbaugh 1995, Kok 1998, Van Noordenburg 1999, Hulshoff et al. 2001). In combination with a Runge-Kutta time integration

scheme (to be discussed later), it is a highly popular scheme mainly due to its simplicity, robustness and computational efficiency.

As stated before, at every surface element a local Riemann problem is considered. Let j and $j + 1$ be given states, i.e. nodes which represent the dual mesh cell centers (Fig. 4.3).

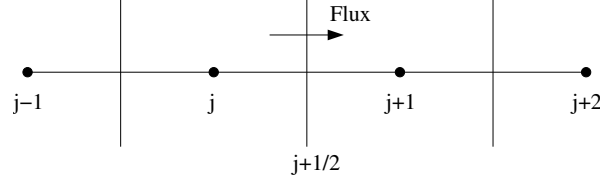


FIGURE 4.3: *Local Riemann problem. The numerical flux at interface $j + 1/2$ is computed as function of the flow variables evaluated in cell-centers $\{j - 1, j, j + 1, j + 2\}$.*

Then the flux tensor to be evaluated at surface $j + 1/2$ is expressed as

$$\mathbf{F}_{j+1/2} = \frac{\mathbf{F}[\mathbf{w}_j] + \mathbf{F}[\mathbf{w}_{j+1}]}{2} - \mathbf{D}_{j+1/2}, \quad (4.11)$$

where the first term on the right-hand side is the central difference flux tensor and $\mathbf{d}_{j+1/2} \equiv \mathbf{D}_{j+1/2} \cdot \mathbf{n}$ is the dissipation flux vector defined as a blending of second-order differences (to obtain acceptable representations of shock waves) and fourth-order differences (to damp high wave number modes and to prevent odd-even decoupling) of the modified conservative variables, i.e.

$$\mathbf{d}_{j+1/2} = R_{j+1/2} \left\{ \epsilon_{j+1/2}^{(2)} (\hat{\mathbf{w}}_{j+1} - \hat{\mathbf{w}}_j) - \epsilon_{j+1/2}^{(4)} (\hat{\mathbf{w}}_{j+2} - 3\hat{\mathbf{w}}_{j+1} + 3\hat{\mathbf{w}}_j - \hat{\mathbf{w}}_{j-1}) \right\}, \quad (4.12)$$

where $\hat{\mathbf{w}}$ is the vector $(\rho, \rho u, \rho v, \rho w, \rho H)^T$. The scaling factor $R_{j+1/2}$ ensures that the dissipation fluxes have the correct magnitude compared to the convection fluxes. It is defined as the average of the spectral radius of the Euler flux Jacobian, related to the local maximum wave speed, i.e.

$$R_{j+1/2} = \frac{1}{2}(R_j + R_{j+1}), \quad R_j = |\mathbf{u}_j| + c_j, \quad (4.13)$$

where \mathbf{u}_j is the local advection speed and c_j is the local speed of sound. The coefficients of the second-order and fourth-order differences are adapted to the flow, i.e.

$$\epsilon_{j+1/2}^{(2)} = \text{MIN}\{k^{(2)}\bar{\nu}, \frac{1}{2}\}, \quad (4.14)$$

$$\epsilon_{j+1/2}^{(4)} = \text{MAX}\{k^{(4)} - \beta^{(4)}\bar{\nu}, 0\}, \quad (4.15)$$

where $\bar{\nu}$ is a shock sensor, i.e.

$$\bar{\nu} = \text{MAX}\{\nu_j, \nu_{j+1}\}, \quad (4.16)$$

$$\nu_j = \left| \frac{p_{j+1} - 2p_j + p_{j-1}}{p_{j+1} + 2p_j + p_{j-1}} \right|. \quad (4.17)$$

Typical values for the constants $k^{(2)}$ and $k^{(4)}$ are in the ranges $\frac{1}{4}$ to $\frac{1}{2}$ and $\frac{1}{64}$ to $\frac{1}{32}$, respectively (Swanson and Turkel 1997) and $\beta^{(4)} = 2$ (Wesseling 2001). Note that the numerator in Eq. (4.17) is proportional to the second-derivative of the pressure at cell j . Near shocks, $\epsilon_{j+1/2}^{(4)}$ is switched off, since then $\bar{\nu}$ will be large. In smooth regions of the flow for which $\bar{\nu}$ is small, $\epsilon_{j+1/2}^{(2)}$ will be small and the fourth-order dissipation takes over.

The computation of the dissipation terms for unstructured meshes is more complex than for structured meshes. Therefore we explain the method that has been implemented by consideration of the two-dimensional case (Fig. 4.4). We wish to compute the Laplacian $\nabla^2 \hat{w}_a$

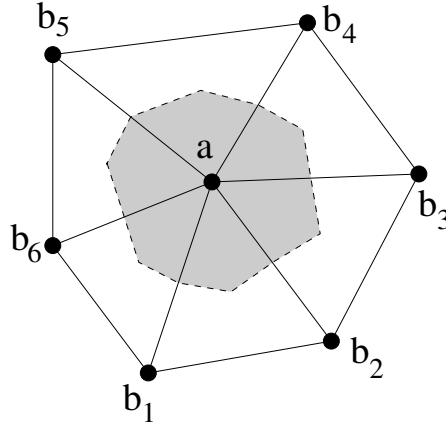


FIGURE 4.4: The dissipation in internal cell a depends on the Laplacian in cells a and $\{b_1, \dots, b_6\}$ (two-dimensional mesh). The grey area represents the dual mesh volume V_a .

and bi-harmonic $\nabla^4 \hat{w}_a$ in dual mesh cell a . Therefore two loops over all connectors (edges) are processed, i.e.

$$\nabla^2 \hat{w}_a \approx \frac{1}{V_a} \sum_{j=1,6} \frac{\hat{w}_{b_j} - \hat{w}_a}{\|\mathbf{x}_{b_j} - \mathbf{x}_a\|} S_{ab_j}, \quad (4.18)$$

$$\nabla^4 \hat{w}_a \approx \frac{1}{V_a} \sum_{j=1,6} \frac{\nabla^2 \hat{w}_{b_j} - \nabla^2 \hat{w}_a}{\|\mathbf{x}_{b_j} - \mathbf{x}_a\|} S_{ab_j}, \quad (4.19)$$

where operator $\nabla^4 \equiv \nabla \cdot \nabla(\nabla^2)$. The first loop computes the control-volume averaged value of the Laplacian of a quantity by application of Gauss divergence theorem on the gradient of that quantity. This Laplacian is stored in each cell-center. The second loop computes the bi-harmonic in a dual mesh cell-center by application of Gauss divergence theorem on the gradient of the Laplacian.

Consider again the one-dimensional case of Fig. 4.3. For smooth flows the dissipation terms must be related to third-order differences at the interfaces. For interface $j + 1/2$ this yields

$$\partial^3 \hat{w}_{j+1/2} \approx \partial^2 \hat{w}_{j+1} - \partial^2 \hat{w}_j = \hat{w}_{j+2} - 3\hat{w}_{j+1} + 3\hat{w}_j - \hat{w}_{j-1}, \quad (4.20)$$

which requires data from four cells. For cell j the fourth-order dissipation term is computed by subtracting the third-order differences at the neighboring interfaces, i.e.

$$\partial^4 \hat{\mathbf{w}}_j \approx \partial^3 \hat{\mathbf{w}}_{j+1/2} - \partial^3 \hat{\mathbf{w}}_{j-1/2} = \hat{\mathbf{w}}_{j-2} - 4\hat{\mathbf{w}}_{j-1} + 6\hat{\mathbf{w}}_j - 4\hat{\mathbf{w}}_{j+1} + \hat{\mathbf{w}}_{j+2}, \quad (4.21)$$

which requires data from five cells.

Temporal Discretization When the discretized integral equations Eq. (4.6) are applied to each cell of the computational domain, a system of coupled ordinary differential equations is obtained. An explicit time-stepping scheme is used to discretize the time derivative and flux terms in Eq. (4.6). Consider the system of spatially discretized equations, i.e.

$$\frac{d\mathbf{w}}{dt} + \mathbf{f}[\mathbf{w}] = 0, \quad (4.22)$$

where vector \mathbf{w} is the cell-averaged value of the converted variables and vector \mathbf{f} is the discrete flux vector. The explicit ℓ -stage modified Runge-Kutta method for updating \mathbf{w}_n to \mathbf{w}_{n+1} reads

$$\begin{aligned} \mathbf{w}_0 &= \mathbf{w}_n, \\ \mathbf{w}_k &= \mathbf{w}_0 - \alpha_k \Delta t \mathbf{f}[\mathbf{w}_{k-1}], \quad k = 1, \dots, \ell \\ \mathbf{w}_{n+1} &= \mathbf{w}_\ell, \end{aligned} \quad (4.23)$$

where the time is discretized as $t_n = n\Delta t$.

The traditional four-stage modified Runge-Kutta method, which is second-order time-accurate, has coefficients $\alpha_k \in \{\frac{1}{4}, \frac{1}{3}, \frac{1}{2}, 1\}$. We will use this low-storage method as a relaxation procedure to obtain the steady-state solution.

Consider the flux vector to be split into a central difference term $\mathbf{f}^{(cd)}$ and a dissipation term $\mathbf{f}^{(dis)}$, i.e. $\mathbf{f} \equiv \mathbf{f}^{(cd)} - \mathbf{f}^{(dis)}$. Substitution of the flux vector in Eq. (4.23) and introducing coefficients β_k yields

$$\mathbf{w}_k = \mathbf{w}_0 - \alpha_k \Delta t (\mathbf{f}^{(cd)}[\mathbf{w}_{k-1}] - \mathbf{f}_k^{(dis)}), \quad (4.24)$$

$$\mathbf{f}_k^{(dis)} = \beta_k \mathbf{f}^{(dis)}[\mathbf{w}_{k-1}] + (1 - \beta_k) \mathbf{f}^{(dis)}[\mathbf{w}_{k-2}]. \quad (4.25)$$

The coefficients α_k are chosen to maximize the stability interval along the imaginary axis and the coefficients β_k are chosen to increase the stability interval along the negative real axis. This method is commonly referred to as Jameson's modified Runge-Kutta method. We will use a four-stage scheme with two evaluations of the artificial dissipation analog to Jameson (1995). Its coefficients are

$$\begin{aligned} \alpha_1 &= \frac{1}{3}, & \beta_1 &= 1, \\ \alpha_2 &= \frac{4}{15}, & \beta_2 &= \frac{1}{2}, \\ \alpha_3 &= \frac{5}{9}, & \beta_3 &= 0, \\ \alpha_4 &= 1, & \beta_4 &= 0. \end{aligned} \quad (4.26)$$

For time marching towards a steady state, computation time is minimized when time integration in every control volume is related to its allowable maximum time-step determined

by numerical stability. This procedure is called *local time-stepping*[†], where the time-step is defined as

$$\Delta t = CFL \frac{\frac{1}{4}V^{1/3}}{|\mathbf{u}| + c}, \quad (4.27)$$

where $CFL \sim 1$ is the Courant-Friedrich-Lewy number, V is the volume of the control volume, \mathbf{u} is the local velocity vector and c is the local speed of sound.

Boundary Conditions The preceding paragraphs deal with the computation of fluxes between control volumes in the interior of the computational domain. Volumes on the boundary of this domain, however, share interfaces with this boundary. Depending on the character of the boundary, fluxes over these surfaces need special treatment. At all boundaries, dummy cells (also referred to as ghost cells) located outside the computational domain are introduced. These dummy cells have an associated state vector which is updated according to the character of the boundary.

Two types of boundary conditions are implemented, i) permeable boundaries (subsonic in/outflow) and ii) solid walls. Permeable boundaries will be discussed in detail in Section 4.3.3. At solid walls a simple but robust boundary condition is used, see Fig. 4.5. The

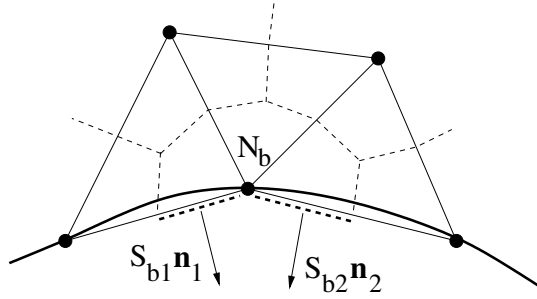


FIGURE 4.5: *Two-dimensional mesh near solid wall.*

physical wall is indicated by the thick solid line, while the relevant part of the boundary of the control volume next to the wall is indicated by the thick dashed line. The wall related surface vector is $S_b \mathbf{n} \equiv S_{b1} \mathbf{n}_1 + S_{b2} \mathbf{n}_2$. Consider the Euler equations in differential form. Then the constraint $\mathbf{u} \cdot \mathbf{n}|_b \equiv 0$ transforms into $\nabla p \cdot \mathbf{n}|_b \equiv 0$. This shows that the pressure p_b at the boundary node N_b can be used in an unmodified way at surface S_b in order to update the flux. In summary, the flux vector $\mathbf{F} \cdot \mathbf{n} S$ (related to the control volume associated with node N_b) is updated by adding $p_b S_b (0, \mathbf{n} \cdot \mathbf{e}_x, \mathbf{n} \cdot \mathbf{e}_y, \mathbf{n} \cdot \mathbf{e}_z, 0)^T$ to this flux vector.

[†]In case of time accurate simulations, the time-step for all cells must be the same. This global time-step is commonly varied every time by forcing it to be the minimum of all local time-steps, provided that this global time-step is small enough to capture all physical time scales.

4.3 Local Preconditioning

4.3.1 Literature Survey

The numerical solution of the Navier-Stokes equations is complicated in the case of incompressible flow, by the lack of an independent equation for the pressure (e.g. an equation of state, relating pressure and density). The absolute pressure is of no significance in an incompressible flow, only the gradient of the pressure affects the flow field. One way to overcome this difficulty was first developed by Chorin (1967), who transformed the equations into a hyperbolic system of equations in pseudo-time. A second way to overcome this difficulty is to construct the pressure field so as to guarantee satisfaction of the continuity equation, see e.g. the SIMPLE pressure-correction algorithm of Patankar (1980).

Turkel (1987) was amongst the first researchers to generalize the method of Chorin of pseudo-compressibility to low speed compressible flow. Turkel concludes with the notion that many authors had already successfully used variations of pseudo-compressibility preconditioning for both the incompressible and compressible flow equations. The various approaches used in these papers have been unified and generalized by Turkel (1987).

Volpe (1993) examined the performance of three compressible flow methods at low free-stream Mach numbers. Consider the two-dimensional inviscid steady flow over a circular cylinder. The surface pressure coefficient has been used as the error indicator, as e.g. errors in any one of the conservative variables would show up as errors in the surface pressure coefficient. Consider computations for various meshes and for Mach numbers M of 0.1, 0.01 and 0.001. For a fixed mesh, the error in the numerical solution increased as the Mach number was decreased! The solution for the $M = 0.001$ case was so poor that symmetry was lacking, even though the numerical solution had reached a steady state (the maximum residual in the density field reduced to machine accuracy)! The discrepancy between computed and analytical solutions decreased when the mesh was refined.

Turkel et al. (1994) examined how preconditioning can be used to improve the accuracy of the steady-state numerical solution, in case of small Mach numbers. They found necessary properties of the artificial viscosity, in order to have convergence as the Mach number goes to zero.

Until 1996 the design of local preconditioners has been solely based on *eigenvalue* analysis. However, Darmofal and Schmid (1996) showed that the *eigenvector* structure also has an influence on the performance of preconditioners. Due to the lack of eigenvector orthogonality, small perturbations in a linearized evolution problem can be significantly amplified over short time scales, while the long time behaviour of the system is governed by the eigenvalues. However, for a nonlinear problem, this short time non-normal growth may completely alter the mean state, resulting in a significant lack of robustness.

The basic goal of preconditioning is to reduce the stiffness of the system, which results in convergence acceleration for time-marching methods. This, though, is not the only possible benefit of preconditioning. Lee (1998) discussed several design criteria for local preconditioning of the Euler equations. These criteria are based on the following list of major benefits.

- *Removal of stiffness.* Local preconditioning can reduce the stiffness of the Euler equations, caused by the range of characteristic speeds. In the nearly incompressible flow regime the stiffness can be entirely removed. In the transonic flow regime, it can be

substantially reduced. In practice, the condition number (i.e. the ratio of largest-to-smallest wavenumbers) becomes a function of the cell aspect ratio.

- *System behaves as a scalar equation.* Preconditioning makes the Euler equations behave more like a scalar equation, because the spread amongst all eigenvectors is reduced. This property is advantageous in applying additional convergence-acceleration techniques.
- *Accuracy preservation for $M \rightarrow 0$.* In the limit of low Mach number M , the accuracy of the spatial discretization can be improved by preconditioning the artificial dissipation term.
- *Decoupling of Euler equations.* Some preconditioning matrices have the property of decoupling the entropy equation from the Euler equations. Such decoupling allows the development of genuinely multidimensional discretizations.

Though local preconditioning provides several benefits, these come at the expense of robustness. Lee (1998) presents four reasons for instability in a stagnation region:

- *Unstable local time-step.* As the local Mach number M decreases, the allowable local time-step for the preconditioned equations increases as M^{-1} , possibly varying strongly from cell to cell.
- *Degeneration of eigenvectors.* Small M reduces the orthogonality between eigenvectors, increasing the chance of transient growth, since the eigenvector basis is not effectively spanning the solution space.
- *Flow angle sensitivity.* The flow angle varies substantially around a stagnation point, and the preconditioned system may be over-sensitive to this variation in flow direction.
- *Vorticity production.* In planar inviscid flows, vorticity is merely convected with the flow speed, production is caused only by wall motion or a shock. However, the preconditioned system may have artificial vorticity production terms, which effect is amplified around stagnation points, where velocity and pressure fields vary substantially.

It can be shown (e.g. Gustafsson 1980) how to derive the singular limit of the Euler equations when the Mach number M goes to zero. When the Euler equations are non-dimensionalized, solutions can be sought in the form of an asymptotic expansion in powers of M (see Appendix A). Collecting terms with equal power of M , shows that in the limit of incompressible flow the pressure is constant in space up to variations of order M^2 . Furthermore it can be shown that the limit solutions satisfy the equations for incompressible (inviscid) flow. Guillard and Viozat (1999) presented an asymptotic analysis in powers of M of the flux-difference splitting approximations of the Euler equations in the limit of low M . They proved that the solutions of the discrete system contain pressure variations of order M . This explains why these kind of approximations of the Euler equations cannot compute accurately low-speed flow. Preconditioning of the numerical dissipation tensor allows to recover a correct scaling of the pressure.

An overview of the *status-quo* of preconditioning for the steady-state compressible inviscid fluid dynamic equations is presented by Turkel (1999) and Venkateswaran and Merkle (1999). They also consider extensions to the Navier-Stokes equations.

4.3.2 Time-Derivative Preconditioning

This subsection follows the preconditioning method of Weiss and Smith (1995) because it can be considered as a rather simple form out of all potential preconditioners, while the wavespeed modification in the subsonic region is suited for the present flow regime.

Preconditioning Matrix The governing equations of motion for an inviscid compressible flow without effects of heat conduction are the Euler equations. In a Cartesian coordinate system these Euler equations, expressing conservation of mass, linear momentum and total energy are given by:

$$\frac{\partial \mathbf{w}}{\partial t} + \frac{\partial \mathbf{f}}{\partial x} + \frac{\partial \mathbf{g}}{\partial y} + \frac{\partial \mathbf{h}}{\partial z} = 0, \quad (4.28)$$

where \mathbf{w} is the vector of conserved variables

$$\mathbf{w} = (\rho, \rho u, \rho v, \rho w, \rho E)^T, \quad (4.29)$$

and \mathbf{f} , \mathbf{g} and \mathbf{h} are the convective flux vectors

$$\begin{aligned} \mathbf{f} &= (\rho u, \rho u^2 + p, \rho uv, \rho uw, \rho u H)^T, \\ \mathbf{g} &= (\rho v, \rho uv, \rho v^2 + p, \rho vw, \rho v H)^T, \\ \mathbf{h} &= (\rho w, \rho uw, \rho vw, \rho w^2 + p, \rho w H)^T, \end{aligned} \quad (4.30)$$

where t is the time, x, y, z are the Cartesian components of the position vector, ρ is the density, u, v, w are the Cartesian velocity components in the x, y, z directions, respectively and p is the static pressure. The total energy per unit mass E is related to the total enthalpy per unit mass H by $H \equiv E + p/\rho$, where $H \equiv h_e + \frac{1}{2}|\mathbf{u}|^2$ and $h_e = C_p T$. The static temperature is denoted with T and the specific heat at constant pressure is denoted with C_p . For flows of variable density fluids, an equation of state, typically of the form $\rho = \rho[p, T]$ must be specified additionally.[‡]

The derivation of the preconditioning matrix begins by transforming the dependent variables in Eq. (4.28) from conserved variables \mathbf{w} to primitive variables \mathbf{q} as follows:

$$\frac{\partial \mathbf{W}}{\partial \mathbf{Q}} \frac{\partial \mathbf{q}}{\partial t} + \frac{\partial \mathbf{f}}{\partial x} + \frac{\partial \mathbf{g}}{\partial y} + \frac{\partial \mathbf{h}}{\partial z} = 0, \quad (4.31)$$

where $\mathbf{q} = (p, u, v, w, T)^T$ and the Jacobian $\frac{\partial \mathbf{W}}{\partial \mathbf{Q}}$ is given by

$$\frac{\partial \mathbf{W}}{\partial \mathbf{Q}} = \begin{bmatrix} \rho_p & 0 & 0 & 0 & \rho_T \\ \rho_p u & \rho & 0 & 0 & \rho_T u \\ \rho_p v & 0 & \rho & 0 & \rho_T v \\ \rho_p w & 0 & 0 & \rho & \rho_T w \\ \rho_p H - 1 & \rho u & \rho v & \rho w & \rho_T H + \rho C_p \end{bmatrix}, \quad (4.32)$$

where $\rho_p = \frac{\partial \rho}{\partial p}|_T$ and $\rho_T = \frac{\partial \rho}{\partial T}|_p$. The choice of primitive variables \mathbf{q} as dependent variables is a natural choice when solving incompressible flows. Furthermore, the choice of pressure as

[‡]For didactic reasons the implicit assumption of a calorically perfect gas, i.e. $p = \rho R T$ and constant C_p , is postponed.

a dependent variable allows the propagation of acoustic waves in the system to be modified. This becomes clear when we transform Eq. (4.31) by multiplying with the transformation matrix \mathbf{K} as follows:

$$\left(\mathbf{K} \frac{\partial \mathbf{W}}{\partial \mathbf{Q}} \right) \frac{\partial \mathbf{q}}{\partial t} + \mathbf{K} \left(\frac{\partial \mathbf{f}}{\partial x} + \frac{\partial \mathbf{g}}{\partial y} + \frac{\partial \mathbf{h}}{\partial z} \right) = 0, \quad (4.33)$$

where

$$\mathbf{K} = \begin{bmatrix} 1 & 0 & 0 & 0 & 0 \\ -u & 1 & 0 & 0 & 0 \\ -v & 0 & 1 & 0 & 0 \\ -w & 0 & 0 & 1 & 0 \\ |\mathbf{u}|^2 - H & -u & -v & -w & 1 \end{bmatrix}. \quad (4.34)$$

The matrix pre-multiplying the time derivative in Eq. (4.33) is given by

$$\mathbf{K} \frac{\partial \mathbf{W}}{\partial \mathbf{Q}} = \begin{bmatrix} \rho_p & 0 & 0 & 0 & \rho_T \\ 0 & \rho & 0 & 0 & 0 \\ 0 & 0 & \rho & 0 & 0 \\ 0 & 0 & 0 & \rho & 0 \\ -1 & 0 & 0 & 0 & \rho C_p \end{bmatrix}. \quad (4.35)$$

Upon inspection of Eqs. (4.33)-(4.35) we see that e.g. the term ρ_p that multiplies the pressure time derivative in the first-row equation controls the speed of propagation of acoustic waves in the system. It is interesting to note that, for a calorically perfect gas, $\rho_p = 1/RT = \gamma/c^2$ where R is the ideal gas constant, c is the acoustic velocity (speed of sound in a quiescent medium) and $\gamma = C_p/C_v$ where C_v is the specific heat at constant volume, whereas for incompressible flow $\rho_p = 0$, consistent with the notion of infinite pressure wave speeds. Thus, if we replace ρ_p by a term proportional to the inverse of the local velocity squared, we can control the eigenvalues of the system such that they are all of the same order.

We precondition the system by replacing the matrix given by Eq. (4.35) with the preconditioning matrix

$$\mathbf{\Gamma} = \begin{bmatrix} \Theta & 0 & 0 & 0 & \rho_T \\ 0 & \rho & 0 & 0 & 0 \\ 0 & 0 & \rho & 0 & 0 \\ 0 & 0 & 0 & \rho & 0 \\ -1 & 0 & 0 & 0 & \rho C_p \end{bmatrix}, \quad (4.36)$$

where Θ is given by

$$\Theta = \frac{1}{U_r^2} - \frac{\rho_T}{\rho C_p}. \quad (4.37)$$

Here U_r is a reference velocity defined as follows:

$$U_r = \begin{cases} \epsilon c, & \text{if } |\mathbf{u}| < \epsilon c \\ |\mathbf{u}|, & \text{if } \epsilon c < |\mathbf{u}| < c \\ c, & \text{if } |\mathbf{u}| > c \end{cases}, \quad (4.38)$$

where ϵ is a small number ($\sim 10^{-5}$) included to prevent singularities at stagnation points[§]. The form of Eq. (4.37) ensures that for a calorically perfect gas, as $U_r \rightarrow c$, Θ reduces to γ/c^2 , consistent with the non-preconditioned Eq. (4.35).

The preconditioned system is obtained by substitution of Eq. (4.36) for Eq. (4.35) in Eq. (4.33) and premultiplying the result by \mathbf{K}^{-1} to yield

$$\boxed{\mathbf{P}^{-1} \frac{\partial \mathbf{q}}{\partial t} + \frac{\partial \mathbf{f}}{\partial x} + \frac{\partial \mathbf{g}}{\partial y} + \frac{\partial \mathbf{h}}{\partial z} = 0}, \quad (4.39)$$

where

$$\mathbf{P}^{-1} = \mathbf{K}^{-1} \mathbf{\Gamma} = \begin{bmatrix} \Theta & 0 & 0 & 0 & \rho_T \\ \Theta u & \rho & 0 & 0 & \rho_T u \\ \Theta v & 0 & \rho & 0 & \rho_T v \\ \Theta w & 0 & 0 & \rho & \rho_T w \\ \Theta H - 1 & \rho u & \rho v & \rho w & \rho_T H + \rho C_p \end{bmatrix}. \quad (4.40)$$

When we write $\Theta = (\Theta - \frac{\gamma}{c^2}) + \frac{\gamma}{c^2}$ it is seen easily that in case of preconditioning additional terms appear in the Euler equations. These terms are $(\frac{1}{U_r^2} - \frac{1}{c^2}) \frac{\partial p}{\partial t} (1, u, v, w, H)^T$ and vanish when $U_r \rightarrow c$.

It is not necessary to multiply \mathbf{P} with Jacobian $\frac{\partial \mathbf{W}}{\partial \mathbf{Q}}$ in order to obtain a system in conservation form. The density is not very appropriate for almost incompressible flow. Spatial derivatives of the density are almost zero and hence not suited for use in artificial viscosity. Consider the primitive variables \mathbf{q} to be updated according to

$$\frac{\partial \mathbf{q}}{\partial t} + \mathbf{P} \left(\frac{\partial \mathbf{f}}{\partial x} + \frac{\partial \mathbf{g}}{\partial y} + \frac{\partial \mathbf{h}}{\partial z} \right) = 0. \quad (4.41)$$

Then the matrix \mathbf{P} equals

$$\mathbf{P} = \begin{bmatrix} \frac{|\mathbf{u}|^2 U_r^2}{2C_p T} & -\frac{u U_r^2}{C_p T} & -\frac{v U_r^2}{C_p T} & -\frac{w U_r^2}{C_p T} & \frac{U_r^2}{C_p T} \\ -\frac{u}{\rho} & \frac{1}{\rho} & 0 & 0 & 0 \\ -\frac{v}{\rho} & 0 & \frac{1}{\rho} & 0 & 0 \\ -\frac{w}{\rho} & 0 & 0 & \frac{1}{\rho} & 0 \\ \frac{|\mathbf{u}|^2}{2\rho C_p} \xi - \frac{T}{\rho} & -\frac{u}{\rho C_p} \xi & -\frac{v}{\rho C_p} \xi & -\frac{w}{\rho C_p} \xi & \frac{1}{\rho C_p} \xi \end{bmatrix}, \quad (4.42)$$

where $\xi = (1 + \frac{U_r^2}{C_p T})$. Rather than updating the conservative variables by matrix multiplication, these variables are updated by employing the updated primitive variables.

The goal is to obtain the steady-state solution of the Euler equations, i.e. $\frac{\partial \mathbf{f}}{\partial x} + \frac{\partial \mathbf{g}}{\partial y} + \frac{\partial \mathbf{h}}{\partial z} = 0$. However, when the implemented preconditioned equations are solved numerically, the following system is approximated to a certain convergence level: $\mathbf{P} \left(\frac{\partial \mathbf{f}}{\partial x} + \frac{\partial \mathbf{g}}{\partial y} + \frac{\partial \mathbf{h}}{\partial z} \right) = 0$. The question rises whether the latter system has the same solution as the original system.

[§]Weiss et al. (1999) considered an additional limitation on U_r by prohibiting amplification of pressure perturbations, i.e. $\epsilon c \rightarrow \epsilon \sqrt{\Delta p / \rho}$. In general, global preconditioning uses a constant reference velocity, while local preconditioning can be divided into global- and local cut-off. A more elaborate discussion is presented in Venkateswaran et al. (2003).

In order to prove that the preconditioned system has a trivial solution, the determinant of \mathbf{P} should be determined, i.e.

$$\det[\mathbf{P}] = \frac{U_r^2}{\rho^4 C_p}. \quad (4.43)$$

The prove of a trivial solution (i.e. $\frac{\partial \mathbf{f}}{\partial x} + \frac{\partial \mathbf{g}}{\partial y} + \frac{\partial \mathbf{h}}{\partial z} = 0$) is completed when we show that $\det[\mathbf{P}] \neq 0$ for any situation. This implies that the situation of $U_r \rightarrow 0$ is prohibited, which is true because $\min[U_r] = \epsilon c > 0$.

Wave Velocities In order to obtain the wave velocities that are present in the preconditioned system, consider one-dimensional flow. Locally a three-dimensional flow can be considered one-dimensional, let's say in \mathbf{e}_x direction.[¶] The characteristic form of Eq. (4.39) is obtained by deleting \mathbf{g} and \mathbf{h} , transforming $\frac{\partial \mathbf{f}}{\partial x}$ into $\frac{\partial \mathbf{f}}{\partial \mathbf{q}} \frac{\partial \mathbf{q}}{\partial x}$ and deleting v and w , yielding:

$$\boxed{\frac{\partial}{\partial t} \mathbf{q}' + \mathbf{S} \frac{\partial}{\partial x} \mathbf{q}' = 0}, \quad (4.44)$$

where $\mathbf{q}' = (p, u, T)^T$ and

$$\mathbf{S} = \begin{bmatrix} \beta U_r^2 u & \rho U_r^2 & 0 \\ \rho^{-1} & u & 0 \\ \frac{u}{C_p \gamma p} (U_r^2 - \gamma RT) & \frac{U_r^2}{C_p} & u \end{bmatrix}. \quad (4.45)$$

The eigenvalues of matrix \mathbf{S} are obtained by solving $\det[\mathbf{S} - \lambda \mathbf{I}] = 0$, yielding the wave velocities of the preconditioned system, i.e. $\lambda = \{u, u' + c', u' - c'\}$ where

$$\begin{aligned} u' &= u(1 - a) \\ c' &= \sqrt{a^2 u^2 + U_r^2} \\ a &= (1 - \beta U_r^2)/2 \\ \beta &= \rho_p + \frac{\rho T}{\rho C_p} \end{aligned}$$

For an ideal gas $\beta = (\gamma RT)^{-1} = c^{-2}$. When $U_r = c$ (at sonic speeds and above), $a = 0$ and the eigenvalues of the preconditioned system take their traditional form $\{u, u \pm c\}$. When $U_r \rightarrow 0$ (at low speeds), $a \rightarrow \frac{1}{2}$ and all eigenvalues become of the same order as u . Even for incompressible fluids ($\beta \equiv 0$), $a = \frac{1}{2}$ regardless of U_r ! In order to show that the preconditioned system remains well conditioned at all speeds, in the following we will introduce the so-called characteristic condition number.

[¶]Consider the three-dimensional Euler equations in symmetric quasi-linear form, i.e. $\frac{\partial}{\partial t} \mathbf{U} + \mathbf{A} \frac{\partial}{\partial x} \mathbf{U} + \mathbf{B} \frac{\partial}{\partial y} \mathbf{U} + \mathbf{C} \frac{\partial}{\partial z} \mathbf{U} = 0$, where the state vector is defined by $d\mathbf{U} = (\frac{dp}{\rho c}, du, dv, dw, dp - c^2 d\rho)^T$. Consider the flow in the direction of some unit vector \mathbf{n} . Then the Euler equations reduce to $\frac{\partial}{\partial t} \mathbf{U}_n + \mathbf{A}_n (\mathbf{n} \cdot \nabla) \mathbf{U}_n = 0$, with matrix $\mathbf{A}_n = \mathbf{A} n_x + \mathbf{B} n_y + \mathbf{C} n_z$. State vector \mathbf{U}_n is defined by $d\mathbf{U}_n = \mathbf{D} d\mathbf{U}$, where \mathbf{D} is a diagonal matrix with diagonal elements $\{1, n_x, n_y, n_z, 1\}$ and others zero. The eigenvalues of matrix \mathbf{A}_n are $\lambda = \{\mathbf{u} \cdot \mathbf{n}, \mathbf{u} \cdot \mathbf{n}, \mathbf{u} \cdot \mathbf{n}, \mathbf{u} \cdot \mathbf{n} \pm c\}$, where $\mathbf{u} = (u, v, w)^T$ is the Cartesian flow speed vector (Lee 1998).

In the field of Computational Fluid Dynamics, two important cases must be distinguished while computing steady flows.

- In order to satisfy the well-known CFL *stability* condition, the propagation distance of all waves must remain within the numerical support of the discretization scheme. For explicit methods, this limits the time-step to a multiple of the cell length divided by the magnitude of the fastest wavespeed.
- *Convergence*, however, will be dominated by the number of iterations required for the slowest waves to propagate across the computational domain.

Thus, a useful quantity in designing preconditioners is the *characteristic condition number* k_c , which is defined as the ratio of largest-to-smallest wavespeed. The goal is to minimize k_c . Consider the convective speed u to be positively defined, i.e. $u > 0$. Then $k_c = (u' + c')/\text{MIN}[u, |u' - c'|]$. In case of the (unpreconditioned) Euler equations this yields

$$\text{Euler: } k_c = \frac{M + 1}{\text{MIN}[M, |M - 1|]}, \quad (4.46)$$

where the Mach number is defined as $M = u/c$. Fig. 4.6 shows k_c as function of the Mach number M for the Euler equations as well as for the preconditioned system,

$$\text{precon. Euler: } k_c = \frac{\sqrt{4 + (1 - M^2)^2} + (1 + M^2)}{\sqrt{4 + (1 - M^2)^2} - (1 + M^2)}, \quad (4.47)$$

when $\epsilon \rightarrow 0$. Consider the Euler equations. The smallest characteristic condition number is obtained when $M = \frac{1}{2}$, resulting in $k_c = 3$. At low Mach numbers, the entropy mode is the slow mode (convecting with the flow speed) which is moving much slower than the acoustic speed. At sonic conditions, the slow mode corresponds to the upstream-running acoustic wave. Clearly, when $M \rightarrow 0$ or $M \rightarrow 1$, $k_c \rightarrow \infty$ and convergence difficulties are expected.

Consider the preconditioned system. When the Mach number approaches zero, the characteristic condition number is bounded, i.e. when $M \rightarrow 0$ then $k_c \rightarrow \frac{\sqrt{5+1}}{\sqrt{5-1}} \approx 2.62$. When $M \rightarrow 1$, $k_c \rightarrow \frac{1+M}{1-M}$, yielding a limit behaviour identical to the Euler equations. When the flow in a stagnation region is considered, i.e. $|\mathbf{u}| \leq \epsilon c$, preconditioning is performed at constant reference velocity U_r . It can be shown in this case, that the condition number can be infinitely large after all, i.e. when $M \rightarrow 0$ it follows that $k_c \sim \epsilon/M \rightarrow \infty$. This might result in a severe lack of robustness of the method.

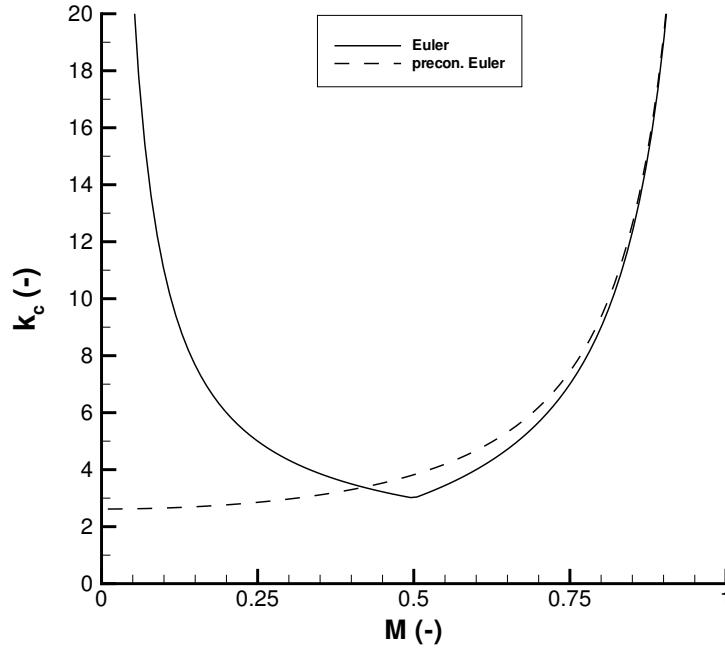


FIGURE 4.6: Characteristic condition number for subsonic flow.

4.3.3 Boundary Conditions

The flow through a valve is considered to be compressible and subsonic. The common way of imposing boundary conditions is to use characteristic boundary conditions (e.g. Tannehill et al. 1997), in this case for the preconditioned system.

Characteristic Formulation In order to obtain the characteristic form of the preconditioned Euler equations, the one-dimensional wave equation derived as Eq. (4.44) is used. The common strategy is to calculate first the left eigenvector associated with each of the three eigenvalues of matrix \mathbf{S} . Subsequently these left eigenvectors will be multiplied with Eq. (4.44), yielding the characteristic equations. The left eigenvector ℓ related to eigenvalue λ can be derived from $\mathbf{S}^T \ell = \lambda \ell$. The complete form of the latter is

$$\begin{pmatrix} \beta U_r^2 u & \rho^{-1} & \frac{u}{C_p \gamma p} (U_r^2 - \gamma RT) \\ \rho U_r^2 & u & \frac{U_r^2}{C_p} \\ 0 & 0 & u \end{pmatrix} \begin{pmatrix} \ell_1 \\ \ell_2 \\ \ell_3 \end{pmatrix} = \begin{pmatrix} \lambda \ell_1 \\ \lambda \ell_2 \\ \lambda \ell_3 \end{pmatrix}. \quad (4.48)$$

Solving for ℓ by taking $\lambda_1 = u$, $\lambda_2 = u' + c'$ and $\lambda_3 = u' - c'$, respectively, yields:

$$\ell_{\lambda_1} \propto \left(\frac{1}{\rho C_p}, 0, -1 \right)^T, \quad (4.49)$$

$$\ell_{\lambda_2} \propto \left(1, \frac{\rho U_r^2}{u' + c' - u}, 0\right)^T, \quad (4.50)$$

$$\ell_{\lambda_3} \propto \left(1, \frac{\rho U_r^2}{u' - c' - u}, 0\right)^T, \quad (4.51)$$

respectively. Finally, the characteristic formulation is obtained when one multiplies the matrix $[\ell_{\lambda_1}, \ell_{\lambda_2}, \ell_{\lambda_3}]^T$ with Eq. (4.44), yielding the compatibility equations

$$\frac{\partial T}{\partial t} + u \frac{\partial T}{\partial x} = \frac{1}{\rho C_p} \left[\frac{\partial p}{\partial t} + u \frac{\partial p}{\partial x} \right], \quad (4.52)$$

$$\frac{\partial u}{\partial t} + (u' + c') \frac{\partial u}{\partial x} = \frac{u - (u' + c')}{\rho U_r^2} \left[\frac{\partial p}{\partial t} + (u' + c') \frac{\partial p}{\partial x} \right], \quad (4.53)$$

$$\frac{\partial u}{\partial t} + (u' - c') \frac{\partial u}{\partial x} = \frac{u - (u' - c')}{\rho U_r^2} \left[\frac{\partial p}{\partial t} + (u' - c') \frac{\partial p}{\partial x} \right], \quad (4.54)$$

along $\frac{dx}{dt} = u$, $\frac{dx}{dt} = u' + c'$ and $\frac{dx}{dt} = u' - c'$, respectively. In case of no preconditioning, i.e. $U_r \rightarrow c$ so $u' \rightarrow u$ and $c' \rightarrow c$, the familiar characteristic formulation of the Euler equations appears (e.g. Laney 1998).

Inlet Flow Consider the inlet boundary of a compressible flow. When subsonic one-dimensional flow is considered, one characteristic $\{u' - c'\}$ is propagating upstream, while two characteristics $\{u, u' + c'\}$ are propagating downstream. Thus two variables must be imposed, while one variable must be constructed from the flow domain. See Fig. 4.7a.

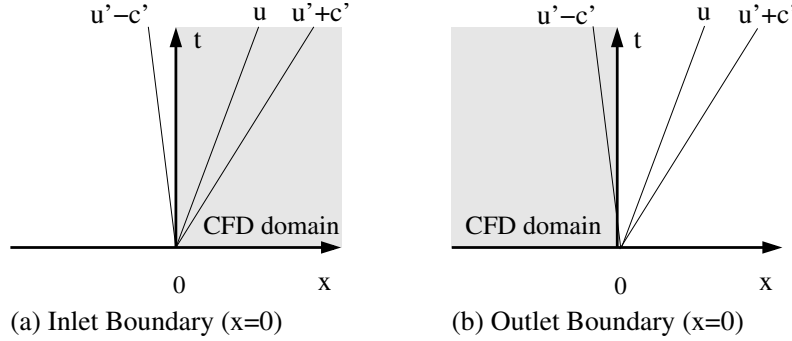


FIGURE 4.7: *Boundary characteristics for subsonic flow. The ghost cells (not shown) located outside the computational (CFD) domain have an associated state vector which is updated by employment of the characteristic(s) leaving the CFD domain.*

In the case of gas flow through a valve in an experimental setup, an appropriate boundary condition would be fixing the inlet velocity u and the inlet temperature T . At the inlet boundary this then fixes c and therewith u' and c' . Now the pressure p can be updated. Setting $\frac{\partial u}{\partial t} \equiv 0$ in Eq. (4.54) leads to

$$\frac{\partial p}{\partial t} = (u' - c') \frac{\rho U_r^2}{u - (u' - c')} \frac{\partial u}{\partial x} - (u' - c') \frac{\partial p}{\partial x}. \quad (4.55)$$

This yields the pressure p at the inlet boundary at the new time level.

Outlet Flow Consider subsonic one-dimensional flow at the outlet boundary. Then two characteristics $\{u, u' + c'\}$ are pointing out of the flow domain, while one $\{u' - c'\}$ is pointing inwards, see Fig. 4.7b. This yields the constraint of imposing one boundary variable and constructing two boundary variables. The static pressure p is set as a constant at the boundary, while constructing the density ρ and convective speed u explicitly in time. We choose to construct the temperature rather than the density for reasons of accuracy at very-low Mach number flow.

Eq. (4.53) is used in an unmodified way to determine u of the inlet ghost cells at every time-step, because $\frac{\partial p}{\partial t} \equiv 0$. Eq. (4.52) relates the static temperature entropy wave to the static pressure entropy wave. Again it can be used in an unmodified way. The equations to be implemented are given by:

$$\frac{\partial T}{\partial t} = -u \frac{\partial T}{\partial x} + \frac{u}{\rho C_p} \frac{\partial p}{\partial x} \quad (4.56)$$

$$\frac{\partial u}{\partial t} = -(u' + c') \left[\frac{\partial u}{\partial x} + \frac{u' + c' - u}{\rho U_r^2} \frac{\partial p}{\partial x} \right]. \quad (4.57)$$

This yields the temperature T and the velocity u at the outlet boundary at the new time level.

The subject of boundary conditions is discussed extensively by Poinso and Lele (1992). They state that if the order of the spatial accuracy near the boundary is equal to the scheme order minus one, the overall accuracy of the scheme is not affected. Therefore, since the JST scheme is second-order accurate, we will use first-order spatial accuracy to discretize Eqs. (4.55) - (4.57). The temporal discretization of Eqs. (4.55) - (4.57) is performed with the same algorithm as the internal cells, i.e. Jameson's modified Runge-Kutta method.

4.3.4 Flux Scheme

Premultiplying the time derivative by a matrix changes the pseudo-time behaviour of the system, see e.g. Eq. (4.39), and enables the acceleration of the convergence to a steady state. Turkel et al. (1994) showed that most central difference schemes and upwinding schemes do not have the correct asymptotic behaviour as the Mach number approaches zero. This effect results, if obtainable, in an *inaccurate* steady-state solution of the governing equations. To correct this, one needs to change the upwinding or equivalently the artificial dissipation of the scheme.

Artificial dissipation is essential to eliminate spurious high wavenumber modes in the solution. Flux schemes can be classified into two families: i) *central difference schemes*, wherein the dissipation is added as an explicit step through the introduction of higher-order derivative terms, ii) *upwind schemes*, where the dissipation is an inherent part of the spatial discretization. In general, one can express the numerical flux as consisting of a central difference contribution and a dissipation/diffusion contribution. To maximize efficiency and accuracy, it is necessary that the dissipation reflects the *new* eigenvalues when preconditioning is applied.

In the present research preconditioning of upwind schemes has been considered to some extent, however, without success for the cases of valve flow. Therefore we adopted the JST scheme for which the artificial dissipation can be controlled explicitly. Because the scaling

factor $R_{j+1/2}$ in the dissipation terms of the flux is a *scalar*, preconditioning of this flux is rather straightforward, i.e.

$$\mathbf{d}_{j+1/2} = R_{j+1/2} \left\{ \epsilon_{j+1/2}^{(2)} (\mathbf{q}_{j+1} - \mathbf{q}_j) - \epsilon_{j+1/2}^{(4)} (\mathbf{q}_{j+2} - 3\mathbf{q}_{j+1} + 3\mathbf{q}_j - \mathbf{q}_{j-1}) \right\}, \quad (4.58)$$

where

$$R_{j+1/2} = \frac{1}{2} (R_j + R_{j+1}), \quad R_j = \text{MAX}\{u'_j + c'_j, |u'_j - c'_j|\}, \quad (4.59)$$

where $u' = |\mathbf{u}|(1 - a)$ and $c' = \sqrt{a^2|\mathbf{u}|^2 + U_r^2}$ are the modified wavespeeds. The preconditioning matrix is multiplied with the central difference flux vector only. The dissipation vector is added separately, where the modified conservative variables $\hat{\mathbf{w}}$ are replaced by the primitive variables \mathbf{q} . As the local Mach number approaches zero, the dissipation scaling factor becomes of the order of the velocity magnitude, rather than the speed of sound.

4.3.5 Time Accuracy

Steady Flow: Local Time-Stepping Following Weiss and Smith (1995), the preconditioned Euler equations are discretized spatially by *preconditioning the discretized Euler equations*, i.e.

$$\frac{d\bar{\mathbf{q}}}{dt} + \mathbf{P} \frac{1}{V} \sum_{\text{faces}} \bar{\mathbf{F}} \cdot \mathbf{n} S = 0, \quad (4.60)$$

where \mathbf{P} is evaluated at the dual mesh cell centroids (i.e. the nodes). This type of discretization is thus allowed only, when it is assumed that $\mathbf{P} = \mathbf{P}[\mathbf{q}]$ is constant in space within a control volume. However, spatial accuracy has a meaning in the steady-state only. This steady-state is not a function of matrix \mathbf{P} because it is under no circumstances singular.

Apart from implementing the preconditioning matrix, preconditioned characteristic boundary conditions and preconditioned flux scheme, the time-step should also be modified according to the new eigenvalues. In case of solving the preconditioned Euler equations (4.60), the denominator $|\mathbf{u}| + c$ in Eq. (4.27) is replaced by $\text{MAX}\{u' + c', |u' - c'|\}$, i.e.

$$\Delta t = CFL \frac{\frac{1}{4} V^{1/3}}{\text{MAX}\{u' + c', |u' - c'|\}}, \quad (4.61)$$

where $u' = |\mathbf{u}|(1 - a)$ and $c' = \sqrt{a^2|\mathbf{u}|^2 + U_r^2}$. This means that the local time-step will be increased substantially when the local Mach number is very low. In case of preconditioning, considering magnitudes of the local velocity vector -instead of the maximum of all directional wavespeeds- is argued by the local clustering of eigenvalues which turns the system to behave as a scalar equation (Lee 1998).

Unsteady Flow: Dual Time-Stepping In order to overcome the problem of preserving time accuracy when employing the preconditioning method, a dual time-stepping procedure is employed. This involves an inner iteration loop in pseudo-time that is wrapped by an outer loop stepping through physical time. Thus, the flow field at each physical time level is treated as a steady-state problem in pseudo-time, with appropriate source terms to provide an influence of the flow history on the current time level. In this way, the physical time-step is not affected by the stiffness of the system.

In the following, physical time is denoted with t and pseudo-time is denoted with τ . Consider the preconditioned spatially discretized Euler equations,

$$\mathbf{P}^{-1} \frac{\partial \mathbf{q}}{\partial \tau} + \frac{\partial \mathbf{w}}{\partial t} + \mathbf{Res}[\mathbf{w}] = 0, \quad (4.62)$$

where we omit overbars for the volume-averaged values of \mathbf{q} and \mathbf{w} and where the residual equals $\mathbf{Res} \equiv \frac{1}{V} \sum_{\text{faces}} \bar{\mathbf{F}} \cdot \mathbf{n} S$. Note that as $\tau \rightarrow \infty$, the first term vanishes and the original Euler equations are recovered. The physical time-dependent term is discretized in an implicit fashion by means of a second-order-accurate, three-point backwards difference in time, i.e.

$$\frac{\partial \mathbf{w}}{\partial t} [t_{n+1}] = \frac{3\mathbf{w}^{(n+1)} - 4\mathbf{w}^{(n)} + \mathbf{w}^{(n-1)}}{2\Delta t} + \mathcal{O}(\Delta t^2), \quad (4.63)$$

where integer n denotes the physical time level, i.e. $t = n\Delta t$. This result is obtained after a Taylor series expansion of $\mathbf{w} [t_n]$ evaluated at time t_{n-1} and t_{n-2} , i.e.

$$\mathbf{w} [t_{n-1}] = \mathbf{w} [t_n] - \Delta t \frac{\partial \mathbf{w}}{\partial t} [t_n] + \frac{1}{2} \Delta t^2 \frac{\partial^2 \mathbf{w}}{\partial t^2} [t_n] + \mathcal{O}(\Delta t^3), \quad (4.64)$$

$$\mathbf{w} [t_{n-2}] = \mathbf{w} [t_n] - 2\Delta t \frac{\partial \mathbf{w}}{\partial t} [t_n] + 2\Delta t^2 \frac{\partial^2 \mathbf{w}}{\partial t^2} [t_n] + \mathcal{O}(\Delta t^3), \quad (4.65)$$

where subtraction of Eq. (4.65) from four times Eq. (4.64) yields Eq. (4.63). In order to start the procedure the solution at time $t = \Delta t$ is computed using a first-order-accurate, two-point backwards difference scheme. A multistage Runge-Kutta algorithm is used to drive the pseudo-time derivative to zero,

$$\begin{aligned} \mathbf{q}^{(0)} &= \mathbf{q} [\tau] \\ \left\{ \mathbf{P}^{-1} + \frac{3}{2} \frac{\Delta \tau}{\Delta t} \frac{\partial \mathbf{W}}{\partial \mathbf{Q}} \right\}^{(k-1)} \Delta \mathbf{q}^{(k)} &= -\alpha_k \Delta \tau \left\{ \frac{3\mathbf{w}^{(k-1)} - 4\mathbf{w}^{(n)} + \mathbf{w}^{(n-1)}}{2\Delta t} + \mathbf{Res}^{(k-1)} \right\} \\ \mathbf{q} [\tau + \Delta \tau] &= \mathbf{q}^{(m)} \end{aligned} \quad (4.66)$$

where $k = 1, 2, \dots, m$ is the stage counter, α_k is the multistage coefficient for stage k and $\Delta \mathbf{q}^{(k)} \equiv \mathbf{q}^{(k)} - \mathbf{q}^{(0)}$. The pseudo time loop drives the solution from n to $n+1$ as $\tau \rightarrow \infty$. The term $\frac{3}{2} \frac{\Delta \tau}{\Delta t} \frac{\partial \mathbf{W}}{\partial \mathbf{Q}}$ is formed on base of an implicit treatment of the physical time derivative term in pseudo time. The matrix that multiplies $\Delta \mathbf{q}^{(k)}$ is inverted analytically and evaluated in a pointwise fashion at stage $k-1$, i.e.

$$\begin{aligned} \left\{ \mathbf{P}^{-1} + \frac{3}{2} \frac{\Delta \tau}{\Delta t} \frac{\partial \mathbf{W}}{\partial \mathbf{Q}} \right\}^{-1} &= \\ \frac{1}{\rho \tilde{\Upsilon}_1} &\begin{pmatrix} \frac{1}{2} |\mathbf{u}|^2 \zeta_1 & -u \zeta_1 & -v \zeta_1 & -w \zeta_1 & \zeta_1 \\ -u & 1 & 0 & 0 & 0 \\ -v & 0 & 1 & 0 & 0 \\ -w & 0 & 0 & 1 & 0 \\ \frac{1}{2} |\mathbf{u}|^2 \zeta_2 - T & -u \zeta_2 & -v \zeta_2 & -w \zeta_2 & \zeta_2 \end{pmatrix}, \end{aligned} \quad (4.67)$$

where

$$\Upsilon_1 = 1 + \frac{3}{2} \frac{\Delta \tau}{\Delta t}, \quad (4.68)$$

$$\Upsilon_2 = \frac{1}{RT} + \frac{1}{\Upsilon_1} \left(\frac{1}{U_r^2} - \frac{1}{c^2} \right), \quad (4.69)$$

$$\zeta_1 = \frac{\rho}{\Upsilon_2 C_p T - 1}, \quad (4.70)$$

$$\zeta_2 = \frac{\Upsilon_2 T}{\Upsilon_2 C_p T - 1}. \quad (4.71)$$

The pseudo-time derivative is driven to zero in the inner iteration loop. The convergence criterion is defined in a formal way by

$$\text{MAX}_i L_2 \left[\frac{\frac{\partial \mathbf{q}}{\partial \tau}|_i}{\mathbf{P}(\frac{\partial \mathbf{w}}{\partial t} + \nabla \cdot \mathbf{F})|_i} \right] \leq \epsilon_{conv}, \quad (4.72)$$

where ϵ_{conv} is a small number. The L_2 -norm of all cells is then computed for every component $i = \{1, \dots, 5\}$ of the column vector separately. The maximum value of these components determines whether the solution is temporary in a steady state. This formal convergence criterion appears to require an excessive amount of computation time. Therefore we will monitor the non-dimensionalized residuals $L_2[\frac{\partial \mathbf{w}}{\partial \tau}]$ only. Weiss and Smith (1995) noticed that after 30 iterations in pseudo time, the residual associated with the continuity equation decreased at least one order of magnitude. The physical (also referred to as global) time-step Δt is limited only by the level of desired temporal accuracy. The pseudo (also referred to as local) time-step $\Delta \tau$ is determined by the stability condition Eq. (4.61) with Δt replaced by $\Delta \tau$. Liu et al. (1998) note that the global time-step cannot be chosen to be very small, i.e. when $\Delta \tau / \Delta t > 1$ slow convergence is observed.

4.4 Test Cases

In order to test the Euler method for its capability of the numerical schemes to operate properly, several test cases have been considered. For the non-preconditioned Euler method verification and validation was performed successfully for the following cases: steady uniform flow, steady bump channel flow, steady Prandtl-Meyer expansion, steady 15°-wedge channel flow, unsteady flow in Sod's Riemann problems and unsteady flow in a 2D Riemann problem of interacting shock waves with expansion fans. However, considering supersonic flows or shock waves are not proper test cases for our goal to simulate subsonic valve flows. Therefore the following test cases (while emphasizing preconditioning modifications) are discussed in more detail.

Steady Uniform Flow Consider a channel with a square cross-section ($0.2 \times 0.2 \text{m}^2$) and a length $L = 20 \text{m}$. The dual mesh containing 580 nodes is generated on a mesh with 1044 tetrahedrons. We want to obtain a steady flow, while employing Jameson's modified Runge-Kutta time marching method, from a non-uniform initial condition. This initial condition is constructed from the outlet static pressure, inlet temperature and a velocity distribution equal to

$$\mathbf{u}[\mathbf{x}, t = 0] = (1 + 0.1 \cos[2\pi x/L]) u_{in} \mathbf{e}_x, \quad (4.73)$$

where u_{in} is the inlet ($x = 0$) boundary condition for the velocity. In order to test the preconditioned Euler method the Mach number is set to $M = u_{in}/c_{in} = 0.01$ and the cut-off

parameter (in the Weiss & Smith preconditioning matrix) is $\epsilon = 0.005$. The JST artificial dissipation parameters are set to $k^{(2)} = 0$, $\beta^{(4)} = 0$ and $k^{(4)} = 0.0313$. Fig. 4.8 shows the effect of time-derivative preconditioning convergence acceleration. The steady-state flow

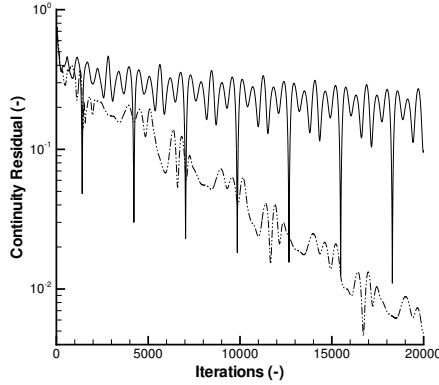


FIGURE 4.8: Time marching of initially disturbed uniform flow at low Mach number (—, Euler; --, preconditioned Euler).

is approximated more accurately by decreasing residuals. These residuals are normalized to yield unity at the first iteration. The residuals for the momentum density in the x -direction show a similar behaviour, except that at the first few iterations a significant increment can be observed for the case without preconditioning. The trivial solution equals the steady uniform flow determined by the three boundary conditions (inlet velocity, inlet temperature and outlet pressure) in absence of lateral velocity components.

Steady Irrotational Flow around Joukowski Aerofoil In case of inviscid fluid-structure interaction simulations, the pressure is an important variable because it provides the coupling mechanism between fluid and structure. However, pressure-velocity decoupling in the steady state solution can often be observed when very low Mach number flow is simulated. Even in case of preconditioning the flux scheme dissipation terms can scale incorrectly (e.g. Edwards and Liou 1998). In order to investigate this potential effect in the present method, an analytical solution of the flow field for $M \rightarrow 0$ is desired. Therefore we choose to simulate the steady irrotational flow around a Joukowski aerofoil. Appendix A presents the rationale of the limit of incompressible flow by lowering the Mach number.

The method of conformal mapping provides the tool to transform a circle in the z -plane into the desired geometry in the ζ -plane, see Fig. 4.9. The complex coordinates are defined by $z = x + iy$ and $\zeta = \xi + i\eta$ where $i = \sqrt{-1}$. We define the circle by the relation $(x + \lambda)^2 + y^2 = R^2$, where the origin of the circle with radius R is located at $(-\lambda, 0)$, where $\lambda/R = \frac{1}{10}$. When the conformal mapping $\zeta = z + \frac{a^2}{z}$ is used, where we specify $a = R - \lambda$, the Joukowski profile of Fig. 4.9b is obtained.

In order to be able to simulate the flow around an aerofoil with an Euler method, the Kutta

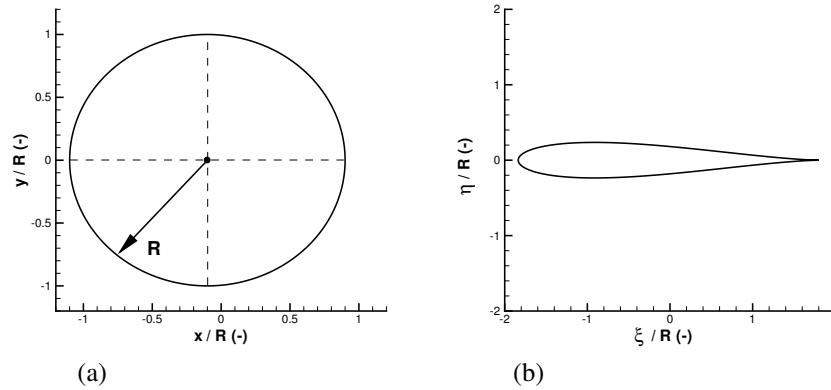


FIGURE 4.9: A circle in the z -plane (a) is mapped into a Joukowski aerofoil in the ζ -plane (b), $\lambda/R = \frac{1}{10}$.

condition is required. For the symmetrical aerofoil in Fig. 4.9b this is obtained when the flow has zero degrees of attack. In order to save computation time, only half of the domain is considered, justified by the symmetric flow solution with respect to the axis $\eta/R = 0$. Irrotational flow around a plane two-dimensional object is nonunique because it allows an arbitrary circulation to be added to the flow (e.g. Kundu 1990). Here we force the circulation to be zero, and obtain the Kutta condition, by applying a wall boundary condition at $\eta = 0$ outside the profile.

The analytical solution is obtained by making use of the complex velocity potential $W[z]$ of the flow around a circular cylinder. The velocity components in the ζ -plane are obtained by

$$u_\zeta - iv_\zeta = \frac{dW}{d\zeta} = \frac{dW}{dz} \frac{d\zeta}{dz} = \frac{1 - \frac{R^2}{(z+\lambda)^2}}{1 - \frac{a^2}{z^2}} U_\infty, \quad (4.74)$$

where U_∞ is the free-stream velocity. The numerator represents the superposition of a uniform flow and a dipole (positioned at the center of the circle) flow field. The velocity components in the ζ -plane as function of ζ are obtained by substituting $z = z[\zeta]$ into Eq. (4.74). The complex coordinate z is obtained from the ζ -plane by the inverse transformation $z = \frac{1}{2}\zeta + \sqrt{\frac{1}{4}\zeta^2 - a^2}$. The static pressure is determined by Bernoulli's equation $p_\infty + \frac{1}{2}\rho U_\infty^2 = p_\zeta + \frac{1}{2}\rho(u_\zeta^2 + v_\zeta^2)$. The flow exhibits no singularity at the cusp-shaped trailing edge, i.e. $\lim_{z \rightarrow a} (u_\zeta - iv_\zeta) \rightarrow \frac{a}{R} U_\infty$ (using the rule of l'Hôpital).

The flow domain (ζ -plane) is discretized by generation of a 2D triangular mesh. After a one-cell extrusion process the prisms are converted to tetrahedral elements, which are used as input for the generation of the median dual mesh. The boundaries of the computational domain must be far away from the profile in order to simulate the theoretical model. The flow domain is chosen as a box of length $30R$, height $12R$ and width $\frac{1}{50}R$. In order to validate whether the length and height of the domain is large enough, the method of characteristic boundary conditions is employed and deviations in flow variables are monitored at the boundaries. The initial condition equals the state spanned by the constant boundary con-

ditions, where the Mach number M equals 0.01. Other parameters are: $k^{(2)} = 0$, $\beta^{(4)} = 0$, $k^{(4)} = 0.01$, $\text{CFL} = 0.5$ and in case of preconditioning $\epsilon = 0.005$. The pressure coefficient is defined by $c_p = \frac{p - p_\infty}{\frac{1}{2}\rho U_\infty^2}$. Fig. 4.10 shows the results when the Euler method is used *without* the implementation of preconditioning. We see that the computed velocity distribution is too

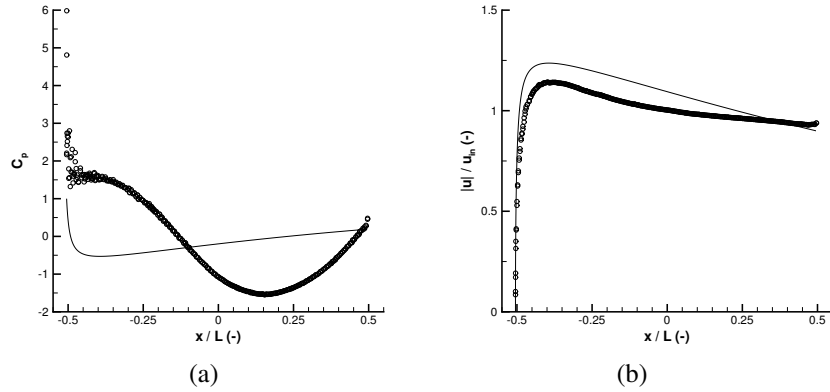


FIGURE 4.10: Flow around Joukowski aerofoil, $M = 0.01$. (a) Pressure coefficient and (b) scaled velocity magnitude, on aerofoil after 20×10^3 pseudo time-steps. Preconditioning is **not** applied (—, analytical solution; \circ , simulation). The length of the aerofoil (projected on the ξ -axis) is denoted by L .

low. An even more serious problem is concerned with the pressure distribution. Increasing the number of iterations towards steady-state does not cure this accuracy problem. Fig. 4.11 shows the results when the Euler method is used for preconditioning switched on. We see that the distribution of velocity and pressure on the aerofoil is in good agreement with the analytical solution. At 20×10^3 iterations the outlet velocity varies less than 0.3% of the inlet velocity. This suggests that the non-reflecting boundaries are indeed sufficiently far away from the aerofoil.

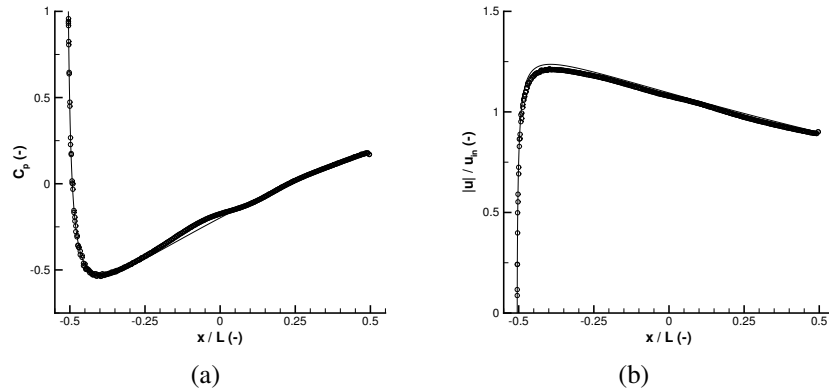


FIGURE 4.11: Flow around Joukowski aerofoil, $M = 0.01$. (a) Pressure coefficient and (b) scaled velocity magnitude, on aerofoil after 20×10^3 pseudo time-steps. Preconditioning is applied (—, analytical solution; \circ , simulation). The length of the aerofoil (projected on the ξ -axis) is denoted by L .

Finally, some additional tests have been performed.

- Consider the flow solution after 20×10^3 pseudo time-steps for the preconditioned Euler method. When the dissipation coefficient $k^{(4)}$ is decreased to 0.005, a restart shows an unstable solution. After approximately 10^3 iterations the residuals go to infinity and the flow near the stagnation point becomes supersonic. This indicates that choosing the dissipation coefficients should be taken with care.
- Consider the inlet Mach number to be set to 0.01. When preconditioning is switched on, while the flux scheme is not preconditioned, the method results in an unstable solution (negative density) after a few iterations. When preconditioning is switched off, while the flux scheme is preconditioned, the solution becomes unstable after a few hundred iterations. This suggests that consistency in the development of a preconditioned Euler method is required.
- Consider again the inlet Mach number to be set to 0.01. First, the case for cut-off parameter $\epsilon = 0.1$ is compared with the case for $\epsilon = 0.005$. It is observed that a faster convergence, but inaccurate solution, is obtained when the cut-off parameter ϵ exceeds M . Second, the case for cut-off parameter $\epsilon = 0.001$ is compared with the case for $\epsilon = 0.005$. The convergence speed of the case for $\epsilon = 0.001$ appeared much less than the case for $\epsilon = 0.005$. Although M exceeds ϵ in both cases, the *local* Mach number could be smaller than ϵ . However, after convergence the minimum local Mach number appeared still larger than ϵ . This suggests that ϵ cannot be *very* small. Turkel (1999) notes that the reasons for this effect are still unclear.

Unsteady Separated Flow around Inclined Plate Yeung and Parkinson (1997) proposed an analytical model for the steady inviscid separated flow around an inclined 2D flat plate. At an inclination smaller than 90° , the Kutta condition is satisfied at both leading and trailing edge of the plate. A boundary condition is formulated based on some experimental results, but no additional empirical information is required. The predicted pressure distributions on the surface for a wide range of angle attack are found to be in good agreement with experimental data. In a recent study by Yeung and Parkinson (2000), their model was completed by incorporating a wake width model. It allows the base pressure, which was treated before as an empirical input, to be determined theoretically. To the opinion of the author, the success of Yeung & Parkinson suggests that the Euler equations can be used to predict the flow force of high-Reynolds number flows around sharp-edged blunt objects. Both models are validated by the experimental work of Fage and Johansen (1927). Fig. 4.12 shows the flow situation schematically.

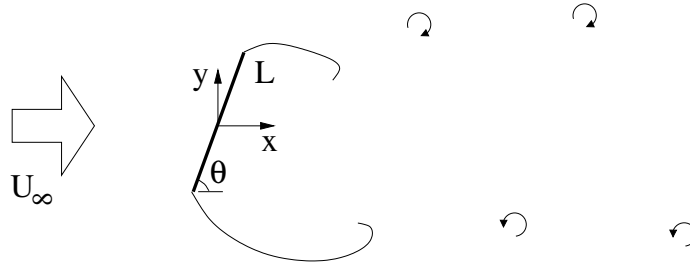


FIGURE 4.12: Sketch of flow around plate with length L and inclination θ .

In order to validate the preconditioned Euler method for capturing steady and unsteady high-Reynolds number flows, we will first investigate quasi-steady flow around a flat plate and subsequently the phenomenon of vortex shedding from this flat plate. The wind-tunnel geometry of Fage & Johansen is used to generate a mesh around the plate. In the experiments this plate has a triangular cross-section. We circumvent mesh generation difficulties near the edges by considering a rectangular shape with the same length and thickness. We consider one plate angle, viz. $\theta = 69.85^\circ$. In the experiment at a distance of $8L$, with plate length L , downstream of the plate center the flow velocity is time-dependent, i.e. oscillatory. However, in the limit of large lateral distances ($> 4L$) the flow reaches a small fluctuating velocity with a mean speed of $1.05U_\infty$. We apply Bernoulli's law (justified by Yeung & Parkinson) to obtain the outlet pressure as function of the inlet pressure and inlet temperature. The experiments are characterized by the Reynolds number $Re = U_\infty L/\nu \sim 1.5 \cdot 10^5$ and Mach number $M_\infty = U_\infty/c_\infty \sim 4.5 \cdot 10^{-2}$.

The first activity consists of obtaining, when possible, a steady flow for $M_\infty = 4.5 \times 10^{-2}$ by means of the local time-stepping procedure (Section 4.3.5). Preconditioning is switched on with cut-off parameter $\epsilon = 0.01$. Other parameters are $CFL = 0.1$, $k^{(2)} = 0.1875$, $k^{(4)} = 0.1250$ and $\beta^{(4)} = 1.0$. After 20×10^3 iterations it appeared that the pressure distribution on the upstream-facing side of the plate is found to be in good agreement with the experimental data except for the nodes adjacent to the edge nodes. Near these edges the pressure showed unphysical peak values ($c_p \equiv \frac{p-p_\infty}{\frac{1}{2}\rho U_\infty^2}$ was approximately 1.5 too high!).

Upon inspection of parameter dependence of this solution this effect was found to be related to the fourth-order differences in the flux dissipation terms. Several restarts were performed while lowering the dissipation coefficients each run. Fig. 4.13 shows the pressure distribution for the case with $k^{(2)} = 0.08$ and $k^{(4)} = 0.02$ after a restart of 500 iterations. The pressure

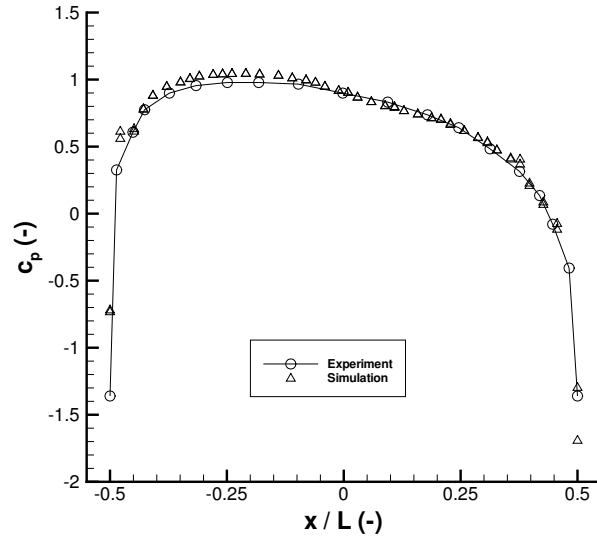


FIGURE 4.13: Pressure coefficient on upstream-facing side of 69.85° inclined plate.

distribution of the simulation is found to be in good agreement with the experimental data. However, the residuals are found to be reduced to a certain level only. This might indicate that the solution is essentially unsteady. Indeed, the pressure distribution on the downstream-facing side of the plate is found to fluctuate in pseudo time, approximately in the range $c_p \in (-1.3, -0.4)$. According to the measurements of Fage & Johansen the time-averaged pressure distribution on the downstream-facing side of the plate is approximately constant, i.e. $c_p \sim -1.36$. Fig. 4.14 shows the velocity field of the flow around the plate at the same pseudo time instant as the previous figure. Flow separation at the sharp edges is observed together with the 'recirculation zone' in the wake of the plate. Additionally we can observe clearly a stagnation point at each side of the plate. Consider the quasi-steady flow solution in the region upstream of the plate. The iso-Mach line $M = \epsilon$ encloses a flow region around the stagnation point with a length scale of $\sim \frac{1}{4}L$. In this region preconditioning is applied with a reference velocity that is not equal to the local speed magnitude, but equal to ϵc , see Eq. (4.38).

In order to test the dual time-stepping algorithm, time-accurate simulations are performed. The quasi-steady flow solution is used as initial condition. Fage & Johansen recorded velocity fluctuations by means of the hot-wire technique. Similarly we will monitor the velocity magnitude at the position $(x/L = 5.0, y/L = 2.5)$. The experiments recorded a shedding

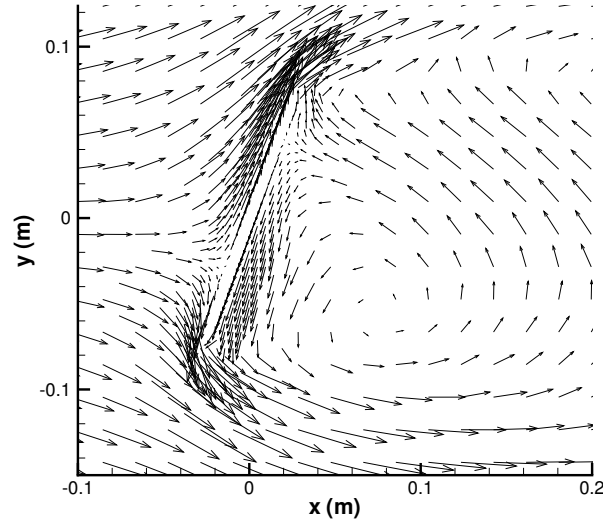


FIGURE 4.14: Velocity field of quasi-steady flow around 69.85° inclined plate.

period of 64 ms. Based on this time scale the physical time-step is set to $\Delta t = 0.5$ ms. This time-step equals 1% of the experimentally measured shedding period (Weiss and Smith (1995) set the time-step to 4% of the shedding period). Various numbers of iterations of the inner loop are tested, yielding the residuals to decrease sufficiently. Table 4.1 shows the related Strouhal numbers $St = \frac{fL}{U_\infty}$, where f is the frequency of vortex shedding. The

TABLE 4.1: Strouhal number versus number of pseudo time-steps ($\Delta t = 0.5$ ms).

nr. of $\Delta\tau$ steps (-)	St (-)
30	0.06
50	0.11
70	0.13
90	0.14

experimental data of Fage and Johansen (1927) yield a Strouhal number of $St = 0.156$ which is slightly higher than the one we observed at the largest chosen number of pseudo time-steps. However, it indicates that the time-accurate preconditioned Euler solver is able to represent unsteady flows at low Mach numbers with respect to upstream-facing pressure distribution and shedding frequency. This statement is in agreement with the results presented by Kiya and Arie (1977). They compared their inviscid vortex shedding model for an inclined plate (60°) with a.o. the experimental data of Abernathy (1962) and Fage and Johansen (1927). Based on the same definition of the Strouhal number Kiya & Arie showed that their inviscid model yields a smaller Strouhal number ($St = 0.14$) than the experiments of Fage & Johansen ($St = 0.17$) and the experiments of Abernathy ($St = 0.19$). The larger Strouhal

number for experimental flows can be understood by the increase of the length scale (effective plate length $> L$) due to viscous effects. An example of the fluctuating velocity profile from our simulations is given in Fig. 4.15. The dual mesh has been generated from a two-cells

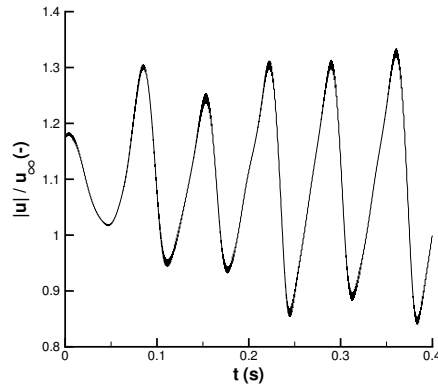


FIGURE 4.15: *Fluctuating velocity of the flow around 69.85° inclined plate at the monitoring position ($x/L = 5.0$, $y/L = 2.5$) for $\Delta t = 0.5$ ms and 90 pseudo time-steps.*

lateral tetrahedral mesh. Therefore we monitor the velocity magnitude at both the right- and left wall boundary of the computational domain. Fig. 4.16 shows the Mach number contours at time $t = 0.4$ s. The phenomenon of vortex shedding is clearly observed. As mentioned by Luo (2004) the instability of shear layers is not observed. It is expected that this effect can be observed when viscosity terms are added to the Euler equations, i.e. when the Navier-Stokes equations are considered.

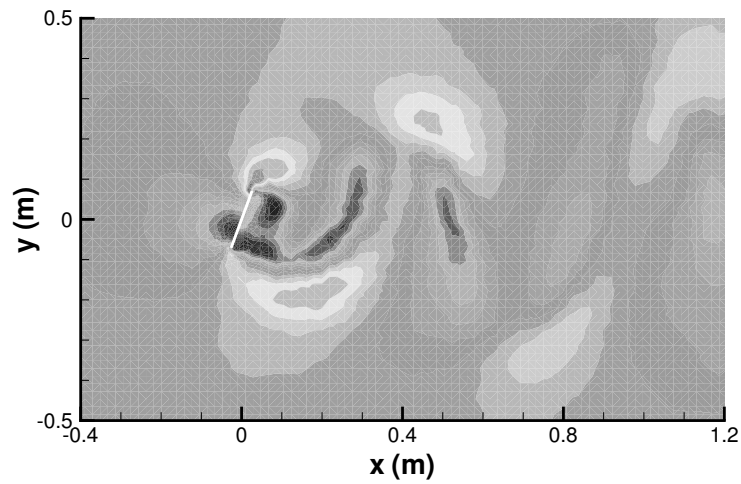


FIGURE 4.16: *Mach number contours ($0.01 \leq M \leq 0.08$, 15 levels) of unsteady flow around 69.85° inclined plate at time $t = 0.4$ s. The actual computational domain is $x \in (-1.2, 1.2)$ m and $y \in (-1.1, 1.1)$ m. Dual time-stepping with $\Delta t = 0.5$ ms and 90 pseudo time-steps.*

5.1 Introduction

Semi-empirical expressions for the dynamical response of compressor valves employ as basic state variables: the valve opening h , the pressure difference Δp across the valve and the volume-flow rate Φ_v through the valve. Simulations using the Basic Valve Theory raise many questions, even when the valve is embedded in a well-defined environment. In order to validate the Basic Valve Theory an experimental method is required which is able to measure accurately the instantaneous valve opening $h[t]$, the instantaneous valve volume-flow rate $\Phi_v[t]$ and the instantaneous valve pressure difference $\Delta p[t]$.

In the literature measurements of both the static component of Δp and Φ_v for a fixed valve opening has been discussed abundantly. A challenging difficulty is the measurement of the dynamic component of Φ_v , additional to the instantaneous values of $h[t]$ and $\Delta p[t]$. Some examples of experimental methods related to valve dynamics are presented in the following. MacLaren et al. (1975) measured both instantaneous valve opening and instantaneous valve pressure difference (of cylinder and plenum chambers) for a reciprocating compressor system. Thomann (1978) conducted an experiment to check his linear stability analysis (Thomann 1976) of a valve connected to a pipe. To that aim the static component of mass-flow rate and the instantaneous valve motion (force transducer) was measured. Ziada et al. (1986) and Ziada et al. (1987) investigated self-excited vibrations of compressor plate valves under steady state conditions. Simultaneous measurements were performed of the instantaneous valve opening (four proximity transducers), the instantaneous valve pressure difference and the static component of the mass-flow rate (orifice plate). Ishizawa et al. (1987) considered the case of flow between parallel disks with a forced sinusoidally oscillating gap width. Measurements were performed of the instantaneous gap width (capacitive transducer), the instantaneous fluid pressures on the lower disk (five positions) and the instantaneous hydrodynamic force (load cell) acting on the lower disk. Van Zon (1989) and Van Zon et al. (1990) considered the flow through a reed valve. The instantaneous volume-flow rate is determined by measurements of the outlet flow speed (hot wire anemometry). The instantaneous valve opening is measured optically. The valve pressure difference is constant for an oscillating reed because of the large volumes of the reed environment. Tarnopolsky et al. (2000) also considered an oscillating reed valve and measured the static component of the volume-flow rate (rotameter), the instantaneous pressure difference and the instantaneous valve opening (accelerometer).

This chapter presents the experimental method to obtain data for the validation of the Basic Valve Theory for unsteady flow conditions. The experimental results concerning the physics of valve dynamics are discussed in Chapter 6. In order to investigate the plate motion and the flow in compressor valves, a simplified compressor valve, referred to as model valve, has been designed (Section 5.2). The experimental setup is presented briefly in Section 5.3. Elaboration of the measurement of the instantaneous valve opening can be found in Section 5.4. The measurement of the static components of the valve pressure difference and the valve volume-flow rate is discussed in Section 5.5. The dynamic components of both valve pressure difference and valve volume-flow rate are obtained by making use of the linear theory of sound propagation. To that aim the model valve is connected to the end of a pipe from which the flow is originating out of a pulsation source. The Two-Microphone Method has been extended for signal reconstruction along this pipe in the time-domain (Section 5.6). Finally, the determination of the mechanical valve parameters is presented in Section 5.7.

5.2 Design of Model Valve

Compressor valves have rather complex geometries. Although the present experimental method has been tested successfully on a commercially available compressor valve, considering a simplified valve is more suited for Computational Fluid Dynamics and theoretical modelling. Therefore a *model valve* has been designed, comprising a geometry that is less complex than a compressor valve, but maintains the essential features of compressor valves. The similarities and differences between the model valve and a commercially available compressor valve will be discussed in Chapter 6. Fig. 5.1 shows a photograph of the model valve and a sketch of the ring plate. Fig. 5.2 shows the model valve assembly with detailed legend.

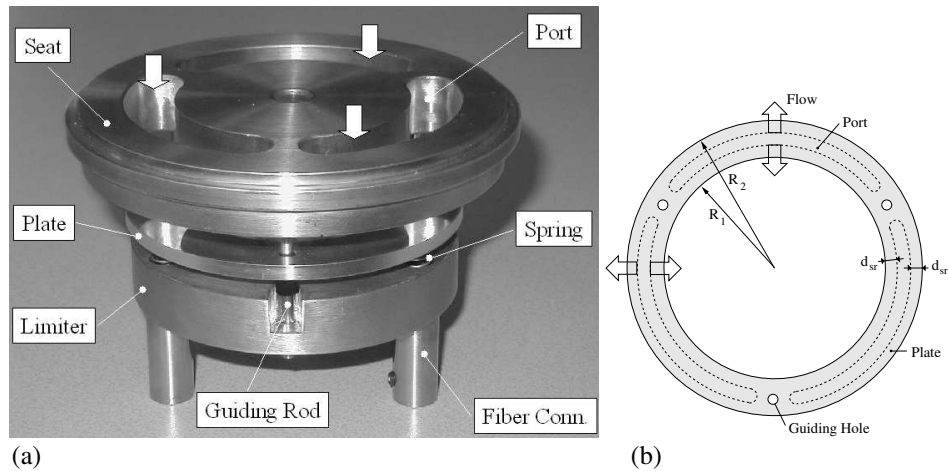


FIGURE 5.1: (a) Photograph of partially dismantled model valve. The flow direction is indicated with arrows. (b) Sketch of partial bottom view of photograph (R_1 is the inner radius and R_2 is the outer radius of the ring plate, d_{sr} is the sealing rim length).

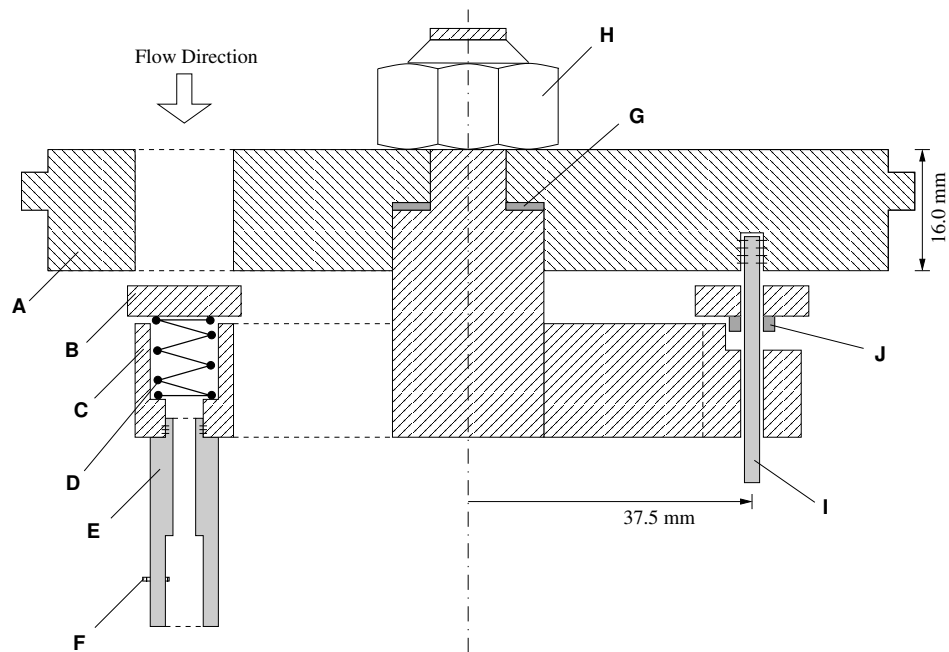


FIGURE 5.2: Model valve assembly (A: seat, B: ring plate, C: limiter, D: spring, E: glasfiber connector; F: imbuss screw to adjust the position of the glasfiber; G: high-tolerance ring to adjust the maximum valve opening, H: locking nut, I: guiding rod, J: nylon tube connected to the plate).

The seat is compatible with a flange, which can be connected to pipe segments (diameter pipe is 101.6 mm). During operation gas is flowing through the port area and separates at the edges of the movable valve part (an aluminium ring plate, Fig. 5.2: B). The limiter (Fig. 5.2: C) is connected to the seat by a centrally positioned cylinder. The maximum valve opening is adjustable by an intermediate ring (Fig. 5.2: G) between seat and limiter. The tolerance of this ring thickness must be very low (0.02 mm) in order to minimize plate obliqueness when pushed against the limiter. Quasi one-dimensional motion of the plate is forced by three guiding rods (separated azimuthally 120° , Fig. 5.2: I). At the downstream side of the plate, a nylon tube (Fig. 5.2: J) is connected to the plate to avoid jamming of plate movement and to force a single degree of freedom (at the expense of additional structural damping, which can be determined empirically). The seat and limiter are constructed from brass, because this material is relatively easy to manufacture, while it is strong enough to sustain plate impacts. To avoid undesired plate vibrations and damping (by means of a gas pocket) the limiter is modified in the region of the guiding rod by removal of brass. Three preloaded springs (Fig. 5.2: D) are positioned in limiter holes (separated azimuthally 120°). In the center of every spring a glassfiber is positioned, mounted on the limiter, to measure the valve opening (Section 5.4).

5.3 Experimental Setup

In order to measure the three valve state variables h , Φ_v and Δp simultaneously, the setup sketched in Fig. 5.3 has been realized. Air is compressed by a screw compressor (adjustable

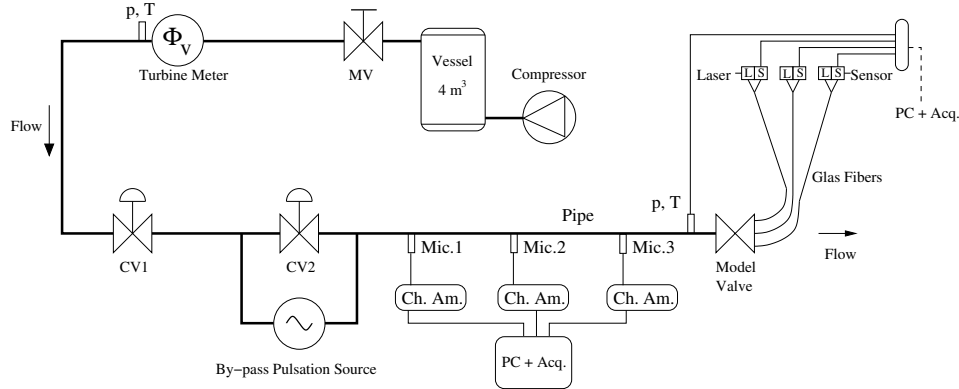


FIGURE 5.3: *Experimental setup (MV: manual valve, CV: control valve, Mic.: microphone, Ch.Am.: charge amplifier, PC+Acq.: personal computer and acquisition interface, L: laser, S: silicon sensor).*

capacity up to 1400 m³/hour at atmospheric pressure) to a pressure of 8 bar. The gas is flowing via a large vessel (4 m³) through a moisture filter and a dust filter. Steady volume-flow rates in the model valve are determined by i) measuring local values with a turbine flow meter, and ii) correcting for the compressibility of the air (Section 5.5). A pressure regulator (CV1) reduces the pressure from 8 bar to atmospheric pressure, thereby preventing pressure pulsations generated further downstream from traveling upstream towards the turbine meter. The pulsation source is a rotating cylinder, which blocks the flow periodically (Peters 2001). The Two-Microphone Method is used to determine the dynamic pressure and dynamic volume-flow rate, just upstream of the model valve (Section 5.6). The static component of the pressure difference across the model valve is measured using a strain gauge transducer (Section 5.5). The opening of the model valve is measured with a light intensity method (Section 5.4).

5.4 Valve Plate Displacement

Early measurements of valve plate displacement have been carried out in the 1930s. The plate was connected to a movable arm carrying a writing stylus. In subsequent decades, many non-contact measurements were performed, e.g. inductive or capacitive transducers (Touber 1976). However, in general displacement sensors have several disadvantages, e.g. sensitivity to temperature changes, lack of commercial availability, large physical dimensions relative to the valve system, restriction to dynamic measurements, small spatial resolution, restriction to metallic materials, and inconvenient displacement range.

A rather new class of methods for monitoring the valve opening is the use of optical sensors, like the Laser Doppler Vibrometer method (Buligan et al. 2002), the Endoscope Video method (Ludu et al. 2000), or the Fiber Optic Displacement method (Prasad and Woollatt 2000).

In the present setup three independent glasfiber bundles are connected to the valve limiter (Fig. 5.1a and Fig. 5.2: E). At every connector laserlight (Thorlabs CPS194, power is 8 mW, wavelength is 820 nm) is reflected at the downstream side of the valve plate. Fig. 5.4 shows a sketch of this situation. This light is captured by the same fiber bundle and sent to an amplified

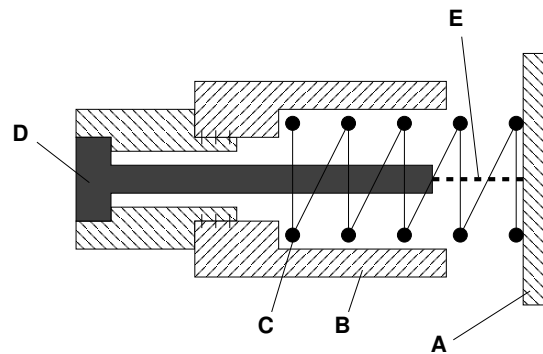


FIGURE 5.4: Sketch of valve assembly to measure the instantaneous valve opening h (A: plate, B: limiter, C: spring, D: glasfiber bundle, E: emitted and reflected laserlight).

silicon detector (Thorlabs PDA55, peak response is 0.6 A/W for 960 nm, 0.9 V/ μ W at 50 Ω and 40 dB gain for 820 nm). The output is directed to the data acquisition system (DIFA, 8 input channels). The intensity of the reflected light is a measure for the distance between plate and fiber's end, and thus for the valve opening. The aluminium plate surface has a high reflection coefficient for the nearly-infrared light. Therefore on the commercially available non-metallic compressor valve plate an aluminium layer has been coated. Calibration takes place by inserting thin rods (feeler gauges) with well-known thicknesses ($\delta h < 0.02$ mm) between seat and plate. Every glasfiber has to be calibrated independently, because fiber mountings (laser, limiter and sensor) are set manually. Typical calibration curves are shown in Fig. 5.5. A common problem of displacement transducers is the offset and range required. At the critical distances, the reciprocal sensitivity increases dramatically, i.e. $dh/dV_{\text{sensor}} \rightarrow \infty$. When the plate is close to the fiber's end (h is large), an offset phenomenon can be expected because the fiber's end is not a point. When the plate is far away from the fiber's

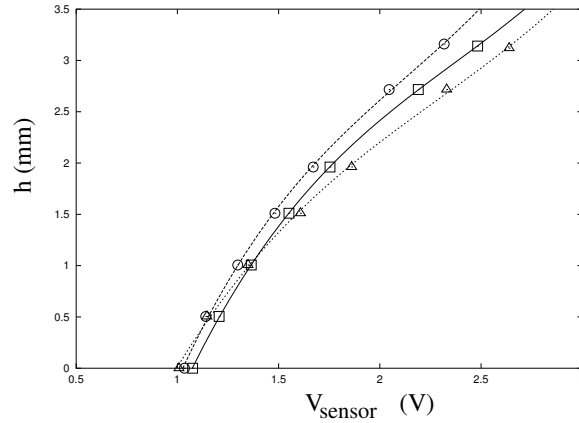


FIGURE 5.5: Valve opening calibration. For every fiber a separate curve is fitted, using a third-order polynomial; $h_{max} = 3.14$ mm.

end (h is small), the captured light intensity is weak. Therefore a curve fitting of a third-order polynomial is used, which requires at least five data points to obtain a regression coefficient.

A limitation of the method is the detection of the valve plate displacement in the case of a rocking valve plate. Calibration of h is performed for situations in which the plate is parallel to the seat's surface. However, the reflected light intensity is a function of the plate tilting angle too. Only for a few angles the calibration can be carried out. Therefore quasi one-dimensional plate motion must be enforced by making use of guiding rods (commercially available compressor valves have guiding rods to prevent plate rotation), at the expense of additional structural damping. The plate obliqueness should be checked on acceptability after each measurement. A related limitation of the method is the detection of h for a colliding valve plate.

5.5 Static Measurements

5.5.1 Valve Pressure Difference

When the air is flowing through the model valve, a piezo-resistive transducer (Druck, DPI 145) determines the static component of the valve pressure difference Δp (with accuracy $\delta \Delta p = 1 \text{ Pa} + 0.05\% \Delta p$). As the valve is mounted at the end of the pipe, the flow downstream of the valve emerges into the laboratory. The ambient pressure is therefore used as reference to define Δp . For *steady* pipe flow, the pressure difference across the pipe between pressure transducer and model valve is negligible compared to the pressure difference Δp across the model valve. When an unsteady flow component is superimposed, the time-averaged value of Δp increases due to non-linearity ($\Delta p \sim \Phi_v^2$). Fig. 5.6 illustrates the change (8%) in measured mean pressure at the onset of valve oscillation. Before resonance sets in ($t < 70$ s), the valve plate displacement follows the duty cycle of the screw compressor. This demonstrates that the static component of the pressure difference across the valve should be determined from the time-averaged value of Δp during unsteady flow, rather than

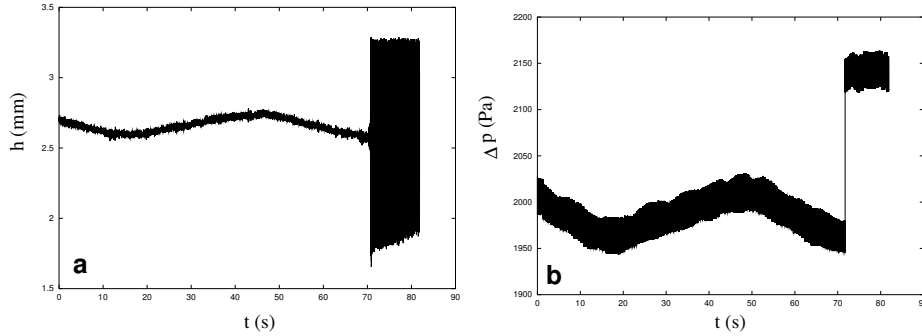


FIGURE 5.6: Increase of time-averaged Δp at onset of unsteady flow. (a) valve opening; (b) pressure difference.

using measured values of Δp for steady flow conditions.

5.5.2 Valve Volume-Flow Rate

The steady flow rate at the location of the turbine meter (Instromet Q75K) is determined by measuring the frequency of the turbine rotation speed (7555.26 pulses per m^3). For local pressures up to 16×10^5 Pa and for local volume-flow rates between 10 and 100 m^3/hour , the measurement error is less than 1%. By assuming one-dimensional steady non-leaking flow of an ideal gas, the valve volume-flow rate Φ_v is obtained by correcting the measured volume-flow rate $\Phi_{v, TM}$ for the drop in gas density, i.e.

$$\Phi_v = \left(\frac{p_{TM}}{p_{up}} \right) \left(\frac{T_{up}}{T_{TM}} \right) \Phi_{v, TM}, \quad (5.1)$$

where subscript TM denotes measurements at the turbine meter and subscript up denotes the inlet position of the model valve. The temperature measurements (with thermocouples) revealed that the static component of the pipe flow can be considered as an isothermal flow, i.e. $T_{TM} \approx T_{up}$.

5.6 Dynamic Measurements: Two-Microphone Method

5.6.1 Introduction

The unsteady values of Δp and Φ_v are obtained by making use of the linear theory of sound propagation and superposition of dynamic quantities and static quantities. The Two-Microphone Method (Chung and Blaser 1980b, Chung and Blaser 1980c, Chung and Blaser 1980a, Bodén and Åbom 1986, Åbom and Bodén 1988) is used to reconstruct the acoustic waves at the inlet of the model valve. A common procedure is to apply this method in Fourier space (at a single frequency). However, we are interested in reconstruction in the time domain, and therefore the method must be extended by using multiple modes. Three piezo-electric transducers, also referred to as microphones (PCB 116A, resonant frequency is 125 kHz, typical sensitivity is 1400 pC/MPa) are mounted flush in the pipe wall (Fig. 5.3). A pistonphone (Brüel & Kjaer, type 4220) is used to calibrate the transducers and charge

amplifiers (Kistler, type 5007, bandwidth $0.1 \text{ Hz} < f < 22 \text{ kHz}$) with an accuracy better than 1 Pa for 250 Hz. A typical amplitude of the pressure oscillation at the fundamental frequency is 600 Pa. The charge amplifiers are set to filter signals outside the range $2 \text{ Hz} < f < 1 \text{ kHz}$.

5.6.2 Wave Reconstruction

When the one-dimensional Euler equations are linearized, plane wave solutions for the pressure amplitude and velocity amplitude are obtained. The present flow is a low Mach number flow, which implies in first approximation identical wave numbers* for upstream- and downstream traveling waves, i.e. $\bar{k} = \omega/c_0$, where ω is the circular frequency and c_0 is the speed of sound. The experiments are performed at conditions that corrections for i) Doppler effects and ii) visco-thermal effects are not necessary, because i) $M = u_0/c_0 \ll 1$ (typically 1.5×10^{-2}) and ii) $Sh = \frac{D}{2} \sqrt{\omega/\nu} \gg 1$ (typically 2.3×10^2), where u_0 is the mean flow velocity, D is the pipe diameter and ν is the kinematic viscosity (e.g. Peters et al. 1993).

Consider the dynamic pressure in Fourier space, i.e.

$$p[x, \omega] = p_+[x, \omega] + p_-[x, \omega] = \int_{-\infty}^{\infty} p[x, t] e^{-i\omega t} dt, \quad (5.2)$$

where p_+ is a traveling pressure wave in positive x -direction (upstream) and p_- is a traveling pressure wave in negative x -direction (downstream), see Fig. 5.7. This decomposition can be

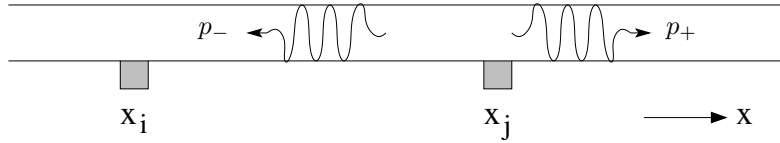


FIGURE 5.7: Wave decomposition for acoustical flow in pipe (x_i and x_j : position of microphones, p_- : left traveling wave, p_+ : right traveling wave).

written as

$$p_+[x, \omega] = \hat{p}_+[\omega] e^{-i\bar{k}x}, \quad (5.3)$$

$$p_-[x, \omega] = \hat{p}_-[\omega] e^{+i\bar{k}x}, \quad (5.4)$$

where \hat{p} is the complex amplitude, $i^2 \equiv -1$ and ω is the circular frequency.

The *reflection coefficient* R_x is defined as the ratio between the complex amplitudes of the upstream- and downstream traveling waves,

$$R_x \equiv \frac{p_-[x, \omega]}{p_+[x, \omega]}. \quad (5.5)$$

The *transfer function* H_{ij} of two measured signals at positions x_i and x_j is defined as

$$H_{ij} \equiv \frac{p[x_i, \omega]}{p[x_j, \omega]}. \quad (5.6)$$

*The quantity k is reserved for the valve spring stiffness. We will use \bar{k} for the wave number.

Using Eqs. (5.2)-(5.6) the transfer function can be written as

$$H_{ij} = \frac{e^{-i\bar{k}(x_i-x)} + R_x e^{i\bar{k}(x_i-x)}}{e^{-i\bar{k}(x_j-x)} + R_x e^{i\bar{k}(x_j-x)}}. \quad (5.7)$$

When the wave number \bar{k} and transfer function H_{ij} are known, the reflection coefficient at position x can be determined, i.e.

$$R_x = \frac{e^{-i\bar{k}(x_i-x)} - H_{ij} e^{-i\bar{k}(x_j-x)}}{H_{ij} e^{i\bar{k}(x_j-x)} - e^{i\bar{k}(x_i-x)}}. \quad (5.8)$$

We can write Eq. (5.2) as $p[x, \omega] = (1 + R_x)p_+[x, \omega]$ by making use of Eq. (5.5). When we substitute Eq. (5.3) into this equation and apply this to position x_i , we obtain

$$p[x, \omega] = \frac{1 + R_x}{1 + R_{x_i}} e^{i\bar{k}(x_i-x)} p[x_i, \omega]. \quad (5.9)$$

Eq. (5.9) can be put in a useful formulation after some algebra, i.e.

$$\boxed{p[x, \omega] = \frac{p[x_i, \omega] \sin[\bar{k}(x_j - x)] + p[x_j, \omega] \sin[\bar{k}(x - x_i)]}{\sin[\bar{k}(x_j - x_i)]}}, \quad (5.10)$$

which shows that the pressure at position x is a weighed average of the pressures measured at positions $x = x_i$ and $x = x_j$. Full reconstruction of the pressure in time, at any position x , is obtained after an inverse Fourier transformation, i.e.

$$p[x, t] = \frac{1}{2\pi} \int_{-\infty}^{\infty} p[x, \omega] e^{i\omega t} d\omega. \quad (5.11)$$

Note that multiplication of the weight factors in the frequency domain is analogous to a convolution product in the time domain.

Volume flow rate fluctuations can be determined by making use of the momentum equation of the linearized Euler equations, i.e.

$$\frac{\partial u}{\partial t} = -\frac{1}{\rho_0} \frac{\partial p}{\partial x}, \quad (5.12)$$

where $u = u[x, t]$ is the velocity amplitude and ρ_0 is the mean density. When Eqs. (5.2)-(5.4) are substituted into this relation we obtain,

$$u[x, \omega] = \frac{1}{\rho_0 c_0} (p_+[x, \omega] - p_-[x, \omega]). \quad (5.13)$$

The volume-flow rate amplitude $\Phi_v[x, t] = u[x, t]A$ can be written as

$$\Phi_v[x, \omega] = \frac{A}{\rho_0 c_0} \left(\frac{1 - R_x}{1 + R_x} \right) p[x, \omega], \quad (5.14)$$

where A is the cross-sectional area of the pipe[†]. We finally obtain a relation for the volume-flow rate after some algebra,

$$\Phi_v[x, \omega] = -i \left(\frac{A}{\rho_0 c_0} \right) \frac{p[x_i, \omega] \cos[\bar{k}(x_j - x)] - p[x_j, \omega] \cos[\bar{k}(x - x_i)]}{\sin[\bar{k}(x_j - x_i)]}. \quad (5.15)$$

Finally, the wave reconstruction in the *time domain* at any position x yields,

$$p[x, t] = \frac{1}{2\pi} \int_{-\infty}^{\infty} \frac{p[x_i, \omega] \sin[\bar{k}(x_j - x)] + p[x_j, \omega] \sin[\bar{k}(x - x_i)]}{\sin[\bar{k}(x_j - x_i)]} e^{i\omega t} d\omega, \quad (5.16)$$

$$\Phi_v[x, t] = \frac{iY}{2\pi} \int_{-\infty}^{\infty} \frac{p[x_j, \omega] \cos[\bar{k}(x - x_i)] - p[x_i, \omega] \cos[\bar{k}(x_j - x)]}{\sin[\bar{k}(x_j - x_i)]} e^{i\omega t} d\omega, \quad (5.17)$$

where the positions of the two microphones are denoted by x_i and x_j . The admittance $Y = \frac{A}{\rho_0 c_0}$. Traditionally this method is used for analysis in the frequency domain. Eqs. (5.16) and (5.17) contain weight factors of the measured pressure fluctuations as function of $\omega = \bar{k}c_0$, yielding convolution integrals for time domain analysis.

Fluctuations of the gas density are not reconstructed, although the evaluation of semi-empirical valve coefficient α , by means of Eq. (3.1), requires the computation of the valve inlet flow density ρ_{up} . Neglecting the fluctuations of the gas density is justified by the acoustical approach, i.e. $\rho[x, t]/\rho_0 \ll 1$.

5.6.3 Time and Frequency Filtering

The acquisition interface samples data from the microphones. Therefore wave reconstruction (Eqs. (5.16) and (5.17)) is performed at a discrete level by using the inverse Fast Fourier Transform (e.g. Lynn and Fuerst 1994). Because this algorithm assumes periodic signals, wrap-around (aliasing) errors are reduced by multiplying the dynamic pressure with the Bingham window (Fig. 5.8), i.e.

$$\text{win} = \begin{cases} \frac{1}{2} - \frac{1}{2} \cos\left[\frac{\pi t}{\epsilon_w T_m}\right] & , \quad 0 < \frac{t}{T_m} < \epsilon_w \\ 1 & , \quad \epsilon_w < \frac{t}{T_m} < 1 - \epsilon_w \\ \frac{1}{2} - \frac{1}{2} \cos\left[\frac{\pi}{\epsilon_w} \left(1 - \frac{t}{T_m}\right)\right] & , \quad 1 - \epsilon_w < \frac{t}{T_m} < 1 \end{cases} \quad (5.18)$$

where T_m is the total measuring time and ϵ_w is a cut-off parameter. From the three microphone signals the pair is chosen that has the highest coherence (based on the cross spectrum and the power spectra).

In order to prevent the introduction of large errors during the reconstruction (Eqs. (5.16) and (5.17) can become singular), the frequency filter of Bodén and Åbom (1986) is applied, i.e.

$$0.1\pi < \bar{k}|x_j - x_i| < 0.8\pi. \quad (5.19)$$

In Fourier space the remaining modes are zero-padded. Note that the measured spectrum peaks should be located in this interval, in order to apply the reconstruction method safely. In

[†]Note that $p_+[x, \omega] = \frac{1}{1+R_x} p[x, \omega]$ and $p_-[x, \omega] = \frac{R_x}{1+R_x} p[x, \omega]$. From Eq. (5.14) we immediately see the familiar relation between R_x and the complex acoustic impedance $z \equiv \frac{p[x, \omega]}{u[x, \omega]}$, i.e. $\frac{z}{\rho_0 c_0} = \frac{1+R_x}{1-R_x}$.

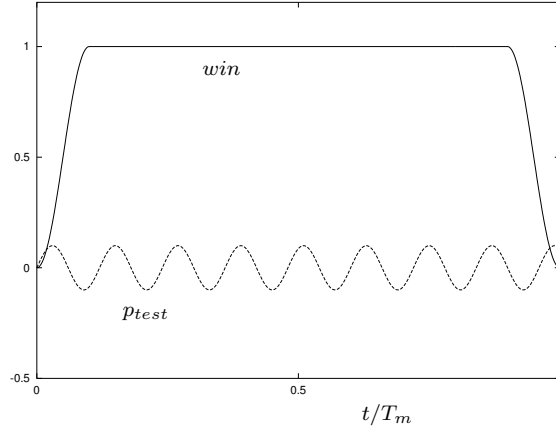


FIGURE 5.8: Bingham window win ($\epsilon_w = 0.1$). During the measuring time T_m , approximately 8.3 periods of the test function p_{test} are processed.

our case e.g. $|x_j - x_i| = 0.60$ m, yielding $28 \text{ Hz} < \frac{1}{2\pi}\omega < 228 \text{ Hz}$. This interval encloses typical valve resonance frequencies and typical pulsation sources from the by-pass system.

The issue of modelling the valve as a *black box*, naturally raises the question how to define the valve inlet. Reconstruction of the root-mean-square pressure amplitude as function of coordinate x reveals that the valve flow inlet can be defined at the geometrical inlet plane (Fig. 5.9). The valve is acoustically compact, i.e. the smallest acoustical wavelength is

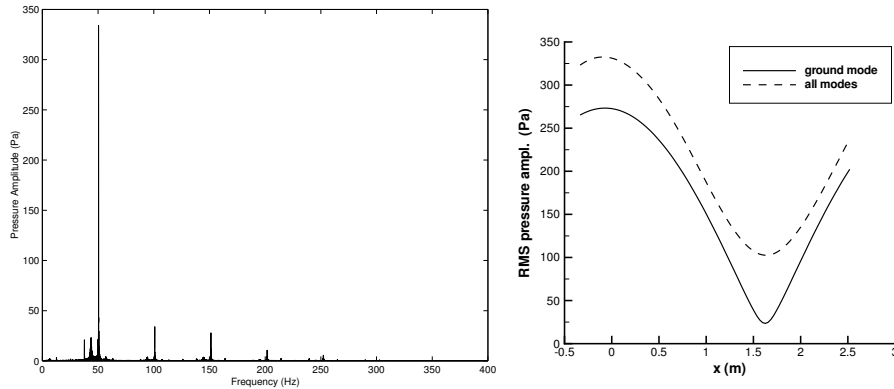


FIGURE 5.9: Example of (a) pressure spectrum at $x = 0.50$ m, and (b) spatial wave reconstruction from microphones located at $x = 0.50$ m and $x = 1.10$ m. The sampling frequency is 800 Hz. All significant modes are captured in the filter of Bodén & Åbom. The valve inlet is located at $x = -0.34$ m and the by-pass end point is located at $x = 2.52$ m.

much larger than then largest geometrical length scale of the valve. The reconstruction of the

root-mean-square pressure amplitude uses Parseval's identity (e.g. Kreyszig 1993), i.e.

$$\frac{1}{T_p} \int_0^{T_p} p[x, t]^2 dt = a_0^2 + \frac{1}{2} \sum_{n=1}^{\infty} (a_n^2 + b_n^2), \quad (5.20)$$

where pressure $p[x, t]$ has time period T_p and mean value a_0 . Furthermore $\{a_n\}$ are the Fourier cosine coefficients and $\{b_n\}$ are the Fourier sine coefficients, all related to the reconstructed discrete spectrum $p[x, \omega]$ (Eq. 5.10).

The dominant mode in the spectrum (Fig. 5.9a) has a frequency of 50.4 Hz. It has been tested that there is no interference with electrical supply sources (50 Hz). The valve resonance frequency (27 Hz) is not observed in the spectrum. Therefore the valve oscillation is acoustically driven, in agreement with the experiments of Ziada et al. (1986).

Simultaneous pressure measurements at three different locations along the pipe makes it possible to illustrate the quality of the reconstruction procedure. In the following, the acoustic wave is reconstructed from microphones 1 and 2 at the location of microphone 3. A typical result of the reconstruction in the time domain is shown in Fig. 5.10. This case represents a

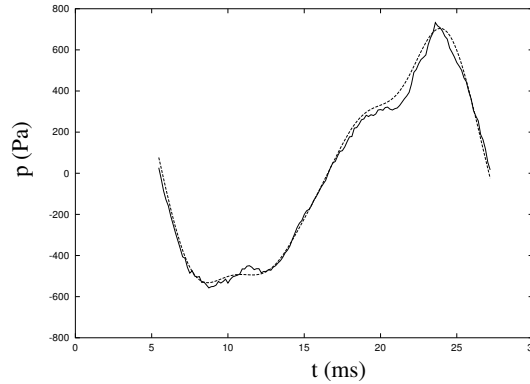


FIGURE 5.10: Comparison of dynamic pressure: —, measurement; --, reconstruction. The microphones at $x_1 = 0.50$ m and $x_2 = 1.10$ m are used to reconstruct the pressure waves at $x_3 = 1.70$ m (the admittance $Y = 1.92 \times 10^{-5}$ m⁴s/kg).

valve plate oscillating with large amplitude.

5.7 Mechanical Parameters of Valve

The effective plate mass m is obtained by measuring the weight of the plate (including 3 nylon tubes) and adding the effective spring mass (inertial effect of one coil spring equals one third of its mass). The damping coefficient ζ is obtained by generating an underdamped oscillation for the case without flow. The amplitude of h decays exponentially in time (Fig. 5.11a). The spring stiffness k is determined by measuring static force and static valve opening h , while the gravity force of added objects of known mass tend to open the valve (Fig. 5.11b). The

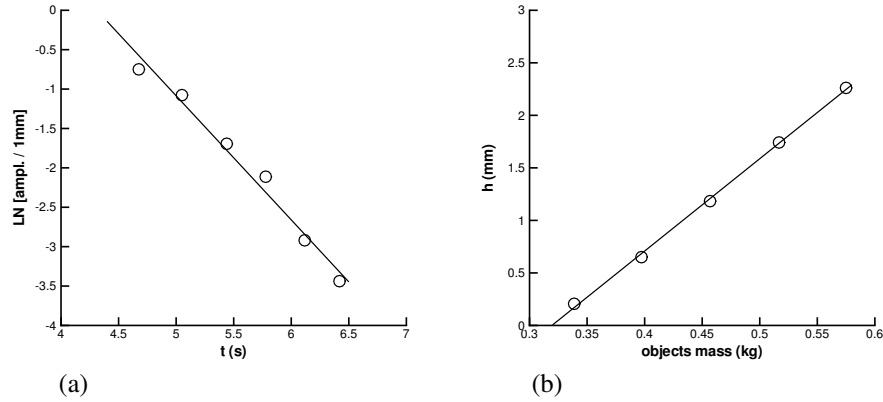


FIGURE 5.11: Determination of (a) damping coefficient ζ (slope $\propto \zeta$), and (b) spring stiffness k (slope $\propto k^{-1}$).

preload distance h_{pl} , total edge length L_g and maximum valve opening h_{max} are obtained by measuring geometrical length scales of valve and springs. The port area A_p is determined from the port length and volume (known from density and mass) of removed brass after milling. Finally, Table 5.1 presents the numerical values of the mechanical parameters of the model valve.

TABLE 5.1: Mechanical parameters of model valve.

Parameter	Symbol	Value
effective plate mass	m	38.54×10^{-3} kg
damping coefficient	ζ	1.45 Ns/m
spring stiffness	k	1116 N/m
preload distance	h_{pl}	3.06 mm
maximum valve opening	h_{max}	3.14 mm
port area	A_p	26.61×10^{-4} m ²
total edge length	L_g	471.2 mm
sealing rim length	d_{sr}	1.00 mm
port length	L_p	16.00 mm

This chapter presents the results that are obtained with the computational method (Chapter 4) and the experimental method (Chapter 5) applied to the flow in valves. Steady flow through a valve for the case of a hovering plate and for the case of a fixed plate is considered in Section 6.1. Unsteady flow through a valve with freely moving valve plate is considered in Section 6.2. Finally, Section 6.3 presents a comparison between the results for a commercially available compressor valve and for the model valve.

6.1 Semi-Empirical Coefficients

6.1.1 Laboratory Experiments

The semi-empirical coefficients $\alpha[h]$ and $c_g[h]$ are obtained by generating a (quasi-)steady flow in the present experimental setup (Section 5.3). This flow is a result of fluid-structure interaction, because for a *hovering* valve plate the spring force $k(h + h_{pl})$ is balanced by the gas force acting on the plate. The steady gas force results in a unique combination of the valve opening h and i) the volume-flow rate Φ_v in the valve, i.e. $\Phi_v[h]$, and ii) the pressure difference Δp across the valve, i.e. $\Delta p[h]$. This (quasi-)steady state of the valve is obtained by distinguishing six states (Fig. 6.1). Consider the case of a fully closed valve that responds to a slowly opening upstream located control valve. Then the following subsequent states will appear:

1. fully closed valve,
2. at very small valve openings resonance sets in, the plate is colliding against the seat and later on against the limiter,
3. fully opened valve.

When the upstream located control valve is slowly closed, the following subsequent states appear:

4. (quasi-)steady state,
 5. at very small valve openings resonance sets in, the plate is colliding against the seat (slowly opening the control valve does not switch the system back to state 4) but to state 2)),
-

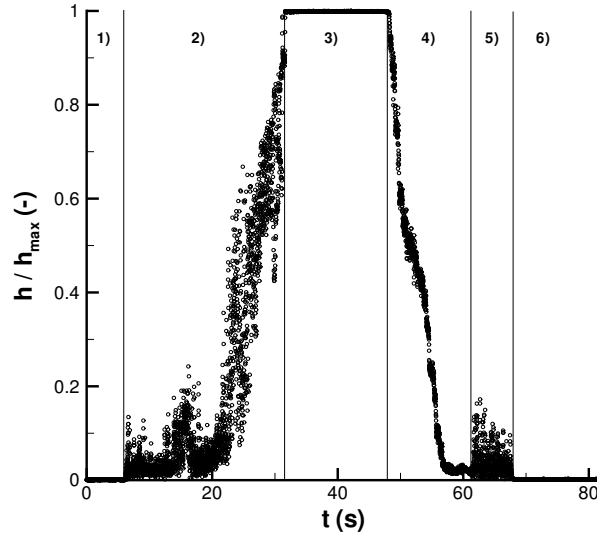


FIGURE 6.1: History of valve opening during slowly changing pressure difference (six states are distinguished, sample frequency is 100 Hz).

6. fully closed valve.

During state 4) the coefficients $\alpha[h]$ and $c_g[h]$, which are defined by respectively Eqs. (3.1) and (3.4), are determined (see Fig. 6.2). In Fig. 6.2 the valve opening h denotes the averaged value of the three-point measurement of the present setup. Parabolic regression fits of the coefficients $\alpha[h]$ and $c_g[h]$ appeared to be adequate. The standard deviation of $h[t]$ is less than 1% of its mean value. For the model valve the present results show an almost constant value of 1.2 for the gas force coefficient c_g and a slightly decreasing value from 0.9 to 0.7 for the flow coefficient α . For a ring plate compressor valve Frenkel (1969) reports α monotonically decreasing from 0.8 to 0.5 and c_g monotonically increasing from 1.0 to 1.3, both for $h/h_{max} \in (0.2, 1.0)$.

6.1.2 Computational Fluid Dynamics

One of the objectives of this study is to investigate the ability of the preconditioned Euler method (Chapter 4) to predict the semi-empirical coefficients $\alpha[h]$ and $c_g[h]$. The mesh-related computational methods for the flow around valve-like boundaries (i.e. geometries with sharp edges, (multiple) 90° flow direction changes and internal (small gap) flow) that are reported in the literature deal mostly with *incompressible viscous flow* (e.g. Deschamps et al. 1996, Kerh et al. 1997, Pérez-Segarra et al. 1999, Matos et al. 1999, Ottitsch and Scarpinato 2000, Possamai et al. 2001, Matos et al. 2002). Fewer methods consider *compressible viscous flow* (e.g. Cyklis 1994, Nkonga 2000, Will and Flade 2003). No studies have been reported concerning *inviscid compressible flow*, i.e. the Euler equations. Almost all computational studies solving the multi-dimensional Euler equations are dealing with external flow around

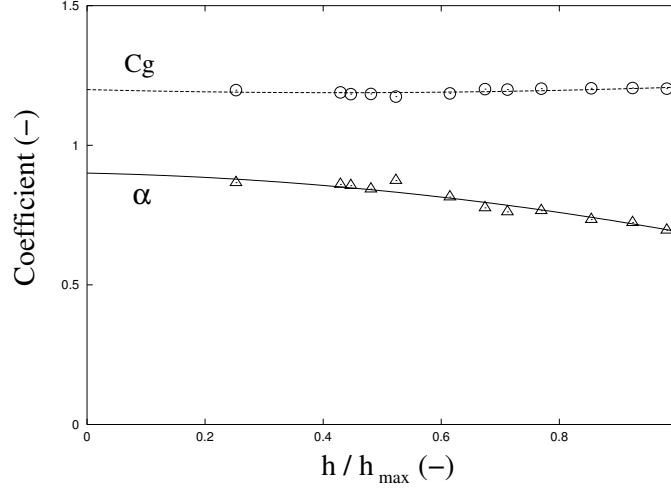


FIGURE 6.2: Measured semi-empirical coefficients as function of h/h_{max} for the model valve. The lines represent parabolic regression fits: $c_g = 1.20 - 0.05(\frac{h}{h_{max}}) + 0.06(\frac{h}{h_{max}})^2$ and $\alpha = 0.90 - 0.04(\frac{h}{h_{max}}) - 0.17(\frac{h}{h_{max}})^2$.

aerodynamically shaped bodies. In Section 4.1 we discuss the motivation of employing the preconditioned Euler method for unstructured meshes to tackle the problem of Computational Fluid Dynamics for compressor valves. If such a method is successful it would be very helpful in the design of valves and it would reduce the need for costly manufacturing processes and laboratory experiments. In the following paragraphs we discuss the geometry and mesh generation, the flow around a fixed plate and the flow around a hovering plate, respectively.

Geometry and Mesh For the purpose of validating valve theories, a model valve has been designed (Section 5.2) with a less complex geometry than commercially available compressor valves. In the laboratory this model valve is embedded in a system of two flanges. The system is mounted on the pipe end of the experimental setup (Fig. 5.3). In the present computational study the geometry of the model valve and the system of flanges of the experimental setup is adapted slightly, to enable mesh generation without employing extremely specialized features of the mesh generation program.

The three port channels of the experimental model valve are combined into one port channel with inner radius R_i and outer radius R_o . Key parameters are the cross-sectional port area A_p and the total edge length L_g of the plate. These parameters A_p and L_g are kept equal to the ones of the experimental model valve, while the inner radius R_i and outer radius R_o of the three port channels are modified to determine the computational geometry with a single port channel. Solving the system

$$\begin{aligned} A_p &= \pi(R_o^2 - R_i^2), \\ L_g &= 2\pi \left(\underbrace{R_i - d_{sr}}_{\text{inner radius of plate}} + \underbrace{R_o + d_{sr}}_{\text{outer radius of plate}} \right), \end{aligned}$$

where d_{sr} is the sealing rim length (Fig. 5.1b), for these two radii yields the transformations

$$\begin{aligned} R_i &= 31.00 \text{ mm} \rightarrow 31.85 \text{ mm}, \\ R_o &= 44.00 \text{ mm} \rightarrow 43.15 \text{ mm}. \end{aligned}$$

In order to save computation time we consider axi-symmetric non-swirling flow (as first order approximation of the flow in the experiments) by solving the three-dimensional Euler equations in a 'piece-of-pie'-like geometry. Fig. 6.3 shows the mesh in the meridian plane of the computational domain.

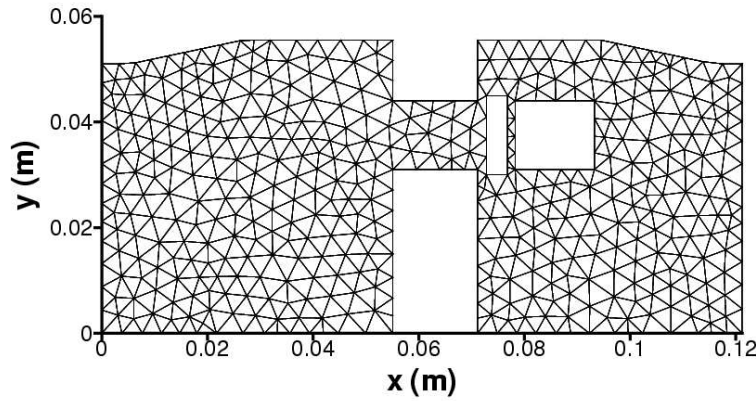


FIGURE 6.3: *Geometry and coarse mesh of the model valve suited for computational fluid dynamics. This plane ($z = 0$) shows the faces of the tetrahedral elements located on the plane $z = 0$ as a mesh of triangular elements. The inlet plane is $x = 0.0$ mm, the outlet plane is $x = 121.2$ mm and the axis of symmetry is the x -axis.*

Alternatively, the Euler equations formulated in cylindrical coordinates could have been considered (e.g. Put 2003). However, source terms ($\propto 1/r$) would appear and local preconditioning of the new 'hyperbolic' system would induce additional difficulties.

The three-dimensional mesh is generated by filling the 'piece-of-pie'-like geometry with tetrahedral elements. In this way the aspect ratio of all elements are close to unity. Simulations with a mesh that was generated by rotational extrusion of a pure two-dimensional (planar) triangular mesh (where the pentahedral- and pyramid elements are converted to tetrahedral elements) resulted in unstable solutions caused by the stagnation flow computed on distorted stretched cells. A 'piece-of-pie' angle of 30° was chosen, because any smaller angle yields severe difficulties in mesh generation procedures (even for 'thin-cuts') and larger angles lead to a too large number of elements (leading to unacceptable computation times or requiring too much computer memory). Furthermore, an extension of the domain in axial direction was applied because the flow showed reversal at the exit plane, resulting in a switch in the appropriate characteristic boundary condition.

Fixed Valve Plate Laboratory experiments were conducted by fixation of the plate at a large opening of $h = 1.70$ mm (to be discussed in Section 6.1.3, $h/h_{max} = 0.54$). The valve boundary conditions for this experiment are: inlet speed $u_{in} = 0.75$ m/s, inlet temperature $T_{in} = 290.5$ K and outlet pressure $p_{out} = 102335$ Pa. The measured time-averaged pressure difference then equals $\Delta p = 2787$ Pa. The question arises whether it is possible to predict this pressure drop by employing the Euler method for (un)steady flows. The flow can be characterized with an inlet Mach number of $M_{in} = 2 \times 10^{-3}$ and a mean gap flow Mach number of $M_{gap} = 0.20$. Thus application of preconditioning seems necessary because the range in local Mach numbers is large (slow convergence) and the minimum value is very low (inaccurate solution).

Unfortunately, numerical solutions with sufficient accuracy have **not** been obtained. The problem is related to numerical instabilities driving the residuals towards infinity. These problems and several solution approaches that have been considered are summarized in the following:

- *Effects of Geometry and Mesh.*
 1. When a mesh is generated by rotational extrusion of a triangular mesh over a small angle, say 5° , numerical simulations start to get unstable in the regions of the domain where the cells have large aspect ratios. This typically occurs near the edges in the gap between seat and plate. Mesh generation for smaller angles yields severe problems near the axis of symmetry.
 2. Often the simulations result in reversed flow at the outlet boundary. A common procedure to cure this problem in external flows is to extend the computational domain in axial direction with a coarser mesh. However, the flow in a valve can not be considered as the analogy of an external flow that separates from a bluff body. In that case the shed vortices are convected with a mean stream and numerically filtering (coarse mesh) of the flow fluctuations results in the proper number of outward directed characteristics. When the flow in a valve separates at the sharp edges of plate and seat, a jet is generated. It is not clear whether the solution of the preconditioned Euler method would convergence towards a situation in which this jet would develop in a vortex or not. Computations for the flow through a stepwise convergent channel (Appendix C) show that a separation bubble is growing in pseudo-time until reversed flow occurs at the outlet plane. Domain extension with a coarser mesh did not cure this problem.
 3. Some numerical instabilities (for $k^{(2)} > 0$) are related to the unrealistic formation of regions with local supersonic flow near boundary edges of 90° . When these angles are modified to 45° no numerical instabilities were observed in these regions. The case of flow around a diamond-shaped object with 90° top angle yielded numerically stable solutions. The case of external flow around a 90° inclined plate yielded numerically stable solutions. However, including a 'valve port' in the preceding case gave rise to instability problems (Appendix C).
 - *Effects of Artificial Dissipation.*
 1. The numerical values of the artificial dissipation coefficients $k^{(2)}$ and $k^{(4)}$ have to be chosen with care. On the one hand, these coefficients should be large enough to avoid numerical instability. On the other hand, these coefficients should be small enough to obtain accurate results.
-

2. Consider the case of the model valve and the initial condition to be equal to the inlet speed vector, the inlet temperature and the outlet pressure. Then the artificial dissipation coefficients should be relatively large to avoid numerical instability, since the initial condition does not approximate the (expected) final solution very well. However, the strategy of lowering these coefficients (to obtain an accurate solution) for certain intervals in pseudo-time (see Section 4.4) does not cure the problem. When the dissipation coefficient is large (typically $k^{(4)} = 0.3$), numerical mass sinks (the local Mach number is typically $M \approx 10^{-4}$) can be observed in the internal flow domain and mass sources (the local Mach number is typically $M \approx 10^{-3}$) can be observed in the nodes on the solid walls. When $k^{(4)} = 0.3$ was lowered the sources disappeared. However, in parts of the computational domain where the flow has large velocity gradients, numerical instability sets in.

3. Consider the case of $k^{(2)} > 0$ and the observation of the appearance of numerical instabilities near the solid wall boundary cells. It has been observed that setting $k^{(2)}$ to zero (and $\beta^{(4)} = 0$) delays the appearance of numerical instability near these solid wall boundaries.

4. Consider the case of flow reversal at the outlet. Setting the dissipation to zero in the outlet-facing internal cells resulted still in flow reversal, slightly earlier in pseudo time. Making the factor $k^{(4)}$ a function of the axial position (increasing with x) led to divergence.

- *Effects of Initial Condition.*

In most studies local time-stepping towards the steady state is performed from an initial condition in which the flow variables have a constant value (equal to the inlet- and outlet boundary values). In case this initial state deviates largely from the physical solution, numerical instabilities may lead to divergence of the numerical procedure. Therefore other types of the initial condition may be sought for. In case of a 'regular' domain (e.g. Appendix C) the concept of *domain partitioning* can be applied for the initial state rather easily. The initial condition is set at different values for different parts of the domain. Compared to the constant initial condition, partitioning increases the convergence rate, provided that some knowledge of the solution is used. However, for 'irregular' domains like compressor valves, domain partitioning of the initial state is not straightforward. Applications of 'Riemann-like' states and setting the solid wall boundary-facing cells to zero speed have not been successful for the model valve.

- *Effects of Boundary Condition.*

1. Often the simulations result in reversed flow at the outlet boundary. Unfortunately, most of the simulations carried out in the present study were automatically stopped by the growth of numerical instabilities near the outlet. During the last period of the present research the following alternative was applied. Employing the new outlet boundary condition $\mathbf{u} \cdot \mathbf{n} = 0$ (in addition to $p = p_{out}$) in case of flow reversal, did not yield numerically stable solutions. After a substantial time unrealistically high values for the density were observed in the vicinity of the solid wall and the outlet boundary.

2. In order to start the local time-stepping algorithm with a high flow rate, the outlet pressure can be set to an unrealistic low value for a certain number of time-steps. How-

ever, it was observed that the increment of this pressure towards the physical boundary value must be very low to maintain numerical stability. Thus this procedure could be useful only when e.g. multigrid or parallel multi-block algorithms increase the computation speed.

- *Effects of Preconditioning.*

1. When preconditioning is switched on, the numerical instabilities have been found to get initiated earlier in pseudo time. Using a smaller CFL number could prevent the solution to become unstable (e.g. Lee 1998). In the case of the external flow around a 90° inclined plate, setting $CFL = 0.1$ rather than $CFL = 0.5$ resulted similarly in a numerically unstable solution after a factor 5.2 larger number of iterations.

2. For the case of the model valve, no systematic study has been presented on the effects of the cut-off parameter ϵ . In the case of flow through a port and around a 90° inclined plate, very low temperatures in the low-speed ($M \sim 10^{-3}$) wake of the plate resulted in numerical instabilities (Appendix C). The inlet Mach number was 4.5×10^{-2} and preconditioning was switched on with $\epsilon = 10^{-2}$. Simulations with cut-off parameter equal to 10^{-3} yielded a lower convergence rate and numerically unstable results earlier in pseudo time.

Fig. 6.4 shows the result of the velocity field in a modified model valve. This modified

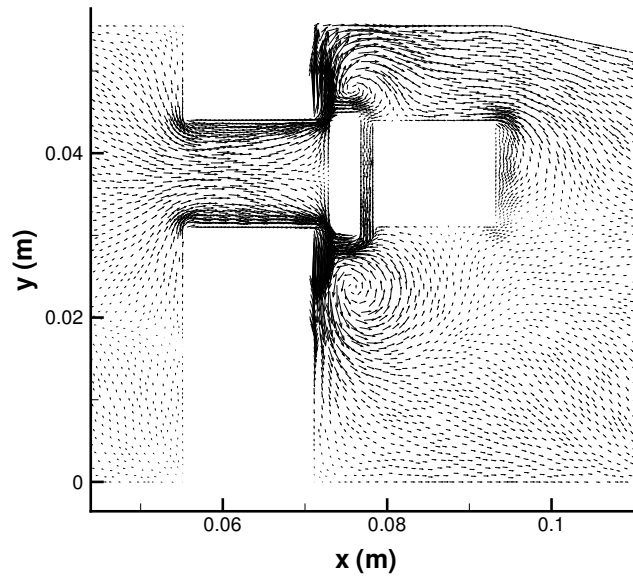


FIGURE 6.4: *Velocity field of 2D planar flow in modified model valve after 5000 pseudo time-steps ($M_{in} = 0.15$, $k^{(2)} = 0.2$, $\beta^{(4)} = 1.0$, $k^{(4)} = 0.15$, preconditioning switched off).*

model valve forces the flow to be 2D planar since the lateral length is relatively small (dimensions are $171.3 \times 51.0 \times 1.0 \text{ mm}^3$). The solution has not been converged towards a steady-state, because of the problem of numerical instability. Nevertheless this solution suggests that the flow regime as sketched by Böswirth (2000) could be present, see Fig. 6.5. When the left subfigure in Fig. 6.5 is compared with the non-converged solution in Fig. 6.4,

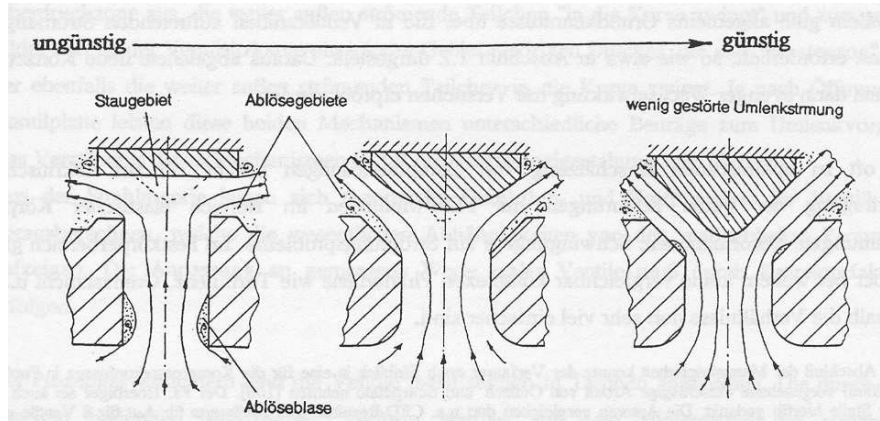


FIGURE 6.5: Process gas is often contaminated with small solid particles that deposit in compressor valves. Valves with intensively separated flows (left) require shorter maintenance intervals. In left figure: Ablöseblase = 'separation bubble', Staugebiet = stagnation region, Ablösegebiete = 'dead water' regions. From Böswirth (2000).

several similarities can be observed. Firstly, in both cases at the port entrance a 'separation bubble' is present. However, in the Euler method i) the vorticity is generated artificially via flow separation at sharp edges, and ii) the reattachment length of the shear layer is not steady. This observation is presented in more detail in Appendix C for the case of the flow through a stepwise convergent channel. Secondly, the flow approaching the plate in the internal part of the port is stagnating. Fig. 6.4 shows a stagnation point on the plate, while in Fig. 6.5 the stagnation region is sketched with a dashed line. Thirdly, the flow separates at the sharp edges of the seat and plate and forms a jet. However, the 'dead water' regions characterized by low local Mach number is likely to be essentially unsteady. In Fig. 6.5 a small vortex is sketched in the 'dead water' region between plate and shear layer originating from the plate. In the non-converged solution of the Euler method two vortices are present. This suggests that the flow is indeed unsteady. Unfortunately, the numerical simulation terminates because of numerical instability (supersonic flow in the upper gap between seat and plate).

We feel that the concept of local preconditioning of the Euler equations is not suited for highly stagnated flow regions in complex geometries. Furthermore, for unstructured meshes there is a fundamental problem of accurately approximating the third-order difference at solid wall boundary faces. The present assumption of equal Laplacian in ghost cell and boundary cell could yield an inaccurate description of the fourth-order dissipation term of the control volume next to the boundary. Additionally, the present node-centered (i.e. dual-mesh) method could also give inaccurate discretizations near plane solid wall boundaries.

This boundary flux is computed by assigning zero normal velocity at the boundary interface. However, the flow evaluation is assigned to the node which lies on this solid wall. No articles have been published so far on the subject of unstructured preconditioned Euler methods for stagnated flow regimes. However, Lee (1998) gives a clear overview of the 'major problems plaguing Euler preconditioners' and illustrates the loss of robustness around stagnation points already for a simple two-dimensional stagnation flow field.

Hovering Valve Plate The hovering valve plate is an example of a (simple) fluid-structure interaction phenomenon. However, successful application of the preconditioned Euler method has *not* been obtained, since this method could not be applied successfully to the preceding case of a fixed valve plate. Prediction of semi-empirical coefficients $\alpha[h]$ and $c_g[h]$ must be performed by fixation of the valve opening h in the computational domain and adaptation of the inflow and outflow boundary conditions. For a certain inlet speed, a pressure difference must be computed for the (unsteady) valve flow. The gas force acting on the plate must be computed by integration of the pressure along the plate surface. The boundary conditions must then be adapted to yield a gas force that is equal to the steady spring force $k(h_{pl} + h)$. First approximations are obtained by forcing the inlet speed on base of the measured volume-flow rate and adaptation of the valve outlet pressure. The 'converged' pressure drop then determines the computed $\alpha[h]$ and $c_g[h]$. When adaptation of the outlet pressure is absent, two values of $c_g[h]$ must be plotted, i.e. one based on a spring force and the other based on the integrated pressure force acting on the hovering plate.

6.1.3 Reverse Flow

It is expected that when a compressor valve experiences strong backflow pulsations (for a discharge valve: in the plenum chamber, for a suction valve: in the cylinder) or the valve is nearly closed, flow reversal in this valve can occur. In order to estimate the flow coefficient $\alpha[h]$ for reverse flow, the valve-flanges system was mounted on the pipe end with the valve limiter upstream. The plate was *fixed* along the guiding rods and the glasfibers were removed. Care has been taken that the flow is not disturbed by the modifications.

Valve theories often include the factor $sign[\Delta p]$ in the volume-flow rate equation (Eq. 3.1), i.e.

$$\Phi_v = \alpha[h] sign[\Delta p] L_g h \sqrt{\frac{2}{\rho_{up}} |\Delta p|}, \quad (6.1)$$

enforcing that the square-root is operating on a non-negative number. During flow reversal the flow rate gets only a minus sign, implying the same flow resistance. However, this is not realistic. Idelchik (1994) showed that the flow around a single movable (top-hinged) flap has a higher resistance coefficient (i.e. $1/\alpha^2$ is larger) when the flow is entering the device with smaller port area (intake configuration) with respect to the higher port area (exhaust configuration) for any flap angle. The magnitude of the vena contracta factor for the case of reverse flow is not the same as for the case of regular flow. Results of the model valve indeed show this behaviour, see Fig. 6.6. When the pressure difference increases the flow rate increases too. However, for a small valve opening ($h = 0.83$ mm) this effect is not as pronounced as for a large valve opening ($h = 1.70$ mm). For the same flow rate reversing the flow direction results in an additional pressure drop. Furthermore Fig. 6.6 has a lower flow rate below which we do not show experimental data. This is related to an increased

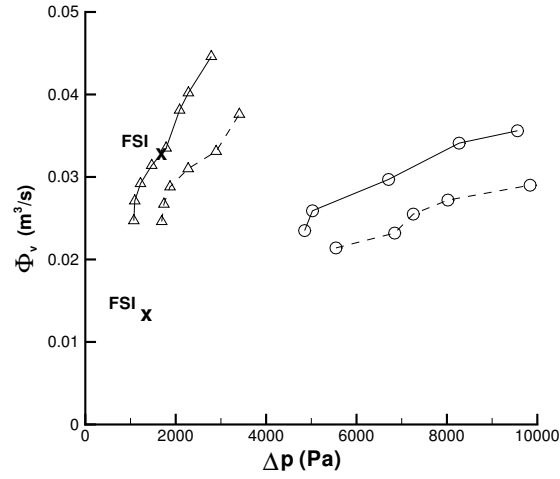


FIGURE 6.6: *Steady flow through model valve with fixed valve opening: —, normal flow direction; --, reverse flow. $h = 0.83$ mm is denoted by \circ and $h = 1.70$ mm is denoted by Δ . The case of a hovering valve plate is denoted by FSI and symbol \times .*

measurement error when the turbine meter is used for local volume-flow rates less than $10 \text{ m}^3/\text{hour}$. In order to present the change in vena contracta factor during flow reversal, we define the Reynolds number using the port length L_p and a mean flow velocity in the port cross-sectional area A_p , i.e.

$$Re = \rho \frac{\Phi_v L_p}{A_p \mu}, \quad (6.2)$$

where μ is the dynamic viscosity. Although characterizing the flow regime would be more logical when the valve opening h is used as length scale, we prefer to use the constant parameter L_p rather than h because the latter is a variable for the case of the full unsteady flow problem. Fig. 6.7 shows a sketch of the setup. The plate is fixed by inserting rings/nuts between the plate and both limiter and seat at the location of the three guiding rods. In this way the plate cannot move and the flow is not disturbed, but the total thickness of these rings must be precisely the same as the maximum valve opening. The high Reynolds number flow is expected to form jets at different positions. Fig. 6.8 shows the vena contracta coefficient during flow reversal. Flow coefficient α is observed to decrease with approximately 0.2, within a wide range of the Reynolds number, indicating an increased flow resistance during reversal (from —to --lines). Furthermore, when the pressure difference is increased in several steps and subsequently decreased in several steps, hysteresis is not observed for the flow in a valve with a fixed plate.

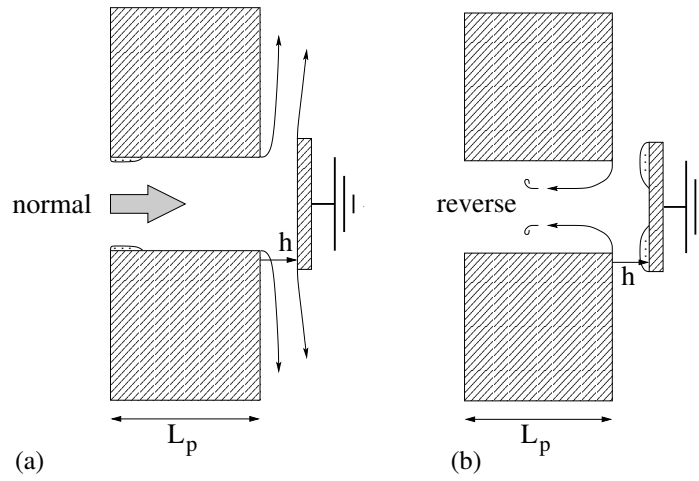


FIGURE 6.7: Sketch of flow around a fixed valve plate in (a) normal and (b) reverse direction. The case of reverse flow (b) could also consist of fully separated flow from the plate, rather than reattached flow.

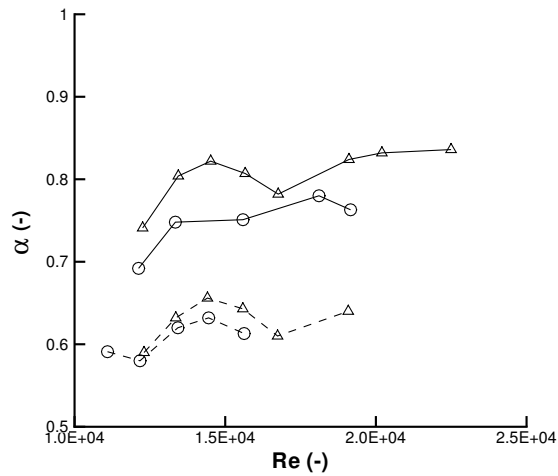


FIGURE 6.8: Steady flow through model valve with fixed valve opening: —, normal flow direction; ---, reverse flow. $h = 0.83$ mm is denoted by \circ and $h = 1.70$ mm is denoted by Δ .

6.2 Unsteady Flow

6.2.1 Restitution Coefficient

The valve plate is limited in its travel by the valve seat ($h = 0$) and by the limiter ($h = h_{max}$). When a moving body impacts a fixed wall it will bounce and reverse its direction of motion with a velocity that is generally lower than the velocity before impact. The restitution coefficient e_{res} is defined in Eq. (3.2), i.e.

$$\frac{dh}{dt}[t^+] = -e_{res} \frac{dh}{dt}[t^-], \quad h[t^\pm] \in \{0, h_{max}\}. \quad (6.3)$$

This coefficient cannot be predicted from the elastic properties of the valve material and geometry alone. There are many other (fluid-structure interaction) factors involved. In absence of flow, visual observation suggests inelastic ($e_{res} = 0$) impacts. When a mathematical model of a compressor considers such inelastic valve plate collisions, conditions for transitions between several phases of operation (e.g. expansion, suction valve plate in motion and suction valve fully open) have to be taken into account (e.g. Toubert 1976). However, online sampling of $h[t]$ reveals that at timescales of $\mathcal{O}\{10^{-3} \text{ s}\}$ and length scales of $\mathcal{O}\{10^{-4} \text{ m}\}$ semi-elastic collisions occur. Fig. 6.9 presents an example of the plate height and plate speed as function of time for two collision events between the valve plate and limiter. Based on multiple rebounds the model valve has the following restitution coefficients:

- for limiter $e_{res} = 0.2 \pm 0.1$,
- for seat $e_{res} = 0.3 \pm 0.1$.

Similar to compressor valves, severe tumbling effects are only present when the valve plate is close to the seat. This discussion is continued in Section 6.3 (compressor valve) and Section 7.1 (conclusions).

6.2.2 Validation of Basic Valve Theory

The Basic Valve Theory is a closed description when coefficients $\alpha[h]$ and $c_g[h]$ are known. However, we wish to ask ourselves whether the flow through a valve with oscillating plate can be described with a quasi-steady flow model. Validation of this statement can be sought in several ways. One way is to integrate the equations of motion of the plate, Eq. (3.2), for prescribed experimentally determined valve pressure difference $\Delta p[t]$ and to compare the simulation results for $h[t]$ with the experimentally measured plate height. Consider the valve to remain open and exclude collisions, i.e. $0 < h < h_{max}$. Then the equation of plate motion can be written as a coupled system with two independent variables h and \dot{h} , i.e.

$$\frac{d}{dt} \mathbf{s} + \mathbf{A} \mathbf{s} = \mathbf{f}[\mathbf{s}, t], \quad (6.4)$$

where unknown $\mathbf{s} \equiv (\dot{h}, h)^T$, matrix $\mathbf{A} = \begin{pmatrix} \zeta/m & k/m \\ -1 & 0 \end{pmatrix}$ and source term $\mathbf{f} = (-\frac{k}{m}h_{pl} + c_g[h] \frac{A_p}{m} \Delta p[t], 0)^T$ with the mechanical valve parameters: damping coefficient ζ , spring stiffness k , effective plate mass m , preload distance h_{pl} and port area A_p . Because matrix \mathbf{A} is

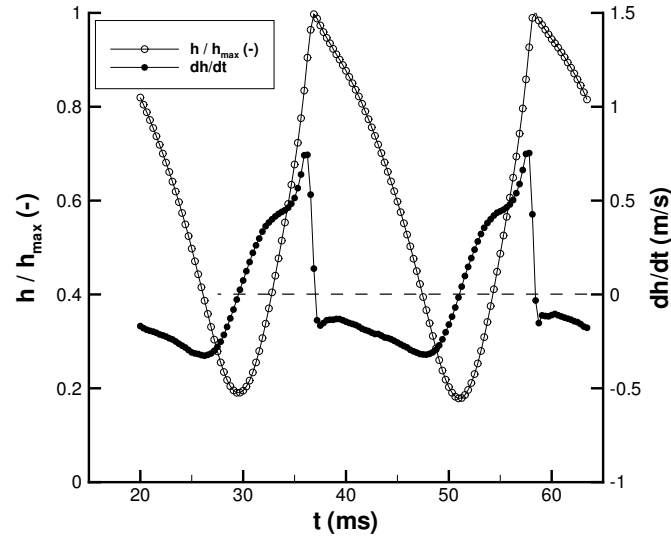


FIGURE 6.9: Collisions between plate and limiter for the model valve. The valve opening h/h_{max} is measured ($h_{max} = 3.14$ mm, sampling frequency is 3.2 kHz). The plate speed dh/dt is computed from $h[t]$ with the central difference scheme.

constant a semi-implicit time integration can be performed for unknown s^{n+1} , i.e.

$$\frac{s^{n+1} - s^n}{\Delta t} + \mathbf{A} \frac{1}{2} (s^{n+1} + s^n) = \mathbf{f} [s^n, t^n], \quad (6.5)$$

where time $t^n = n\Delta t$ for integer n and time-step Δt .

Consider the following experiment in which the model valve is mounted on the end of a pipe. Firstly, a steady flow is generated which includes a hovering valve plate. Secondly, the pulsation source is activated leading to a rotating hollow cylinder in the by-pass (see Fig. 5.3). In order to avoid undesired acoustical oscillations, the control valve located just downstream of the pulsation source (not drawn in Fig. 5.3) was fully closed during the generation of the steady flow. Thirdly, this control valve is opened while the hollow cylinder is rotating already. Fig. 6.10a shows a typical result of comparison between simulation and experiment. The frequency and phase angle of every mode are in good agreement, while the predicted amplitude is too large. The algebraic flow rate relation, Eq. (3.1), can be used to compare the *dynamic* flow coefficient (α based on experimentally determined $\Phi_v[t]$, $h[t]$ and $\Delta p[t]$) with the *quasi-steady* flow coefficient ($\alpha[h]$ based on experimentally determined $h[t]$), see Fig. 6.10b. In this case predicting the flow force with the quasi-steady flow assumption yields moderate to good agreement. However, the predicted flow rate through the valve by employing the quasi-steady flow assumption displays large deviations from the measured flow rate. Fig. 6.10c reveals that hysteretic changes in flow pattern should be taken into account. The hysteresis in the flow coefficient can certainly not be explained by inertial

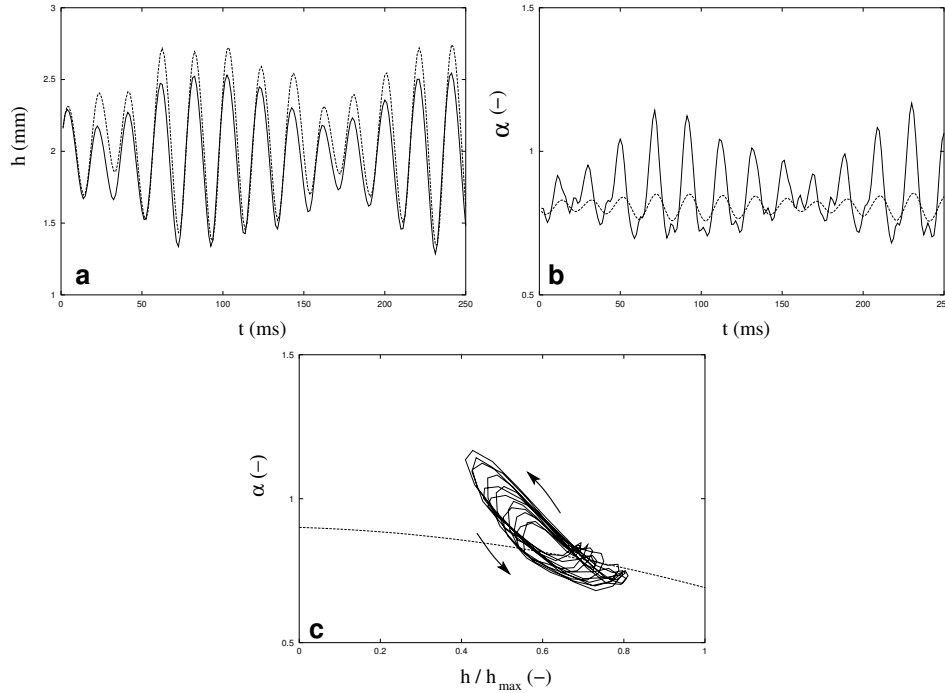


FIGURE 6.10: Validation of Basic Valve Theory: —, experiment; --, theory. (a) valve opening; (b) flow coefficient as function of time; (c) flow coefficient as function of valve opening for $t \in (0, 250)$ ms. Parameters: $\frac{\zeta}{m\Omega} = 0.12$, $\frac{k}{m\Omega^2} = 0.29$, $\frac{h_{pl}}{h_{max}} = 0.97$, $\frac{A_p}{L_g^2} = 1.20 \times 10^{-2}$, where Ω is the circular frequency of the fundamental mode of pulsation. The sampling frequency is $15.9 \frac{\Omega}{2\pi} = \frac{1}{\Delta t}$.

effects in the flow, because the Strouhal number* $St = \mathcal{O}\{10^{-3}\}$ is much too low. We expect this effect to be caused by a periodically detaching ($\alpha \approx 0.7$) and reattaching ($\alpha \approx 1.0$) separated flow from the seat. These two distinct flow regimes are sketched by Böswirth (2000) for the opening phase of a compressor valve, see Fig. 6.11. The counterclockwise direction of the hysteresis is also reported by Van Zon (1989) and Van Zon et al. (1990). The volume-flow rate during the opening stage is smaller than the one during the closing stage, i.e. $\Phi_v[h, \dot{h} > 0] < \Phi_v[h, \dot{h} < 0]$.

*The Strouhal number is based on the fundamental frequency of the flow rate, mean valve opening and mean valve outlet velocity.

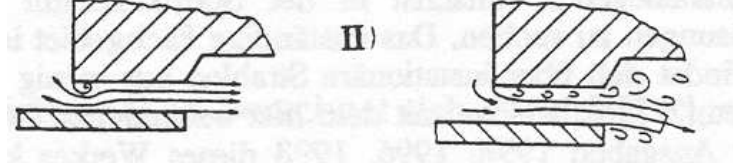


FIGURE 6.11: Flow regimes in a valve during the opening phase. A separation bubble (left) is generated on the seat and becomes longer until a jet (right) is generated. From Böswirth (2000).

In the following analysis the Basic Valve Theory is extended, referred to as the *Extended Valve Theory*, taking into account:

- the flow inertia in the valve port, i.e.

$$\Delta p = \frac{1}{2}\rho \left(\frac{\Phi_v}{\alpha L_g h} \right)^2 + \rho \frac{L_p}{A_p} \frac{d}{dt} \Phi_v, \quad (6.6)$$

- the plate speed, modulating the outlet flow rate, i.e.

$$\Phi_v = \alpha L_g h \sqrt{\frac{2}{\rho} \Delta p} - \pi (R_2^2 - R_1^2) \frac{dh}{dt}, \quad (6.7)$$

- the laminar gap flow for $h < 0.5 d_{sr}$, i.e.

$$\Delta p = \frac{6\mu}{\pi h^3} \left(\frac{d_{sr}}{R_2 - R_1} \right) \Phi_v, \quad (6.8)$$

where L_p is the axial port length, R_1 and R_2 are the inner radius and outer radius of the ring plate, respectively. The dynamic viscosity is denoted by μ and the sealing rim length is denoted by d_{sr} . Laminar flow is expected when the plate is positioned parallel to the seat at very small valve opening. Therefore the extrapolation of the fitted curves for the semi-empirical relations $c_g[h]$ and $\alpha[h]$ (Fig. 6.2) should be interpreted with care for $h/h_{max} < 0.2$. Steady flow in that region has not been obtained in the present study.

Employing the Extended Valve Theory to the conditions of Fig. 6.10 ($h/d_{sr} > 1.3$ where $d_{sr}/h_{max} = 0.3$) does not improve the predictions of the Basic Valve Theory significantly, i.e. the standard deviations are

$$\begin{aligned} \sigma[h_{BVT} - h_{EVT}]/h_{max} &= 1.3 \times 10^{-4}, \\ \sigma[\Phi_{v,BVT} - \Phi_{v,EVT}]/\Phi_{v,mean} &= 6.1 \times 10^{-4}, \end{aligned}$$

for $t \in (0, 250)$ ms. Subscript *BVT* denotes the Basic Valve Theory (Section 3.2) and subscript *EVT* denotes the Extended Valve Theory (Eqs. 6.6 - 6.8).

6.3 Model Valve versus Compressor Valve

The model valve has been designed in the parameter range (plate mass m , spring stiffness k , preload distance h_{pl} , port area A_p , sealing rim length d_{sr} and maximum valve opening h_{max}) of a commercially available compressor valve. However, several differences have been introduced (Table 6.1). The plate of the compressor valve has been coated on the downstream

TABLE 6.1: *Design differences between model valve and compressor valve.*

Item	Compressor Valve	Model Valve
port channels	convergent, multiple concentric	prismatic, single ring
valve plate	disk with holes, non-metallic	ring plate, aluminium
discharge channels	divergent	prismatic
guiding rods	two, near center	three, near pipe wall

side with an aluminium layer in order to reflect laser light with a high efficiency. The two guiding rods of the compressor valve prevent plate rotation. Plate rotation could change the flow behaviour significantly. However, for the compressor valve these rods are located at a small radius relative to the valve axis of symmetry, increasing the possibility of plate rocking (Fig. 6.12). For the compressor valve the possibility of plate jamming during operation would

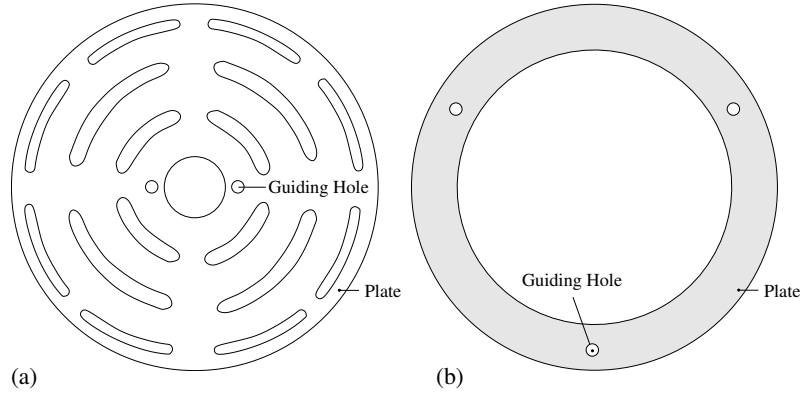


FIGURE 6.12: *Guiding holes in valve plate: (a) compressor valve, (b) model valve.*

be increased when these holes are located further away from the axis of symmetry. For both valves the plate has sharp edges at the up- and downstream side. In both cases air cannot flow through the springs. Furthermore, in contrast with the model valve, the compressor valve has slightly convergent channels in the seat and slightly divergent channels in the limiter.

Fig. 6.13 presents the steady flow effects by comparison of the semi-empirical coefficients for the two valves. The coefficients of the model were already shown in Section 6.1.1. The compressor valve has similar global properties, viz. gas force coefficient $c_g \equiv \frac{F_g}{A_p \Delta p} > 1$ (Eq. 3.4) and flow coefficient $\alpha < 1$. However, the compressor valve shows an increasing value of the gas force coefficient with increasing valve opening while the model valve shows a

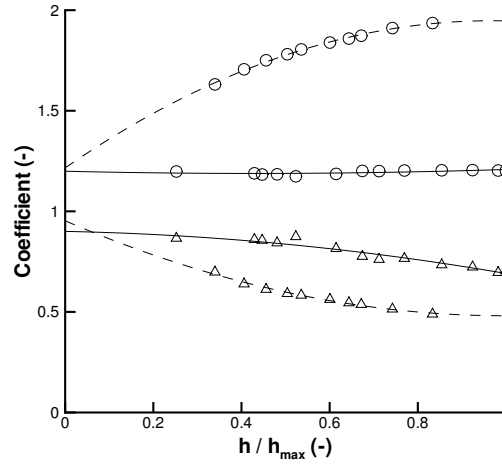


FIGURE 6.13: *Semi-empirical coefficients: —, model valve; --, compressor valve. Gas force coefficient c_g is denoted by \circ and flow coefficient α is denoted by Δ .*

constant coefficient c_g . Furthermore the vena contracta factor α is decreasing with increasing valve opening for both valves. It seems that for $h/h_{max} \rightarrow 0$ the coefficient α has the same value (≈ 0.9) for both valves. Unfortunately this limit of a steadily closing valve has not been measured (due to the onset of resonance for small valve openings). The extrapolation of α and c_g for $h/h_{max} \rightarrow 0$ is not meaningful because viscous effects become dominant.

For unsteady flow we observed severe plate obliqueness (rocking) of the compressor valve. The valve plate displacement method did not yield accurate results for the plate height. Therefore the Basic Valve Theory could not be validated and no dynamic measurements of the valve state variables Δp and Φ_v are presented. Fig. 6.14 shows typical time traces of the colliding plate of the compressor valve. It is observed that when the plate collides against the limiter (Fig. 6.14a), the light intensity method yields valve openings larger than its physical maximum, i.e. $h > h_{max}$, which is not realistic. Furthermore it is observed that when the plate collides against the seat (Fig. 6.14b), the light intensity method yields valve openings smaller than its physical minimum, i.e. $h < 0$, which is also not realistic. Both cases show that when the plate angle is large, the light intensity method needs improvement.

The unsteady flow effects are presented by comparison of the restitution coefficients during the discharge process (Table 6.2). Collisions of the plate against the limiter resulted in nearly

TABLE 6.2: *Restitution coefficients of model valve and compressor valve.*

	Compressor Valve	Model Valve
Limiter	≈ 0	0.2 ± 0.1
Seat	> 0 (rocking)	0.3 ± 0.1 (rocking)

parallel impacts for both valves. The compressor valve showed ideal behaviour ($e_{res} \approx 0$)

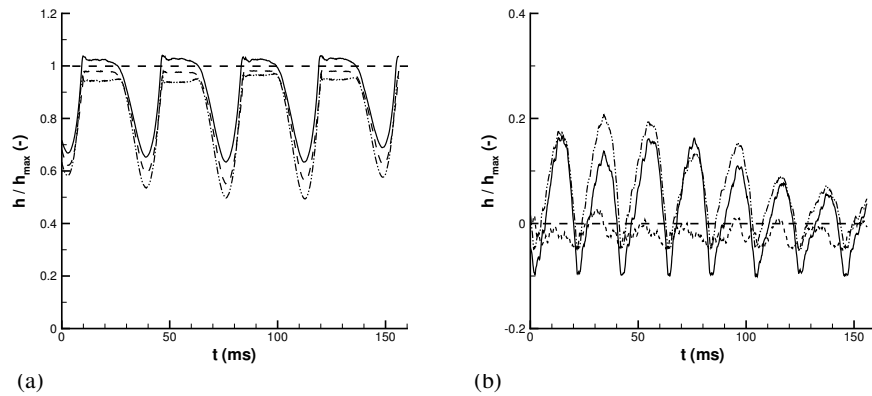


FIGURE 6.14: Collision events of compressor valve for (a) plate-limiter and (b) plate-seat. Measured time traces are shown for three glas fibers ($h_{max} = 2.42$ mm, sampling frequency is 12.8 kHz).

of nearly inelastic collisions (Fig. 6.14a). The restitution coefficient for the seat could not be determined accurately for the compressor valve because of large plate angles (Fig. 6.14b). Clearly these collisions are not inelastic. The model valve has a slightly larger restitution coefficient for its seat compared to its limiter.

It is observed that the plate has almost parallel impacts against the limiter while the impact against the seat often occurs in severe oblique plate positions. This suggests that there is an 'air cushion' between plate and limiter, that acts as a fluid damper. For the plate-seat interaction such a cushion is apparently not present. For the compressor valve the following observations enhance this hypothesis:

- Plate collisions against the limiter: The maximum plate height is reached at glas fiber, say, 1 only, while the minimum plate height is reached at glas fiber, say, 2 only (Fig. 6.14a).
- Plate collisions against the seat: The maximum plate height is alternatively reached at glas fibers 1 and 2 (Fig. 6.14b). This can be related to plate rocking in which the axis of symmetry is passing through to the two guiding holes.

Furthermore, the parallel impacts are enhanced by the large spring force acting on the plate (in opposite direction to the gas force) in case h approaches h_{max} . This spring force is decreased when the plate collides on the seat ($h = 0$).

CONCLUSIONS AND DISCUSSION



Reciprocating compressors are widely used in gas transportation, gas storage and process industries. The compressor valves are the primary cause (36%) of unscheduled compressor shutdowns (Section 1.1). Semi-empirical expressions for the dynamical response of compressor valves use the valve opening h , the pressure difference Δp across the valve and the volume-flow rate Φ_v through the valve as basic state variables (Sections 2.2 and 3.2). In the gas industry these traditional valve models are used to predict the performance of complex reciprocating compressor systems. An example (Section 3.3) has been presented where the position of a defect valve can be deduced from experimentally obtained data on pressure and temperature increments at certain monitoring positions. The goal of the present study has been twofold, i.e. i) analysis of the semi-empirical coefficients as they appear in traditional valve theories and ii) validation of the quasi-steady flow assumption by means of accurate dynamic measurements of the valve state variables.

7.1 Conclusions

Semi-Empirical Coefficients In order to be able to compare the results of different valve designs, all of the traditional valve models have been captured in a single model, which we refer to as the Basic Valve Theory (Section 3.2). The two semi-empirical coefficients involved are the flow coefficient $\alpha[h]$ (Eq. 3.1), also referred to as vena contracta factor, and the gas force coefficient $c_g[h]$ (Eq. 3.4). For the steady flow through a circular disk valve two limiting cases (Section 3.3.1) have been considered: Stokes flow and inviscid flow. For a small valve opening Stokes flow is assumed, leading to $\alpha \propto h^2$ (for given Δp) and $c_g > 0$ (independent of h). Inviscid flow analysis yields $\alpha \approx 1$ and $c_g \approx 1$.

Experiments have been conducted to determine the relationship between the semi-empirical coefficients and the valve opening (Table 7.1). Linear stability analysis of a valve interacting with its environment (Section 3.3.2) suggests that the derivatives $d\alpha/dh$ and dc_g/dh are important parameters. This is demonstrated for the case of self-excited valve vibrations due to acoustic coupling. The coefficient c_g was determined from experiments in which the valve plate is hovering, i.e. the steady gas force acting on the valve plate is balanced by the spring force. However, conducting experiments with a nearly steady flow across a hovering valve plate is not an easy task. Therefore in Table 7.1 the coefficients related to small valve openings are followed by the question mark and only the trend (increasing or decreasing value for $h > 0$) is indicated. The theory (Section 3.3.1) is only able to predict the gas force coefficient

TABLE 7.1: *Semi-empirical coefficients of several valves. CACV is a commercially available compressor valve as described in Section 6.3. In case of a range (\rightarrow) the valve opening h is assumed to increase.*

Coef- ficient	Circular disk valve (analytical)	Model valve (single ring plate)	CACV (plate with holes)	Ring plate valve (Frenkel 1969)
α	< 1 (small h) > 1 (large h)	0.9? \rightarrow 0.7	0.9? \rightarrow 0.5	0.8? \rightarrow 0.5
c_g	> 1	≈ 1.2	1.2? \rightarrow 2.0	1.0? \rightarrow 1.3

c_g correctly as a number approximately equal to one, while the vena contracta factor α cannot be predicted with uniform inviscid flow theory. The two compressor valves (i.e. CACV and ring plate valve) have gas force coefficients that increase with the valve opening. Our specially designed model valve has a constant gas force coefficient c_g . The measured vena contracta factor α for $h/h_{max} > \frac{1}{4}$ decreases with increasing valve opening h .

It is expected that when a compressor valve experiences strong backflow pulsations, or when the valve is nearly closed, flow reversal in the valve can occur. In order to estimate the flow coefficient $\alpha[h]$ for reverse flow, the valve was positioned with the limiter upstream (Section 6.1.3). The plate was *fixed* along the guiding rods. Two cases were investigated, i.e. $h/h_{max} = 0.26$ and $h/h_{max} = 0.54$. In case of flow reversal, the flow coefficient α is observed to decrease with approximately 0.2 compared to the case of normal flow direction, independently of the Reynolds number.

An alternative way of determining the semi-empirical coefficients $\alpha[h]$ and $c_g[h]$ could be the application of Computational Fluid Dynamics (e.g. Deschamps et al. 1996, Pérez-Segarra et al. 1999, Ottitsch and Scarpinato 2000). Most CFD methods employ turbulence models suitable for incompressible flow. The preconditioned Euler method (Chapter 4) as an alternative to the existing methods, has not been applied successfully in the present study. Effects of geometry, mesh, artificial dissipation, initial condition, boundary conditions and preconditioning have been explored extensively (Section 6.1.2). However, all studies resulted in numerically unstable solutions. On the other hand, this method has been applied successfully on several test cases, e.g. the steady irrotational flow around a Joukowski aerofoil and the unsteady separated flow around an inclined plate (Section 4.4). The loss of robustness in stagnation regions of the flow field has not been elaborated much in the literature (Lee 1998). In order to compute the flow in a compressor valve by application of the preconditioned Euler method, the study should be focused on the subject of local time-stepping algorithms in stagnation regions of the flow. Employing viscous flow methods including turbulence models in regions of separated flow, is expected to yield severe interpretation problems of the averaged flow quantities (e.g. Gharib 1996, Pérez-Segarra et al. 1999, Ottitsch and Scarpinato 2000). Therefore we feel that the study of valve flows by means of Direct Numerical Simulation is the only direction of research which will yield accurate results, provided that computer capacity and speed is increased significantly.

Valve Dynamics In order to validate traditional valve models for unsteady flow, accurate experiments have been realized (Chapter 5) to measure simultaneously the valve opening h , the pressure difference Δp across the valve, and the volume-flow rate Φ_v through the valve. The experimental method employed provides both the mean values of Δp and Φ_v (Section 5.5), as well as the fluctuating part of these quantities. The method achieves an accuracy of $\delta h/h_{max} < 2\%$, $\delta \Delta p/\Delta p[h_{max}] < 1\%$ and $\delta \Phi_v/\Phi_v[h_{max}] < 2\%$.

Results for unsteady flow through the model valve (Section 5.2) show that the Basic Valve Theory (Section 3.2) is able to predict the gas force acting on the valve plate reasonably accurately (Section 6.2.2). However, for a given pressure difference, the flow rate through the valve is underpredicted (Section 6.2.2). The Basic Valve Theory has been extended, taking into account flow inertia in the port, valve 'breathing', and laminar gap flow resistance (Section 3.4.2). Results show that the extended theory does not describe the fluid-structure interaction better than the Basic Valve Theory. Furthermore these results show that the model for the volume-flow rate Φ_v should be improved in order to predict the observed fluctuations and hysteresis in the vena contracta factor α of approximately 30% (Fig. 6.10c). The hysteresis in α cannot be explained by inertial effects in the flow because the Strouhal number $St = \mathcal{O}\{10^{-3}\}$ is much too low. We expect this effect to be caused by a periodically detaching and reattaching flow, separated from the seat. The fact that in our experiments extensions of the Basic Valve Theory do not significantly improve its performance cannot be generalized to actual situations in compressor valves. The large number and the large range of parameters in valve design (plate mass, spring stiffness, preload distance, geometry of valve port, etc.) has to be explored further before one can generalize our conclusions.

Collisions of the plate against the seat and the limiter are commonly modelled by means of a restitution coefficient e_{res} . Experiments with the model valve (Section 6.2.1) and a compressor valve (Section 6.3) showed that for both valves this coefficient for the limiter has a lower value than for the seat. In addition it is observed that the plate has almost parallel impacts against the limiter while the impact against the seat often occurs in severe oblique plate positions. It suggests that for the limiter there is a 'gas pocket' or 'air cushion' between plate and limiter, that acts as a fluid damper. For the plate-seat interaction such a cushion is not present. The observation of oblique plate impacts at the seat rather than at the limiter is consistent with Böswirth's hypothesis (Section 1.1).

7.2 Discussion

Limitations of the Experimental Method Compressor valves have non-parallel plate impacts during the closure events. In our experimental method the valve plate displacement method can only be applied when the plate angle θ is not large. The model valve plate, however, is forced to move nearly purely translational in which the angle θ cannot exceed approximately 0.5° . Light intensity measurements for oblique plate positions showed no significant dependence on this angle. Improving the present method by calibration of the light intensity method for oblique plate positions could be useful for compressor valves. However, preliminary calibrations showed that only a few number of plate angles could be measured, limited by the usage of feeler gauges.

Measurement of semi-empirical coefficients for small valve openings ($h/h_{max} < 0.25$) is difficult because of the coupling between valve oscillations and pipe flow acoustical modes. For small valve openings, resonance sets in and destroys the required steady valve flow. In the field of wind instrument research, often an orifice plays the role of a non-linear absorber, suppressing possible reed oscillations (Dalmont et al. 2003). The present experimental set-up could be improved (to determine $\alpha[h]$ and $c_g[h]$ for small h) by employment of this technique. Alternatively the usage of a short pipe element (i.e. a large acoustical fundamental frequency) or the implementation of damping devices (Peters 2001) could avoid valve oscillations.

The presented dynamic measurements of the valve state variables, by employment of the pulsation source by-pass in the present setup, resulted in an acoustically driven valve oscillation (Section 5.6). However, the ratio of pulsation frequency f_p and valve resonance frequency f_v could be an important parameter in valve design ($f_p/f_v = 1.9$ in Fig. 6.10). It is known from *in-situ* measurements of the cylinder pressure in a reciprocating compressor that when the piston drives the cylinder volume towards its minimum, standing waves in the cylinder gas modulate the discharge flow with a large frequency ($f_p/f_v > 1$). Note that the piston frequency is always smaller than f_v . In order to conduct experiments in a wide range of the parameter f_p/f_v , the pipe in the present setup must have a larger length because of the frequency restriction in the Two-Microphone Method (Eq. 5.19).

Future Computational Studies The Basic Valve Theory relates the valve state variables by means of semi-empirical coefficients. Although some effects of flow compressibility can be taken into account (Eq. 3.1), the valve is assumed to be an acoustically compact area. This means that valve closure events feature huge pressure peaks for given flow rates. In Section 3.3.3 it was found that the Basic Valve Theory can handle valve closures, provided that the valve environment is a compressible medium. However, whether a semi-empirical approach can be used to predict valve closing events is still an open question.

Computational studies of the flow topology through valves with moving boundaries are slowly appearing in literature (e.g. Matos et al. 1999, Nkonga 2000, Will and Flade 2003, Stijnen et al. 2004) and could be used to validate semi-empirical theories for unsteady flow situations. From the upcoming algorithms handling moving boundaries (e.g. fixed mesh methods (Lattice Boltzmann, Level Set, Cartesian Cut-Cell), moving mesh methods (Arbitrary Euler-Lagrange), vortex methods (no mesh at all) and space-time discontinuous Galerkin methods) only a few studies have been published dealing with the fully closing event of a valve (e.g. Stijnen et al. 2004). When applying Finite-Volume, Finite-Element or Finite-Difference methods to the problem of closing valves, one has to deal with a collapsing mesh.

A pilot study for the present research revealed that a Finite-Difference integrated space-time method cannot be applied for vanishing domains (Van den Berg 2002). The CFL-condition induces the computation time to increase without bound. Finite-Volume- and Finite-Element integrated space-time methods are capable of handling vanishing domains, provided that the unstructured mesh has a high quality.

The results for the model valve suggest that the gas force acting on the plate can be considered to be a quasi-steady force, while the flow rate does not behave quasi-steadily. This could explain why research engineers in the compressor community have difficulties predicting the valve impact speeds $\dot{h}[t^\pm]$, while the trend of valve opening $h[t]$ can be predicted rather accurately. Moreover, impact speeds should be key parameters in valve design, rather than effective flow area solely. In the literature (Section 2.2.2) differences are reported in computational results for the computed valve flow force and the effective flow area employing different turbulence models. Therefore if valve dynamics cannot be predicted accurately with semi-empirical theories, valve dynamics provide a fine challenge.

Future Flow Regime Studies In the present study a model valve (reflecting basic properties of a compressor valve) has been designed to investigate the flow by means of analytical, computational and experimental methods. We learned that the geometry of such a model valve must be simplified considerably in order to be able to study the fluid dynamical effects of valves over a wide range of parameters. Therefore we propose a future line of research in which the flow regime is subject of interest, rather than the flow force acting on the plate. It is recommended that the model valve is designed such that the flow can be approximated as a planar 2D flow (similar *Ansatz* as Horsten (1990)). This would allow convenient comparison with analytical/numerical predictions of the flow properties. Additionally, forcing the plate motion with a truly single-degree of freedom could be accomplished more easily (e.g. guiding rails) than for the present model valve. When different experiments are performed for i) a fixed plate with a pipe flow pulsation source, and ii) a forced-oscillating plate without pipe flow pulsation source, effects of the valve flow inertia and the plate speed momentum injection could be decoupled. Additionally, the case in which the valve opening becomes of the order of the sealing rim length ($h \approx d_{sr}$) can be considered accurately. The flow regime is expected to change due to reattachment of the separated shear layer. The influence of the driving frequency on this effect (vena contracta factor) is at present not known.

The recovery of plate kinetic energy after collision with the limiter is lower than for the case of collision with the seat (see e.g. Fig. 6.14). This effect could be related to the presence of an 'air cushion' between plate and limiter. Similar to the work of Deverge et al. (2003) one could apply the equation for conservation of mass and the Bernoulli equation for unsteady flow. This yields the pressure distribution in the gap between plate and limiter. Integrating the pressure over the plate surface yields the gas force acting on the plate. This force depends on the sign of the plate motion ($sign[\dot{h}]$) because of the direction of the jet flow separated from the edges of plate and limiter. Comparison of the plate motion obtained from measurement with that obtained from theory could fortify the arguments for the presence of an 'air cushion'.

NEARLY INCOMPRESSIBLE FLOW



This appendix shows that in case of low Mach number flow, the Euler equations reduce to the incompressible inviscid flow equations. The first section follows the textbook approach of Kundu (1990), while the second section follows the elaborated approach of Guillard and Viozat (1999).

A.1 Local Mach Number

Compressibility effects are determined by the magnitude of the local Mach number, defined as

$$M = \frac{u}{c}, \quad (\text{A.1})$$

where u is the magnitude of the local speed of the flow, and c is the local speed of sound given by

$$c^2 = \left(\frac{\partial p}{\partial \rho} \right)_S, \quad (\text{A.2})$$

where the subscript S signifies that the partial derivative is taken at constant entropy. To assess how large the local Mach number has to be for the compressibility effects to be appreciable in a steady flow, consider the 1D continuity equation for steady flow, i.e.

$$u \frac{\partial \rho}{\partial x} + \rho \frac{\partial u}{\partial x} = 0. \quad (\text{A.3})$$

The incompressibility assumption requires that

$$\left| u \frac{\partial \rho}{\partial x} \right| \ll \left| \rho \frac{\partial u}{\partial x} \right| \Rightarrow \left| \frac{\delta \rho}{\rho} \right| \ll \left| \frac{\delta u}{u} \right|. \quad (\text{A.4})$$

Pressure variations can be estimated from the definition of c , giving

$$\delta p \sim c^2 \delta \rho. \quad (\text{A.5})$$

Conservation of momentum of the inviscid steady flow requires that

$$u \delta u \sim \frac{\delta p}{\rho}. \quad (\text{A.6})$$

Combining Eqs. (A.5) and (A.6), we obtain

$$\frac{\delta\rho}{\rho} \sim \frac{u^2}{c^2} \frac{\delta u}{u}. \quad (\text{A.7})$$

Finally, comparing Eqs. (A.4) and (A.7), we find that variations in the density are negligible if

$$M^2 \ll 1. \quad (\text{A.8})$$

A.2 Global Mach Number

In order to assess whether the governing equations for *unsteady 3D* inviscid flows can be reduced to the governing equations for incompressible flows, we start with the Euler equations for a calorically perfect gas, i.e.

$$\frac{\partial}{\partial t}\rho + \nabla \cdot (\rho\mathbf{u}) = 0, \quad (\text{A.9})$$

$$\frac{\partial}{\partial t}(\rho\mathbf{u}) + \nabla \cdot (\rho\mathbf{u}\mathbf{u}) + \nabla p = 0, \quad (\text{A.10})$$

$$\frac{\partial}{\partial t}(\rho E) + \nabla \cdot (\rho\mathbf{u}E + \mathbf{u}p) = 0, \quad (\text{A.11})$$

$$p = (\gamma - 1)\rho \left[E - \frac{1}{2}\mathbf{u} \cdot \mathbf{u} \right], \quad (\text{A.12})$$

where the closed system of equations has the unknowns $\{\rho, \mathbf{u}, p, E\}$. The second step consists of non-dimensionalization of these equations with the dimensional reference quantities $\{\rho^*, u^*, \rho^*(a^*)^2, (a^*)^2\}$, respectively. The reference length scale is δ^* and the reference time scale is δ^*/u^* . These scales are the maximum values of the initial condition, where the speed of sound a^* is determined from $(a^*)^2 = \gamma \max[p(\mathbf{x}, t = 0)]/\rho^*$. When we substitute these scales into the Euler equations, and denote the non-dimensional variables with a tilde, the following set of equations is obtained,

$$\frac{\partial}{\partial \tilde{t}}\tilde{\rho} + \tilde{\nabla} \cdot (\tilde{\rho}\tilde{\mathbf{u}}) = 0, \quad (\text{A.13})$$

$$\frac{\partial}{\partial \tilde{t}}(\tilde{\rho}\tilde{\mathbf{u}}) + \tilde{\nabla} \cdot (\tilde{\rho}\tilde{\mathbf{u}}\tilde{\mathbf{u}}) + \frac{1}{M_*^2}\tilde{\nabla}\tilde{p} = 0, \quad (\text{A.14})$$

$$\frac{\partial}{\partial \tilde{t}}(\tilde{\rho}\tilde{E}) + \tilde{\nabla} \cdot (\tilde{\rho}\tilde{\mathbf{u}}\tilde{E} + \tilde{\mathbf{u}}\tilde{p}) = 0, \quad (\text{A.15})$$

$$\tilde{p} = (\gamma - 1)\tilde{\rho} \left[\tilde{E} - \frac{1}{2}M_*^2\tilde{\mathbf{u}} \cdot \tilde{\mathbf{u}} \right], \quad (\text{A.16})$$

where $M_* = u^*/a^*$ is the global (reference) Mach number. The third step is the asymptotic expansion of the solution in powers of the Mach number M_* , for $M_* \rightarrow 0$, i.e.

$$\begin{pmatrix} \tilde{\rho} \\ \tilde{\mathbf{u}} \\ \tilde{p} \\ \tilde{E} \end{pmatrix} = \begin{pmatrix} \tilde{\rho}_0 \\ \tilde{\mathbf{u}}_0 \\ \tilde{p}_0 \\ \tilde{E}_0 \end{pmatrix} + M_* \begin{pmatrix} \tilde{\rho}_1 \\ \tilde{\mathbf{u}}_1 \\ \tilde{p}_1 \\ \tilde{E}_1 \end{pmatrix} + M_*^2 \begin{pmatrix} \tilde{\rho}_2 \\ \tilde{\mathbf{u}}_2 \\ \tilde{p}_2 \\ \tilde{E}_2 \end{pmatrix} + \mathcal{O}(M_*^3) \quad (\text{A.17})$$

When this expansion of the solution is substituted in the non-dimensional Euler equations, terms with the same order of M_* can be collected, yielding

- Order $\mathcal{O}(M_*^{-2})$:

$$\tilde{\nabla} \tilde{p}_0 = 0, \quad (\text{A.18})$$

- Order $\mathcal{O}(M_*^{-1})$:

$$\tilde{\nabla} \tilde{p}_1 = 0, \quad (\text{A.19})$$

- Order $\mathcal{O}(1)$:

$$\frac{\partial}{\partial \tilde{t}} \tilde{\rho}_0 + \tilde{\nabla} \cdot (\tilde{\rho}_0 \tilde{\mathbf{u}}_0) = 0, \quad (\text{A.20})$$

$$\frac{\partial}{\partial \tilde{t}} (\tilde{\rho}_0 \tilde{\mathbf{u}}_0) + \tilde{\nabla} \cdot (\tilde{\rho}_0 \tilde{\mathbf{u}}_0 \tilde{\mathbf{u}}_0) + \tilde{\nabla} \tilde{p}_2 = 0, \quad (\text{A.21})$$

$$\frac{\partial}{\partial \tilde{t}} (\tilde{\rho}_0 \tilde{E}_0) + \tilde{\nabla} \cdot (\tilde{\rho}_0 \tilde{\mathbf{u}}_0 \tilde{E}_0 + \tilde{\mathbf{u}}_0 \tilde{p}_0) = 0, \quad (\text{A.22})$$

$$\tilde{p}_0 = (\gamma - 1) \tilde{\rho}_0 \tilde{E}_0, \quad (\text{A.23})$$

- Order $\mathcal{O}(M_*)$:

$$\frac{\partial}{\partial \tilde{t}} \tilde{\rho}_1 + \tilde{\nabla} \cdot (\tilde{\rho}_0 \tilde{\mathbf{u}}_1 + \tilde{\rho}_1 \tilde{\mathbf{u}}_0) = 0, \quad (\text{A.24})$$

$$\frac{\partial}{\partial \tilde{t}} (\tilde{\rho}_0 \tilde{\mathbf{u}}_1 + \tilde{\rho}_1 \tilde{\mathbf{u}}_0) + \tilde{\nabla} \cdot (\tilde{\rho}_0 \tilde{\mathbf{u}}_0 \tilde{\mathbf{u}}_1 + \tilde{\rho}_0 \tilde{\mathbf{u}}_1 \tilde{\mathbf{u}}_0 + \tilde{\rho}_1 \tilde{\mathbf{u}}_0 \tilde{\mathbf{u}}_0) + \tilde{\nabla} \tilde{p}_3 = 0, \quad (\text{A.25})$$

$$\begin{aligned} \frac{\partial}{\partial \tilde{t}} (\tilde{\rho}_0 \tilde{E}_1 + \tilde{\rho}_1 \tilde{E}_0) + \tilde{\nabla} \cdot (\tilde{\rho}_0 \tilde{\mathbf{u}}_0 \tilde{E}_1 + \tilde{\rho}_0 \tilde{\mathbf{u}}_1 \tilde{E}_0 + \\ \tilde{\rho}_1 \tilde{\mathbf{u}}_0 \tilde{E}_0 + \tilde{\mathbf{u}}_0 \tilde{p}_1 + \tilde{\mathbf{u}}_1 \tilde{p}_0) = 0, \end{aligned} \quad (\text{A.26})$$

$$\tilde{p}_1 = (\gamma - 1) \left[\tilde{\rho}_0 \tilde{E}_1 + \tilde{\rho}_1 \tilde{E}_0 \right]. \quad (\text{A.27})$$

Eqs. (A.18) and (A.19) imply that the pressure is constant in space up to variations of $\mathcal{O}(M_*^2)$, i.e.

$$\tilde{p}(\tilde{\mathbf{x}}, \tilde{t}) = \mathcal{P}(\tilde{t}) + M_*^2 \tilde{p}_2(\tilde{\mathbf{x}}, \tilde{t}). \quad (\text{A.28})$$

The final step is to assume an open boundary, where the pressure is constant, i.e. $\tilde{p}(\tilde{\mathbf{x}}_b, \tilde{t}) = \tilde{p}_b$. For $M_* \rightarrow 0$ this means $\frac{\partial}{\partial \tilde{t}} \mathcal{P} = 0$ and additionally $\frac{\partial}{\partial \tilde{t}} \tilde{p}_0 = 0$. When the latter is used together with Eq. (A.18), the order $\mathcal{O}(1)$ equation of state Eq. (A.23) yields

$$\frac{\partial}{\partial \tilde{t}} (\tilde{\rho}_0 \tilde{E}_0) = \frac{1}{\gamma - 1} \frac{\partial}{\partial \tilde{t}} \tilde{p}_0 = 0, \quad (\text{A.29})$$

$$\nabla(\tilde{\rho}_0 \tilde{E}_0) = \frac{1}{\gamma - 1} \nabla \tilde{p}_0 = 0. \quad (\text{A.30})$$

Combining these results with the order $\mathcal{O}(1)$ energy equation Eq. (A.22), yields the constraint

$$\tilde{\nabla} \cdot \tilde{\mathbf{u}}_0 = 0. \quad (\text{A.31})$$

We conclude by the following summary: In the limiting case of $M_* \rightarrow 0$, the Euler equations reduce to the equations for incompressible flow,

$$\tilde{\nabla} \cdot \tilde{\mathbf{u}} = 0, \tag{A.32}$$

$$\frac{\partial}{\partial t} \tilde{\mathbf{u}} + (\tilde{\mathbf{u}} \cdot \tilde{\nabla}) \tilde{\mathbf{u}} = \frac{-1}{\tilde{\rho}} \tilde{\nabla} \tilde{p}, \tag{A.33}$$

where the pressure variations are constant in space up to $\mathcal{O}(M_*^2)$.

TWO-STAGE AIR COMPRESSOR



This appendix presents the governing equations of the two-stage compressor system as discussed in Section 3.5. For convenience, the complete nomenclature for these equations is presented first.

B.1 Nomenclature

A	cross-sectional area
A_p	port area
c_g	gas force coefficient
D_i	pipe diameter
e_{res}	restitution coefficient
F	gas force
h	valve opening
k	spring constant
L	pipe length
L_g	valve gap length
m	mass in cylinder
m_v	effective plate mass
p	pressure
R	perfect gas constant
T	absolute temperature
t	time
V	volume
x	dynamic displacement of piston

Greek Symbols

α	flow coefficient
γ	ratio of specific heats
ΔL_g	reducing gap length
ζ	valve damping coefficient
λ	wall friction factor
ρ	density
Φ	<i>mass</i> -flow rate
ω	circular frequency of piston

Subscripts and Notations

<i>cyl</i>	cylinder
<i>d</i>	discharge
<i>dc</i>	discharge chamber
<i>i</i>	intercooler
<i>id</i>	downstream of intercooler
<i>iu</i>	upstream of intercooler
<i>max</i>	maximum value
<i>min</i>	minimum value
<i>pl</i>	preload
<i>s</i>	suction
<i>sc</i>	suction chamber
<i>w</i>	cooling water
1, 2	stage 1 or 2
\pm	before (-) or after (+) collision
$[\dots]$	functional argument
$sign[arg]$	$sign = +1$ when $arg > 0$, else $sign = -1$

B.2 Governing Equations

Cylinders The pistons are considered to move harmonically (crank rod length \ll piston rod length), i.e.

$$x_1 = \frac{V_{cyl1} - 2V_{min1}}{2A_{cyl1}} \sin[\omega t], \quad (\text{B.1})$$

$$V_1 = \frac{1}{2}V_{cyl1} - A_{cyl1}x_1, \quad (\text{B.2})$$

for the stage-one compressor, and

$$x_2 = \frac{V_{cyl2} - 2V_{min2}}{2A_{cyl2}} \sin[\omega t], \quad (\text{B.3})$$

$$V_2 = \frac{1}{2}V_{cyl2} + A_{cyl2}x_2, \quad (\text{B.4})$$

for the stage-two compressor. The air is considered to be a calorically perfect gas. The flow of air in the cylinders is modelled by application of the conservation of mass and energy, i.e.

$$\frac{d}{dt}m_1 = \Phi_{s1} - \Phi_{d1}, \quad (\text{B.5})$$

$$\frac{d}{dt}p_1 = \frac{\gamma}{V_1} \left(\frac{p_{sc1}}{\rho_{sc1}} \Phi_{s1} - \frac{p_1}{\rho_1} \Phi_{d1} - p_1 \frac{d}{dt}V_1 \right), \quad (\text{B.6})$$

$$\rho_1 = \frac{m_1}{V_1}, \quad (\text{B.7})$$

for the stage-one compressor, and

$$\frac{d}{dt}m_2 = \Phi_{s2} - \Phi_{d2}, \quad (\text{B.8})$$

$$\frac{d}{dt}p_2 = \frac{\gamma}{V_2} \left(\frac{p_{sc2}}{\rho_{sc2}} \Phi_{s2} - \frac{p_2}{\rho_2} \Phi_{d2} - p_2 \frac{d}{dt}V_2 \right), \quad (\text{B.9})$$

$$\rho_2 = \frac{m_2}{V_2}, \quad (\text{B.10})$$

for the stage-two compressor. In the energy balance the kinetic energy of the gas is neglected and heat exchange between the gas and piston or cylinder walls is ignored. Adiabatic reversible processes are assumed, thus the isentropic flow state is changed by i) the work transferred by the piston to the gas, and ii) the flow through the valves. In an operating compressor, flow in directions opposite to the arrows in Fig. 3.16 may be present. In such cases of reverse flow the energy equations (B.6) and (B.9) are modified with the proper upstream pressure and upstream density.

Valve Dynamics The valves are considered as mass-spring systems with a single degree of freedom, i.e.

$$\begin{cases} m_v \frac{d^2}{dt^2} h_{s1} + \zeta \frac{d}{dt} h_{s1} + k(h_{pl} + h_{s1}) = F_{s1} & , \quad 0 < h_{s1} < h_{max} \\ \frac{d}{dt} h_{s1}[t_+] = -e_{res} \frac{d}{dt} h_{s1}[t_-] & , \quad h_{s1}[t_{\pm}] \in \{0, h_{max}\} \end{cases} \quad (\text{B.11})$$

$$\begin{cases} m_v \frac{d^2}{dt^2} h_{d1} + \zeta \frac{d}{dt} h_{d1} + k(h_{pl} + h_{d1}) = F_{d1} & , \quad 0 < h_{d1} < h_{max} \\ \frac{d}{dt} h_{d1}[t_+] = -e_{res} \frac{d}{dt} h_{d1}[t_-] & , \quad h_{d1}[t_{\pm}] \in \{0, h_{max}\} \end{cases} \quad (\text{B.12})$$

$$\begin{cases} m_v \frac{d^2}{dt^2} h_{s2} + \zeta \frac{d}{dt} h_{s2} + k(h_{pl} + h_{s2}) = F_{s2} & , \quad 0 < h_{s2} < h_{max} \\ \frac{d}{dt} h_{s2}[t_+] = -e_{res} \frac{d}{dt} h_{s2}[t_-] & , \quad h_{s2}[t_{\pm}] \in \{0, h_{max}\} \end{cases} \quad (\text{B.13})$$

$$\begin{cases} m_v \frac{d^2}{dt^2} h_{d2} + \zeta \frac{d}{dt} h_{d2} + k(h_{pl} + h_{d2}) = F_{d2} & , \quad 0 < h_{d2} < h_{max} \\ \frac{d}{dt} h_{d2}[t_+] = -e_{res} \frac{d}{dt} h_{d2}[t_-] & , \quad h_{d2}[t_{\pm}] \in \{0, h_{max}\} \end{cases} \quad (\text{B.14})$$

where the restitution coefficient e_{res} represents the semi-empirical description of the collision events between valve plate and structure (seat or limiter). The gas force acting on the valve plate is expressed as

$$F_{s1} = c_g[h_{s1}]A_p(p_{sc1} - p_1), \quad (\text{B.15})$$

$$F_{d1} = c_g[h_{d1}]A_p(p_1 - p_{dc1}), \quad (\text{B.16})$$

$$F_{s2} = c_g[h_{s2}]A_p(p_{sc2} - p_2), \quad (\text{B.17})$$

$$F_{d2} = c_g[h_{d2}]A_p(p_2 - p_{dc2}), \quad (\text{B.18})$$

where the gas force coefficient c_g is a semi-empirical function of the valve opening. The mass-flow rate through the valves is expressed as

$$\Phi_{s1} = \alpha[h_{s1}]L_g h_{s1} \sqrt{2\rho_{sc1}|p_{sc1} - p_1|} \text{sign}[p_{sc1} - p_1], \quad (\text{B.19})$$

$$\Phi_{d1} = \alpha[h_{d1}]L_g h_{d1} \sqrt{2\rho_1|p_1 - p_{dc1}|} \text{sign}[p_1 - p_{dc1}], \quad (\text{B.20})$$

$$\Phi_{s2} = \alpha[h_{s2}]L_g h_{s2} \sqrt{2\rho_{sc2}|p_{sc2} - p_2|} \text{sign}[p_{sc2} - p_2], \quad (\text{B.21})$$

$$\Phi_{d2} = \alpha[h_{d2}]L_g h_{d2} \sqrt{2\rho_2|p_2 - p_{dc2}|} \text{sign}[p_2 - p_{dc2}], \quad (\text{B.22})$$

where the flow coefficient α is a semi-empirical function of the valve opening.

Plenum Chambers Conservation of mass applied to the air in the plenum chambers (situated adjacent to the cylinders to suppress pulsations) yield,

$$\frac{d}{dt}\rho_{sc1} = \frac{1}{V_{sc1}} (\Phi_s - \Phi_{s1}), \quad (\text{B.23})$$

$$\frac{d}{dt}\rho_{dc1} = \frac{1}{V_{dc1}} (\Phi_{d1} - \Phi_i), \quad (\text{B.24})$$

$$\frac{d}{dt}\rho_{sc2} = \frac{1}{V_{sc2}} (\Phi_i - \Phi_{s2}), \quad (\text{B.25})$$

$$\frac{d}{dt}\rho_{dc2} = \frac{1}{V_{dc2}} (\Phi_{d2} - \Phi_d). \quad (\text{B.26})$$

Conservation of energy applied to the air in the plenum chambers yield,

$$\frac{d}{dt}p_{sc1} = \frac{\gamma}{V_{sc1}} \left(\frac{p_s}{\rho_s} \Phi_s - \frac{p_{sc1}}{\rho_{sc1}} \Phi_{s1} \right), \quad (\text{B.27})$$

$$\frac{d}{dt}p_{dc1} = \frac{\gamma}{V_{dc1}} \left(\frac{p_1}{\rho_1} \Phi_{d1} - \frac{p_{dc1}}{\rho_{dc1}} \Phi_i \right), \quad (\text{B.28})$$

$$\frac{d}{dt}p_{sc2} = \frac{\gamma}{V_{sc2}} \left(\frac{p_{i2}}{\rho_{id}} \Phi_i - \frac{p_{sc2}}{\rho_{sc2}} \Phi_{s2} \right), \quad (\text{B.29})$$

$$\frac{d}{dt}p_{dc2} = \frac{\gamma}{V_{dc2}} \left(\frac{p_2}{\rho_2} \Phi_{d2} - \frac{p_{dc2}}{\rho_{dc2}} \Phi_d \right). \quad (\text{B.30})$$

For reverse flow, the remarks on Eqs. (B.6) and (B.9) are valid for Eqs. (B.27) - (B.30) too. Incompressible flow through an orifice is considered when the gas enters at the suction chambers and the gas leaves the discharge chambers, i.e.

$$\Phi_s = \alpha_s A_s \sqrt{2\rho_s |p_s - p_{sc1}|} \text{sign}[p_s - p_{sc1}], \quad (\text{B.31})$$

$$\Phi_i = \alpha_i A_i \sqrt{2\rho_{dc1} |p_{dc1} - p_{i1}|} \text{sign}[p_{dc1} - p_{i1}], \quad (\text{B.32})$$

$$\Phi_i = \alpha_i A_i \sqrt{2\rho_{id} |p_{i2} - p_{sc2}|} \text{sign}[p_{i2} - p_{sc2}], \quad (\text{B.33})$$

$$\Phi_d = \alpha_d A_d \sqrt{2\rho_{dc2} |p_{dc2} - p_d|} \text{sign}[p_{dc2} - p_d]. \quad (\text{B.34})$$

Effects of compressibility can be taken into account by multiplication of the flow rates with $1 - \frac{1}{\gamma} \frac{\Delta p}{p_{up}}$, where Δp is the pressure difference and p_{up} is the upstream pressure.

Piping System and Intercooler Air is flowing from the discharge chamber of stage one to the intercooler through a pipeline. After heat exchange in the intercooler the air is flowing from the intercooler, through another pipeline, to the suction chamber of stage two. The pipe flow is assumed to be an incompressible one-dimensional flow, i.e.

$$p_{i1} - p_{iu} = \frac{L_{iu}}{A_i} \frac{d}{dt} \Phi_i + \lambda \frac{L_{iu}}{D_i} \frac{1}{2\rho_{dc1}} \left(\frac{\Phi_i}{A_i} \right)^2 \text{sign}[\Phi_i], \quad (\text{B.35})$$

$$p_{id} - p_{i2} = \frac{L_{id}}{A_i} \frac{d}{dt} \Phi_i + \lambda \frac{L_{id}}{D_i} \frac{1}{2\rho_{id}} \left(\frac{\Phi_i}{A_i} \right)^2 \text{sign}[\Phi_i], \quad (\text{B.36})$$

where the time-derivative term represents the flow inertia and λ is the wall friction factor. The intercooler consists of a tube bundle with counter-current flowing cold water. It is assumed that the pressure difference of the air flow is negligible during the intercooling. According to the perfect gas law, then the product of density and absolute temperature is constant. Therefore heat exchange from the hot air to the cold water is increasing the density of the air, i.e.

$$p_{iu} = p_{id}, \quad (\text{B.37})$$

$$\rho_{id} = \frac{p_{iu}}{RT_w}. \quad (\text{B.38})$$

B.3 Input Parameters

0.89×10^{-3}	V_{min1}	minimum volume cylinder 1	(m ³)
0.31×10^{-3}	V_{min2}	minimum volume cylinder 2	(m ³)
10.0×10^{-3}	V_{cyl1}	total volume cylinder 1	(m ³)
3.5×10^{-3}	V_{cyl2}	total volume cylinder 2	(m ³)
0.343	D_{cyl1}	diameter of cylinder 1	(m)
0.203	D_{cyl2}	diameter of cylinder 2	(m)
12.5	$\omega/2\pi$	frequency of piston	(Hz)
50×10^{-3}	m_v	valve plate effective mass	(kg)
0.0	ζ	valve damping constant	(kg/s)
5000	k	valve spring constant	(N/m)
5.0×10^{-3}	h_{pl}	valve preload distance	(m)
1.0×10^{-3}	h_{max}	valve maximum opening	(m)
0.1	e_{res}	valve restitution coefficient	(-)
1.2	c_g	valve gas force coefficient	(-)
0.6	α	valve flow rate coefficient	(-)
34.0×10^{-4}	A_p	valve port area	(m ²)
1.4	L_g	valve gap length	(m)
0.14	ΔL_g	defect valve gap length removal	(m)
1.0×10^5	p_s	suction pressure	(Pa)
293.15	T_s	suction temperature	(K)
8.0×10^5	p_d	discharge pressure	(Pa)
10.0×10^{-3}	V_{sc1}	volume suction chamber 1	(m ³)
20.0×10^{-3}	V_{dc1}	volume discharge chamber 1	(m ³)
20.0×10^{-3}	V_{sc2}	volume suction chamber 2	(m ³)
20.0×10^{-3}	V_{dc2}	volume discharge chamber 2	(m ³)
0.8	α_i	orifice flow rate coefficient	(-)
2.0×10^{-2}	D_{or}	orifice diameter	(m)
297.15	T_w	temperature cooling water	(K)
1.0	L_i	pipe length ic/compr (>0)	(m)
2.2×10^{-2}	D_i	pipe diameter ic/compr	(m)
1.4	γ	ratio of specific heats	(-)
287.0	R	ideal gas constant	(J/kgK)
8.0×10^{-6}	Δt	time-step	(s)

VENA CONTRACTA



C.1 Theory

The vena contracta effect causes a jet flow through the aperture, formed by the sharp edges of seat and plate, which has a cross-sectional area that is smaller than the aperture itself. The flow coefficient α was defined in Eq. (3.1) and is also referred to as contraction ratio, vena contracta- coefficient/factor/parameter. In order to investigate the influence of both the geometry and compressibility on this coefficient, this section considers the 2D planar flow through a diaphragm (Fig. C.1). In this case we will define the vena contracta factor as the

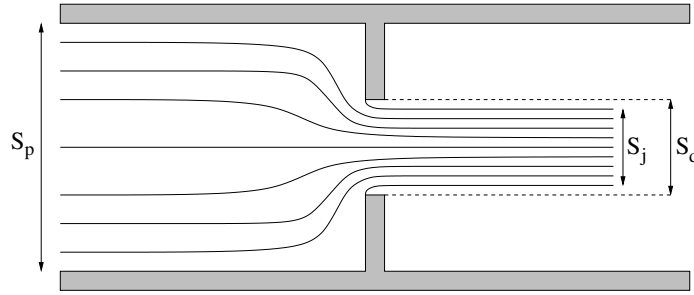


FIGURE C.1: Sketch of streamlines of the planar flow through a diaphragm.

ratio of the jet area S_j and the diaphragm area S_d , i.e.

$$\alpha\left[\frac{S_d}{S_p}, M_j\right] = \frac{S_j}{S_d}, \quad (\text{C.1})$$

where this coefficient is a function of both the confinement ratio (diaphragm area S_d over channel (pipe) area S_p) and the jet Mach number M_j .

Busemann (1937) employed the hodograph method for an incompressible planar flow and derived an implicit expression for the contraction ratio $\alpha_0 \equiv \alpha\left[\frac{S_d}{S_p}, 0\right]$, i.e.

$$\alpha_0 = \frac{\pi}{\pi + 2 \left(\frac{1}{\alpha_0} \frac{S_p}{S_d} - \alpha_0 \frac{S_d}{S_p} \right) \arctan\left[\alpha_0 \frac{S_d}{S_p}\right]}. \quad (\text{C.2})$$

The solution of Kirchhoff is found as the asymptotic solution by taking the limit of $S_d \ll S_p$. This case resembles the incompressible flow through a hole in an infinitely extended thin plate, resulting in $\alpha_0 = \frac{\pi}{\pi+2} \approx 0.61$. The solution of the implicit expression Eq. (C.2) is shown in Fig. C.2. Note that for $\frac{S_d}{S_p} < 0.2$ Kirchhoff's result provides a good approximation.

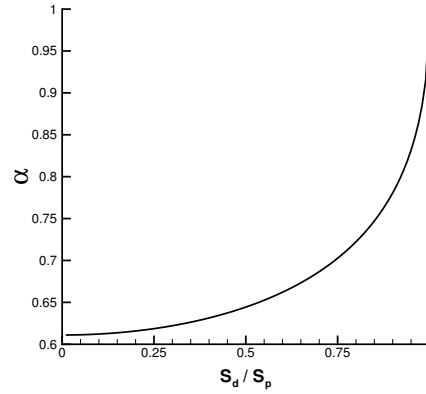


FIGURE C.2: Contraction ratio $\alpha[\frac{S_d}{S_p}, 0]$ as function of the ratio of diaphragm area and pipe cross-section (Eq. C.2).

Furthermore the limit of $\frac{S_d}{S_p} = 1$ in Eq. (C.2) yields the trivial solution of a uniform flow, i.e. $\alpha_0 = 1$. In case of an axi-symmetric incompressible flow through a diaphragm in an infinitely extended thin plate the vena contracta factor is only slightly smaller than in case of planar flow. Bloch (1969) found $\alpha_0 = 0.59$ for axi-symmetric flow, while Kirchhoff's result is 0.61 for planar flow.

In order to take into account effects of compressibility, several approaches are presented in literature (e.g. Hofmans 1998). Chaplygin derived an exact solution for the planar compressible flow through a hole in a thin plate ($\frac{S_d}{S_p} \ll 1$) by employing the hodograph method (Sears 1954). This solution is shown in Fig. C.3. The limit of $M_j = 0$ yields the incompressible flow solution of Kirchhoff.

In order to approximate the general solution Hofmans (1998) proposed an interpolation between the solutions of Busemann (1937) and (Sears 1954), i.e.

$$\alpha[\frac{S_d}{S_p}, M_j] = \alpha[\frac{S_d}{S_p}, 0] + \alpha[0, M_j] - \alpha[0, 0], \quad (\text{C.3})$$

where the last term is the famous result of Kirchhoff, i.e. $\alpha[0, 0] = \frac{\pi}{\pi+2}$.

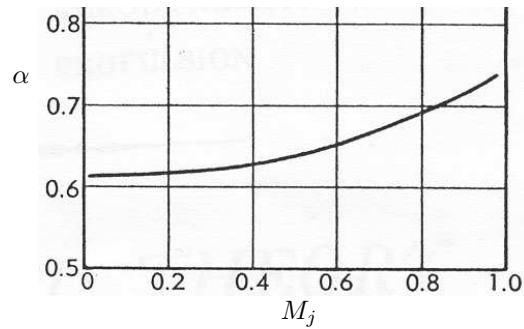


FIGURE C.3: Contraction ratio $\alpha[0, M_j]$ as function of the jet Mach number for the flow through a hole in an infinitely extended thin plate. From Sears (1954).

C.2 Computational Fluid Dynamics

For arbitrary Mach number and arbitrary diaphragm opening the preconditioned Euler method (Chapter 4) seems to be suited for testing the hypothesis of Eq. (C.3). Local preconditioning is necessary because i) the local Mach number in the whole domain is expected to vary significantly for high jet Mach number flow, and ii) the minimum local Mach number could be extremely low.

In the present computational study, numerically stable solutions have **not** been obtained. Some of the difficulties in this study are illustrated in the following. In order to save computation time the computational domain will be defined as the upper half in Fig. C.1, since the solution is expected to be symmetrical. The numerical solution of the flow through the diaphragm intended to become unsteady by means of vortex shedding. Rather than a diaphragm, a stepwise convergent channel has been considered. Figs. C.4 and C.5 show the formation of the jet and the artificial recirculation region from the sharp edge. During the local time-stepping procedure this region propagates towards the outlet boundary. As soon as the outlet flow reverses an additional boundary condition of zero speed is applied.

Section 6.1.2 presents a computational study for the flow through the model valve. Effects of geometry, mesh, artificial dissipation, initial condition, boundary condition and preconditioning have been explored extensively. Unfortunately, solutions with sufficient accuracy have not been obtained. However, the flow around a 70° inclined plate has been computed successfully (Section 4.4). In order to investigate the applicability of the preconditioned Euler method for computing valve flows, in the following several flow configurations are considered. Figs. C.6 and C.7 present the result of the local time-stepping algorithm applied for the case of the external flow around a 90° inclined plate. Figs. C.8 and C.9 present the result of the local time-stepping algorithm applied to the internal flow in a valve configuration. This configuration is adapted from the preceding case by inclusion of a port ($h/d_{sr} = 3$ and $L/d_{sr} = 15$, where L is the plate length).

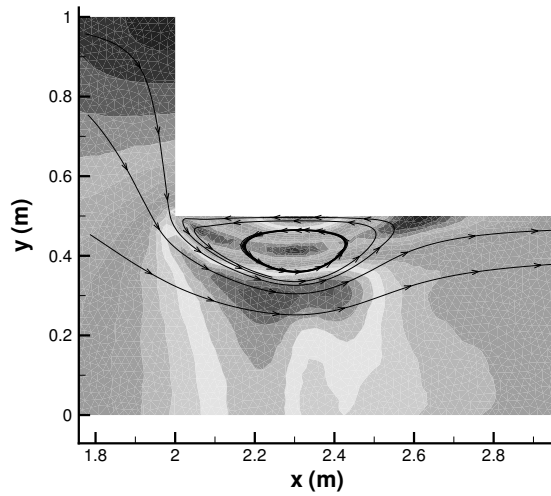


FIGURE C.4: Jet formation in stepwise convergent channel after 5×10^3 iterations. Four streamlines are shown in a contour plot of the local Mach number ($M_{in} = 0.15$, $k^{(4)} = 0.01$, preconditioning switched off, domain dimensions are $5000 \times 1000 \times 10 \text{ mm}^3$).

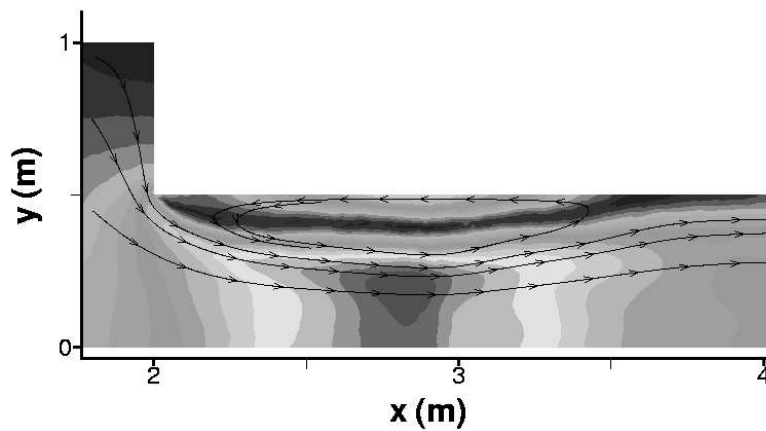


FIGURE C.5: Jet formation in stepwise convergent channel after 20×10^3 iterations. Four streamlines are shown in a contour plot of the local Mach number ($M_{in} = 0.15$, $k^{(4)} = 0.01$, preconditioning switched off, domain dimensions are $5000 \times 1000 \times 10 \text{ mm}^3$).

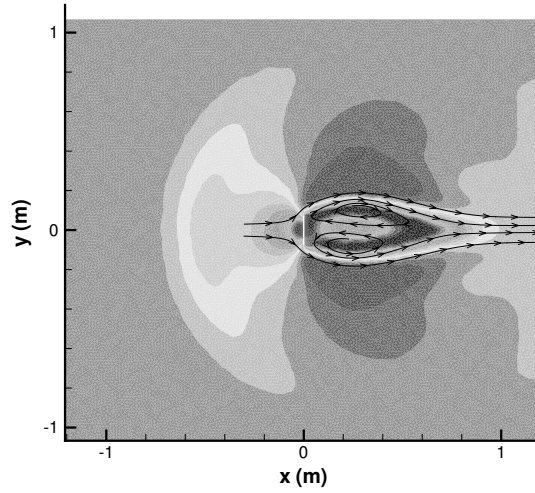


FIGURE C.6: Flow around 90° inclined plate, 4 streamlines are shown (10^4 iterations, contour plot of Mach number for $0.01 \leq M \leq 0.05$ and 15 levels, preconditioning switched on, $\epsilon = 0.01$, $k^{(4)} = 0.08$, $CFL = 0.1$, $M_{in} = 4.5 \times 10^{-2}$).

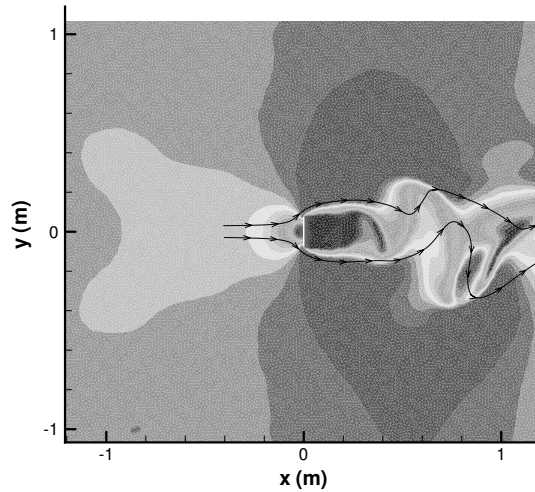


FIGURE C.7: Flow around 90° inclined plate, 2 streamlines are shown (3×10^4 iterations, contour plot of Mach number for $0.01 \leq M \leq 0.05$ and 15 levels, preconditioning switched on, $\epsilon = 0.01$, $k^{(4)} = 0.02$, $CFL = 0.1$, $M_{in} = 4.5 \times 10^{-2}$).

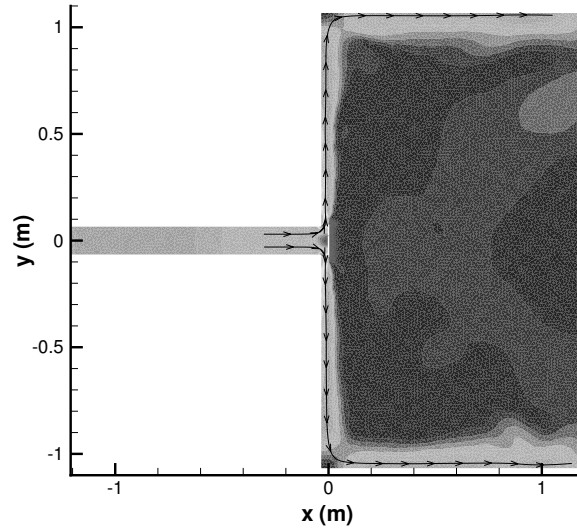


FIGURE C.8: *Flow through port and around 90° inclined plate, 2 streamlines are shown (50×10^3 iterations, contour plot of Mach number for $0.01 \leq M \leq 0.08$ and 15 levels, preconditioning switched on, $\epsilon = 0.01$, $k^{(4)} = 0.02$, $CFL = 0.1$, $M_{in} = 4.5 \times 10^{-2}$).*

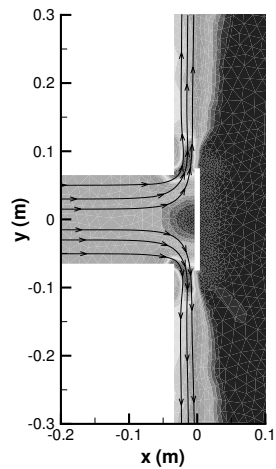


FIGURE C.9: *Flow through port and around 90° inclined plate, 6 streamlines are shown (50×10^3 iterations, contour plot of Mach number for $0.01 \leq M \leq 0.08$ and 15 levels, preconditioning switched on, $\epsilon = 0.01$, $k^{(4)} = 0.02$, $CFL = 0.1$, $M_{in} = 4.5 \times 10^{-2}$).*

REFERENCES

- Abernathy, F. H.: 1962, Flow over an inclined flat plate, *J. Basic Eng., Trans. ASME* **84**, 380.
- Åbom, M. and Bodén, H.: 1988, Error analysis of two-microphone measurements in ducts with flow, *J. Acoust. Soc. Am.* **83**, 2429–2438.
- Artner, D.: 1999, Thermoplastics in reciprocating compressor valves: Part I - influence on efficiency and reliability, *Proc. IMechE Conf. Trans. C542/074* pp. 375–385.
- Artner, D. and Spiegl, B.: 2001, Functional composites - the solution for better reliability of compressor valves, *Proc. EFRC Conf., Den Haag* pp. 83–91.
- Backus, J.: 1963, Small-vibration theory of the clarinet, *J. Acoust. Soc. Am.* **35**, 305.
- Batchelor, G. K.: 2000, An introduction to fluid dynamics, Cambridge University Press, Cambridge.
- Belmabrouk, H. and Michard, M.: 2001, Analysis of the swirl effect on turbulent length scales in an ICE cylinder by two-point LDV, *Int. J. Heat Fluid Flow* **22**, 417–423.
- Birch, J. M. and Dickinson, M. H.: 2001, Spanwise flow and the attachment of the leading-edge vortex on insect wings, *Nature* **412**, 729–733.
- Bloch, E.: 1969, Numerical solution of free boundary problems by the method of steepest descent, *Phys. Fluids, suppl. II* pp. 129–132.
- Bluestein, D., Rambod, E. and Gharib, M.: 2000, Vortex shedding as a mechanism for free emboli formation in mechanical heart valves, *J. Biomech. Eng.* **122**, 125–134.
- Bodén, H. and Åbom, M.: 1986, Influence of errors on the two-microphone method for measuring acoustic properties in ducts, *J. Acoust. Soc. Am.* **79**, 541–549.
- Böswirth, L.: 2000, Strömung und Ventilplattenbewegung in Kolbenverdichterventilen, Eigenverlag, Vienna.
- Böswirth, L.: 2001, Öllebe-Effekte in Kolbenverdichterventilen, *Proc. EFRC Conf., Den Haag* pp. 33–43.
- Brower, W. B., Eisler, E., Filkorn, E. J., Gonenc, J., Plati, C. and Stagnitti, J.: 1993, On the compressible flow through an orifice, *J. Fluids Eng., Trans. ASME* **115**, 660–664.
- Buchanan, R. A. and Watkins, G.: 1976, The industrial archaeology of the stationary steam engine, Allen Lane.
- Buligan, G., Paone, N., Revel, G. M. and Tomasini, E. P.: 2002, Valve lift measurement by optical techniques in compressors, *Proc. Int. Compr. Eng. Conf. C13-5, Purdue* .
- Busemann, A.: 1937, Hodographmethode der Gasdynamik, *Zeitschrift für angew. Math. und Mech.* **17**, 73–79.
-

- Caillé, V. and Laumonier, J.: 1998, Effect of periodic aerodynamic pulsation on flow over a confined butterfly valve, *Exp. Fluids* **25**, 362–368.
- Caughey, D. A. and Turkel, E.: 1988, Effects of numerical dissipation on finite-volume solutions of compressible flow problems, *AIAA paper* **88-0621**.
- Chen, J. M. and Fang, Y. C.: 1998, Lock-on of vortex shedding due to rotational oscillations of a flat plate in a uniform stream, *J. Fluids Struct.* **12**, 779–798.
- Chima, R. V., Turkel, E. and Schaffer, S.: 1987, Comparison of three explicit multi grid methods for the Euler and Navier-Stokes equations, *AIAA paper* **87-0602**.
- Chorin, A. J.: 1967, A numerical method for solving incompressible viscous flow problems, *J. Comp. Phys.* **2**, 12–26.
- Chow, W. L., Ke, Z. P. and Lu, J. Q.: 1995, The interaction between a jet and a flat plate - an inviscid analysis, *J. Fluids Eng., Trans. ASME* **117**, 623–627.
- Chung, J. Y. and Blaser, D. A.: 1980a, Transfer function method of measuring acoustic intensity in a duct system with flow, *J. Acoust. Soc. Am.* **68**, 1570–1577.
- Chung, J. Y. and Blaser, D. A.: 1980b, Transfer function method of measuring in-duct acoustic properties: I Theory, *J. Acoust. Soc. Am.* **68**, 907–913.
- Chung, J. Y. and Blaser, D. A.: 1980c, Transfer function method of measuring in-duct acoustic properties: II Experiment, *J. Acoust. Soc. Am.* **68**, 914–921.
- Cierniak, S.: 2001, Life-Cycle-Costs von Kolben- und Turbokompressoren, *Erdöl Erdgas Kohle* **11**, 511–517.
- Costagliola, M.: 1950, The theory of spring-loaded valves for reciprocating compressors, *J. Appl. Mech.* pp. 415–420.
- Cremers, J., Friedel, L. and Pallaks, B.: 2001, Validated sizing rule against chatter of relief valves during gas service, *J. Loss Prev. Process Ind.* **14**, 261–267.
- Crighton, D. G., Dowling, A. P., Ffowcs Williams, J. E., Heckl, M. and Leppington, F. G.: 1992, *Modern methods in analytical acoustics*, Springer-Verlag, London.
- Cyklis, P.: 1994, CFD simulation of the flow through reciprocating compressor self-acting valves, *Proc. Int. Compr. Eng. Conf., Purdue* pp. 427–432.
- Dalmont, J. P., Gilbert, J. and Ollivier, S.: 2003, Nonlinear characteristics of single-reed instruments: Quasistatic volume flow and reed opening measurements, *J. Acoust. Soc. Am.* **114**, 2253–2262.
- Danbon, F. and Sollic, C.: 2000, Aerodynamic torque of a butterfly valve - influence of an elbow on the time-mean and instantaneous aerodynamic torque, *J. Fluids Eng., Trans. ASME* **122**, 337–344.
- Darmofal, D. L. and Schmid, P. J.: 1996, The importance of eigenvectors for local preconditioners of the Euler equations, *J. Comp. Phys.* **127**, 346–362.
- De Hart, J., Baaijens, F. P. T., Peters, G. W. M. and Schreurs, P. J. G.: 2003, A computational fluid-structure interaction analysis of a fiber-reinforced stentless aortic valve, *J. Biomechanics* **36**, 699–712.
- De Vries, M. P., Schutte, H. K., Veldman, A. E. P. and Verkerke, G. J.: 2002, Glottal flow through a two-mass model: Comparison of Navier-Stokes solutions with simplified models, *J. Acoust. Soc. Am.* **111**, 1847–1853.
- Den Hartog, J. P.: 1985, *Mechanical vibrations*, Dover.
- Deschamps, C. J., Ferreira, R. T. S. and Prata, A. T.: 1996, Turbulent flow through valves of reciprocating compressors, *Proc. Int. Compr. Eng. Conf., Purdue* pp. 377–382.
-

- Deverge, M., Pelorson, X., Vilain, C., Lagrée, P. Y., Chentouf, F., Willems, J. and Hirschberg, A.: 2003, Influence of collision on the flow through in-vitro rigid models of the vocal folds, *J. Acoust. Soc. Am.* **114**, 3354–3362.
- Dickinson, M. H., Lehmann, F. O. and Sane, S. P.: 1999, Wing rotation and the aerodynamic basis of insect flight, *Science* **284**, 1954–1960.
- Dowell, E. H. and Hall, K. C.: 2001, Modeling of fluid-structure interaction, *Annu. Rev. Fluid Mech.* **33**, 445–490.
- Edwards, J. R. and Liou, M. S.: 1998, Low-diffusion flux-splitting methods for flows at all speeds, *AIAA J.* **36**, 1610–1617.
- Ellington, C. P.: 1984a, The aerodynamics of hovering insect flight: I. The quasi-steady analysis, *Phil. Trans. Roy. Soc. London B* **305**, 1–15.
- Ellington, C. P.: 1984b, The aerodynamics of hovering insect flight: IV. Aerodynamic mechanisms, *Phil. Trans. Roy. Soc. London B* **305**, 79–113.
- Ellington, C. P.: 1984c, The aerodynamics of hovering insect flight: V. A vortex theory, *Phil. Trans. Roy. Soc. London B* **305**, 115–144.
- Elson, J. P. and Soedel, W.: 1974, Simulation of the interaction of compressor valves with acoustic back pressures in long discharge lines, *J. Sound. Vibr.* **34**, 211–220.
- Page, A. and Johansen, F. C.: 1927, On the flow of air behind an inclined flat plate of infinite span, *Proc. Roy. Soc. London A* **116**, 170–197.
- Firstenberg, M. S., Vandervoort, P. M., Greenberg, N. L., Smedira, N. G., McCarthy, P. M., Garcia, M. J. and Thomas, J. D.: 2000, Noninvasive estimation of transmitral pressure drop across the normal mitral valve in humans: Importance of convective and inertial forces during left ventricular filling, *J. Am. Coll. Cardiology* **36**, 1942–1945.
- Fox, R. W. and McDonald, A. T.: 1994, Introduction to fluid mechanics, John Wiley & Sons, Purdue.
- Frenkel, M. I.: 1969, Kolbenverdichter: Theorie, Konstruktion und Projektierung, VEB Verlag Technik, Berlin.
- Fritz, C., Wolfe, J., Kergomard, J. and Caussé, R.: 2003, Playing frequency shift due to the interaction between the vocal tract of the musician and the clarinet, *Proc. SMAC Conf.* pp. 263–266.
- Frommann, O. and Friedel, L.: 1998, Analysis of safety relief valve chatter induced by pressure waves in gas flow, *J. Loss Prev. Process Ind.* **11**, 279–290.
- Fry, S. N., Sayaman, R. and Dickinson, M. H.: 2003, The aerodynamics of free-flight maneuvers in *Drosophila*, *Science* **300**, 495–498.
- Gharib, M.: 1996, Perspective: The experimentalist and the problem of turbulence in the age of supercomputers, *J. Fluids Eng., Trans. ASME* **118**, 233–242.
- Gharib, M., Kremers, D., Koochesfahani, M. M. and Kemp, M.: 2002, Leonardo's vision of flow visualization, *Exp. Fluids* **33**, 219–223.
- Goldsworthy, F. A.: 1953, On the flow in a high-pressure valve, *Proc. Roy. Soc. London A* **218**, 69–87.
- Guillard, H. and Viozat, C.: 1999, On the behaviour of upwind schemes in the low Mach number limit, *Computers Fluids* **28**, 63–86.
- Gustafsson, B.: 1980, Asymptotic expansions for hyperbolic problems with different time-scales, *SIAM J. Numer. Anal.* **17**, 623–634.
- Hamilton, J. F. and Schwerzler, D. D.: 1978, Computer aided design studies of a multiple cylinder refrigeration compressor, *J. Mech. Design, Trans. ASME* **100**, 599–603.
-

- Hayashi, S., Hayase, T. and Kurahashi, T.: 1997, Chaos in a hydraulic control valve, *J. Fluids Struct.* **11**, 693–716.
- Hirschberg, A., Van de Laar, R. W. A., Marrou-Maurières, J. P., Wijnands, A. P. J., Dane, H. J., Kruijswijk, S. G. and Houtsma, A. J. M.: 1990, A quasi-stationary model of air flow in the reed channel of single-reed woodwind instruments, *Acustica* **70**, 146–154.
- Hofmans, G. C. J.: 1998, Vortex sound in confined flows, PhD thesis, Eindhoven University of Technology, The Netherlands.
- Horsten, J. B. A. M.: 1990, On the analysis of moving heart valves: A numerical fluid-structure interaction model, PhD thesis, Eindhoven University of Technology, The Netherlands.
- Huang, C. and Kim, R. H.: 1996, Three-dimensional analysis of partially open butterfly valve flows, *J. Fluids Eng., Trans. ASME* **118**, 562–568.
- Huang, Z. J., Merkle, C. L., Abdallah, S. and Tarbell, J. M.: 1994, Numerical simulation of unsteady laminar flow through a tilting disk heart valve: Prediction of vortex shedding, *J. Biomechanics* **27**, 391–402.
- Hulshoff, S. J., Hirschberg, A. and Hofmans, G. C. J.: 2001, Sound production of vortex-nozzle interactions, *J. Fluid Mech.* **439**, 335–352.
- Idelchik, I. E.: 1994, Handbook of hydraulic resistance, CRC Press.
- Ingard, K. U.: 1988, Fundamentals of waves and oscillations, Cambridge Univ. Press.
- Ishizawa, S., Watanabe, T. and Takahashi, K.: 1987, Unsteady viscous flow between parallel disks with a time-varying gap width and a central fluid source, *J. Fluids Eng., Trans. ASME* **109**, 394–402.
- Jameson, A.: 1995, Analysis and design of numerical schemes for gas dynamics, 1: artificial diffusion, upwind biasing, limiters and their effect on accuracy and multigrid convergence, *Comp. Fluid Dyn.* **4**, 171–218.
- Jameson, A., Schmidt, W. and Turkel, E.: 1981, Numerical solution of the Euler equations by finite volume methods using Runge-Kutta time-stepping schemes, *AIAA paper* **81-1259**.
- Joo, J. M., Oh, S. K., Kim, G. K. and Kim, S. H.: 2000, Optimal valve design for reciprocating compressor, *Proc. Int. Compr. Eng. Conf., Purdue* pp. 451–458.
- Jorgenson, P. and Chima, R.: 1989, An unconditionally stable Runge-Kutta method for unsteady flows, *AIAA paper* **89-0205**.
- Kerh, T., Lee, J. J. and Wellford, L. C.: 1997, Transient fluid-structure interaction in a control valve, *J. Fluids Eng., Trans. ASME* **119**, 354–359.
- Khalifa, H. E. and Liu, X.: 1998, Analysis of stiction effect on the dynamics of compressor suction valve, *Proc. Int. Compr. Eng. Conf., Purdue* pp. 87–92.
- Kiya, M. and Arie, M.: 1977, A contribution to an inviscid vortex-shedding model for an inclined flat plate in uniform flow, *J. Fluid Mech.* **82**, 223–240.
- Kok, J. C.: 1998, An industrially applicable solver for compressible turbulent flows, PhD thesis, Delft University of Technology, The Netherlands.
- Kolkman, P. A.: 1980, Development of vibration-free gate design: Learning from experience and theory, *Practical Experiences with flow-induced vibrations*, Ed. Naudascher and Rockwell, Springer-Verlag, CI pp. 351–373.
- Kreyszig, E.: 1993, Advanced engineering mathematics, John Wiley & Sons, Columbus.
- Kruisbrink, A. C. H.: 1996, The dynamic behaviour of check valves in pipeline systems, PhD thesis, Delft University Press, The Netherlands.
-

- Kundu, P. K.: 1990, Fluid mechanics, Academic Press, Dania.
- Lamb, H.: 1932, Hydrodynamics, Cambridge University Press.
- Laney, C. B.: 1998, Computational gasdynamics, Cambridge University Press.
- Lee, D.: 1998, Design criteria for local Euler preconditioning, *J. Comp. Phys.* **144**, 423–459.
- Lee, T. S.: 1999, Air influence on hydraulic transients on fluid system with air valves, *J. Fluids Eng., Trans. ASME* **121**, 646–650.
- Leonard, S. M.: 1996, Increase reliability of reciprocating hydrogen compressors, *Hydrocarbon Processing Jan.*, 67–74.
- Linke, A., Fischer, M. and Göldner, H.: 1974, Komplexrechenprogramm zur Optimierung und Simulation des Arbeitsprozeßablaufs und des Ventilverhaltens von Hubkolbenverdichtern, *Luft- und Kältetechnik* **10**, 302–306.
- Liu, C., Zheng, X. and Sung, C. H.: 1998, Preconditioned multigrid methods for unsteady incompressible flows, *J. Comp. Phys.* **139**, 35–57.
- Ludu, A., Betto, A. and Regner, G.: 2000, Endoscope video of compressor valve motion and pressure measurement assist simulations for design improvements, *Proc. Int. Compr. Eng. Conf., Purdue* pp. 443–450.
- Luo, X.: 2004, Unsteady flows with phase transition, PhD thesis, Eindhoven University of Technology, The Netherlands.
- Lynn, P. A. and Fuerst, W.: 1994, Introductory digital signal processing, John Wiley & Sons, Bristol, New York.
- Machu, E. H.: 1994, The two-dimensional motion of the valve plate of a reciprocating compressor valve, *Proc. Int. Compr. Eng. Conf., Purdue* pp. 403–408.
- Machu, E. H.: 2001, Valve dynamics of reciprocating compressor valves with more than one degree of freedom, *Proc. IMechE Conf. Trans. C591/018* pp. 503–519.
- MacLaren, J. F. T., Tramschek, A. B., Sanjines, A. and Pastrana, O. F.: 1975, Unsteady flow in a two-stage intercooled reciprocating compressor system, *Conf. Inst. Mech. Eng. C106/75* pp. 51–62.
- Maier, A., Sheldrake, T. H. and Wilcock, D.: 2000a, Geometric parameters influencing flow in an axisymmetric IC engine inlet port assembly: Part I - valve flow characteristics, *J. Fluids Eng., Trans. ASME* **122**, 650–657.
- Maier, A., Sheldrake, T. H. and Wilcock, D.: 2000b, Geometric parameters influencing flow in an axisymmetric IC engine inlet port assembly: Part II - parametric variation of valve geometry, *J. Fluids Eng., Trans. ASME* **122**, 658–665.
- Marassi, M., Castellini, P., Pinotti, M. and Scalise, L.: 2004, Cardiac valve prosthesis flow performances measured by 2D and 3D-stereo particle image velocimetry, *Exp. Fluids* **36**, 176–186.
- Matos, F. F. S., Prata, A. T. and Deschamps, C. J.: 1999, Numerical analysis of the dynamic behaviour of plate valves in reciprocating compressors, *Proc. IMechE Conf. Trans. C542/031* pp. 453–462.
- Matos, F. F. S., Prata, A. T. and Deschamps, C. J.: 2002, Numerical simulation of the dynamics of reed type valves, *Proc. Int. Compr. Eng. Conf. C15-2, Purdue* .
- Mavriplis, D. J.: 1997, Unstructured grid techniques, *Annu. Rev. Fluid Mech.* **29**, 473–514.
- McElhaney, K. L.: 2000, An analysis of check valve performance characteristics based on valve design, *Nucl. Eng. Design* **197**, 169–182.
- Merati, P., Macelt, M. J. and Erickson, R. B.: 2001, Flow investigation around a V-sector ball valve, *J. Fluids Eng., Trans. ASME* **123**, 662–671.
-

- Middleton, J. W.: 2001, Reciprocating compressors: reliability in design: a practical approach, *Proc. EFRC Conf., Den Haag* p. 95.
- Miller, F. K. and Brisson, J. G.: 1999, Development of a low-dissipation valve for use in a cold-cycle dilution refrigerator, *Cryogenics* **39**, 859–863.
- Milton, B. E., Behnia, M. and Ellerman, D. M.: 2001, Fuel deposition and re-atomisation from fuel/air flows through engine inlet valves, *Int. J. Heat Fluid Flow* **22**, 350–357.
- Misra, A., Behdinan, K. and Cleghorn, W. L.: 2002, Self-excited vibration of a control valve due to fluid-structure interaction, *J. Fluids Struct.* **16**, 649–665.
- Naudascher, E. and Rockwell, D.: 1994, Flow-induced vibrations: An engineering guide, A.A. Balkema, Rotterdam.
- Nederveen, C. J.: 1969, Acoustical aspects of woodwind instruments, F. Knuf, Amsterdam.
- Nieter, J. J. and Singh, R.: 1984, A computer simulation study of compressor tuning phenomena, *J. Sound Vibr.* **97**, 475–488.
- Nkonga, B.: 2000, On the conservative and accurate CFD approximations for moving meshes and moving boundaries, *Comput. Meth. Appl. Mech. Eng.* **190**, 1801–1825.
- Ottitsch, F. and Scarpinato, P.: 2000, CFD a viable engineering tool for compressor valve design or just a toy?, *Proc. Int. Compr. Eng. Conf., Purdue* pp. 423–428.
- Pandey, K. N. and Chand, S.: 2003, An energy based fatigue crack growth model, *Int. J. Fatigue* **25**, 771–778.
- Patankar, S. V.: 1980, Numerical heat transfer and fluid flow, Hemisphere Publishing Corporation.
- Pérez-Segarra, C. D., Cadafalch, J., Rigola, J. and Oliva, A.: 1999, Numerical study of turbulent fluid-flow through valves, *Proc. IMechE Conf. Trans. C542/021* pp. 399–408.
- Peters, M. C. A. M.: 2001, Evaluation of low frequency pulsation damping devices, *Proc. EFRC Conf., Den Haag* pp. 253–264.
- Peters, M. C. A. M., Hirschberg, A., Reijnen, A. J. and Wijnands, A. P. J.: 1993, Damping and reflection coefficient measurements for an open pipe at low Mach and low Helmholtz numbers, *J. Fluid Mech.* **256**, 499–534.
- Poinsot, T. J. and Lele, S. K.: 1992, Boundary conditions for direct simulations of compressible viscous flows, *J. Comp. Phys.* **101**, 104–129.
- Popiel, C. O. and Turner, J. T.: 1991, Visualization of high-blockage flow behind a flat plate in a rectangular channel, *J. Fluids Eng., Trans. ASME* **113**, 143–146.
- Possamai, F. C., Ferreira, R. T. S. and Prata, A. T.: 2001, Pressure distribution in laminar radial flow through inclined disks, *Int. J. Heat Fluid Flow* **22**, 440–449.
- Prasad, B. G. S. and Woollatt, D.: 2000, Valve dynamic measurements in a VIP compressor, *Proc. Int. Compr. Eng. Conf., Purdue* pp. 361–368.
- Pulliam, T. H.: 1986, Artificial dissipation models for the Euler equations, *AIAA J.* **24**, 1931–1940.
- Pullin, D. I. and Wang, Z. J.: 2004, Unsteady forces on an accelerating plate and application to hovering insect flight, *J. Fluid Mech.* **509**, 1–21.
- Put, F.: 2003, Numerical simulation of condensation in transonic flows, PhD thesis, University of Twente, The Netherlands.
- Quartapelle, L. and Napolitano, M.: 1983, Force and moment in incompressible flows, *AIAA J.* **21**, 911–913.
-

- Rienstra, S. W. and Hirschberg, A.: 2001, An introduction to acoustics, IWDE 01-03, Eindhoven University of Technology, The Netherlands.
- Roe, P. L.: 1981, Approximate Riemann solvers, parameter vectors, and difference schemes, *J. Comp. Phys.* **43**, 357–372.
- Roe, P. L.: 1986, Characteristic-based schemes for the Euler equations, *Annu. Rev. Fluid Mech.* **18**, 337–365.
- Rolt, L. T. C.: 1963, Thomas Newcomen: The prehistory of the steam engine.
- Rosenfeld, M., Avrahami, I. and Einav, S.: 2002, Unsteady effects on the flow across tilting disk valves, *J. Biomech. Eng.* **124**, 21–29.
- Sears, W. R.: 1954, General theory of high speed aerodynamics, vol. VI, Princeton University Press, Princeton.
- Sirbaugh, J. R.: 1995, A fourth order dissipation model for vortex dominated flows, *AIAA paper* **95-2168**.
- Spiegl, B. J., Mlekusch, B. A. and Artner, D.: 1999, Thermoplastics in reciprocating compressor valves: Part II - stress calculations in short-fibre reinforced thermoplastic (SF RTP) compressor valve plates, *Proc. IMechE Conf. Trans. C542/038* pp. 387–398.
- St Hilaire, A. O., Wilson, T. A. and Beavers, G. S.: 1971, Aerodynamic excitation of the harmonium reed, *J. Fluid Mech.* **49**, 803–816.
- Stehr, H., Pavlevski, M. and Divadkar, N.: 2003, Process know-how and the effects on product design and engineering, *Proc. EFRC Conf., Vienna* pp. 219–224.
- Steinrück, P.: 2003, Joint research at the EFRC, *Proc. EFRC Conf., Vienna* pp. 177–181.
- Stijnen, J. M. A., De Hart, J., Bovendeerd, P. H. M. and Van de Vosse, F. N.: 2004, Evaluation of a fictitious domain method for predicting dynamic response of mechanical heart valves, *J. Fluids Struct.* **19**, 835–850.
- Sung, H. J., Kim, Y. N. and Hyun, J. M.: 1994, Discrete vortex simulation of pulsating flow behind a normal plate, *J. Fluids Eng., Trans. ASME* **116**, 862–869.
- Swanson, R. C. and Turkel, E.: 1997, Multistage schemes with multigrid for Euler and Navier-Stokes equations, *NASA Tech. paper* **3631**.
- Tannehill, J. C., Anderson, D. A. and Pletcher, R. H.: 1997, Computational fluid mechanics and heat transfer, Taylor & Francis.
- Tarnopolsky, A. Z., Fletcher, N. H. and Lai, J. C. S.: 2000, Oscillating reed valves- an experimental study, *J. Acoust. Soc. Am.* **108**, 400–406.
- Thiel, E.: 1990, Kinematik und Druckverlust selbsttätiger Ventile oszillierender Verdrängerpumpen, PhD thesis, Universität Erlangen-Nürnberg, Germany.
- Thomann, H.: 1976, Oscillations of a simple valve connected to a pipe, *J. Appl. Math. Phys.* **27**, 23–40.
- Thomann, H.: 1978, Oscillations of a simple valve connected to a pipe: part II Experiments, *J. Appl. Math. Phys.* **29**, 75–84.
- Touber, S.: 1976, A contribution to the improvement of compressor valve design, PhD thesis, University of Delft, The Netherlands.
- Turkel, E.: 1987, Preconditioned methods for solving the incompressible and low speed compressible equations, *J. Comp. Phys.* **72**, 277–298.
- Turkel, E.: 1999, Preconditioning techniques in computational fluid dynamics, *Annu. Rev. Fluid Mech.* **31**, 385–416.
-

- Turkel, E., Fiterman, A. and Van Leer, B.: 1994, Preconditioning and the limit of the compressible to the incompressible flow equations for finite difference schemes, *In: Frontiers of computational fluid dynamics*, Ed. Caughey and Hafez pp. 215–234.
- Ulrich, J. and Zengerle, R.: 1996, Static and dynamic flow simulation of a KOH-etched microvalve using the finite-element method, *Sensors Actuators A* **53**, 379–385.
- Van den Berg, J.: 2002, Space-time discretization of hyperbolic conservation equations, Report TS-11, University of Twente, The Netherlands.
- Van Noordenburg, M. B. H.: 1999, On leading-edge vortex flow and vortex breakdown, PhD thesis, University of Twente, The Netherlands.
- Van Steenhoven, A. A. and Van Dongen, M. E. H.: 1979, Model studies of the closing behaviour of the aortic valve, *J. Fluid Mech.* **90**, 21–32.
- Van Zon, J. C. P.: 1989, Stromingsgeïnduceerde klepinstabiliteiten, Report R-1024-A, Eindhoven University of Technology, The Netherlands.
- Van Zon, J., Hirschberg, A., Gilbert, J. and Wijnands, A. P. J.: 1990, Flow through the reed channel of a single reed music instrument, *Suppl. J. Physique, Coll. Physique C2* **51**, 821–824.
- Venkateswaran, S., Li, D. and Merkle, C. L.: 2003, Influence of stagnation regions on preconditioned solutions at low speeds, *AIAA paper* **03-0435**.
- Venkateswaran, S. and Merkle, L.: 1999, Analysis of preconditioning methods for the Euler and Navier-Stokes equations, *Von Karman Inst., Lect. Ser.* 1999-03 .
- Vilain, C. E., Pelorson, X., Fraysse, C., Deverge, M., Hirschberg, A. and Willems, J.: 2004, Experimental validation of a quasi-steady theory for the flow through the glottis, *J. Sound Vibr.* **276**, 475–490.
- Volpe, G.: 1993, Performance of compressible flow codes at low Mach numbers, *AIAA J.* **31**, 49–56.
- Weclas, M., Melling, A. and Durst, F.: 1998, Flow separation in the inlet valve gap of piston engines, *Prog. Energy Combust. Sci.* **24**, 165–195.
- Weiss, J. M., Maruszewski, J. P. and Smith, W. A.: 1999, Implicit solution of preconditioned Navier-Stokes equations using algebraic multigrid, *AIAA J.* **37**, 29–36.
- Weiss, J. M. and Smith, W. A.: 1995, Preconditioning applied to variable and constant density flows, *AIAA J.* **33**, 2050–2057.
- Wesseling, P.: 2001, Principles of computational fluid dynamics, Springer, Delft.
- Westphal, M.: 1893, Beitrag zur Grössenbestimmung von Pumpenventilen, *Z.d.V.D.I.* **37**, 381–386.
- Will, G. and Flade, G.: 2003, Simulation of the flow in ring valves, *Proc. EFRC Conf., Vienna* pp. 239–244.
- Yeung, W. W. H. and Parkinson, G. V.: 1997, On the steady separated flow around an inclined flat plate, *J. Fluid Mech.* **333**, 403–413.
- Yeung, W. W. H. and Parkinson, G. V.: 2000, Base pressure prediction in bluff-body potential-flow models, *J. Fluid Mech.* **423**, 381–394.
- Ziada, S., Shine, S. J. and Bühlmann, E. T.: 1986, Self-excited vibrations of reciprocating compressor plate valves, *Proc. Int. Compr. Eng. Conf., Purdue* pp. 398–414.
- Ziada, S., Shine, S. J. and Bühlmann, E. T.: 1987, Tests on the flutter of a multi-ring plate valve, *Proc. Int. Conf. Flow Induced Vibr., BHRA* **J2**, 393–401.
-

SUMMARY

Motivation & Objective. Reciprocating compressors are widely used in gas transportation, gas storage and petrochemical industries. They are able to compress gas in a wide range of pressure ratios and flow rates. In reciprocating compressors, the piston motion results in periodic increases and decreases in the cylinder volume. The entry and exit ports to the cylinder are regulated by valves that periodically open and close. The compressor can be considered as the heart of an installation and must operate reliably for several years. The compressor valves have been identified as the primary cause of unscheduled shutdowns of reciprocating compressors.

The principle of operation of all types of automatic valves is similar, although structural details may differ considerably. Therefore, it is possible to distinguish the same *basic functional elements* in valves of different design. Consider the discharge of gas in a reciprocating compressor. When gas is flowing from the high pressure side in the cylinder volume through the *port* of the discharge valve into the plenum chamber, the flow separates at the sharp edges of the *seat* and the *plate*. This plate is connected to a *preloaded spring* which on its turn is connected to the *limiter*, which is fixed in space. Because of the action of the gas force, the plate is pushed against the limiter. When the pressure in the cylinder volume of the compressor becomes sufficiently low, the discharge process is stopped automatically, because the gas force acting on the plate is not able to keep the valve open. The spring force pushes the plate on the seat and closes the valve.

For more than a century people have been modeling the fluid-structure interaction phenomena that are present in automatic valves. The majority of these theories makes use of semi-empirical coefficients. These coefficients have to be determined experimentally assuming quasi-steady flow. We refer to these theories as traditional valve theories. The objective of the present research is twofold, i.e. i) the analysis of the semi-empirical coefficients as they appear in traditional valve theory, ii) the validation of the quasi-steady flow assumption in traditional valve theory.

Basic Valve Theory. The historical developments of valve design, application, research and modeling have been discussed for different types of automatic valves as they appear in nature and engineering. For most of the cases a valve is considered as a mechanical device and for valve design fluid dynamical aspects are secondary. The traditional valve theories have been unified in one theory which we refer to as the Basic Valve Theory. This theory considers the valve as a *black box* and provides a semi-empirical description of the valve state variables. The state variables are: i) the pressure difference across the valve, ii) the volume-flow rate through the valve and iii) the valve opening (plate height). Linear and non-linear

properties of this theory have been investigated by means of stability analysis and numerical simulations. For two limiting cases, i.e. Stokes flow and inviscid flow, the coefficients in the semi-empirical expressions have been obtained. In order to show the diagnostic properties of the Basic Valve Theory, a two-stage compressor system has been analysed.

Computational Fluid Dynamics. The flow in a compressor valve can be characterized as a high Reynolds number with a large variation in local Mach number. Therefore the present computational study employs the flow model based on the Euler equations for describing inviscid compressible flow. To handle the regions with low velocities, the method of local preconditioning has been applied. Time-derivative preconditioning increases the convergence speed of the method. Preconditioning of the artificial dissipation terms in the flux scheme increases the numerical accuracy in regions with very low Mach number. The geometry of compressor valves is rather complex. Therefore the Euler equations are discretized for an unstructured mesh. Several test cases show the ability of the computational method to simulate steady- and unsteady low Mach number flows. However, in the case of the flow through valves, it has been found that this method suffers from numerical instabilities. Several strategies to tackle this problem have been discussed, addressing modifications of: geometry and mesh, artificial dissipation, initial condition and boundary conditions. We feel that the preconditioned Euler method for unstructured meshes is not suited for computations of flows with large stagnation regions such as occur in compressor valves.

Laboratory Experiments. A *model valve* has been designed with a geometry that is simpler than commercial compressor valves. In the experimental setup this model valve has been mounted at the end of a pipe. An experimental method has been designed that is able to measure simultaneously the instantaneous pressure difference across the valve, the instantaneous volume-flow rate through the valve and the instantaneous valve opening. Assuming acoustical flow in the pipe, the Two-Microphone Method has been extended towards reconstruction in the time domain of both the dynamic pressure and the dynamic flow rate. A light-intensity method has been employed to measure the valve opening.

Steady flow experiments have been performed for a 'hovering' valve plate. The semi-empirical coefficients of the model valve and a commercially available compressor valve have been compared. Reverse flow experiments showed an increased flow resistance that is approximately constant for a wide range of the Reynolds number.

The Basic Valve Theory is based on steady flow characteristics. Therefore unsteady flow conditions in the model valve have been considered in order to assess effects of unsteadiness on the performance of the Basic Valve Theory. The instantaneous gas force was predicted rather accurately by the theory. However, it has also been observed that flow hysteresis effects are present. These effects are postulated to be caused by a periodically detaching and reattaching flow at the seat. This hypothesis has been enforced by predicting the valve state variables, employing the Extended Valve Theory. The Extended Valve Theory takes into account the flow inertia in the port and the plate speed. However, further exploration of the validity of the Extended Valve Theory for a broader range of parameters has to be performed.

For a commercial compressor valve also unsteady flow experiments have been conducted. For the limiter almost inelastic plate collisions have been observed. The collisions of the plate with the seat resulted in severe rocking effects. These effects are postulated to be caused by the absence of gas damping, the relatively low spring force and the position of the guiding holes in the plate.

SAMENVATTING

Motivatie & Doel. Zuigercompressoren worden wereldwijd toegepast in de gas transport-, gas opslag- en petrochemische industrie. Deze compressoren kunnen gas comprimeren in een groot bereik van drukverhoudingen en debieten. In een zuigercompressor resulteert de beweging van de zuiger in een periodiek toenemen en afnemen van het volume in de cilinder. De intree- en uitlaat poorten van dit volume worden geregeld door kleppen (ventielen) die periodiek open en dicht gaan. De compressor kan als het hart van een installatie worden beschouwd en dient gedurende vele jaren betrouwbaar te zijn. De compressor kleppen kunnen worden geïdentificeerd als de hoofdoorzaak van onvoorziene compressor uitval.

Ondanks het feit dat geometrische details van de klep behoorlijk kunnen verschillen, is het principe van de werking van alle typen compressor kleppen gelijk. Daarom kunnen dezelfde basis elementen in diverse kleppen worden onderscheiden. Als gas van de hoge-druk zijde in de cilinder door de *poort* van de ontladklep stroomt, zal de stroming loslaten aan de scherpe randen van de *zitting* en de *plaat*. Deze plaat is verbonden met een *voorgespannen veer* die op haar beurt is verbonden met het *stop element*. Dit stop element is gefixeerd. Door het gas wordt de plaat tegen het stop element gedrukt. Als de druk in de cilinder van de compressor afneemt neemt de gaskracht af, zodat als de gaskracht voldoende laag is de klep niet meer open kan worden gehouden. De veerkracht drukt de plaat tegen de zitting, sluit de klep en stopt automatisch het ontladproces.

Al meer dan een eeuw is de wisselwerking tussen fluidum en klep in automatische kleppen gemodelleerd. De meerderheid van deze modellen maakt gebruik van semi-empirische uitdrukkingen. De parameters in deze uitdrukkingen dienen experimenteel bepaald te worden voor stationaire stromingen. Deze modellen worden traditionele klep modellen genoemd. Het doel van dit onderzoek is tweeledig: i) de analyse van de parameters in de semi-empirische uitdrukkingen, en ii) de validatie van de aanname dat de stroming als quasi-stationair mag worden beschouwd.

Basale Klep Theorie. In het proefschrift worden de historische ontwikkelingen van klep ontwerp, toepassing, onderzoek en modellering gepresenteerd voor verschillende typen van automatische kleppen zoals die voorkomen in de natuur en de techniek. In de meeste gevallen wordt een klep beschouwd als een mechanisch apparaat waarbij voor het klep ontwerp de stromingseigenschappen minder belangrijk worden geacht. De traditionele klep modellen zijn gebaseerd op een theorie die we de Basale Klep Theorie noemen. Deze theorie beschouwt de klep als een *zwarte doos* en geeft het verband tussen toestandsvariabelen middels semi-empirische uitdrukkingen. De toestandsvariabelen zijn: i) de drukval over de klep, ii) het volume debiet door de klep en iii) de klep opening (plaat hoogte). Lineaire en niet-lineaire

eigenschappen van deze theorie zijn onderzocht middels een stabiliteits analyse en numerieke simulaties. Voor twee limiet gevallen, namelijk de Stokes stroming en de niet-viskeuze stroming, zijn de parameters in de semi-empirische uitdrukkingen bepaald. Om de voorspellende waarde van de Basale Klep Theorie te onderzoeken is een twee-traps compressor systeem geanalyseerd. Deze analyse is in staat om te indentificeren welke van de vier kleppen defect is.

Numerieke Stromingsleer. De stroming door een compressor klep kan worden gekarakteriseerd als een stroming met een hoog Reynolds getal en met een grote variatie in lokaal Mach getal. Daarom wordt in de numerieke studie gebruik gemaakt van de Euler vergelijkingen voor de beschrijving van een niet-viskeuze compressibele stroming. Om de gebieden met lage snelheden aan te kunnen worden gebruikt wordt gemaakt van lokaal preconditioneren. Dit zorgt voor een verhoogde convergentiesnelheid en tegelijkertijd voor een nauwkeurige representatie van de stroming in gebieden met een laag Mach getal. De geometrie van een compressor klep en zijn directe omgeving is ingewikkeld. Daarom worden de Euler vergelijkingen gediscrètiseerd op een ongestructureerd grid. Diverse test problemen laten zien dat de methode in staat is om zowel stationaire als instationaire stromingen met laag Mach getal te simuleren. Echter, in het geval van een klepstroming zijn er geen numeriek stabiele oplossingen gevonden. Diverse strategieën om dit probleem op te lossen zijn besproken zoals aanpassing van de geometrie, aanpassen van kunstmatige dissipatie, andere beginvoorwaarde en verbeterde randvoorwaarden. De indruk bestaat dat de gepreconditioneerde Euler vergelijkingen, gediscrètiseerd op een ongestructureerd grid niet geschikt is voor berekeningen van stromingen met grote 'dood-water' gebieden zoals de stroming in compressor kleppen.

Laboratorium Experimenten. Er is een *modelklep* ontworpen met een eenvoudigere geometrie dan die van commerciële compressor kleppen. In de experimentele opstelling is de modelklep bevestigd aan het uiteinde van een pijp. Een experimentele methode is ontworpen om gelijktijdig het drukverschil over de modelklep, het debiet door de modelklep en de opening van de modelklep te meten. Dit isoleert meettechnisch de klep van zijn omgeving zodat de Basale Klep Theorie gevalideerd kan worden. De Twee-Microfoon Methode is uitgebreid van analyse in het frequentie domein naar reconstructies in het tijd domein. Voor akoestische golven in de pijp kan nu zowel de dynamische druk als het dynamische debiet worden bepaald. Een licht-intensiteit methode wordt gebruikt om de klep opening te meten.

Stationaire stromingen zijn opgewekt voor een 'zwevende' klep plaat. De parameters in de semi-empirische uitdrukkingen bepaald voor de modelklep zijn vergeleken met die bepaald voor een commerciële compressor klep. Experimenten waarbij de richting van de stroming is omgedraaid lieten een constante verhoogde stromingsweerstand zien, dit voor een groot bereik van het Reynolds getal.

De Basale Klep Theorie is gebaseerd op de aanname van een quasi-stationaire stroming. Voor de validatie van deze aanname zijn experimenten uitgevoerd met instationaire stromingen door de modelklep. Het blijkt dat de gaskracht redelijk nauwkeurig wordt voorspeld door de Basale Klep Theorie. Echter, er is ook waargenomen dat hysteresis effecten optreden. De hypothese is dat deze effecten worden veroorzaakt door het periodiek loslaten en opnieuw aanhechten van de stroming over de klepzitting. Deze hypothese wordt versterkt door de resultaten van een uitbreiding van de Basale Klep Theorie, waarin de traagheid van de gasstroming in de poort zowel als de plaat snelheid in rekening worden gebracht. Echter, verder onderzoek naar de uitbreiding van de Basale Klep Theorie is nodig in een grotere parameter ruimte.

Voor een commerciële compressor klep zijn instationaire stromingen onderzocht. Bijna inelastische botsingen tussen plaat en stop element zijn waargenomen. De botsingen tussen plaat en zitting resulteerden in hevige schommel effecten. Deze effecten worden toegeschreven aan: afwezigheid van gas demping, relatief kleine veerkracht en de positie van de geleidingsgaatjes in de plaat.

DANKWOORD

Het onderzoek dat in dit proefschrift wordt beschreven heb ik uitgevoerd van mei 2001 tot mei 2005 in de groep Technische Stromingsleer van de Universiteit Twente. Hierbij wil ik iedereen bedanken die heeft bijgedragen aan dit onderzoek. Echter, sommigen wil ik in het bijzonder bedanken.

Mijn eerste promotor Harry Hoeijmakers en mijn dagelijks begeleider Rob Hagmeijer formuleerden het onderzoeksvoorstel. Naast het aandragen van voor mij geheel nieuwe concepten (zoals preconditionering van de Euler vergelijkingen) hebben jullie altijd met goede zorg mijn vorderingen begeleid en veel ruimte open gelaten om mezelf te ontwikkelen tot zelfstandig onderzoeker. Ik meen dat het is gelukt! Mijn tweede promotor Mico Hirschberg dank ik voor zijn onophoudelijke stroom van ideeën voor mogelijke onderzoeksonderwerpen en het uitbuiten van resultaten!

Op de vakgroep heb ik altijd met plezier gediscussieerd en geleefd met de afstudeerders en de vele promovendi. In het bijzonder dank ik Christian Veldhuis en Frits Put voor de uitwisselingen van successen en discussies over zwakke en sterke punten van algoritmen uit de numerieke stromingsleer. Zowaar kreeg de afkorting CFD humoristische herdefinities (van Continuous Failure & Disappointment tot Coffee Filling Duty). Hüseyin Özdemir dank ik voor zijn enthousiaste hulp bij het oplossen van allerlei software problemen, en in het bijzonder voor zijn hulp bij het maken van het omslag van dit proefschrift. Verder dank ik Philip Kelleners voor de behulpzame uitleg van EFD-Flow en zijn MeshMan.

De vele cursussen, excursies, workshops en conferenties waren altijd een aardige combinatie van werk en secundaire arbeidsvoorwaarden. Hierbij denk ik met name aan de activiteiten van het Burgerscentrum en het European Forum for Reciprocating Compressors (EFRC). Door de inspanningen van Carsten Martens (ICEM) heb ik zeer snel een basis niveau grid generatie geleerd. Door Hans Vermeer en Edo Wissink (Grasso Products) en Lau Koop (Thomassen Compression) is mij in een vroegtijdig stadium de complexe praktijk van het bouwen en analyseren van zuigercompressoren duidelijk geworden. Carlos Infante Ferreira liet mij geduldig vele copieën maken van zijn proceedings van de compressor conferenties in Purdue. Bedankt allemaal!

Tijdens de zomer van 2003 en het voorjaar van 2004 heb ik met plezier experimenteel onderzoek verricht bij de afdeling Flow and Structural Dynamics (PULSIM) van TNO-TPD in Delft. Het was een bijzonder leerzame en gezellige tijd door de omgang met de groepsleden. In het bijzonder dank ik René Peters voor het mogelijk maken van metingen op de Luchtstroming Test Faciliteit. Verder, Jeroen Bolle en Jan Smeulers kwamen vrijwel wekelijks met zowel aandachtspunten van meettechnische zaken als voorstellen tot verbetering van de

modelklep. Graham McMeeking dank ik voor het aanbrengen van de aluminium coating op een kunststof klepplaat. Verder bedank ik Jaap van der List voor het construeren van mijn speciale model klep. Jouw enthousiasme en precisie werk deed me zeer goed!

During the final stage of my PhD-project I participated in the Basic Product Training course of Ariel Corporation. I would like to thank EFRC, in particular Siegmund Cierniak and George Kopsick, for this free-of-charge trip to Mount Vernon, USA. The informal discussions with end-users made me realize that reciprocating compressors have a truly complex task in a wide field of operation.

Tenslotte dank ik de mensen die ik het langste ken. Mijn broer en familie voor interesse en relativerende opmerkingen. Mijn ouders voor al het voorbereidende werk door studie aanmoediging gedurende alle fasen in mijn jeugd en voor de onvoorwaardelijke zorg!

CURRICULUM VITAE

Remco Habing werd op 30 juli 1975 geboren in Hengelo (O). Op het Eindhovens Protestants Lyceum haalde hij in 1992 het HAVO diploma. Hierna startte hij de studie Technische Natuurkunde aan de Hogeschool Eindhoven. Tijdens de gekozen differentiatie Toegepaste Natuurkunde werd een stage uitgevoerd bij het Natuurkundig Laboratorium van Philips in Eindhoven onder begeleiding van dr. G.W. 't Hooft. Het onderwerp betrof: 'Meting van de Levensduur van Minderheidsladingsdragers in III-V Halfgeleiders'. De afstudeeropdracht werd uitgevoerd bij Océ Research in Venlo onder begeleiding van ing. J.P.J.C. Rooijackers. Het onderwerp betrof: 'Printkwaliteit van Pixellijnen'. In juni 1996 werd het diploma behaald.

Hierna startte hij de studie Technische Natuurkunde aan de Technische Universiteit Eindhoven. De afstudeeropdracht werd uitgevoerd in de vakgroep Werveldynamica onder begeleiding van prof.dr.ir. G.J.F. Van Heijst en dr. H.J.H. Clercx. Het onderwerp betrof: 'Vortex Statistics of Decaying 2D Turbulence'. In december 1999 werd het diploma behaald.

Hierna startte hij als medewerker onderzoek aan de Universiteit Twente bij de vakgroep Technische Stromingsleer. Na een periode van oriëntatie op promotie onderzoek aan meer-fasen stromingen werd in mei 2001 een begin gemaakt met het onderzoek aan compressor kleppen. Tijdens twee perioden van in totaal 5 maanden is experimenteel onderzoek verricht bij de afdeling Flow and Structural Dynamics van TNO-TPD in Delft. Het onderzoek aan compressor kleppen, uitgevoerd onder begeleiding van prof.dr.ir. H.W.M. Hoeijmakers, prof.dr.ir. A. Hirschberg en dr.ir. R. Hagmeijer, resulteerde in dit proefschrift.
